UNIVERSITY OF MESSINA

DEPARTMENT OF ENGINEERING

DOCTORAL PROGRAM IN

“CHEMISTRY AND ENGINEERING OF MATERIALS AND CONSTRUCTIONS”

New Nanomaterials for the Development of High-performance Chemical Sensors for Environmental Applications

Doctoral Thesis of:

Simona Crispi

Supervisor:

Prof. Giovanni Neri

PhD Coordinator:

Prof. Edoardo Proverbio

XXXVI Cycle Doctorial Course: 2022/20223

SSD CHIM-07

Acknowledgments

I am happy how I spent these PhD years because I gained a lot of experience and had the opportunity to compare and interact with research groups or researchers from different sectors. For me, it was a period of growth from a professional and personal point of view.

I would like to express my thanks to my supervisor, **Prof. Giovanni Neri**, for welcoming me into his research group, believing in me and giving me the opportunity to learn. I also thank him for supporting me over these years, giving me security in the most anxious moments.

I thank the prof. **Nicola Pinna** for welcoming me into his research group, giving me the opportunity to learn atomic layer deposition and also to be able to use the instrumentation independently.

I offer my thanks to Prof. **Claudia Espro** and **Daniela Ianazzo** for helping me over these years.

I thank my dear colleagues and friends **Angelo, Rahyanne, Viviana and Kaveh** for collaborating, for helping me and above all for passing on their experience and kindness to me, lightening even the heaviest days.

A special thank you to my **Husband,** the one who supports me every day, who gives me the strength to face my days and above all who takes care of me.

Overview of Research activity

The ecosystem is the set of living organisms and non-living substances with which the former establish an exchange of matter and energy, in a delimited area. It changes over the years, followed by adaptation by living and non-living species. The change can be of natural origin, that is, it follows cycles; man-made effects are often added to natural cycles. Man, in addition to being part of the ecosystem, influences its change with his development. The social, economic, and technological development that has occurred over the years has caused an enormous impact on the natural cycle of the ecosystem. Excessive emission of pollutants into the environment has caused serious impacts on living and non-living species. Formation of acid rains, excessive climate change, greenhouse effect and biodiversity are the main consequences found. At the beginning of the 20th century, man took action with regulations aimed at reducing polluting emissions and environmental impacts. In addition to reducing emissions, they must be monitored, therefore various advanced technologies are adopted, such as spectroscopy, chromatography and so on. In recent years, sensors-based technology adopted for monitoring has been gaining traction. A sensor is a device or module that detects physical or chemical changes, such as pressure, heat, humidity, motion, force, concentrations, which are converted into signals that can be detected and analyzed. Nowadays we are surrounded by sensors, so much so that we find them in smartphones, in fire alarms, even in the biological sector to simply detect glucose in the blood, so we can say that we encounter them in everyday life.

The PhD project focused on the development of chemical sensors with particular attention to conductometric gas sensors and then with electrochemical sensors. The design of a chemical sensor follows several phases, the first of which focuses on the study of the analyte or gas that is intended to be detected and the most suitable sensitive material to be used. The second phase concerns the synthesis of the sensitive material, we try to synthesize nanomaterials using simple methods. Once the nanomaterial has been synthesized, in the next phase it is characterized with appropriate analytical techniques to verify its morphology and chemical-physical properties. Subsequently, methods of deposition of the nanomaterial on the sensor platform for fabricating the sensor devices are developed and finally sensing tests are carried out to validate their performances in the laboratory and in field.

In this project, sensitive nanomaterials were synthesized and deposited on suitable platforms. Sol-gel, spray-pyrolysis, Atomic Layer Deposition (ALD) and co-precipitation have been adopted to design new sensitive nanomaterials to be deposited on resistive platforms for the development of conductometric gas sensors and on screen-printed carbon electrode (SPCE) platform for fabricating electrochemical sensors. Semiconductor metal oxides such as zinc oxide (ZnO), cobalt oxide/iron oxide heterojunctions (Co_3O_4/Fe_2O_3), cobalt oxide/ copper oxide (Co_3O_4/ CuO), carbon dots from biomass, films with specific thicknesses (WS_2 and NiO), nickel ferrite spinels ($NiFe_2O_4$) and metal-organic compounds (MOFs) have been developed for the design of chemical sensors discussed in this thesis. The developed conductometric sensors allow the detection of gases such as formaldehyde, NO, NO_2, NH_3, ethanol, acetone. The electrochemical sensor was designed for the monitoring of glucose.

Thesis Outline

➢ Chapter 1: The Environment

The first chapter briefly discusses man's impact on the environment. An impact that the promoter himself is trying to remedy. The types of pollution and its management through control and monitoring agencies will be discussed. There are also different systems and methods that will be briefly listed for each pollutant.

➢ Chapter 2: Sensors

A brief overview of sensors will be given in this chapter describing what a sensor is and the classifications. Chemical sensors will be described, classified and the main parameters for developing a chemical sensor will be discussed.

➢ Chapter 3: Chemoresistive sensor

With this chapter we will enter the heart of the thesis and will represent the basic concepts to be able to understand the research activity discussed in the following chapters. The mechanisms of a chemoresistive sensor and the nanomaterials of which a sensor can be developed, will be described. The sensitive nanomaterials and the syntheses to obtain them will be described. Finally, the design and fabrication of the device will be described.

➢ Chapter 4: Experimental Methods and Characterization Techniques

The chapter represents the first part of the experimental activity; in fact it will cover all the design phases of a conductometric gas sensor from the synthesis of the nanomaterial to the sensing tests. The characterizations carried out on the nanomaterials obtained will be described, as will their deposition on the device, the type of device used and finally the instrumental apparatus used with a detailed description.

➢ Chapter 5: Results and Discussion

The second part of the experimental activity will be discussed in this chapter. Individual developed nanomaterials will be treated in detail, describing the synthesis, the characterizations carried out and the tests carried out for the development of the final sensor. The nanomaterials were grouped according to the corresponding syntheses. They have been divided into sensitive materials obtained via: sol-gel method; pyrolysis method; Atomic Layer deposition method (ALD), plant-assisted method and co-precipitation method.

➢ Chapter 6: Side work

In this chapter, the research activity concerning the development of a non-enzymatic electrochemical glucose sensor will be discussed. In this part, the nanomaterial synthesis and characterization has been highlighted as well as the fabrication of the electrochemical sensors. The electrochemical techniques adopted during this research activity and the data obtained, were discussed. The non-enzymatic glucose sensor was validated in laboratory for detection of glucose in the blood.

➢ Chapter 7: General Conclusions

Summary chapter of the projects carried out.

Table of contents

Chapter 1: The Environment

1.1 Environmental pollution

Environmental changes are part of cycles and interactions that occur naturally. Man has always been connected to nature in all its forms. His actions, however, have often led to situations of exploitation of natural resources and environmental pollution. In December 1952, an intense gray fog descended on the sky over London for over five days, taking with it a considerable number of victims. From that day on, the environmental question appears to be increasingly debated by public opinion and by political decision-makers; a new sensitivity grows and develops, interconnected with a new form of international cooperation on environmental issues. In 1956, in fact, the English Parliament issued the *Clean Air Act*, a decree, the objective of which was to reduce emissions from domestic heating and industrial waste. The case of London was by no means isolated or circumscribed in time or space. In the following years, many other cities were protagonists of similar events.

Between the '60s and '90s political movements arose all over the globe proposing important developments and strategic plans in issues such as air pollution, the nuclear plan, the exploitation of natural resources and climate change. The European Union, first of all, in the TFEU (*Treaty on the Functioning of the European Union*) has inserted some articles which govern the combined action of individual countries for environmental development: first of all, article 191, in section "environment", explains the objectives that the EU pursues, including the improvement of the quality of the environment, the protection of human health, the prudent use of natural resources and the international promotion of measures aimed at solving the problems regional or global environment and, in particular, to combat climate change. Despite the regulations, the continuous energy demand, and the continuous economic development due to a growing population increase does not guarantee a total reduction of pollutants [1].

Air pollution is an environmental health problem that affects the lives of everyone on earth, for this reason the importance of classifying *indoor* and *outdoor* pollution arises to identify its causes and pollutants. Indoor air pollution is the contamination of air quality in closed environments such as workplaces, homes, and schools, caused by dust, dirt and emissions of certain chemical compounds. In indoor pollution, the particles and gases that lead to the onset of the phenomenon are identified. Particles (PM) are made up of soot and dust present in the air. While gases include mainly carbon monoxide (CO), nitrogen oxide (NOx), sulfur oxide (SOx), formaldehyde (CH_2O) and Volatile Organic Compounds (VOCs). The main sources are heating systems, paints, household cleaning products, cigarette smoke and the presence of mold. The increase in the concentration of these pollutants is observed in environments with high temperatures and poorly ventilated environments. Ventilation of a closed space allows the reduction of pollutants and avoids their accumulation. Specific health problems have been observed in this class of pollution such as inflammation of the eyes and throat and severe migraines. The World Health Organization (WHO) also identifies "sick building syndrome", which affects people who spend a significant amount of time indoors. (see Figure 1.1.)

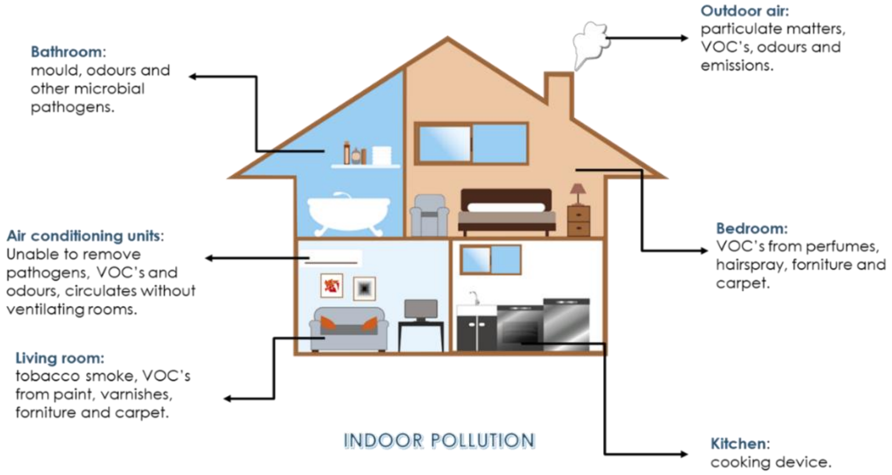

Figure 1.1. Main sources of pollutants.

Outdoor pollution is the contamination of the air outside. Generally, the major pollutants are sulfur dioxide (SOx), ozone (O_3), nitrogen oxides (NO_x), carbon dioxide (CO_2) and hydrocarbon gases. Mainly, depending on the area, it is the result of emissions from sources such as factories, fossil fuels and vehicles (see Figure 1.2.). In this case the health problems are linked to the time of exposure to these pollutants. Exposure-related effects can be a short term which include inflammation of the lungs and throat. An example is sulfur dioxide, it causes a narrowing of the airways, causing breathing problems, chest pain and wheezing. High levels of sulfur dioxide can also cause burning in the nose. Or ozone can trigger allergic symptoms.

Instead, long-term exposures may lead to an increased risk of cardiovascular and respiratory diseases [2-4].

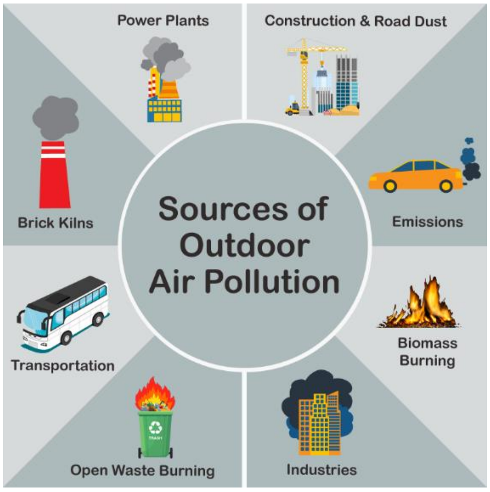

Figure 1.2. Main sources of outdoor pollutants.

It is also possible to make a more generic classification of pollutants, dividing them into primary and secondary. The primaries include toxic gases such as NOx and CO from vehicle exhausts, SOx from industrial plants, CH_4 from food digestion of animals, Radon gas from radioactive decay within the Earth's crust and Sulphur, Chlorine from vulcanic activity [5]. To the secondary ones, the pollutants that are not emitted directly but are the reaction products originating from the interaction of the primaries.

Different global organizations collect and distribute environmental data globally. Various world organizations collect and distribute environmental data at a global level, among these the United Nations (UN) monitors the climate, food supplies, population and health. The Food and Agricultural Organization (FAO) together with the Foreign Agricultural Service (FAS) monitors world food production, pesticide consumption, use of raw materials and soil (including its degradation), forests and fisheries. The World Meteorological Organization (WMO), the World Weather Watch (WWW) and the World Health Organization (WHO) monitor the global state of climate, atmosphere, air, water and food contamination. In particular, the Global Atmosphere Watch monitors atmospheric pollutants, chlorofluorocarbons (CFCs) and ozone, while the International Atomic Energy Agency monitors isotope fallout. All data is collected in a database and disseminated in the form of statistical reports [2].

1.2 Environmental monitoring

Continuous monitoring based on studies and detections of pollutants present in the environment allows the identification and reduction of impacts. Specifically, environmental monitoring includes the protection of water resources (including surface and groundwater), the detection of pollution sources, the management and disposal of waste (including possible impacts on human health), the control of air quality, the protection and management of natural resources, the evaluation of climate change, endangered species, finally a non-negligible factor is the consideration of continuous population growth linked to continuous economic development.

Earth's water is sensitive to pollution which derives from punctual sources such as industrial wastes and diffuse sources such as agrochemicals. The effects of water pollution are diverse and frequent and in many cases the compounds are toxic to aquatic fauna or carcinogens for humans if they enter drinking water supplies. Environmental protection agencies regularly analyze water samples to obtain continuous indications on the health status of water bodies. The most monitored parameters are pH, dissolved oxygen, toxicity, conductivity and suspended solids [6]. There are various methods used for water monitoring, an example is a high-resolution mass spectrometry (HR-MS), which identifies the masses of pollutants present [7], and in Table 1.1. are listed the major techniques adopted for a specific pollutant.

Table 1.1. Analytical techniques adopted to water monitoring for each pollutant.

Main pollutants	Analytical technique
Ammonia and Phosphates	ion-selective electrode and colour chemistry plus photometry
Nitrates	ion-selective electrode, colour chemistry plus photometry and UV adsoption
Metals	Voltammetry and colour chemistry plus photometry
Oils and Solvents	UV fluorescence, UV photometry, electromagnetic absorption and optical scatter and reflection.
Biochemical Oxygen Demand (BOD)	Biomass oxygen consumption
Chemical Oxygen Demand (COD) and Total Organic Carbon (TOC)	Thermal and chemical oxidation plus IR-based CO_2 detection, ozone oxidation/consumption and UV spectrometry.
Toxicity	Bacterial oxygen consumption, algal fluorescence and microbial respiration inhibition.
Dissolved Oxygen (DO)	Clark electrode and fluorescence quenching
Suspended solids	IR and visible light scatter and optical absorption

However, the analytical techniques for the emissions of air monitoring are different and depend on the type of pollutant to be detected and are showed in Table 1.2. [6]

Table 1.2. Analytical techniques adopted to air monitoring for each pollutant.

Main pollutants	Analytical technique
CO_2, CO and CH_4	Fourier-transform infra-red absorption spectroscopy (FTIR), non-dispersive infra-red absorption (NDIR) and tunable laser diode absorption spectroscopy (TLDAS).
Particulate matter (PMs)	Triboelectric, opacity and β-ray attenuation
Volatile Organic Compounds (VOCs)	flame ionisation detector (FID) and Gas Chromatography (GC)
NH_3	Fourier-transform infra-red absorption spectroscopy (FTIR), non-dispersive infra-red absorption (NDIR), tunable laser diode absorption spectroscopy (TLDAS) and chemiluminescence.
Benzene	Gas Chromatography (GC)
Metals	laser-induced breakdown spectroscopy (LIBS) and inductively coupled plasma mass spectroscopy (ICP-MS) on the laboratory.

The need to monitor the environment to protect it and protect human health becomes a challenge for scientific research with numerous detection techniques, which in many cases are expensive and are not capable of real-time detection. Since the 21st century, however, greater attention has been paid to the development of sensors that are simple to obtain, with low production costs and real-time detection.

1.3 References

1. S. Dhall, B.R. Mehta, A.K. Tyagi, K. Sood, *A review on environmental gas sensors: Materials and technologies*, Sensors International 2 (2021) 100116.
2. J.F. Artiola, I.L. Pepper, M.L. Brusseau, *Environmental Monitoring and Characterization*, Elsevier, (2004).
3. A. Chmielewski, *Monitoring, Control and Effects of Air Pollution Book, in Tech*, Crotaia (2011), ISBN 9789533075266.
4. A. Mirzaei, S. G. Leonardi, G. Neri, *Detection of hazardous volatile organic compounds (VOCs) by metal oxide nanostructures-based gas sensors: A review*, Ceram. Int., 42 (2016) 15119.
5. L. Xiong, R.G. Compton, *Amperometric gas detection: a review*, Int. J. Electrochem. Sci. 9 (2014) 7152–7181.
6. R. Bogue*, Environmental sensing: strategies, technologies and applications, Sensors review*, 28 (2008) 275-282.
7. B.I. Escher, H.M. Stapleton, E.L. Schymanski, *Tracking complex mixtures of chemicals in our changing environment*, Science 24 (2020) 367, 388–392.

Chapter 2: Sensors

2.1 Introduction

Nowadays, we see the results of science and technology through devices such as computers, photocopiers, smartphones, microwave ovens, refrigerators, air conditioning and television remote controls, smoke detectors, infrared (IR) thermometers, turning lamps on and off. These underlying technologies use sensors. A sensor is a device or module that detects physical changes, such as pressure, heat, humidity, motion, force, which are converted into signals that can be detected and analyzed [1,2]. A transducer, on the other hand, is a device that converts a quantity of energy from one form to another. The sensor is the basis of a measurement system. An ideal sensor has range, drift, calibration, sensitivity, selectivity, linearity, high resolution, reproducibility, repeatability and response time [3,4]. The advancement of sensor technology has become increasingly important, due to various applications.

In everyday life, sensor technology can be used in various ways to improve transportation, medical care, nanotechnology, mobile devices, and so on. Sensors have become an indispensable part of modern life [5]. Describing some examples of them, we find: temperature sensors used in manufacturing, agriculture, and the healthcare sectors [6,7]; proximity sensors [8]; pressure sensor, enable the creation of IoT (Internet of Things) systems that monitor pressure systems and devices [9]; Infrared (IR) sensors, which emits or detects infrared radiation and can detect and measure the heat radiated from objects [10]; humidity sensor [11] ; optical sensors, devices based on the conversion of a light signal into an electrical signal [12]; chemical sensor, whose purpose is to detect liquid and gases that include chemical changes, also, among the chemical sensors there are biosensors, a device that collect biological signals to transform them into data [5] and so on. The sensor class to use depends on the needs of the application.

2.2 Classification of sensors

It is often common to classify sensors into different categories [13,14], listed below:

- *Active and passive sensors*, whose active sensors require an external energy source for activation (such as microphones, thermistors, strain gauges and capacitive devices and inductive sensors). Active sensors are defined as parametric since the output is a function of the parameter. Passive sensors, on the other hand, do not require external energy sources (such as thermocouples, piezoelectric sensors and photodiodes). Passive sensors are in fact defined as self-generating.
- *Contact and non-contact sensors*, specifically, contact sensors require physical contact to have one stimulus (such as temperature sensors) while non-contact sensors do not require a stimulus physical contact (an example are optical and magnetic sensors).
- *Absolute and relative sensors*. Absolute sensors react to a stimulus on an absolute scale, an example are the thermistor and the strain gauge. The relative sensors detect a stimulus that can be fixed or variable, an example could be a thermocouple, which allows the temperature difference to be measured.
- *Analog and digital sensor*. An analog sensor transforms a physical quantity into an analogue form (i.e., continuous over time), these include thermocouples, resistance temperature detectors (RTDs) and strain gauges. A digital sensor instead generates an impulse. Encoders are part of it.
- *Signal Detection* based on the form of detection they can be further classified into *physical* (measure a physical quantity such as force, acceleration, flow velocity, mass, volume, density and pressure), *chemical* (a device that converts chemical information into an analytically useful signal, such as the concentration of an analyte), *thermal* (used to monitor temperature changes, generally consisting of thermocouples, thermistors and RTDs) and *biological* sensors (monitor biomolecular processes such as antibody/antigen or enzymatic interactions or cellular communication processes).

2.3 Chemical sensor

A chemical sensor is a device capable of detecting the presence of a specific substance in a specific environment, generating a signal capable of providing qualitative or quantitative information relating to the analyte species. This ability is linked to the ability of the device to transform the interaction between sensor and analyte species into a measurable signal. The interaction occurs if the sensor consists of a chemical receptor (sensitive element), capable of modifying one of its properties interacting with the analyte, and a transducer capable of interpreting and transforming the modification undergone by the receptor in a useful signal, generally electrical. In Figure 2.1 is shown a schematic representation of a chemical sensor [15].

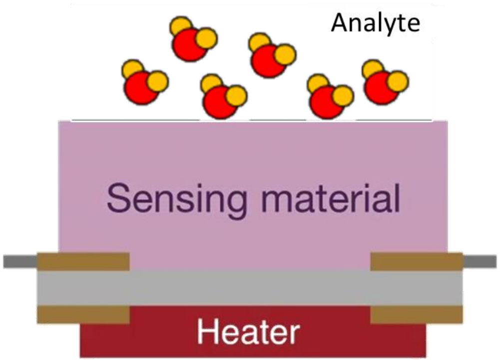

Figure 2.1. Representation of chemical sensor.

The nature of interaction between receptor and analyte species may be different. A *physical* interaction linked to the variation of electrical, optical, temperature or mass properties can be observed; *chemistry,* if the reaction between receptor and analyte involves an electrical signal; and *biochemistry*, if the signal is given by a basic biochemical process. It is not always possible to clearly distinguish the processes that are established as more than one process can occur, for example in the case of the adsorption of the analyte on the sensor surface, it is possible that two processes, physical and chemical, occur [15].

Considering that in the same environment they can be present at the same time different substances, it is necessary to use the most appropriate sensor depending on what want to analyze. Some applications may require detection of a single gas in a certain environment, in which case the sensor is required to have the ability to exclude from measures the influence of other possible substances present. Sensors are typically designed to function in well-defined conditions and for specific analytes present in certain types of environments. Other situations may instead require the detection and quantification of a specific substance or multiple substances present simultaneously in an environment. In this case, a single sensor could not be used, and even the use of multiple sensors would not guarantee adequate accuracy due to the poor specificity of each of them. In fact, a chemical sensor does not detect a single substance but rather a group or family of substances that can generate interference signals. To obtain satisfactory results, one of the strategies adopted is to use multi-component devices, consisting of a series of sensors coupled to software complexes capable of analyzing the individual signals produced. These devices are called sensor arrays and are the basis of multiple systems complexes known as electronic noses [16].

Chemical sensors are widely used in different applications such as clinical diagnostics, industrial safety and hygiene systems, process controls and product, quality controls, human comfort, emissions monitoring, and in the automotive sector, contributing to both economic and social benefits.

2.4 Main parameters of a chemical sensor

The main parameters of a sensor can be resume in accuracy, sensitivity, linearity, selectivity, interference ratio, response time, recovery time, reproducibility, hysteresis, and drift [15,17].

The *accuracy* is the ability to return a result the more like the real value of the measured variable. So that it can be defined the accuracy of an instrument, it is necessary to compare the measurement with a standard reference.

Sensitivity is the smallest variation that an instrument is capable of measuring. It is mathematically expressed as the ratio of the change in value measured R and the variation of the real value E of the quantity considered, for small variations such as:

$$S = \frac{dR}{dE} \tag{2.1}$$

It represents the slope of the tangent to the response curve of the instrument. In the case of linear instruments, the sensitivity will be constant.

Linearity is linked to the response trend in comparisons of an input signal. The closer the response curve is to a straight line, the more the system is said to be linear. Most chemical sensors are characterized by limited ranges of linearity of response with the concentration of the analyte.

Selectivity is one of the fundamental parameters for a chemical sensor, it represents the ability to detect a substance when this is mixed with others, without it being affected by related interference in the presence of the latter.

The *interference ratio* is an aspect linked to the selectivity of the device, as mentioned above, selectivity it is never absolute. Commonly, the signal returned by the sensor in the presence of a given concentration of analyte, it is different if detected in an atmosphere rather than another.

The *response time* is defined as the time interval necessary for the sensor so that its signal goes from a given initial reference value to a certain percentage of the final value that would correspond to a given concentration of analyte.

The *recovery time* in analogy to the response time is defined as that time interval necessary for the sensor for its signal to return to one certain percentage of the reference signal when it is no longer exposed to the species analyte.

The r*eproducibility* of a sensor is the ability of that device to provide the same output signal several times over time when subjected to the same quantity input.

The *hysteresis* is that phenomenon whereby a sensor presents an output signal function of the signal it assumed an instant before the last measurement. To example if we proceeded with a calibration in concentration increase ed another decreasing, a sensor subject to hysteresis would show a deviation in the response trend with the concentration of the analyte. Many electrochemical sensors exhibit hysteresis. This is often due to a residual amount of analyte reaction products, adsorbed on the sensitive surface of the sensor.

The *drift* is the variation in the output signal of an instrument when subjected to the same input signal for a certain period. In a chemical sensor the drift manifests itself with a variation over time of the output signal when subjected for long periods to the same concentration of analyte species.

2.5 Classification of the chemical sensors

Depending on the operating principle of the transducer, chemical sensors can be classified into: optical, acoustic or mass, calorimetric, biosensors, electrochemical and solid state sensors.

Optical sensors exploit the variation of an optical property of the analyte when this interacts with the receptor. The devices can then operate on variations of absorbance, reflectance, or by exploiting photoluminescence phenomena or photoionization. Sensors, that work by exploiting variations in absorbance or reflectance, use electromagnetic sources capable of interacting with the analyte, the most common ones they use infrared (IR) radiation. IR detection systems can be used for an unlimited number of applications. Detectable species must be in molecular shape and therefore made up of at least two atomic species. This aspect is necessary to obtain vibrational modes of the molecule and therefore radiation adsorption. IR sensors are highly selective and offer ranges of detectability ranging from a few parts per million up to concentrations of 100% of species to detect. Optical sensors that exploit photoluminescence phenomena and photoionization uses high energy electromagnetic sources, commonly ultraviolet (UV) or laser sources, to promote photonic emission or electronic that can be correlated to the type of substance and its concentration. Another type of optical sensors uses simple visible light detectors to measure the intensity of chemiluminescence phenomena that occur for specific molecules on particulars receptors [18].

Mass-sensitive chemical sensors transform the change in this quantity in a generally electrical signal. The change in mass is caused by accumulation of the analyte on the sensitive element of the device. To this class of chemical sensors belong to piezoelectric devices, which are based on the measurement of frequency variation of a quartz disk (oscillator). When the molecules of analyte species adsorb on the sensitive element placed on the oscillator, modifying the mass of the system and therefore its typical oscillation frequency. Piezoelectric sensors can be used both in the gaseous phase and in solution. This class of sensors also include surface wave acoustic devices (Surface Acoustic Wave, SAW), whose operation is based on modifying the propagation speed of a surface acoustic wave due to the mass variation following an accumulation of the analyte on the sensitive surface [19].

Calorimetric sensors have been used to monitor combustible gases. The operating principle is based on the detection of the exothermic combustion of gases caused by a temperature variation, the quantity of heat released is proportional to the quantity of burnt molecules, and a sensitive resistive device detects this variation. The sensor is made up of a Pt wire, a pair of pellistors (an active catalytic element is integrated with an electrically coupled catalytically passive reference element) to form a Wheastone bridge. The presence of combustible gases causes an imbalance in the bridge, as a result, the resistance changes with increasing temperature. They are cheap sensors but there is a risk of poisoning the catalyst [20].

Biosensors are a particular class of chemical sensors whose classification is mainly linked to the biological nature of the sensitive element. The most common receptors used are enzymes, bacteria, yeasts, antibodies and animal tissues or vegetables. Generally, the receptor reacts directly with the analyte substance or acts as an intermediary as a biocatalyst, producing one or more detectable effects for using an appropriate transducer. For this reason, biosensors can use optical, thermal, acoustic transduction systems, although in most cases are electrochemical [21].

Electrochemical sensors transform the electrochemical interactions between the analyte species and an electrode in an electrical signal. Commonly, they exploit reactions of oxidation-reduction, i.e. chemical reactions in which transfers of electrons, can occur through electrical stimulation or spontaneously. The sensors can be potentiometric sensors, which measure the potential of a working electrode (ion selective electrode) against a reference electrode; or voltametric sensors, they measure current flow at a constant or variable potential [19,22].

Solid state sensors exploit the variation of an electrical property of the sensitive material when it interacts with the analyte substance. This class of sensors include field effect transistors (FETs) and resistive metal oxide (MOS) sensors. A typical FET gas sensor is composed by a source and a drain electrode, a sensing material, insulating gate oxide, and an electrode gate. The response of the sensor to a gas is determined by changes in the conductance of materials before or after exposure to the target gas. The answer depends on the intrinsic properties of materials, such as work function, carrier mobility, number of layers, defect density and the band gap. One must also consider the bias voltage, the sources and the drain electrodes with adequate work functions for the transduction of electrical signals [23].

2.6 References

1. A.A. Ensafi, *An introduction to sensors and biosensors.* Electrochemical Biosensors, 1st ed.; A.A. Ensafi, Ed.; Elsevier: Cambridge, MA, USA (2019) 1–10.
2. A.A. Ensafi, H. Karimi-Maleh,; M. Ghiaci, M. Arshadi, *Characterization of Mn-nanoparticles decorated organo-functionalized* SiO_2 *-*Al_2O_3 *mixed-oxide as a novel electrochemical sensor: Application for voltammetric determination of captopril*, J. Mater. Chem. 21 (2011) 15022–15030.
3. D.R. Theavenot, K. Toth, R.A. Durst, G.S. Wilson, *Electrochemical biosensors: Recommended definitions and classification,* Biosens. Bioelectron. 16 (2001) 121–131.
4. C. Dincer, R. Bruch, E. Costa-Rama, M.T. Fernández-Abedul, A. Merkoçi, A. Manz, G.A. Urban, F. Güder, Disposable *Sensors in Diagnostics, Food, and Environmental Monitoring*. Adv. Mater. 31 (2019) 1806739.
5. M. Javaid, A. Haleem, S. Rab, R. Pratap Singh, R. Suman, *Sensors for daily life: A review,* Sensors International 2 (2021) 100121.
6. P.R. Childs, J.R. Greenwood, C.A. Long, Review of temperature measurement, Rev. Sci. Instrum. 71 (8) (2000) 2959–2978.
7. V.K. Rai, *Temperature sensors and optical sensors*, Appl. Phys. B 88 (2) (2007) 297–303.
8. F. Dehkhoda, J. Frounchi, H. Veladi, *Capacitive proximity sensor design tool based on finite element analysis*, Sens. Rev. (2010).
9. Y. Zang, F. Zhang, C.A. Di, D. Zhu, *Advances of flexible pressure sensors toward artificial intelligence and health care applications*, Materials Horizons 2 (2) (2015) 140–156.
10. D. Xu, Y. Wang, B. Xiong, T. Li, *MEMS-based thermoelectric infrared sensors: a review,* Front. Mech. Eng. 12 (4) (2017) 557–566.
11. A. Kapic, A. Tsirou, P.G. Verdini, S. Carrara, *Humidity sensors for high energy physics applications: a review,* IEEE Sensor. J. 20 (18) (2020) 10335–10344.
12. M.F. Ferreira, E. Castro-Camus, D.J. Ottaway, J.M. Lopez-Higuera, X. Feng, W. Jin, Q. Quan, *Roadmap on optical sensors,* J. Opt. 19 (8) (2017), 083001.
13. V.K. Khanna, *Introduction to nanosensors*, Nanosensors: Physical, Chemical, and Biological, 1st ed.; V.K. Khanna, Ed.; CRC Press: Boca Raton, FL, USA (2012) 37–40.

14. R.M. White, *A sensor classification scheme*, IEEE Trans. Ultrason. Ferroelectr. Freq. Control. 34 (1987) 124–126.
15. A. D'Amico, C. Di Natale*, Introduction to sensors*, ARACNE editor, (2008).
16. Di Gilio, J. Palmisani, S. Petraccone, A. Fornaro, G. de Gennaro, *An integrated high temporal resolution approach to monitor VOCs concentrations and odor annoyance near a petroleum plant*, Environmental Engineering and Management Journal 10 (2018), 2373-2378.
17. Dey, *Semiconductor metal oxide gas sensors: A review*, Materials Science & Engineering B 229 (2018) 206–217.
18. McDonagh, C. S. Burke, and B. D. MacCraith, *Optical Chemical Sensors*, Chem. Rev. 108 (2) (2008) 400-422.
19. P. Kassala, D.M. Steinbergb and I.M. Steinberg*, Wireless chemical sensors and biosensors: a review*, Sensors and Actuators B, 266 (2018) 228-245.
20. N. Illyaskutty, O. Kansizoglu, O. Akdag, B. Ojha, J. Knoblauch ID and H. Kohler, *Miniaturized Single Chip Arrangement of a Wheatstone Bridge Based Calorimetric Gas Sensor*, Chemosensors 6 (2018) 22.
21. Wadhera, T. Kakkar, D. Wadhwa, G. Wadhawa, B. Raji, *Recent Advances and Progress in Development of the Field Effect Transistor Biosensor: A Review*, J. Electron. Mater. 48 (2019) 7635–7646.
22. X. Panga, Marvin D. Shawb, S. Gillot, A.C. Lewis, *The impacts of water vapour and co-pollutants on the performance of electrochemical gas sensors used for air quality monitoring,* Sensors and Actuators B 266 (2018) 674–684.
23. M. Rajapakse, G. Anderson, C. Zhang, R. Musa, J. Walter, M. Yu, G. Sumanasekera and J.B. Jasinski, *Gas adsorption and light interaction mechanism in phosphorene-based field-effect transistors*, Phys. Chem. Chem. Phys., 22 (2020) 5949–5958.

Chapter 3: Chemoresistive Sensors

3.1 Introduction

Solid state sensors include resistive sensors. Chemoresistive-type gas sensors are the most marketed sensor type due to their simplicity of manufacture, high sensitivity, long-term stability, and especially low cost [1]. The device is structured by two metal electrodes interdigitated on an insulating substrate (alumina or silicon oxide) and a heater under the substrate to heat the sensor [2]. A sensing layer is deposited between metal electrodes. The pair of electrodes are incorporated inside of the sensitive material allow the measurement of the resistance related to the concentration of the adsorbed gas. The heating element is used to control and maintain the temperature of the sensitive element at optimal operating conditions. The heater is commonly made of platinum or one of its alloys and depending on the structure and geometry of the sensor, it can be a wire or a deposited coil above a substrate.

The sensing layer is a nanomaterial which can be a semiconductor metal oxide (MOS), a conductive polymer or a carbon compounds (such as carbon nanotubes and graphene), metal-organic compounds (MOF), also heterojunctions composed from MOS and carbon part. The electrical resistance/conductance of sensitive materials change second the physical adsorption between the sensing layer and the gas target. The mechanism is closely related to the intrinsic nature of sensing layer, as surface area, donor density, porosity, acid–base property, the presence of catalyst, and operating temperature [3].

3.2. Mechanism of a chemoresistive gas sensor

The operating principle of chemoresistive gas sensors is related to the properties of the sensitive film to vary its electrical characteristics when a gas interacts with it. In particular, the variation in electrical conductivity is the measurable parameter that can be correlated with the gas concentration.

Regarding the electrical conductivity of semiconductor materials, it is possible to distinguish two different one's mechanisms depending on whether they affect the bulk or the surface of the grains. The conductivity of bulk is linked to the crystalline lattice that constitutes the individual grains of which the material is made, while the surface conductivity depends on the geometry that it delimits the boundary between one grain and the adjacent one. These regions known as edges of grain, have unsaturated bonds which favor the interaction with the gas and therefore the conductivity variation. In the case of chemoresistive sensors the conductivity of surface is of greater interest for operational purposes [4].

In crystal lattice structures, the electrons of atoms that constitute cannot take on any energetic value but rather is they are allowed to locate themselves only and exclusively at appropriate energy levels included intervals. These intervals are known as energy bands permitted, the forbidden energy intervals between the permitted bands take the band name gap. In a crystal the highest energy range populated by electrons is called the *valence band* (VB), while the higher energy interval is separated from a forbidden energy gap it is called *conduction band* (CB). Only electrons present in the conduction band contribute to the electrical conductivity of the material [5]. Depending on the width of the band gap, it is possible to distinguish three different classes of materials such as insulators, semiconductors and metals, as in Figure 3.1. The insulators are characterized by a large forbidden gap between the valence band and the conduction band (≥10 eV) therefore, will be necessary to provide high energy values so that an electron can be promoted to the valence band and be like that available for management. The opposite situation is presented by the materials metallic in which the valence band and the conduction band are overlapped, the energy gap in this case is zero. Under these conditions, the electrons already being available in conduction band, the material has electrical conductivity for any temperature value. Semiconductor materials have an intermediate behavior. In this case the energy interval forbidden turns out to be sufficiently small (~ 0.5 ÷ 5 eV) so that even small energies are sufficient to promote the electrons into the conduction band. This can be obtained by increasing the temperature.

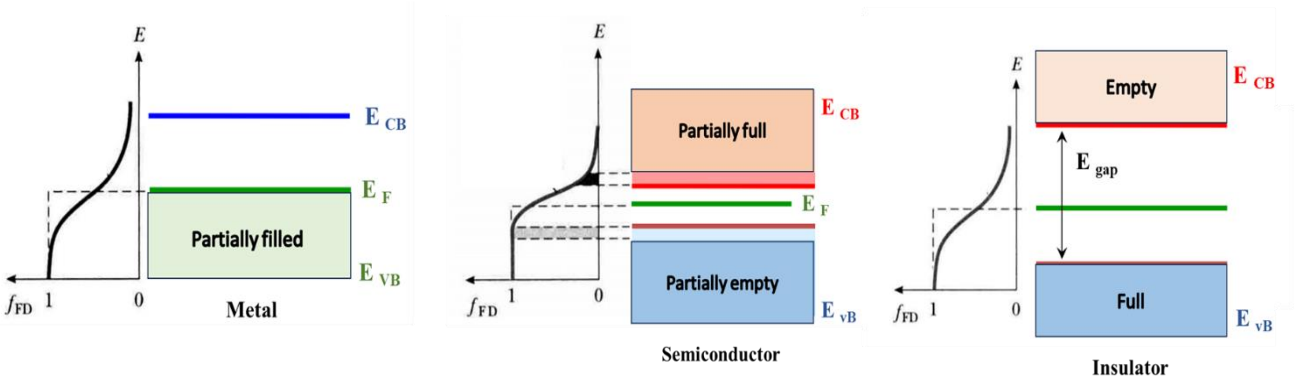

Figure 3.1. Band diagram of metal, semiconductor and insulator.

Regarding semiconductors, the presence of irregularities in the lattice crystalline gives the possibility of having available states within the forbidden gap, favoring the promotion of electrons into the conduction band. This condition allows an increase in electrical conductivity of the material. On the external surface of the crystalline grains or at the interface between a grain and the other, there is inevitably an abrupt interruption in the structural regularity of the lattice. Consequently, the atoms arranged along this region are in one state intrinsically different from those located inside the crystal, therefore present several atoms different than bulk. Not being bonded on one side with other atoms are electrically unsaturated, this causes the surface atoms present a high reactivity towards molecules of species different when compared to an atom present inside the resulting crystal stabilized by neighboring atoms. At the grain boundaries the regularity is loss of the lattice that characterizes the crystal. This perturbation of the lattice periodicity is often sufficient to create new energy states localized within the levels prohibited between valence and conduction band.

If we consider ionic solids (such as many metal oxides), the presence of a different number of ions or surface charges generates a condition in which the cations tend to attract electrons acting as acceptors, anions possessing an extra electron tend to behave as donors. At the surface of the grain, they are present free energy states and therefore the possibility of having donor or acceptor levels in the band prohibited. The presence of free energy states creates a migration of electrons from within of the bulk towards the surface, to reduce the free energy of the system. Such a phenomenon leads to the establishment of a layer of surface charge accumulation counterbalanced by an accumulation of charge of opposite sign due to the bulk atoms that are behave like donors. A double layer made up of ions is therefore formed positively charged which act as space charge localized inside of the crystal, and by negatively charged surface layers. Consequently, come to create a depletion region with a corresponding electric field associated with it. In the grain boundaries of a polycrystalline material, due to the effect of described phenomenon, a Schottky potential is established. For an electron to migrate between one grain and another it is necessary that sufficient energy is provided to overcome this barrier [6].

The resistance variation mechanism is different in the case of semiconductors *n-type* or *p-type* and in the case of oxidizing or reducing gaseous species. The distinction between *n-type or p-type* semiconductors consists in doping the semiconductor with atoms of other materials, giving it an excess of negative (*n-type*) or positive (*p-type*) charges, (see Figure 3.2). In a *n-type* semiconductor where the majority carriers are electrons, the interaction with a reducing gas result in an increase in conductivity, on the contrary the interaction with an oxidizing gas such as oxygen, results in a reduction in conductivity. In the case of *p-type* semiconductors where the carriers' gaps are the majority, the behavior in the presence of the two gaseous species is opposite to the previous case [7].

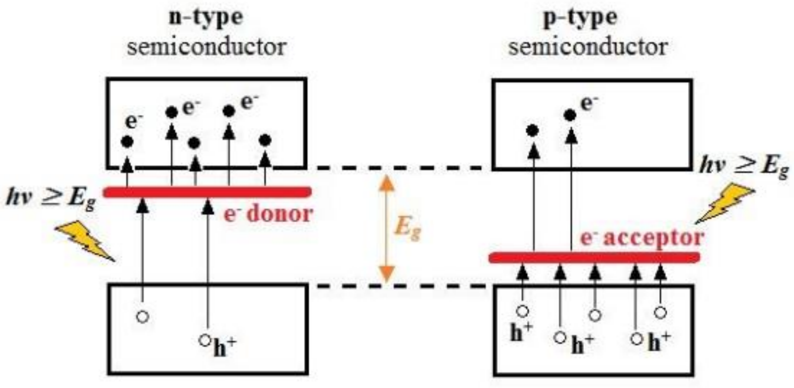

Figure 3.2. Diagram of *n-* and *p-type* semiconductor [8].

The semiconductor is exposed to air, this involves an interaction of the material with oxygen (O_2) molecules, and this influence the response of the sensor. Chemisorption of O_2 molecules is promoted by the formation of oxygen vacancies from the surface of the material as metals have a higher oxidation state than the group of elements. The following phenomenon is observed in equation 3.1:

$$O^{2-}_{(bulk)} \leftrightarrow \frac{1}{2} O_{2(g)} + V_O^{2-} \leftrightarrow \frac{1}{2} O_{2(g)} + V_O^{-} + e^{-} \leftrightarrow \frac{1}{2} O_{2(g)} + V_O + 2\,e^{-} \tag{3.1}$$

Donor states (reduced metal cations) or oxygen vacancies are available to chemisorb oxygen molecules present in air as shown in equation 3.2 or available to restore lattice O^{2-} anions, as in equation 3.3.

$$O_{2(g)} + 4\,e^{-} \leftrightarrow O_2^{-}{}_{(ads)} + 3\,e^{-} \leftrightarrow 2\,O^{-}{}_{(ads)} + 2\,e^{-} \leftrightarrow 2O^{2-}{}_{(ads)} \tag{3.2}$$

$$O_{2(g)} + 2\,V_O + 4\,e^{-} \leftrightarrow 2\,O^{2-}{}_{(bulk)} \tag{3.3}$$

As a result, the donor states are less occupied by electrons, the negative charge is localized on the chemisorbed oxygen, a potential barrier is formed and in the case of an *n-type* semiconductor, the conductivity decreases. As the temperature increases, the equilibria expressed in equation 3.2 shift to the right. The mechanism can be further explained by the ionosorption model. In fact, if the *n-type* semiconductor interacts with a reducing gas, the potential barrier decreases, as the gas molecules oxidize due to the presence of chemisorbed oxygen molecules. The removal of chemisorbed oxygen species releases electrons and increases the conductivity of the semiconductor (the potential barrier decreases). Opposite phenomenon with oxidizing gases where there is a competitive behavior between gases that are strong electron acceptors compared to oxygen. The opposite is the mechanism with a *p-type* semiconductor. The interaction of the semiconductor with oxygen molecules in air leads to a lowering of the potential barrier, as the surface atoms ionize leading to the formation of h^+ holes [9].

The sensor's response to a gas can also be described by an analytical model described by Naisbitt. The model assumes that the response is influenced by the structure of the material [10]. In the model, it is assumed that the material is divided into the *surface*, the region in which the outermost electrical layer is located; *grain boundary*, the outer region of the grain below the depletion region; and from the *bulk*, the innermost region of the material. The distance between the surface and the grain boundary is called the *Debye length*, represents the width of the depletion region or the separation distance of the charges. The response and resistance of the sensor will be influenced by the contribution of each part of the material. A contribution to the resistance variation is given only by the regions exposed to the gas. The surface is sensitive to the gas while the bulk, being inaccessible to the gas, shows a contribution independent of the concentration of the latter. The grain boundary features a behavior dependent on gas concentration and grain overlap. A good synthesis of the material will have grain boundaries with behavior like that of the remaining bulk, if instead it is poorly sintered the entire grain boundary region can be considered sensitive to the gas.

The three-region model can be compared to a three-resistance circuit (see Figure 3.3) and described by the following equation 3.4:

$$R_T = \gamma_{GB}\,(1 + A\,[X]) + \frac{1}{\frac{1}{\gamma_B} + \frac{1}{\gamma_S\,(1+A[X])}} \tag{3.4}$$

R_T represents the total response of the sensor, i.e. the ratio between the resistance value when the sensor is exposed to the gas and the resistance value in air (or baseline), $R_T = R_{gas}/R_{air}$. The terms represent the individual responses of the three regions to target gas, respectively $\gamma_{GB,B,S}$ of the grain boundary, of the bulk, of the surface, even in this case expressed as a ratio between the resistances. A different relationship between the dimensions of the grains compared to the extension of the surface area can make one contribution negligible compared to the other. For very small particles can be considered the absence of the bulk region so that the entire grain can be considered as a surface.

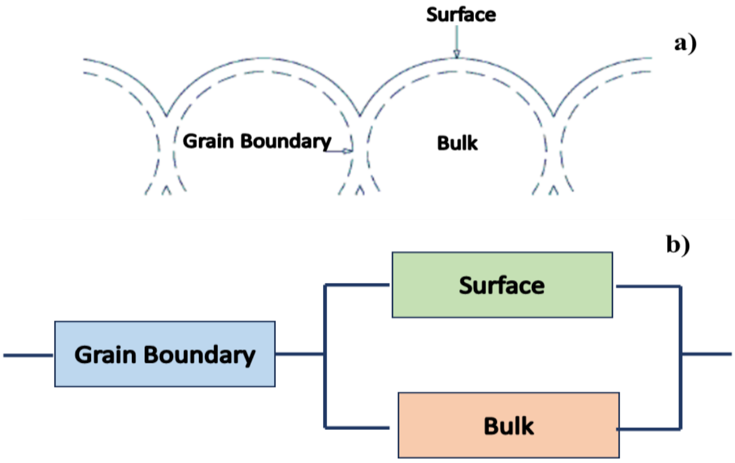

Figure 3.3. (a) Naisbitt model of three regions: bulk, grain boundary and surface; (b) Circuit of the model.

As previously described, there are several nanomaterials that can be deposited on the device, the mechanisms described so far specifically concern metal oxide semiconductors (MOS), a particularly different matter is considered for carbon-based materials. The charge transfer mechanism of carbon-based materials (such as carbon nanotubes, graphene, carbon dots, etc.) occurs by physisorption of gases on the surfaces of the sensitive material. The nanomaterials will interact with the target gases *via* Van der Walls interactions or donor-acceptor interaction. Adsorption is often favored by the presence of some functional groups (-O, -OH and -COOH) present on the surface of the sensitive layer. The greater the number of sites, the greater the binding energy that is established [11].

3.3 Adsorption phenomena

When the gas comes into direct contact with the sensitive material, interacts generating chemical-physical changes and the potential barrier established between the crystalline grains' changes with a consequent change in the conductivity of the sensor. *Adsorption* is the physical phenomenon interaction that leads to the formation of weak bonds on the part of the gas molecules with the atoms or ions present on the surface of the grains. Depending on the interaction forces that are established between molecules and atoms surfaces of the sensitive material, different types of adsorptions can occur such as physisorption, chemisorption and ionosorption.

Physisorption is a physical adsorption mechanism characterized by weak interaction forces between the material (solid or liquid) and the target gas. Only forces of an electrostatic nature are established due to bonds of Van Der Waals type. The low temperatures favor the formation of physical adsorption.

Chemisorption, in contrast to the previous one, is an adsorption type chemical characterized by bond strengths of the same order of magnitude as that of chemical bonds. In this case an exchange occurs charges between the adsorbed molecule and the surface of the adsorbent material, creating a strong chemical bond. The energy values associated with this mechanism are much larger than in the case of physisorption. Referring to the mechanism of a MOS, chemisorption involves an exchange of charges, chemical-physical mechanisms are triggered which lead to the change in conductivity of the material.

Ionosorption is a particular adsorption process intermediate between the two previous processes. The interaction is natural electrostatic as in physisorption, but the electrostatic forces are due to the adsorbate attracting an electron from a surface state of the adsorbent material. So, it happens an exchange of charges, but a chemical bond does not occur.

3.4 Interference phenomena

Semiconductors are not completely selective for a specific target gas and electrical conductivity can vary due to the presence of interferents. The major interferents are oxygen and humidity.

Oxygen is a reactive gas, its power strongly oxidizing makes it capable of reacting with various materials. According to what has already been discussed, the operating principle of solid-state gas sensors is based on the different concentration of oxygen adsorbed on the sensitive layer. The purpose of oxygen is to ionosorb on the surface of the grains of the sensitive layer in such a way as to remove electrons from the bulk, thus increasing the electrical resistance of the material in *n-type* semiconductors, opposite condition in *p-type* semiconductors. When a hypothetical target gas reaches the sensor, the oxygen, being like the gas, will tend to bind chemically to this by forming a new molecule and releasing the electrons into precedence taken away from sensitive material, this translates into a variation of electrical conductivity of the material which will be read as a response signal.

The presence of humidity can alter the conductivity of the sensor. The effects of water molecules adsorbed on the surface of sensitive materials can be multiple. In the case of sensors that work in air, water molecules tend to react with the adsorbed oxygen ions reducing the resistance of the material and therefore sensitivity. Thus, the water molecules deposited on the layer sensitive, behave as a barrier, inhibiting the adsorption of the gases of interest resulting in a sensitivity reduction effect [4]. The process of adsorption of water molecules leads to the formation of ions hydroxyls OH^- directly on the surface of the grains. This effect manifests itself as an increase in electrical conductivity in the case of *n-type* semiconductors, while in the case of *p-type* semiconductors, no particular effects are observed. The remaining hydrogen ions resulting from the dissociation of water molecules, react with oxygen atoms allowing the release of electrons and therefore a further increase in conductivity. The presence of water adsorbed on the sensor is not always a thing negative. In some cases hydroxyl ions, in particular environments, give rise to specific mechanisms that make the sensor sensitive to other otherwise undetectable species. Typical is the case when working in a reducing environment, for example detecting monoxide of carbon in the presence of hydrogen [12].

At high temperatures, desorption of hydroxyl ions occurs, in this case the presence of humidity becomes insignificant, and the sensor behaves as if it were in dry working conditions. However, it must be considered that the temperature plays a crucial role on the behavior of the sensor in terms of electric conducibility and also on the adsorption kinetics [9].

The presence of a dopant added to the semiconductor could reduce interference phenomena and improve the performance of the base material [13].

3.5 Sensing materials

Each sensitive layer developed for a gas sensor shows specific chemical-physical properties which are also linked to its size. Nanoparticles, i.e. particles measuring between 1 and 100 nanometers, are developed of carbon, metal, metal oxides or organic matter. Nanoparticles have unique physical characteristics, chemical and biological properties at the nanoscale compared to the respective particles at a higher scale. This phenomenon is due to a relatively larger surface area compared to the volume, a greater reactivity or stability in a chemical process, greater mechanical resistance, and so on. Nanoparticles differ in size and shape. The size and shape of the materials contribute to classify them as 0-D, 1-D, 2-D and 3-D.

MOSs are very versatile materials such that they can obtain materials of different sizes from 0-D to 3-D, however, one aspect to consider is the grain size, as has already been discussed above. The response of a MOS increases when the particle size is comparable to or smaller than the Debye length [14]. Therefore, 0-D MOSs show a dimension of the order of 100nm. 1-D MOSs possesses a high surface area to volume ratio, high porosity and specifications electronic properties. 1-D MOS are nanorods, nanowire, nanobelts, nanotubes and also complex structures as core-shell and fiber-tube. [15]. Instead, 2-D MOSs with geometries of nanosheets, nanoplates, nanodisks and so on have also been designed. One of the recurring problems of 2-D MOS is the tendency to aggregate due to Van der Waals interactions in the synthesis process [16], resulting in a decrease in surface area. The problem is bypassed by reducing the size and porosity of the nanomaterial. 3-Ds are generally designed to be porous or hierarchical architecture with a less agglomerated configuration. They arise from the assembly of 0-D, 1-D and 2-D units which gives it a large surface area and greater interaction with gases [17,18].

Carbon-based materials can be used as sensing materials of different sizes. It is possible to have quantum dots (QDs) of dimensions from 2 nm to 20 nm, for 0-D dimensions. The sensitivity of the QD is related to the electron transfer capacity and the ability to deliver active sites. [19,20]

The class of *1-D* nanomaterials includes carbon nanotubes (CNTs). CNTs have a high surface-to-volume ratio, higher than that of graphite, and also possess many active sites [15]. The structure causes them to have anisotropic dielectric properties such as to allow the same nanotube to carry a high current through a negligible heating effect [21]. In the detection of target gases, they do not require high working temperatures. They are also materials that possess a high mechanical resistance conferred by sp^2 hybridization and to improve their performance can be functionalized. Generally, CNTs are divided into single-walled (SWCNTs) and multi-walled (MWCNT) according to layer numbers. The bandgap of CNTs varies with diameter (as $1/R \sim 0.6$ eV d^{-1} (nm) [22]. For SWCNTs, diameters between 0.8 and 2 nm are reported, since the diameter size and the chiral angle influence their behavior as a semiconductor or metal. It has been demonstrated that, in some circumstances, SWCNTs have higher performance and sensitivity than a metal [15]. MWCNTs with a diameter between 5 and 100 nm originate from concentric layers of SWCNTs. Also important in gas detection [23]. To further improve the performance of 1-D nanomaterials it is possible to develop *p-type* MOS/CNTs and *n-type* MOS/CNTs composites. Graphene is 2-D carbon-based allotrope with a honeycomb hexagonal lattice structure, like CNTs, is a material that shows good physical, chemical and structural properties in fact high the mobility of the electrons, good stability at room temperature and large surface areas, important properties to be adopted as a sensitive material in a gas sensor. Generally, better detection of target gases is given by graphene oxide (GO) and reduced graphene (rGO) due to the presence of functional groups on the surface (-O, -COOH and -OH) [24].

Transition Metal Dichalcogenides (TMDs) are another class of 2-D sensitive nanomaterials, they are formed by covalent bonds X – M – X with a sandwich structure, where X correspond to chalcogen (generally S, Se or Te) and M is a transition metal (Mo or W) [25]. The most studied and synthetized TMDs in the literature are the WS_2, MoS_2, SnS_2, WSe_2, $MoSe_2$, and so on [26-28]. From 2-D TMDs obtained 3-D TMDs with more performance [29].

Graphitic Carbon Nitride (*g-*C_3N_4) is a 2-D nanomaterial often designed as an easily modifiable porous structure, as it is not very sensitive when pure. It has a bandgap ≈2.7 eV, exhibits a layered structure similar to graphite [30]. The 2-D aromatic planes are connected to each other by weak Van der Waals forces. The detection mechanisms are linked to the functional groups (C=O and O=COH) obtained from an oxidation process of the pure material with H_2SO_4 [31].

2-D *transition metal carbides/nitrides (MXenes*) are excellent nanomaterials due to their versatility and excellent conductivity. The detection is given by the functional groups -F, -O and -OH [32]. They are still nanomaterials under study.

3.6 Synthesis of nanomaterials

Nanomaterials are synthesized by both *top-down* and *bottom-up* approaches, as in Figure 3.4. For each approach there are different synthesis methods.

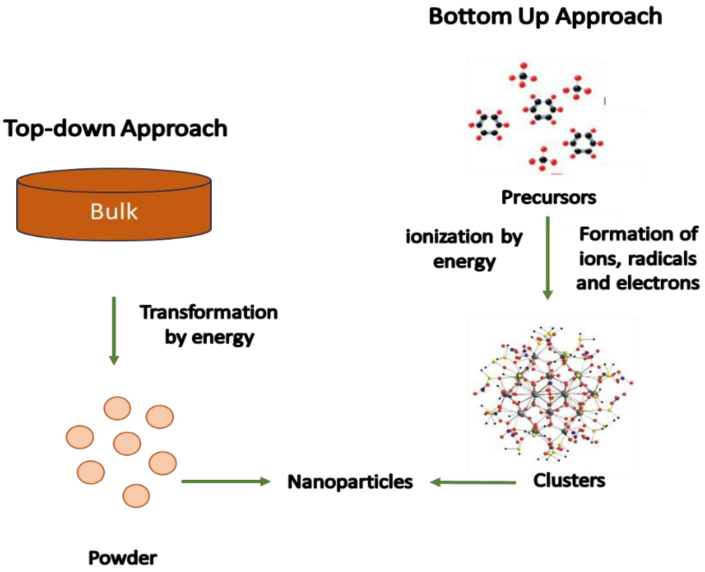

Figure 3.4. Top-down and bottom-up approaches.

The *top-down method* consists in reducing the bulk material into nanomaterial. Mechanical milling, nanolithography, laser ablation, sputtering and thermal decomposition are the most widely adopted syntheses.

In *mechanical milling* the bulk material is milled in an inert atmosphere and annealed synthesis can be affected by plastic deformation, by fracturing leading to a decrease in particle size and by cold welding causing an increase in particle size [33]. The mechanism is explained in Figure 3.5.

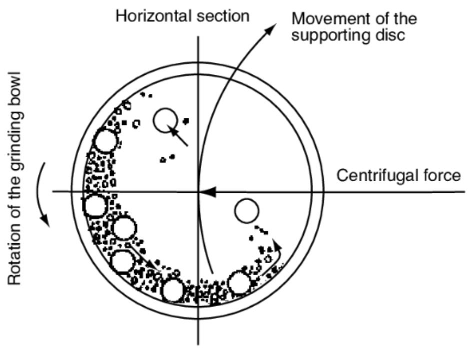

Figure 3.5. Mechanical milling process.

Nanolithography is the fabrication of nanoscale structures in a range between 1 and 100 nm. It is a process of printing a structure onto a light-sensitive material, as in Figure 3.6. The most used techniques are based on optics, electron beam, nanoimprint, and scanning probe. It is a very specific technique and allows to obtain perfect structures but requires complex equipment [34, 35].

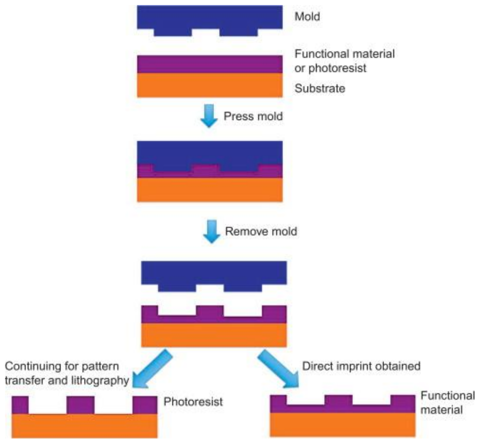

Figure 3.6. Mechanism of nanolithography. [36]

Laser ablation in solution (LASiS) consists of the irradiation of a metal immersed in a liquid. The solution in contact with the laser beam condenses and produces nanoparticles [37]. It can be considered a "green" method due to the absence of specific chemical reagents or stabilizers. The schematic mechanism is explained in Figure 3.7.

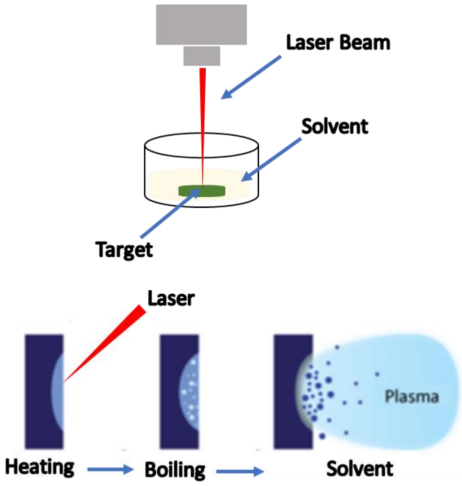

Figure 3.7. Schematic mechanism of Laser ablation in solution.

Sputtering is the deposition of nanoparticles in the form of ions on a surface [38]. The shape of the particles is determined by the temperature, the layer thickness and the subsequent annealing process [39]. The synthesis takes place inside a chamber in the presence of argon. The continuous application of a voltage on a metal target causes the breakdown of the gas into Ar^+ ions and electrons, forming a luminescent discharge. The positively charged ions are accelerated and collide with the target, which results in the formation of atoms suitable for film formation on the substrate [40]. Mechanism of sputtering is reported in Figure 3.8.

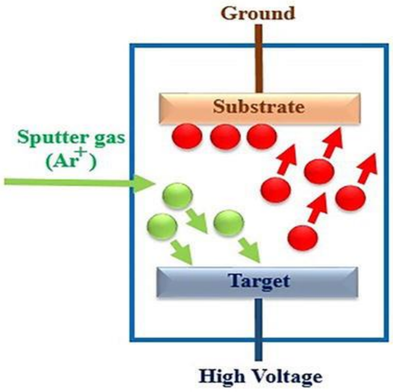

Figure 3.8. Mechanism of Sputtering deposition.

Thermal decomposition consists of an endothermic chemical decomposition, the heat breaks the chemical bonds in the compound [41]. The temperature depends on the decomposition temperature of the bulk material. The representation in Figure 3.9.

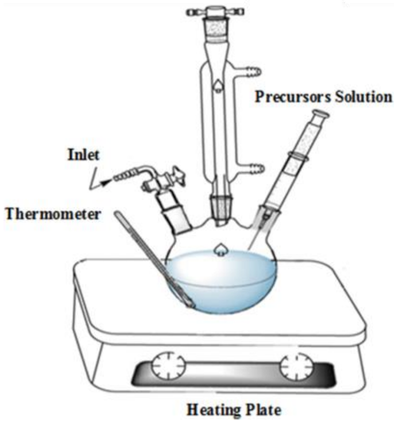

Figure 3.9. Representation of thermal decomposition.

The bottom-up method starts from the atom to the clusters up to the nanoparticles. Sol-gel, spinning, chemical vapor deposition (CVD), atomic layer deposition (ALD), pyrolysis and biosynthesis are the most adopted synthesis methods for this approach.

In the *sol-gel* method, a sol is obtained, a colloidal solution in a liquid phase, and a gel, a solid immersed in a solvent [42]. This method allows an excellent control of the texture and surface properties of the materials and can described in five steps. The first step consists in the hydrolysis of precursors such as metal alkoxides. The reaction takes place in water or in an organic solvent, it can also take place in the presence of an acid or a base to improve the reaction. The amount of water influences the gel formation. Below is an example of hydrolysis:

$$\text{M-OR} + H_2O \rightarrow \text{MOH} + \text{ROH} \tag{3.5}$$

M is a metal and R is an alkyl group (C_nH_{2n+1}). The next step involves the condensation of adjacent molecules, where water and alcohol are eliminated, and metal oxide bonds are formed. Condensation can occur either through the formation of a hydroxyl bridge with the metal (called *olation* process, -OH-) or through the formation of a bridge with oxygen (called *oxalation* process, -O-). Below is the reaction:

$$\text{M-OH} + \text{XO-M} \rightarrow \text{M-O-M} + \text{XOH} \tag{3.6}$$

where X is a hydrogen or alkyl group. The result is an increase in the viscosity of the solvent forming a porous structure that keeps the liquid in gel phase. The size and cross-linking of colloidal particles mainly depend on the precursor and the pH of the solution. Aging is the third phase, where a precipitation of the gel network is achieved. At this stage it decreases porosity and increases the thickness between the colloidal particles. The synthesis continues with the drying process, as in Figure 3.10. This process is complicated due to water and organic components. There are several methods, an example is atmospheric/thermal drying (involves the formation of a xerogel, low surface area and greater pore volume), supercritical drying (an aerogel is formed, greater surface area and volume) and freeze-drying (a cryogel forms, due to freezing), each having different implications on the structure of the gel network. An important parameter during drying is the relative humidity (RH) which directly affects the stability and performance of nanomaterials. The final phase consists of heat treatment/calcination, in which residues and water molecules are eliminated. The calcination temperature is a very important parameter in controlling the pore size and density of the material.

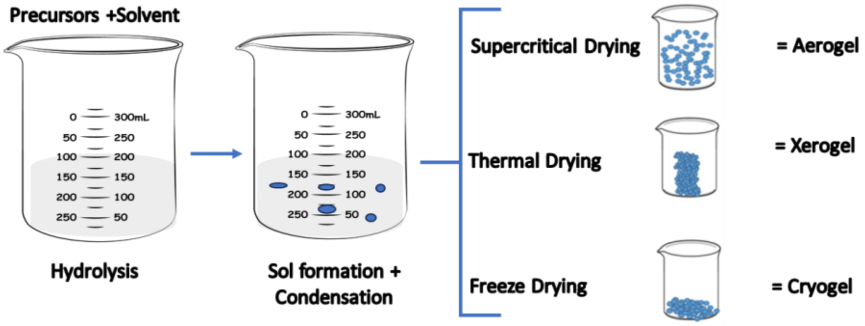

Figure 3.10. Drying process of sol-gel method.

Spinning is achieved via a rotating disk reactor inside a chamber/reactor. The reactor chamber is subjected to flows of inert gas (such as argon) to eliminate oxygen and avoid further chemical reactions (see Figure 3.11) [43]. The precursor is a liquid inserted into the chamber, where the rotation of the disk causes the atoms or molecules to fuse together, and the precipitate is collected and dried [44]. The structure and properties of nanoparticles is determined by liquid flow rate, disk rotation speed, liquid/precursor ratio, feed position, disk surface area.

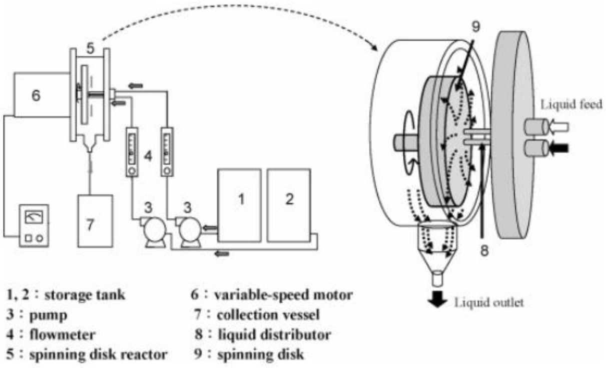

Figure 3.11. Experimental apparatus of spinning method. [43]

Chemical vapor deposition (CVD) is the deposition of a thin layer of gaseous reagents on a substrate. The technique is characterized by four phases: introduction of the reagent gases inside of the room; adsorption of reagents on the substrate; decomposition of gases on surface; desorption of the reaction products. In the first phase, the reactant gases (precursors) are introduced into the reactor together with other inert gases (carriers) which have the purpose of transporting the precursor towards the substrate. In the second phase the gas molecules adsorb on the surface of the substrate by binding by means of weak bonds such as Van Der Waals forces or creating chemical bonds with the surface atoms of the substrate, depending if physical or chemical adsorption occurs respectively. In the third phase the gas precursor, due to the high temperature at which the substrate is maintained, decomposes forming free radicals of the desired species which tend to bind to the surface of the substrate itself. The other atoms released by the decomposition process react forming gaseous molecules. In the fourth phase, the gaseous products of the reaction desorbed from the surface are evacuated from inside the reactor by means of a system to empty [45]. The phases are showed in Figure 3.12. It is a controlled synthesis, but which also adopts toxic reagents.

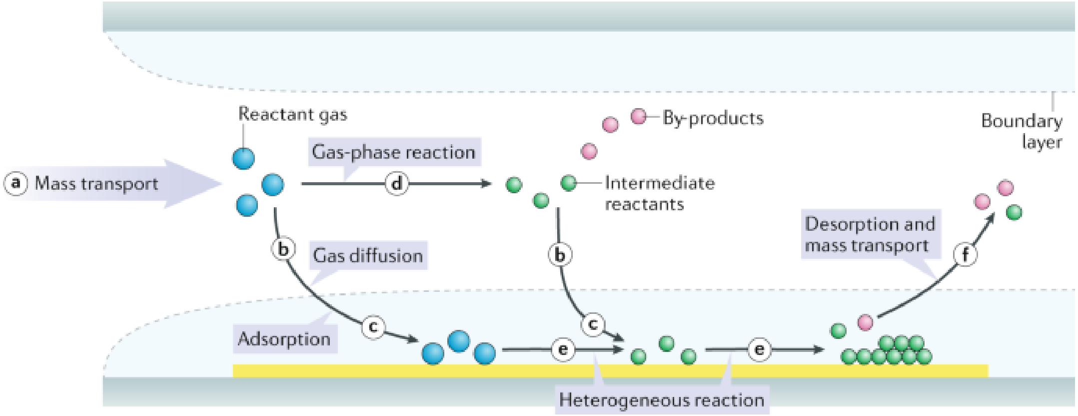

Figure 3.12. Steps of CVD process [46].

Similar to CVD, it is *Atomic Layer Deposition (ALD)* in Figure 3.13, a synthesis characterized by a succession of cycles of chemical reactions that occur between precursors. The precursors can be in a solid or liquid phase, and one of the precursors, generally, is an organo-metallic compound or chloride, and must possess the chemical element to be deposited, while the second precursor is an oxidizing gas (such as oxygen) or reducing agent (such as hydrogen). The reactions take place in vacuum conditions and in the presence of an inert gas adopted to eliminate secondary products or clean the reaction environment after a first reaction cycle. The reaction of the two precursors occurs in the vapor phase, in fact before starting a cycle, the evaporation temperatures of the precursors are defined. Each reaction cycle follows the following process which can be divided into phases: (I) evaporation of the first precursor and deposition on the substrate. The substrate is placed inside a chamber where it is heated to a certain temperature; (II) injection of an inert gas (Ar) to eliminate any precursor residues; (III) injection of the second precursor; (IV) inert gas injection; (V) new reaction cycle. An ideal ALD process is characterized by a linear increase in the amount of deposited material as a function of the number of ALD cycles. The "*growth per cycle*" or GPC is the amount of material deposited per ALD cycle, a parameter that does not explain the reaction kinetics but only the number of chemisorption sites on the growth surface linked to the reactivity, the number of accessible surface sites and morphology of the surface. There is also a parameter defined as the "*ALD window*", it is the temperature range in which growth conditions prevail. In some cases, if the temperature is too much low, no growth is observed, due to the thermal the energy is insufficient to drive surface chemistry. Or an apparently faster growth is observed, often related to phenomena of physisorption. At elevated temperatures, higher growth rates are often observed, caused by thermal decomposition of the precursor on the surface [47].

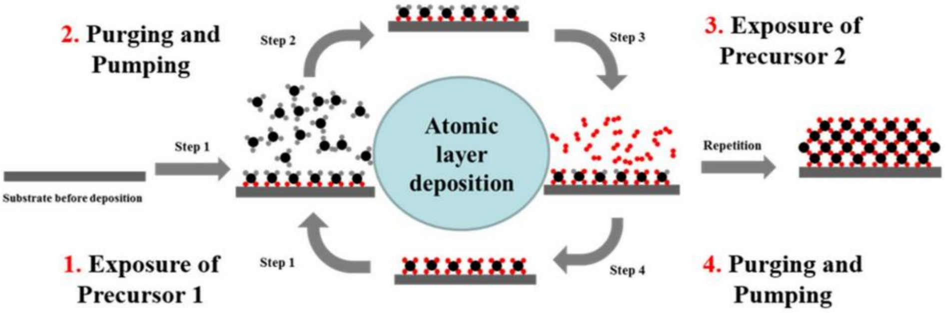

Figure 3.13. Mechanism of Atomic Layer Deposition (ALD). [48]

Pyrolysis is the synthesis method most adopted by industries. A precursor in liquid or vapor phase is introduced into a high-pressure oven. Nanoparticles are obtained from combustion. The ovens are flame, laser or plasma. Compared to other synthesis methods, it is very simple and economical [49]. In Figure 3.14 an example of process.

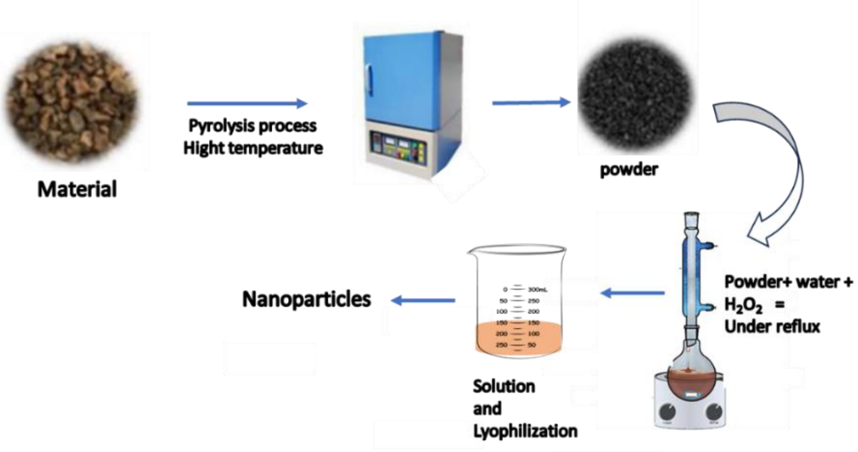

Figure 3.14. Example of one pyrolysis method.

Biosynthesis uses bacteria or plant extracts together with precursors to produce nanoparticles [50].

3.7 Design of a conductometric gas sensor

The sensitive layer that constitutes the sensor is deposited on an appropriate support, called substrate, which performs the dual function of electrically isolating the elements circuits suitable for reading the signal and ensuring thermal stability during the operation. The substrate is composed of three elements such as a load-bearing structure, a coil and a series of interdigitated contacts. The load-bearing structure is the element that gives solidity to the sensor and has the purpose of electrically isolating the heater from the interdigitated and contacts. This mount is commonly made in insulating ceramic material, generally alumina, (Al_2O_3), sometimes also in silicon, and they are available in different sizes, usually rectangular in shape, pre-cut using laser technique. The contacts, over which the sensitive layer is deposited, are made of material with high electrical conductivity to minimize contact resistance with the film improving the sensitivity of the sensor. Platinum (Pt) is commonly used. The heater is also made of Pt [51]. The use of platinum allows to prevent damage to the sensor, as it is a resistant material to corrosion, has a low coefficient of thermal expansion and high temperature fusion (1768 °C), these characteristics make it the most suitable material for this use.

The purpose of the heater is to bring the sensor to working temperature. The operation is typical of a resistor carrying an electric current. In fact, by applying an appropriate voltage value to the terminals, a current will circulate which, due to the resistance encountered, will dissipate a certain power due to the Joule.

The correct preparation of the sensitive material and its deposition on the substrate in order to create a sensitive film with adequate characteristics, they constitute a crucial point in the semiconductor sensor manufacturing process. Different manufacturing methods can be used for manufacturing of semiconductor sensors. The factors that should be considered in order to select the most appropriate technique include *cost*, *purity* (the presence of impurities in the structure significantly alters the characteristics of the semiconductor material, the technique used should not contaminate the film made), *porosity* (if the material is highly porous the specific surface area will be high increasing the possibility of interaction with gases, therefore increases the sensitivity), *reliability* (the technique must guarantee that the film created is capable of work according to the required specifications for a given period of time) and *reproducibility* (two or more sensors should present the same operating characteristics if produced with the same technique). Added to these aspects are the small dimensions and reduced energy consumption. If the device is to be used in mobile or wireless network devices it is necessary to have a consumption of the order of several microwatts [52].

In new technologies there is a tendency to miniaturize devices. A recent development in the field of microelectronics is the microelectromechanical system (MEMS), very compact, with low energy consumption [53]. Gas sensors can be integrated into MEMS platforms. MEMS are electromechanical systems of 3D geometry. They are built on silicon wafers as platforms. Manufacturing involves the use of photolithography method e post-processing techniques. A MEMS, showed in Figure 3.15, consists of a dielectric or insulating material that acts as a microheater, a thin film of sensitive material and interdigitated platinum (Pt) electrodes, nichrome (Ni) or tungsten (W). Furthermore, the geometry and the configuration of microheater can be modulated. The first devices fabricated in the 1990s [54].

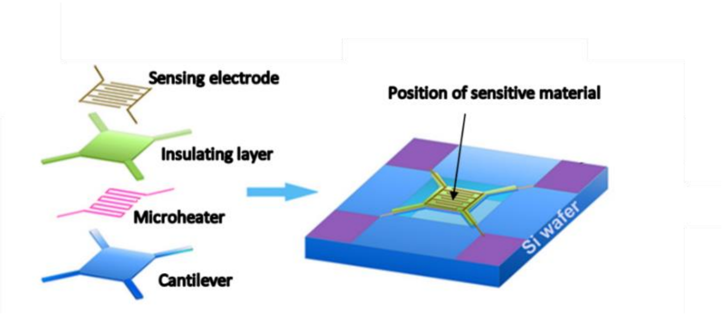

Figure 3.15. Schematic representation of MEMS.

Classic gas sensors have operating temperatures in a range between 100-500°C. There are different strategies to reduce these temperatures, in some cases try to dope the material with noble metals [55], in others try to create heterojunctions [56], or develop composites with rGO or conducting polymers [57, 58]. A good strategy studied in recent years is to use UV light. If UV light provides an energy that is equal to or higher than the band gap energy of the sensitive material, the electrons and holes can become excited, which facilitates the chemisorption of oxygen molecules on the surface to generate more O_2^- improving the chemical activity of the surface by working at room temperature, according to the following mechanism:

$$h\nu \rightarrow h^+ + e^- \tag{3.7}$$

$$O_2 + e^-_{(h\nu)} \rightarrow O_2^- (h\nu) \rightarrow O_{2\,(h\nu)}^{\,-} \tag{3.8}$$

ν is the frequency of the illuminated light and h is Planck's constant [59]. Subsequently, the release of electrons and the desorption of oxygen species favor the reduction of the thickness of the depletion layer and the decrease of the electrical resistance [60].

The sensors discussed so far, they are all devices with rigid structures, whereas there is a tendency among science to develop a class of *flexible* sensors. A flexible sensor is a device that can undergo deformations without changing its properties. The idea was born with the aim of being able to wear a sensor in workplaces where high concentrations of pollutants occur [61]. If integrated into wireless technology and connected to an IoT system, they offer real-time information [62]. Polyethylene terephthalate (PET) [63], polyimide (PI) [64] and Kapton [65] are the major substrates adopted to develop a flexible sensor. Graphene and its the derivatives, on the other hand, are developed as sensitive materials due to their high mechanical resistance, good stability, high carrier mobility and good flexibility [66]. Among wearable devices, gas sensors developed on textile (as showed in Figure 3.16) can be found in the literature. An example is the sensor of Yun et al. based on a cotton yarn composite decorated with RGO [67]. The sensor detected NO_2 at room temperature and even after washing the tissue, the sensor continued to maintain its values property, demonstrating its excellent performance in different conditions. The resistance and stability to washing had been attributed to chemical resistance to water and detergents, also to mechanical resistance to shear resulting from friction between the wire and the magnetic stirrer when washing the sensor.

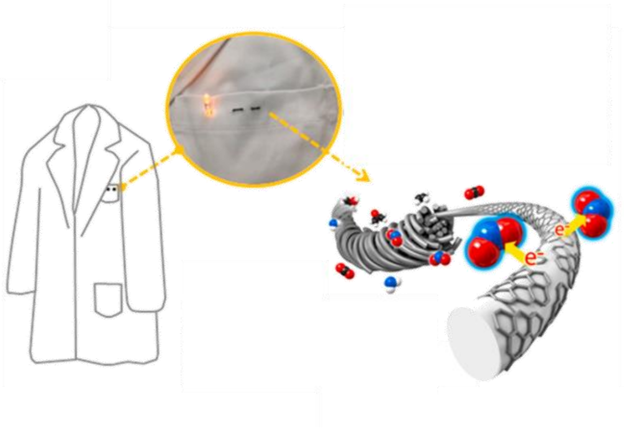

Figure 3.16. Electronic-textile (e-textile) gas sensor based on a composite of RGO-decorated cotton yarn, an example of flexible sensor [67].

3.8 Fabrication of a sensor

The development of miniaturized sensors is favored by specific deposition techniques, some of which are most used Screen Printing, Chemical Vapor Deposition (CVD), Atomic Layer Deposition (ALD), Spray pyrolysis, Spin coating, Dip coating and Elettrospinning [68]. Some of these techniques coincide with the methods of synthesis of sensitive material and have been described in the previous paragraph 3.6.

Screen printing is a technique known for creation of images on various substrates (paper, wood, plastic, ceramic, etc.) such as in Figure 3.17. There technique is easy to use and typically shows two processes: preparation of mask (or stencil) and molding onto the substrate. The mask represents the negative of the geometry that is intended to be obtained on the substrate and can be directly achieved on a knitted fabric by means of an emulsion. Screen printing consists of in extruding an ink through the meshes finely intertwined with a suitably shaped mask. In the case of semiconductor sensors, the technique is used for the deposition of thick films of metal oxide. The paste is made up of oxide powder desired metal, to which specific organic additives are added with the aim of obtain an ink with appropriate rheological properties to be able to be deposited for screen printing. The thickness of the deposited layer is variable in the range of 1-100 μm depending on a whole series of parameters which characterize the process and the material to be deposited, such as: the size of the particles constituting dust; the viscosity of the screen printing paste; the size of shirts that make up the mask; the speed of the squeegee; the distance between the screen and the substrate. After the deposition of the film, the technique has further terminal phases, drying and firing, respectively, which are essential if the film is the layer sensitive sensor. The term *drying* refers to the treatment of drying of the deposit, to promote the evaporation of the volatile components. This process can be conducted at room temperature or in oven but with temperatures not exceeding 200 °C. It is important that during this phase the material does not undergo chemical or structural modifications. Instead, *firing* is the process of cooking material at a sufficiently high temperature in order to promote the sintering process of the grains constituting the powder. The process is generally conducted in a muffle, a temperature between 300 °C and 800 °C, in operation of the material and the physical and structural properties that you intend to obtain.

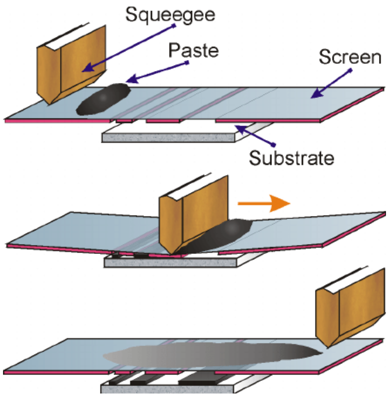

Figure 3.17. Example of screen-printing process.

The *Spray pyrolysis* technique is a method used for the deposition of thin films which consists of vaporizing a solution on the surface of a superheated substrate which reacts due to the temperature to form the desired compound. There are different techniques for making the film on the substrate and they depend on the substance you intend to deposit. The simplest process is to directly vaporize the desired substance, solubilized in a solvent, on the substrate. Following evaporation of the solvent, a solid film remains. Another process alternatively uses a solvent that evaporates before the droplets reach the substrate, in which case they arrive on the surface directly solid reagents which, due to the effect of temperature, will react to give the compound desired. This approach is used when the solvent would alter the reaction compound formation. Other techniques instead involve the process of formation of the compound to be deposited occurs directly in the vapor phase, where the material adheres to the substrate due to the impact speed. See Figure 3.18.

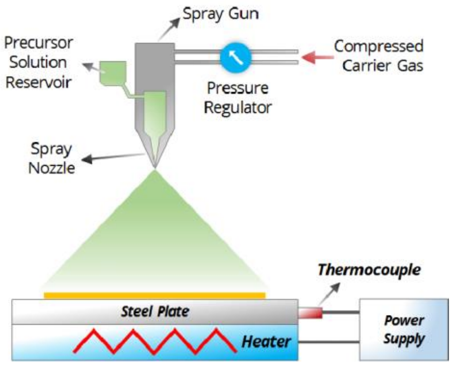

Figure 3.18. Spray pyrolysis process.

The *Spin coating* technique is a process of deposition of thick or thin films that exploits the effect of the centrifugal force induced by the high-speed rotation of the substrate. The technique (see Figure 3.19) consists in depositing a drop of a suspension of the desired substance, or of the sol-gel solution, on the substrate, which is rotated by means of a spin coater (or spinner). Forces are created as a result of rotation centrifuges that reached and exceeded the value of the viscous reactions of the suspension, they tend to widen the drop with a consequent reduction in thickness. The thinning effect is linked to the simultaneous action of viscous forces and evaporation of the solvent. At first the effect dominates of viscous forces, in fact, the drop expands until an equilibrium is established between them and the centrifugal force. After, the reduction in thickness by effect prevails of the evaporation of the solvent which also results in an increase in viscosity of the remaining solution.

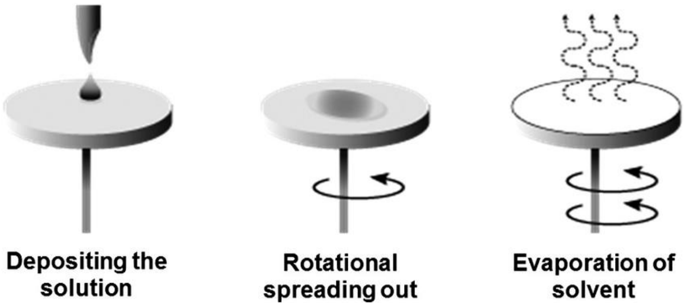

Figure 3.19. Spin coating technique.

The deposition technique for *Dip coating* consists of immersing the substrate directly within a solution or suspension of the substance being intended to deposit. The process, in Figure 3.20, can be summarized in three phases: immersion; extraction; drying. The immersion phase simply involves submerging the substrate to be covered with the film inside the tank containing the material solution desired. The phase does not require particular attention other than to avoid sudden changes agitation of the liquid. The most important phase is that of extracting the substrate, in fact it is precisely during this phase that the film settles on it. The extraction speed determines the thickness of the film obtained, in particular, the higher it is, the higher the greater the deposited thickness will be. The last phase involves drainage and drying which can be carried out at temperatures higher than room temperature in order to accelerate the solvent evaporation process.

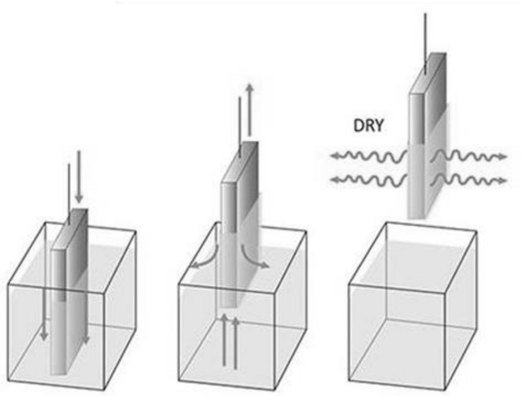

Figure 3.20. Dip-coating deposition.

Electrospinning is a process often used in industry textile to create fibrous structures (see Figure 3.21). The fibers obtained by electrospinning show high specific surface area and very thin fiber diameter. Electrospinning has been mainly used for the preparation of nanofibers polymeric. The method consists in extrusion, through thin tip of a needle of a syringe, a solution, or a polymer melt. The solution polymer is pushed through the needle by a pump that applies pressure to the syringe plunger. At the same time an electric potential difference is applied between the tip of the syringe, generally positive, and the collecting surface on which it is located will deposit the nanofibers. The intense electric field polarizes the polymer solution which is then expelled when the electrostatic repulsion between the charged molecules positively overcomes surface tension. The thin stream of solution is further stretched to nanometric diameters by electrostatic attraction exerted by the negatively charged collector plane. The applied voltages are of the order of kV and depend on the concentration of the polymer solution, viscosity, temperature and humidity. The solution filament proceeds towards the negatively charged collector and the solvent evaporates resulting in the formation of the fiber which moves spirally along a cone, due to of the hydrodynamic instability, finally settles, randomly on the collector. With this technique, thin films with thicknesses ranging from a few are obtained micrometers to hundreds of micrometers formed by nanofibers of macroscopic length (tens of centimeters) and nanometric diameter, densely intertwined.

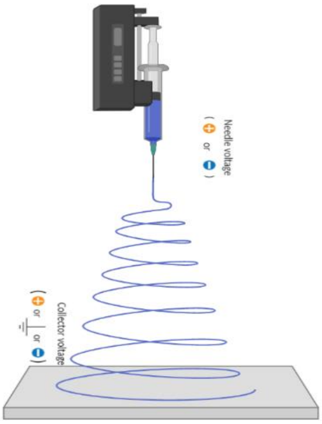

Figure 3.21. Schematic process of electrospinning deposition.

3.9 References

1. P. Srinivasan, M. Ezhilan, AJ Kulandaisamy, K.J. Babu and J.B.B. Rayappan, *J. Mater. Sci.: Mater. Elettrone.*, 30 (2019) 15825–15847.
2. H. Du, W. Yang, W. Yi, Y. Sun, N. Yu, J. Wang, *Oxygen-plasma-assisted enhanced acetone-sensing properties of ZnO nanofibers by electrospinning*, ACS Appl. Mater. Interfaces 12 (2020) 23084–23093.
3. A. Mirzaei, K. Janghorban, B. Hashemi, G. Neri, *Metal-core@metal oxide-shell nanomaterials for gas-sensing applications: a review*, J Nanopart Res 17 (2015) 371.
4. T. Lin, Xin Lv, Z. Hu, A. Xu and C. Feng, *Semiconductor Metal Oxides as Chemoresistive Sensors for Detecting Volatile Organic Compounds*, Sensors 19 (2019) 233.
5. A. Dey, Semiconductor metal oxide gas sensors: A review, Materials Science & Engineering B 229 (2018) 206–217.
6. G. Korotcenkov, B.K. Ch, Metal oxide composites in conductometric gas sensors: Achievements and challenges, Sensors and Actuators B 244 (2017) 182–210.
7. Z. Li, H. Li, Z. Wu, M. Wang, Jingting Luo, H. Torun, P. Hu, C. Yang, M. Grundmann, X. Liud and Y. Fu, *Advances in designs and mechanisms of semiconducting metal oxide nanostructures for high-precision gas sensors operated at room temperature*, Mater. Horiz. 6 (2019) 470.
8. O. Monforta, G. Plesch, *Bismuth vanadate-based semiconductor photocatalysts: a short critical review on the efficiency and the mechanism of photodegradation of organic pollutants*, Environmental Science and Pollution Research 25 (2018) 19362-19379.
9. A. Marikutsa, M. Rumyantseva, E. A. Konstantinova and A. Gaskov, *The Key Role of Active Sites in the Development of Selective Metal Oxide Sensor Materials*, Sensors 21 (2021) 2554.
10. S.C. Naisbitt, K.F.E. Pratt, D.E. Williams, I.P. Parkin, *A microstructural model of semiconducting gas sensor response: The effects of sintering temperature on the response of chromium titanate (CTO) to carbon monoxide*, Sensors and Actuators B 114 (2006) 969–977.

11. S. Crispi, G. Nocito, F. Nastasi, G. Condorelli, A.G. Ricciardulli, P. Samorì, S. Conoci, G. Neri, *Development of a novel C-dots conductometric sensor for NO sensing*, Sensors and Actuators: B. Chemical 390 (2023) 133957.
12. H. Yamaura, Y. Iwasaki, S. Hirao, and H. Yahiro, *CuO/SnO2–In2O3 sensor for monitoring CO concentration in a reducing atmosphere*, Sensors and Actuators B: Chemical 153 (2011) 465-467.
13. N. Goel, K. Kunal, A. Kushwaha, M. Kumar, *Metal oxide semiconductors for gas sensing*, Engineering Reports. 5 (2023) 12604.
14. C. N. Xu, J. Tamaki, N. Miura, N. Yamazoe, *Grain size effects on gas sensitivity of porous* SnO_2*-based elements*, Sens. Actuators B 3 (1991) 147.
15. K. Hata, D.N. Futaba, K. Mizuno, T. Namai, M. Yumura, S. Iijima, *Water-Assisted Highly Efficient Synthesis of Impurity-Free Single-Walled Carbon Nanotubes*, Science 306 (2004) 1362.
16. M.-Y. Li, C.-H. Chen, Y. Shi, L.-J. Li, *Heterostructures based on two-dimensional layered materials and their potential applications*, Mater. Today 19 (2016) 322.
17. C. Su, L. Zhang, Y. Han, X. Chen, S. Wang, M. Zeng, N. Hu, Y. Su, Z. Zhou, H. Wei, Z. Yang, *Glucose-assisted synthesis of hierarchical flower-like* Co_3O_4 *nanostructures assembled by porous nanosheets for enhanced acetone sensing*, Sens. Actuators B 288 (2019) 699.
18. Z. Tao, Y. Li, B. Zhang, G. Sun, M. Xiao, H. Bala, J. Cao, Z. Zhang, Y. Wang, *Synthesis of urchin-like In2O3 hollow spheres for selective and quantitative detection of formaldehyde*, Sens. Actuators, B 298 (2019) 126889.
19. G. Xu, S. Zeng, B. Zhang, M. T. Swihart, K.-T. Yong, P. N. Prasad, *New Generation Cadmium-Free Quantum Dots for Biophotonics and Nanomedicine*, Chem. Rev. 116 (2016) 12234.
20. F. Qiao, Y. Xie, Z. Weng, H. Chu, *Ligand engineering of colloid quantum dots and their application in all-inorganic tandem solar cells*, J. Energy Chem. 50 (2020) 230.
21. S. Lijima, *Helical microtubules of graphitic carbon*, Nature 56 (1991) 354.
22. C. L Kane, E. J. Mele, Size*, Shape, and Low Energy Electronic Structure of Carbon Nanotubes*, Phys. Rev. Lett. 78 (1997) 10.

23. A. H. Al Husseini, A.M.A. Al-Sammarraie, W.R. Saleh, *Specific NH_3 Gas Sensor Worked at Room Temperature Based on MWCNTs-OH Network*, Nano Hybrids Compos. 23 (2018) 8.
24. H.J. Yoon, D.H. Jun, J.H. Yang, Z. Zhou, S.S. Yang, M.M.-C. Cheng, *Carbon dioxide gas sensor using a graphene sheet*, Sens. Actuators, B 157 (2011) 310.
25. Q.H. Wang, K. Kalantar-Zadeh, A. Kis, J.N. Coleman, M.S. Strano, *Electrochemical Control of Photoluminescence in Two-Dimensional MoS_2 Nanoflakes*, ACS Nanotechnol.7 (2013) 699.
26. Y. Kim, S. Lee, J.-G. Song, K. Y. Ko, W. J. Woo, S. W. Lee, M. Park, H. Lee, Z. Lee, H. Choi, W.-H. Kim, J. Park, H. Kim, *Function 2D Transition Metal Dichalcogenide Heterostructures for p- and n-Type Photovoltaic Self-Powered Gas Sensor*, Adv. Mater. 30 (2020) 2003360.
27. K. Hayashi, M. Kataoka, H. Jippo, M. Ohfuchi, S. Sato, *Vacancy-Assisted Selective Detection of Low-ppb Formaldehyde in Two-Dimensional Layered SnS_2*, ACS Appl. Mater. Interfaces 12 (2020) 12207.
28. P. Panigrahi, T. Hussain, A. Karton, R. Ahuja, *Elemental Substitution of Two-Dimensional Transition Metal Dichalcogenides ($MoSe_2$ and $MoTe_2$): Implications for Enhanced Gas Sensing*, ACS Sens. 4 (2019) 2646.
29. Y.-Z. Chen, S.-H. Lee, T.-Y. Su, S.-C. Wu, P.-J. Chen, Y.-L. *Chueh, Phase-modulated 3D-hierarchical 1T/2H WSe2 nanoscrews by a plasma-assisted selenization process as high performance NO gas sensors with a ppb-level detection limit*, J. Mater. Chem. A 7 (2019) 2231.
30. P. Srinivasan, S. Samanta, A. Krishnakumar, J.B.B. Rayappan, K. Kamalakannan, *Insights into g-C_3N_4 as a chemi-resistive gas sensor for VOCs and humidity – a review of the state of the art and recent advancements*, J. Mater. Chem. A 9 (2021) 10612.
31. S. Li, Z. Wang, X. Wang, F. Sun, K. Gao, N. Hao, Z. Zhang, Z. Ma, H. Li, X. Huang, W. Huang, *Orientation controlled preparation of nanoporous carbon nitride fibers and related composite for gas sensing under ambient conditions*, Nano Res. 10 (2017) 1710.
32. W. Huang, L. Hu, Y. Tang, Z. Xie, H. Zhang, *Recent Advances in Functional 2D MXene-Based Nanostructures for Next-Generation Devices*, Adv. Funct. Mater. 30 (2020) 2005223.

33. T.P. Yadav, R.M. Yadav, D. P. Singh, *Mechanical Milling: a Top Down Approach for the Synthesis of Nanomaterials and Nanocomposites*, Nanoscience and Nanotechnology 2(3) (2012) 22-48.
34. A. Pimpin and W. Srituravanich , *Review on Micro- and Nanolithography Techniques and their Applications*, Engineering Journal 16 (2012) 37–55.
35. J.C. Hulteen, D.A. Treichel, M.T, Smith, M.L. Duval, T.R. Jensen and R.P. Van Duyne, *Nanosphere Lithography: Size-Tunable Silver Nanoparticle and Surface Cluster Arrays* , J. Phys. Chem. B (19)103 (1999) 3854–3863.
36. L. Yang, *Nanotechnology-Enhanced Orthopedic Materials*, A volume in Woodhead Publishing Series in Biomaterials (2015) Elsevier, ISBN 978-0-85709-844-3.
37. V. Amendola and M. Meneghetti, *Laser ablation synthesis in solution and size manipulation of noble metal nanoparticles*, Physical Chem. Chem.Physics 21 (2009) 3805.
38. P. Shah and A.Ã. Gavrin, *Synthesis of nanoparticles using high-pressure sputtering for magnetic domain imaging*, Journal of Magnetism and Magnetic Materials 301 (2006) 118–23.
39. E. Lugscheider, S. Bärwulf, C. Barimani, M. Riester and H. Hilgers, *Magnetron-sputtered hard material coatings on thermoplastic polymers for clean room applications*, Surf. Coatings Technol. 108-109 (1998) 398–402.
40. H. Ghazal and N. Sohail, *Sputtering Deposition*, Chapter from volume Thin films (2022).
41. M. Salavati-Niasari, F. Davar and N. Mir, *Synthesis and characterization of metallic copper nanoparticles via thermal decomposition*, Polyhedron 27 (2008) 3514–8.
42. M. Parashar, V.K. Shukla, R. Singh, *Metal oxides nanoparticles via sol–gel method: a review on synthesis, characterization and applications*, Journal of Materials Science: Materials in Electronics (2020).
43. C. Y. Tai, C. Tai, M. Chang and H. Liu, *Synthesis of Magnesium Hydroxide and Oxide Nanoparticles Using a Spinning Disk Reactor*, Ind. Eng. Chem. Res. (17) 46 (2007) 5536–5541.
44. S. Mohammadi, A. Harvey and K.V. Boodhoo, *Synthesis of TiO_2 nanoparticles in a spinning disc reactor*, Chem. Eng. J. 258 (2014) 171–84.

45. S. Bhaviripudi, E. Mile, S.A.S. Iii, A. T. Zare, M.S. Dresselhaus, A.M. Belcher and J. Kong, *CVD Synthesis of Single-Walled Carbon Nanotubes from Gold Nanoparticle Catalysts,* J. Am. Chem. Soc. (6) 129 (2007) 1516–1517.
46. L. Sun, G. Yuan, L. Gao, J. Yang, M. Chhowalla, M.H. Gharahcheshmeh, K.K. Gleason, Y.S. Choi, B.H. Hong & Z. Liu, *Chemical vapour deposition,* Nat Rev Methods Primers 1, 5 (2021).
47. R.W. Johnson, A. Hultqvist and S.F. Bent, *A brief review of atomic layer deposition: from fundamentals to applications,* Materials Today 17 (2014).
48. S.Y. Kim, B. J. Cha, S. Saqlain, H.O. Seo and Y.D. Kim, *Atomic Layer Deposition for Preparation of Highly Efficient Catalysts for Dry Reforming of Methane*, Catalysts 9 (2019) 266.
49. R.D. Amato, M. Falconieri, S. Gagliardi, E. Popovici, E. Serra, G. Terranova and E. Borsella, *Pyrolysis Synthesis of ceramic nanoparticles by laser pyrolysis : From research to applications,* J. Anal. Appl. Pyrolysis (2013) 104, 461–9.
50. S. Hasan, *A Review on Nanoparticles: Their Synthesis and Types Biosynthesis : Mechanism* , Res. J. Recent. Sci., 4 (2015) 9–11.
51. S. M. Majhi, A. Mirzaei, H.W. Kim, S.S. Kim, T. W. Kim, *Recent advances in energy-saving chemiresistive gas sensors: A review,* Nano Energy 79 (2021) 105369.
52. R. Ahmad, S.M. Majhi, X.X. Zhang, T.M. Swager, K.N. Salama, *Recent progress and perspectives of gas sensors based on vertically oriented ZnO nanomaterials,* Adv. Colloid Interface Sci. 270 (2019) 1–27.
53. J. Burgues, S. Marco, *Low power operation of temperature-modulated metal oxide semiconductor gas sensors*, Sensors 18 (2018) 339.
54. S.S. Modal, S. Roy, C.K. Sarkar, *Design and electrothermal analysis of MEMS based microheater array for gas sensor using INVAR alloy*, 2012 International Conference on Communications, Devices and Intelligent Systems (CODIS), Kolkata, (2012) 468–471.
55. S. Arunkumar, T. Hou, Y.B. Kim, B. Choi, S.H. Park, S. Jung, D.W. Lee, Au *Decorated ZnO hierarchical architectures: facile synthesis, tunable morphology and enhanced CO detection at room temperature*, Sens. Actuators, B 243 (2017) 990–1001.

56. N. Jayababua, M. Polojua, J. Shruthia, M. Reddy, *Semi shield driven p-n heterostructures and their role in enhancing the room temperature ethanol gas sensing performance of NiO/SnO_2 nanocomposites*, Ceram. Int. 45 (2019) 15134.
57. R. You, D.D. Han, F. Liu, Y.L. Zhang, G. Lu, *Fabrication of flexible room temperature NO2 sensors by direct laser writing of In_2O_3 and graphene oxide composites*, Sens. Actuators, B: Chem. 277 (2018) 114–120.
58. F.I.M. Alia, S.T. Mahmoud, F. Awwadb, Y.E. Greishc, A.F.S. Abu-Hani, *Low power consumption and fast response H_2S gas sensor based on a chitosan-CuO hybrid nanocomposite thin film*, Carbohydr. Polym. 236 (2020) 116064.
59. H. Chen, Y. Liu, C. Xie, J. Wu, D. Zeng, Y. Liao, *A comparative study on UV light activated porous TiO_2 and ZnO film sensors for gas sensing at room temperature*, Ceram. Int. 38 (2012) 503–509.
60. J. Cui, L. Shi, T. Xie, D. Wang, Y. Lin, *UV-light illumination room temperature HCHO gas-sensing mechanism of ZnO with different nanostructures*, Sens. Actuators, B: Chem. 227 (2016) 220–226.
61. A. Nag, S.C. Mukhopadhyay, J. Kosel, *Wearable flexible sensors: a review*, IEEE Sens. J. 17 (2017) 3949–3960.
62. A. Pantelopoulos, N.G. Bourbakis, *A survey on wearable sensor-based systems for health monitoring and prognosis*, IEEE T. Syst. Man Cy. C 40 (2009) 1–12.
63. Z.Q. Zheng, J.D. Yao, B. Wang, G.W. Yang, *Light-controlling, flexible and transparent ethanol gas sensor based on ZnO nanoparticles for wearable devices*, Sci. Rep. 5 (2015), 11070.
64. Z. Zheng, J. Yao, B. Wang, G. Yang, *A flexible, transparent and high-performance gas sensor based on layer-materials for wearable technology*, Nanotechnology vol. 28 (2017), 415501.
65. P.M. Perillo, D.F. Rodríguez, *Low temperature trimethylamine flexible gas sensor based on TiO2 membrane nanotubes*, J. Alloys Compd. 657 (2016) 765–769.
66. E. Singh, M. Meyyappan, H.S. Nalwa, *Flexible graphene-based wearable gas and chemical sensors*, ACS Appl. Mater. Interfaces 9 (2017) 34544–34586.
67. Y.J. Yun, W.G. Hong, N.J. Choi, B.H. Kim, Y. Jun, H.K. Lee, *Ultrasensitive and highly selective graphene-based single yarn for use in wearable gas sensor*, Sci. Rep. 5 (2015), 10904.

68. B. Zhang and P-X Gao, *Metal Oxide Nanoarrays for Chemical Sensing: A Review of Fabrication Methods, Sensing Modes, and Their Inter-correlations*, Front. Mater. 6 (2019) 55.

Chapter 4: Experimental Methods and Characterization Techniques

4.1 Introduction

The experimental activity carried out during the thesis period was based on the development of semiconductors starting from the synthesis and characterization of the sensitive material, continuing with its deposition on the device and final sensing tests for the evaluation of the sensor's performance.

This chapter will discuss the main design phases of a semiconductor gas sensor carried out, describing in detail the procedure for preparing the gas sensors and the methods of carrying out the various tests conducted with the aim of evaluating the functionality of the semiconductor gas sensor.

4.2 Development of sensitive material

Synthesis is the first step in developing a gas sensor. It is essential that the material is pure and well prepared to obtain accurate analytical results.

The synthesis methods most adopted in experimental activity are sol-gel, pyrrolysis and Atomic Layer Deposition (ALD). The respective methods have already been discussed in paragraph 3.6 and will be treated in detail for each nanomaterial developed in the next paragraphs. Generally, the syntheses are done directly in the laboratory, or the materials are synthesized by other research groups with which collaborations are established.

4.3 Characterization of the sensitive material

The study of a sensitive nanomaterial for a gas sensor from an analytical point of view requires a series of specific approaches and techniques to characterize the properties of the material and evaluate its effectiveness as a gas sensor.

A *morphological analysis* involves characterizing the morphology of the nanomaterial, including particle size, shape, and distribution. Technique such as Scanning Electron Microscopy (SEM) is often used for this purpose and was mostly adopted for the experimental activity. The choice of SEM is given by the possibility of seeing the morphology of materials in the micro- and nanometer range. In fact, it works at a high magnification to 300,000x and even 1000000 (in the last models) in producing images very precisely. In addition to a qualitative analysis, it is possible to do a quantitative analysis for the coupling of an Energy Dispersive X-ray Spectroscopy (EDS). The instrumental apparatus, in Figure 4.1 (a) , is mainly composed of: a source, to generate high energy electrons; a column with electromagnetic lenses, which allow the passage and collimation of electrons; a deflection system; a backscattered and secondary electron detector; a chamber to contain the sample; finally, by a computer system with a screen to view the images and manage the instrument with appropriate software. The analysis of a material consists of inserting the sample into the chamber, subsequently a beam of electrons, generated by the source (collimated by the lenses) interacts and penetrates the depth of the sample. The interaction generates backscattered electrons and secondary electrons. The generated electrons are detected by the detector to obtain the final image that is displayed on the screen. The energy of the electron beam is important for good image resolution, as the image will be rich in surface information if low accelerating voltages (5 kV) are used. In contrast, high accelerating voltages (15-30 kV), penetrating below the surface, produce a reflected signal. The different ones are presented in the Figure 4.1 (b) electron penetration levels through the sample and reflected signals. Furthermore, image quality can be improved with sample tilting of 50°-70° [1].

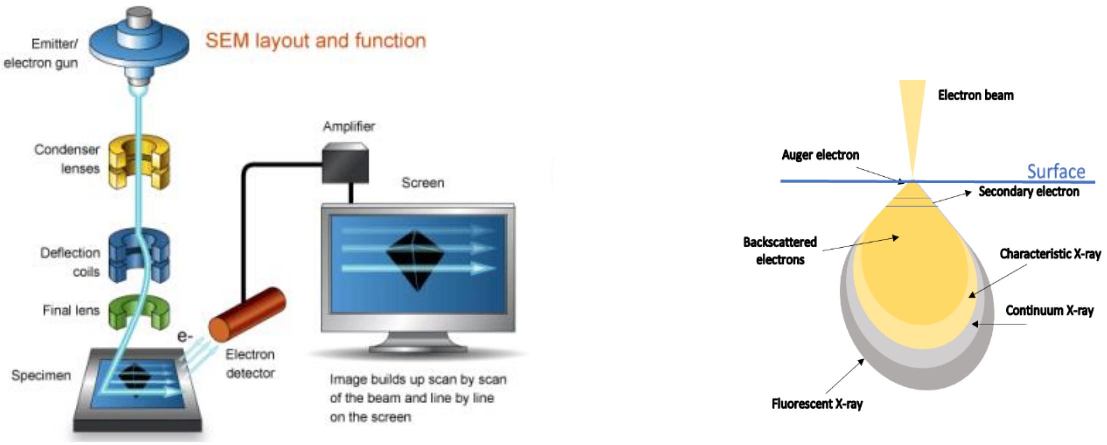

Figure 4.1. (a) Layout of SEM; (b) Electron penetration levels on surface of the sample.

The Transmission electron microscopy (TEM) technique was also adopted during the experimental activity to carry out a more detailed morphological investigation of the material.

TEM uses a focused beam of electrons to interact with a thin sample, providing detailed information about the sample's morphology, crystallography, and chemistry. The instrument is composed of a source or uses an electron gun to produce a stream of high-energy electrons, typically a tungsten filament or a field emission gun. The generated beam is collimated by magnetic lenses. The interaction of the beam with the material generates electrons that are detected by a fluorescent screen and a high-resolution image is obtained that reveals details on an atomic and nanometric scale. In Figure 4.2 a schematic representation.

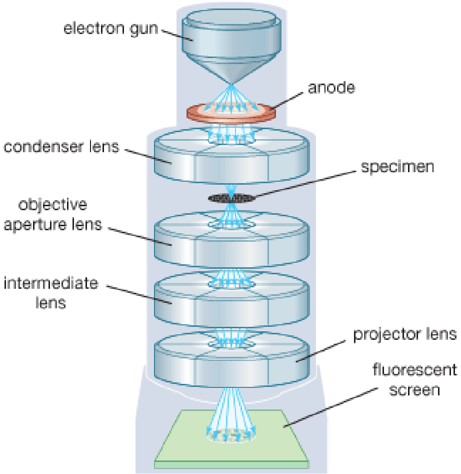

Figure 4.2. Schematic mechanism of TEM.

A *chemical analysis* of the nanomaterial can be determined using techniques such as Energy Dispersive X-ray Spectroscopy (EDS) or Fourier Transform Infrared Spectroscopy (FT-IR). These analyzes can reveal the presence of specific chemical elements, impurities, or chemical bonds.

EDS is a tool closely related to SEM. The chemical composition of the sample is obtained from the interaction of the electron beam (generated by the SEM) with the material. The interaction generates photons characteristic of the material which are detected by the instrument. The same allows to generate a spectrum showing the chemical elements of the material, even a mapping of the elements [1].

Fourier infrared spectroscopy is an absorption technique, where the source is infrared radiation of 0.7 µm-1000 µm wavelength, 14000 cm^{-1}-10 cm^{-1}. The wavelength generated by the source is absorbed by the molecules and causes a change in the dipole moment of the molecule, thus inducing bond vibrations (stretching or bending). These vibrations allow us to recognize a specific bond and therefore determine the chemical composition of the material studied. This possibility is favored by the interferometer based on the Fourier transform, a mathematical function that operates on the signal detected by the interferometer, obtaining the absorption of IR radiation by the sample as a function of the individual irradiation frequencies. What the interferometer produces is not directly the spectrum that is used for the spectrographic investigation, but a graph known as an "interferogram", a representation of the intensity of IR absorption by the sample as a function of time. The application of the Fourier transform converts the initial interferogram into the graphical form of the spectrum (see Figure 4.3). The most used is the mid-infrared region in the range 4000-400 cm^{-1} (2.5–25 μm). Most of the characteristic bonds of the functional groups of the compounds are found in the region of 4000 cm $^{-1}$-1300 cm $^{-1}$. There are also unique bonds for each molecule or "fingerprints" found in the regions between 1300 cm $^{-1}$- 400 cm $^{-1}$. The presence of water in the material interferes with the analysis, therefore the samples must be dehydrated [2].

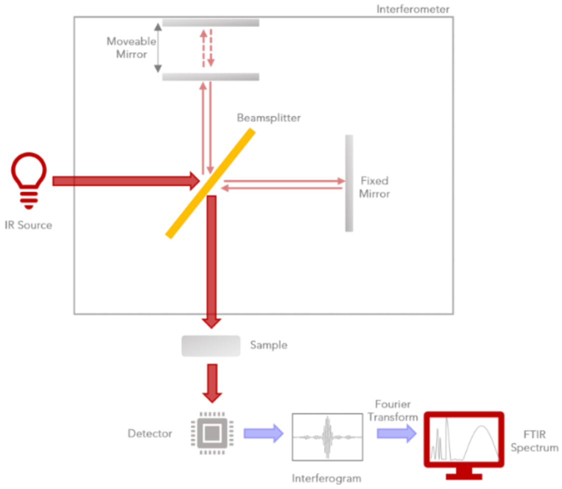

Figure 4.3. Schematic representation of FTIR instrument.

The *crystalline structure* of the material can be studied using the X-ray diffraction (XRD) technique. It is a characterization that allows a qualitative and quantitative analysis. Identify crystal structure, degree of crystallinity, crystallite size and atomic spacing, even crystalline phase. Typically, the obtained spectrum is compared with the JCPDS (Joint Committee on

Powder Diffraction Standards) library. The basic principle of the instrument is given by a monochromatic X-ray beam, by impacting on the surface of a material, the atoms interact with the radiation, which is transmitted, refracted, dispersed and absorbed. Diffraction requires coherent scattering of radiation by the solid. Coherent diffusion occurs due to the dimensional regularity of the unit cells of the solid and the necessary condition for the phenomenon to occur. To have coherent diffusion, the energy of the incident radiation must be equal to the energy of the scattered radiation according to Bragg's law. The directions of the scattered beam depend on the interatomic distance (d_{hkl}) of the plane and the wavelength of the radiation. The intensity of the scattered beam depends on the orientation of the crystal with respect to the direction of the incident X-rays and on the position of each atom within the unit cells. Furthermore, it must be considered that the wavelengths overlap in a constructive and destructive way, giving rise to permitted reflections with non-zero intensity and non-permitted reflections with minimum intensity. The diffraction criteria require the wavelength of the incident radiation, λ, to be less than the distance between the scattering sites. To meet the diffraction criteria, radiation with a wavelength less than 0.2 nm is required. Condition obtained with X-rays and high-energy electrons. The refracted radiation is detected by special films or by a detector. The location and intensity of the reflection refers to the identity and position of the atoms in the unit cell. The Bragg's law is represented by the following equation 4.1:

$$n\lambda = 2d\sin\theta \tag{4.1}$$

n is an integer, d_{hlk} indicates the interplanar distance that generates the diffraction and θ is the angle of incidence of the X-rays. The basic principle is shown in the Figures 4.4 (a) and (b):

Figure 4.4. (a) Schematic representation of XRD instrument; (b) Basic principle of XRD.

From the peaks observed in the spectrum, the composition from the intensity, the phase from the position, the parameters of the unit cells and the spacing of the groups are identified. Furthermore, the dimensions of the crystallites are identified from the width at half height of the peak (FWHM). The size is calculated according to the Scherrer's equation:

$$D = \frac{0.9\lambda}{\beta\cos\theta} \tag{4.2}$$

λ is the X-ray wavelength, β the line broadening at half maximum intensity and θ the Bragg angle [3].

The *characterization of the surface* of the nanomaterial plays an important role in the interaction with gas molecules, the most adopted technique is X-ray photoelectron spectroscopy (XPS). The technique offers the possibility of determining the elemental composition of the surface on defined points, it allows to make a mapping to see the distribution of the elements on a surface, while the high-resolution spectral measurement allows the recognition of surface chemical bonds through peak deconvolution. The basic principle is given by the detection and measurement of photoelectrons emitted from the surface of a material that has been initially irradiated with X-rays coming from a monochromatic source and having a fixed energy (hʋ). The emission of electrons (photoionization process) occurs from a nucleus electron (high binding energy) or from a valence electron (low binding energy). The emitted photoelectrons are focused and directed towards an electronic energy analyzer which can detect them based on their kinetic energy (E_{kin}). The measured kinetic energies of the photoelectrons are then converted to binding energies (E_b) via the equation:

$$E_b= h\upsilon- E_{kin}-W_f \qquad (4.3)$$

W_f is the work function, or the minimum energy needed for an electron to free it from the surface of a material. The binding energies obtained allow the detection of atoms on the surface, since each bond energy is characteristic of an atomic orbital, meaning that each atom generates characteristic peak in the spectrum. The technique guarantees the chemical composition and an analysis of the surface of the material because the interaction of the source with the material involves a greater emission of surface photons which are weakly bound compared to the photons found in the bulk of the material. The electrons emitted from the bulk undergo elastic and inelastic collisions, lose energy and the instrument is unable to detect them. The analyzes are conducted under ultra-high vacuum conditions to avoid contamination. [4] The Figure 4.5 (a) and (b) shows a schematic representation of the instrument.

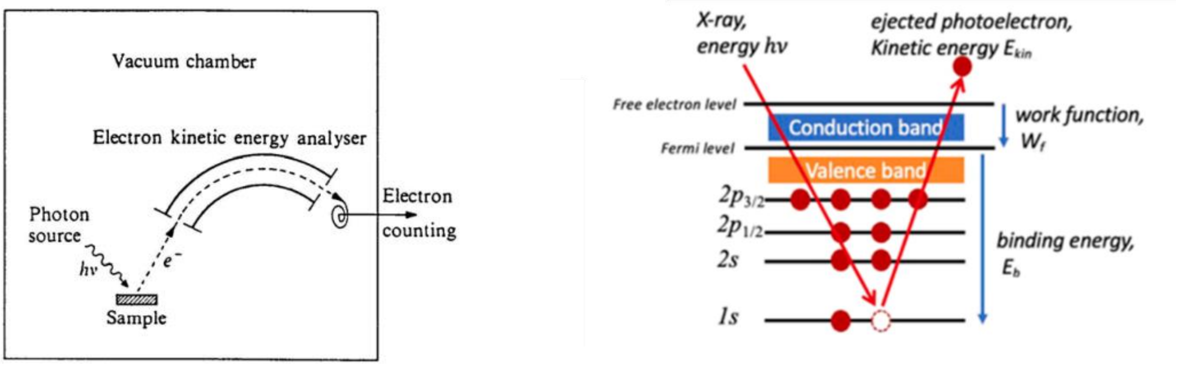

Figure 4.5. (a) Schematic representation of XPS instrument; (b) Representation of basic principle of XPS.

The *specific surface area* of the material is verified with the BET (Brunauer-Emmett-Teller) technique. The technique is based on the physical adsorption of gases on a solid surface (see Figure 5.6). Usually, nitrogen is the common gas used in BET analysis. The method involves exposing the sample of the material to different pressures of nitrogen at a constant temperature. By measuring the amount of gas adsorbed at different pressures, the specific surface area of the material can be calculated. BET theory is closely related to Langmuir theory, where multilayer adsorption is assumed in which all layers are in equilibrium (and do not interact with each other). Multilayer adsorption is a phenomenon that occurs when the surface temperature of the adsorbent is lower than the critical temperature of the gas molecules, the pressure increases until it reaches a value comparable to the vapor pressure of a mass when it condenses [5].

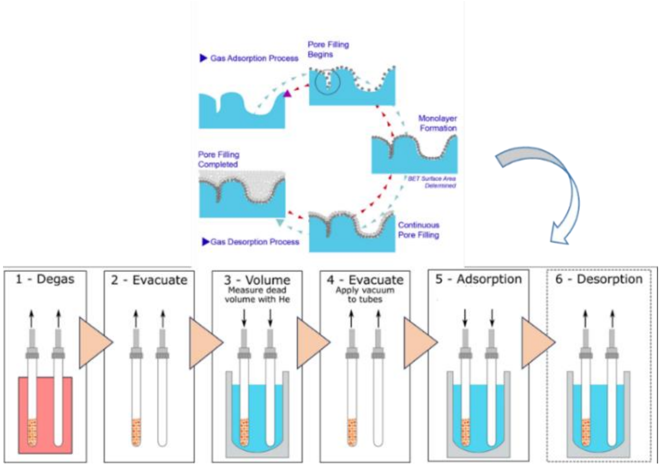

Figure 4.6. Mechanism and basic principles of BET technique.

TGA (Thermogravimetry) and DSC (Differential Scanning Calorimetry) are two *thermal analysis* techniques used to study the thermal properties and stability of samples.

TGA is a technique that measures the change in weight of a sample as a function of temperature or time. The sample is heated in a controlled environment (usually in a flow of inert gas) and the weight change is recorded continuously. The measurement can take place under non-isothermal conditions where the temperature of the material is gradually increased with a constant heating rate, or under isothermal conditions maintaining a constant temperature and recording the mass loss as a function of time at a given temperature [6]. The technique is used to determine the thermal stability of materials, measure the percentage of volatile components or composition of samples, study decomposition reactions, and much more. In Figure 4.7 a schematic representation.

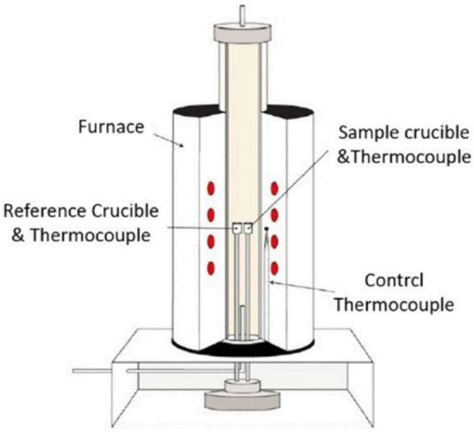

Figure 4.7. Schematic representation of TGA.

DSC measures the difference in heat absorbed or released by a sample compared to a reference as a function of temperature. During the analysis, the sample and reference are subjected to a heating or cooling program. The technique is used to determine thermal transitions in materials, such as melting points, solidification, glass transitions, exothermic or endothermic chemical reactions, and to evaluate the heat capacity, crystallinity, and other thermal properties of samples. The mechanism of the technique is showed in Figure 4.8 [7].

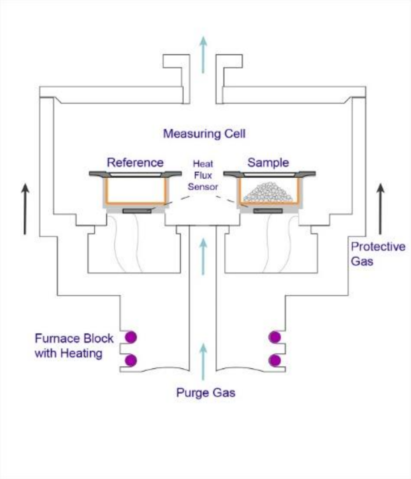

Figure 4.8. Mechanism of DSC technique.

4.4 Experimental procedures of the gas sensor semiconductor

A semiconductor resistive gas sensor consists of film often, electrically contacted by means of two metal terminals and placed above a suitable heatable support. During the experimental activity, a substrate with dimensions of 6 x 3 x 0.4 mm and a rectangular planar geometry was used to create resistive semiconductor sensors. The device consists of a slightly porous alumina support on whose faces they are deposited by means of technique *screen printing*, respectively the interdigitated electrical contacts and the heater, both in platinum. The use of alumina as a carrier material is linked to its chemical stability, in addition to its high thermal and mechanical stability. The use of platinum as a material for the creation of interdigitated contacts is also linked in this case to the high stability in the presence of many chemical species so as to avoid interference in the electrical signal mistakenly attributable to the film sensitive. The high electrical conductivity of this material makes it suitable for charge transfer between the sensitive film and the contacts themselves (reduced resistance of contact) without signal attenuation. Furthermore, the high electrical conductivity associated with thermal stability, make it suitable for the construction of the heater sensor.

In Figure 4.9 is showed the structure of the device and the deposition of material. In fact, the deposition of the sensitive material on the device was carried out via *screen printing* starting from a powder paste or often by *drop casting* starting from an aqueous suspension of the material. An appropriate quantity was deposited on the interdigitated contacts to form a thick film of the order of 1-10 μm. In in no case was it necessary to use binders to stabilize mechanically or favor the adhesion of the film to the ceramic substrate. The samples thus prepared were dried in air at room temperature until upon complete evaporation of the solvent. Where necessary, the samples were subjected to appropriate heat treatment on a plate.

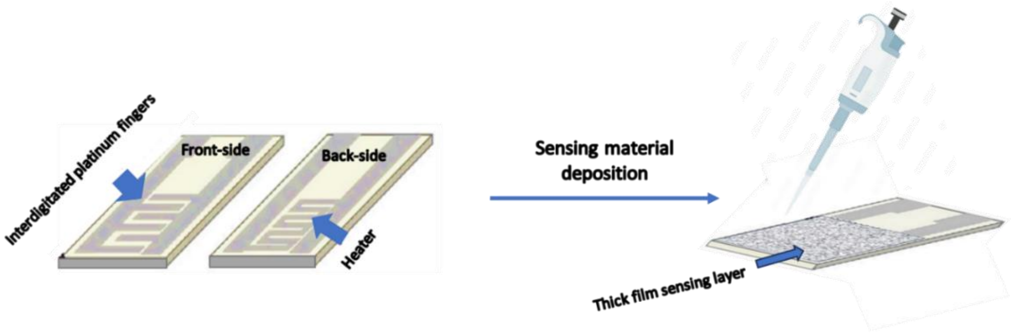

Figure 4.9. Device and deposition of sensing material.

The prepared sensor was housed inside a holder and subsequently inserted inside the measuring chamber of the instrument to carry out the sensing tests.

All tests were conducted in reference atmospheres containing air i.e. 80% nitrogen (N_2) and 20% oxygen (O_2). The target gases, as well as the reference gases, were coming from gaseous mixtures in air or nitrogen contained in certified cylinders. Their concentration was further modified by dilution with nitrogen or otherwise inert gas.

During all tests, the samples were heated up to working temperature desired while they were immersed in a constant flow equal to 100 ml/min of the mixture gaseous. Before starting the sensing tests, the sample signal was stabilized to tolerable values such as not to influence subsequent measurements. Then the samples were subjected to pulses of appropriate duration of the target mixture containing the test analyte species. The responses of the sensors were evaluated as the change in electrical resistance experienced from the sensitive element of the sensor according to equation 4.3 considering the variation of the basic signal and the variation of the resistance in the presence of a target gas.

$$S = \frac{R_{air}}{R_{gas}} \qquad \text{or} \qquad S = \frac{R_{gas}}{R_{air}} \tag{4.3}$$

R_{air} and R_{gas}, both represent the resistance value of the sensor, one in air and the other in the presence of the target gas.

4.5. Experimental apparatus for gas sensing tests

The experimental apparatus used for the tests characterization of gas sensors, consists of a gas flushing system capable of generating gaseous mixtures, to be sent inside a measurement chamber where it is placed the sensor, and by an electronic system for controlling the test conditions, of measurement and acquisition of the response signal of the sensor itself. The main components used for the experimental setup are shown in the Figure 4.10. Below is a detailed description of the parts of the instrumental apparatus.

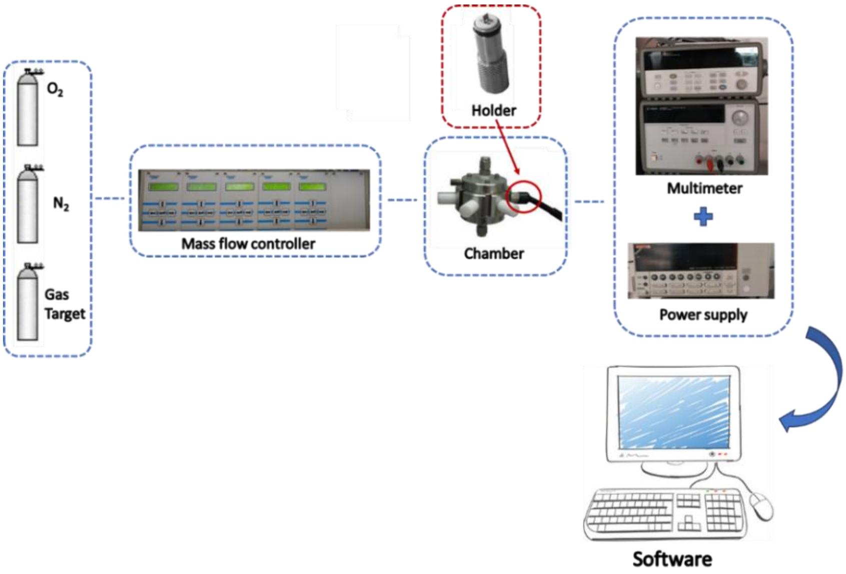

Figure 4.10. Schematic representation of the instrumental apparatus.

The *flushing system* was built to be able to create gaseous mixtures with the desired concentrations of the individuals gas, to be able to manage the flow rates and to be able to divert the flows towards the sensor chamber interest. During the tests, the sensors are continuously exposed to the reference gas as well as to the target gas, this possibility is given by a four-way valve present in the apparatus. The valve has two possible passages given by the rotation of the 90° lever. The first allows to direct the gas flow reference to the sensor chamber, at the same time the target gas flow is diverted directly to the drain. Conversely, the second allows to divert the reference to the exhaust and simultaneously the target gas to the chamber of the sensor. The system allows to adjust the flow rate of the target gas by means of appropriate controls electromechanical regulators placed upstream, so as to set the desired concentrations and wait for the flow to stabilize without affecting the gaseous mixture passing through inside the measurement chamber. This way it will be possible to divert at the moment desired, the target gas to the sensor without the risk of artefacts in the response signal due to poor flow management. The entire system is made using steel pipes which guarantees high stability in the presence of various chemical species and in a humid atmosphere. This allows the possibility of using the system also with substances aggressive substances such as strong acids. In the complete configuration the system involves the use of five regulators of flow (*Mass Flow Controller – MFC*), two of which are used on the line reference and three on the target gas line. According to this configuration it is possibly create gaseous mixtures with variable concentrations for the reference flow than for the target flow. In particular, regarding the reference having a by placing two flow rate regulators it is possible to create binary mixtures with ratio of variable concentrations. Regarding the target flow line, it is possible have three flow regulators. In that case, two of these are employed to adjust the flow of the carrier gas (usually a gaseous mixture identical to that of reference) which has the purpose of diluting the actual target gas, managed by means of the third flow regulator. Acting simultaneously on these last three regulators of flow it is possible to set the desired concentration of the target substance from send to the measurement room. Flow rate regulators, often referred to by the acronym *MFC (Mass Flow Controller*) are devices capable of measuring the mass flow rate of a fluid passing through them and at the same time by acting on appropriate regulation valves, they can regulate the delivery flow. Five flow regulators were used to create the system analogue BRONKHORST EL-FLOW MASS FLOW METER AND CONTROLLER‖ by of which: two of oxygen with a maximum flow rate of 50 nml/min; one of nitrogen at 100 nml/min e two of air at 100 nml/min. Although the regulators are calibrated for operation with gases mentioned, can be used with other types of gas with appropriate prior approval calibration implementable within the controller for devices. The flow regulators used are of the thermoconductive type and therefore based on the operating principle on the measurement of the heat transported by the fluid due to the flow speed and physical characteristics of the gas. The flow regulators are managed by means of an analog controller “BRONKHORST E7000”.

The system provides the possibility of carrying out tests in a humid atmosphere or send chemical species in the vapor state as well as volatile organic compounds to the sensor which are liquid at room temperature, thanks to the presence of a bubbler.

The *bubbler* is a simple ampoule commonly made of glass; inside the which liquid you intend to vaporize is present. The carrier gas is introduced from below inside the bubbling liquid that carries part of this with it, in operation of the saturation limits imposed by the pressure and temperature conditions. The total flow exiting the bubbler will be the sum of the gas flow carrier plus the flow of transported steam. The steam flow transported by the carrier gas is therefore linked to both the flow rate the latter than the partial pressure of the liquid and can be varied by acting on its saturation temperature. The temperature can be controlled by keeping the bubbler submerged inside a thermostated liquid bath by means of which it is possible to set and maintain the desired temperature conditions. This is accomplished by means of a thermocryostat capable of working in both heating and cooling conditions cooling compared to the ambient temperature.

The flows are sent to a *stainless-steel measurement chamber*. The chamber, in figure, consists of a body bearing six radial holes for accommodate sample holders, a splitter and a bottom lid. The splitter has the purpose of dividing the total flow entering the chamber into equal parts towards the six inserted sensors. Collectors for the introduction and expulsion of the gas flow from the chamber. Furthermore, the chamber must guarantee: the reproducibility of the tests carried out even at different times; minimize the internal volume to ensure times rapid evacuation; avoid the presence of recirculation flows or stagnant volumes to do not generate artifacts in the sensor response; guarantee the conditions of almost stationarity of the flow avoiding velocity gradients.

The sample *holder* is a pin made of steel on the outside and slightly porous ceramic on the inside with excellent mechanical properties and thermal resistance. Four electrical contacts are located inside the holder compatible with the substrate used to create the test samples. The dimensions of the plug are such as to be compatible with the seats made on the measuring chamber, the seal between the two parts is achieved by means of a special rubber ring.

The measuring parameter of semiconductor gas sensors is an electrical signal associated with the change in resistance suffered by the sensitive element as a result of the interaction with the gas. The measurement takes place using an *electronic control system* signal acquisition consisting of a power supply, a multimeter and software dedicated.

A *multimeter,* AGILENT 34970A, allows you to precisely detect the resistance value of the film sensitive sensor. It is connected to the interdigitate contacts of the substrate. The read values are then acquired by means of the software to which it is interfaced together with the power supply. The *power supply*, an AGILENT E3632A, consists of two outputs respectively with voltage of 0-15 V with current between 0-7A and 0-25 V with current between 0-4 A to satisfy a wider power range. It supplies a voltage value to the sensor heater so set and maintain a constant temperature during the operating phases. The temperature of the sensor will be linked to the heat dissipated by the heater due to the Joule effect. Both signal acquisition and temperature control are handled for using AGILENT VEE *software*. The main purpose of the software is to acquire the film resistance signal in real time sensitivity of the sensor detected using the multimeter.

4.6 Referens

1. A. Mohammed, A. Abdullah, *Scanning Electron Microscopy (SEM): A review*, Proceedings of 2018 International Conference on Hydraulics and Pneumatics - HERVEX November 7-9, Băile Govora, Romania.
2. M. Krysa, M. Szymanska-Chargot, A. Zdunek, *FT-IR and FT-Raman fingerprints of flavonoids – A review*, Food Chemistry 393 (2022) 133430.
3. H. Khan, A.S. Yerramilli, A. D'Oliveira, T.L. Alford, D. C. Boffito, G.S. Patience, *Experimental methods in chemical engineering: X-ray diffraction spectroscopy—XRD*, Can J Chem Eng. 98 (2020) 1255–1266.
4. R. Ghobeira, P.S.E. Tabaei, R. Morent, N. De Geyter*, Chemical characterization of plasma-activated polymeric surfaces via XPS analyses: A review*, Surfaces and Interfaces 31 (2022) 102087.
5. F. Ambroz, T. J. Macdonald, V. Martis, and I. P. Parkin, *Evaluation of the BET Theory for the Characterization of Meso and Microporous MOFs*, Small Methods 2 (2018) 1800173.
6. S. Gerassimidou, C.A Velis, P.T. Williams and D. Komilis, *Characterization and composition identification of waste-derived fuels obtained from municipal solid waste using thermogravimetry: A review*, Waste Management & Research 38(9) (2020) 942–965.
7. C. Leyva-Porras, P. Cruz-Alcantar, V. Espinosa-Solís, E. Martínez-Guerra, C.I. Piñón-Balderrama, I.C. Martínez and M.Z. Saavedra-Leos, *Application of Differential Scanning Calorimetry (DSC) and Modulated Differential Scanning Calorimetry (MDSC) in Food and Drug Industries*, Polymers 5 (2019) 12.

Chapter 5: Results and Discussion

5.1 Overview

Having described all the phases to develop a semiconductor gas sensor, the experimental activity will be described in detail. The developed sensors will be discussed and grouped according to the synthesis methods.

5.2 Sensing materials *via* Sol-gel method:

5.2.1 Al,Ca-Doped ZnO sensor for Formaldehyde detection

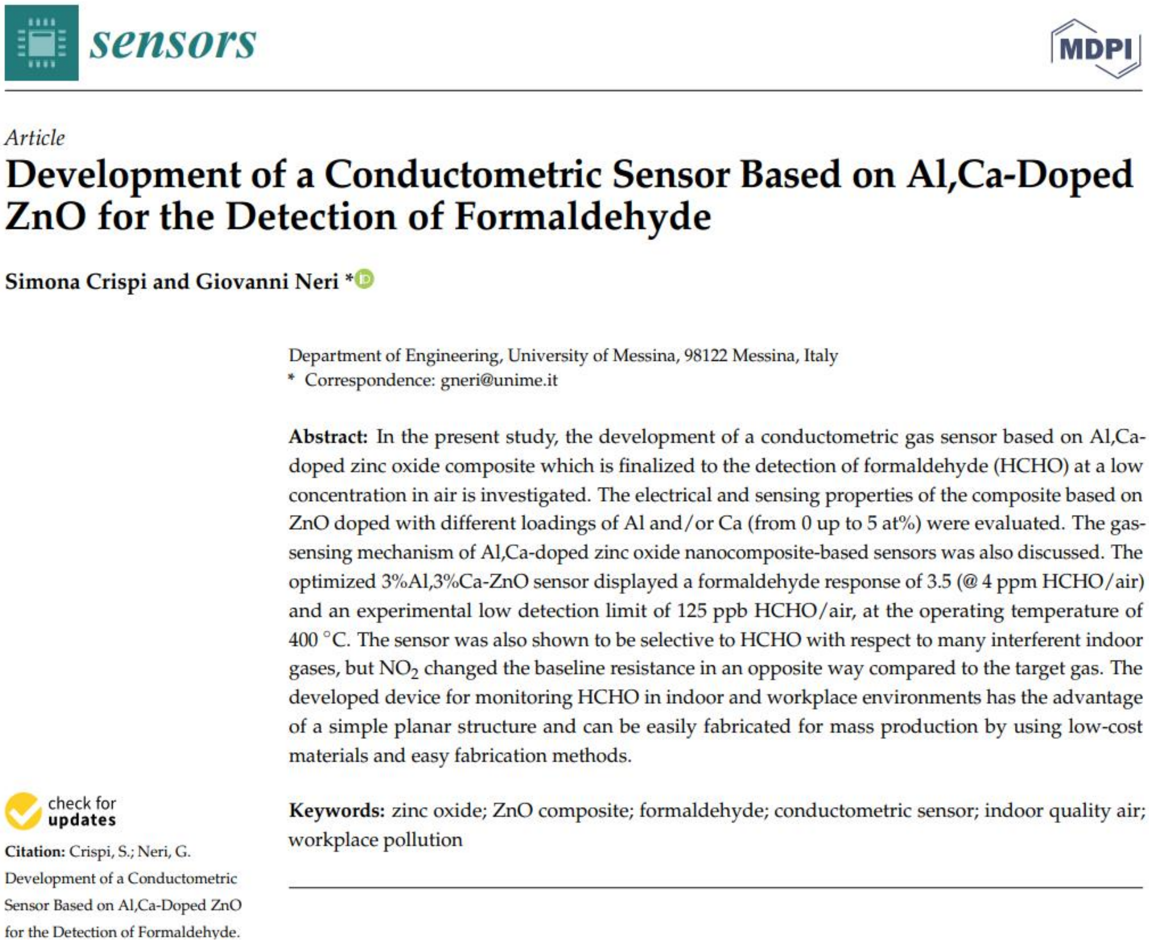

sensors

MDPI

Article

Development of a Conductometric Sensor Based on Al,Ca-Doped ZnO for the Detection of Formaldehyde

Simona Crispi and Giovanni Neri *

Department of Engineering, University of Messina, 98122 Messina, Italy
* Correspondence: gneri@unime.it

Abstract: In the present study, the development of a conductometric gas sensor based on Al,Ca-doped zinc oxide composite which is finalized to the detection of formaldehyde (HCHO) at a low concentration in air is investigated. The electrical and sensing properties of the composite based on ZnO doped with different loadings of Al and/or Ca (from 0 up to 5 at%) were evaluated. The gas-sensing mechanism of Al,Ca-doped zinc oxide nanocomposite-based sensors was also discussed. The optimized 3%Al,3%Ca-ZnO sensor displayed a formaldehyde response of 3.5 (@ 4 ppm HCHO/air) and an experimental low detection limit of 125 ppb HCHO/air, at the operating temperature of 400 °C. The sensor was also shown to be selective to HCHO with respect to many interferent indoor gases, but NO_2 changed the baseline resistance in an opposite way compared to the target gas. The developed device for monitoring HCHO in indoor and workplace environments has the advantage of a simple planar structure and can be easily fabricated for mass production by using low-cost materials and easy fabrication methods.

Keywords: zinc oxide; ZnO composite; formaldehyde; conductometric sensor; indoor quality air; workplace pollution

check for updates

Citation: Crispi, S.; Neri, G. Development of a Conductometric Sensor Based on Al,Ca-Doped ZnO for the Detection of Formaldehyde.

Abstract: In the present study, the development of a conductometric gas sensor based on Al,Ca-doped zinc oxide composite which is finalized to the detection of formaldehyde (HCHO) at a low concentration in air is investigated. The electrical and sensing properties of the composite based on ZnO doped with different loadings of Al and/or Ca (from 0 up to 5 at%) were evaluated. The gas- sensing mechanism of Al,Ca-doped zinc oxide nanocomposite-based sensors was also discussed. The optimized 3%Al,3%Ca-ZnO sensor displayed a formaldehyde response of 3.5 (@ 4 ppm HCHO/air) and an experimental low detection limit of 125 ppb HCHO/air, at the operating temperature of 400 °C. The sensor was also shown to be selective to HCHO with respect to many interferent indoor gases, but NO_2 changed the baseline resistance in an opposite way compared to the target gas. The developed device for monitoring HCHO in indoor and workplace environments has the advantage of a simple planar structure and can be easily fabricated for mass production by using low-cost materials and easy fabrication methods.

5.2.1.1 Introduction

Air pollution does not only affect the external environment that surrounds us, but those places that we consider safe. In fact, the air we breathe indoors such as in our homes, offices, and schools can be unhealthy. This specific pollution is called “indoor pollution” and can be quantified through the indoor air quality (IAQ) index. Attention to this issue has been highlighted by research on the increase in diseases related to the respiratory system in more sensitive subjects, such as children and the elderly, who spend more time indoors [1]. Formaldehyde is also widely used in numerous production processes, so it is a well-known occupational pollutant in the workplace [2].

Pollutants that worsen the indoor air quality generally come from chemical pollutants such as painted walls, furniture, and household cleaning detergents [2]. Among them, formaldehyde (HCHO) is one of the most toxic indoor and workplace pollutants. The International Agency for Research on Cancer (IARC) classifies formaldehyde as a carcinogen. In our homes, formaldehyde is present in very low concentrations, but it tends to accumulate mainly in conditions of low temperature and low humidity. The World Health Organization (WHO) guidelines for indoor air quality set a formaldehyde exposure limit (WHO, 2010) of

0.08 ppm (for an average concentration of 30 min). This limit is set so that there is no development of acute and chronic irritation of the respiratory tract, taking into consideration even the most sensitive subjects, including children and the elderly. In fact, concentrations of 0.4–1.0 ppm of formaldehyde could cause irritation to the eyes, nose, and throat. High concentrations, such as 6 ppm, could cause nasopharyngeal cancer, lung problems, and leukemia. In working places, HCHO has become one of the major threats for the worker's health in the wood, textile, paper, construction, and chemical industries [2].

Many analytical methods have been developed for monitoring HCHO by using conventional analytical techniques, such as mass spectrometry and gas chromatography [3]. Optical techniques also show a low limit of detection (LOD) and a high accuracy and selectivity for the analysis of formaldehyde [4]. However, the cost and the high complexity and poor portability of these techniques are the main factors that limit their use. Therefore, simple and low-cost formaldehyde sensors should be mandatory.

Conductometric sensors based on semiconductor metal oxides are particularly promising for detecting this pollutant and can ensure safe conditions at home and in the workplace. The operating principle is very simple and is based on the variations in resistance in the presence of gaseous species that act as electron donors or acceptors through surface reactions occurring on the surface of the semiconductor sensing material. Different gaseous species can be monitored with a single sensor by varying the operating temperature [5]. Furthermore, they have the advantage of being miniaturized devices and having low production costs. Among the metal oxides reported in the literature that can detect formaldehyde we can cite In_2O_3 [6], NiO [7], SnO_2 [8], and ZnO [9], and so on.

In this paper we focused our attention on the development of a reliable conductometric formaldehyde sensor for indoor applications based on doped-ZnO. The choice fell on ZnO as it is a simple material to obtain and has a low cost. It is an n-type semiconductor, has a 3.37 eV band gap, a 60 meV excitation binding energy, and a 400 $cm^2 V^{-1} s^{-1}$ high electron mobility [10].

It is well known that ZnO is a sensing material with a wide application in conductometric gas sensors, due to its sensitivity towards several gases such as ethanol, nitrogen dioxide, acetone, and ammonia, etc. [11]. The addition of dopants modifies the electrical and gas-sensing properties of the zinc oxide [12]. In several papers in the literature, it has been shown that the presence of dopants belonging to the II and III groups of the periodic table improves the performance of ZnO due to the decrease of the grain boundaries in the lattice, therefore, improving the adsorption mechanisms of target gas. In a first exploratory study, Jaballah et. al., proposed a Ca-doped ZnO sensor for formaldehyde detection. The addition of this dopant has led to the improvement of sensing properties towards the target gas [9].

Here, we aimed to further improve the sensing performance of the zinc oxide for formaldehyde by adding different loadings of Al and Ca dopants. As these two dopants may introduce large changes in the electrical characteristics and interactions with different gases, the ternary Al,Ca-ZnO composite has been optimized previously by our group for monitoring other target gases, such as CO_2 [13], resulting in an effective way to widen the sensing application of a pristine ZnO semiconductor. Focus was given to the optimization of the loading of Ca and Al and their ratio for increasing the sensitivity, decreasing the baseline resistance, and enhancing the selectivity to HCHO, compared to ethanol, the main pollutant interferent in the indoor environment. Furthermore, the study of the sensing mechanism and the reactions that occurred on the surface of pure and doped ZnO when dealing with formaldehyde, are also presented.

5.2.1.2 Materials and Methods

5.2.1.2.1 Synthesis of Al,Ca-Doped ZnO

The Al,Ca-doped ZnO composites were obtained by the sol-gel method following the synthetic procedure presented in the literature [14]. Briefly, 16 g of zinc acetate dehydrate [$Zn(CH3COO)_2·2H_2O$] was used as a precursor in 112 mL of methanol. For the doping aluminum nitrate-9-hydrate [$Al(NO_3)_3·9H_2O$] and calcium chloride-6-hydrate [$CaCl_2·6H_2O$] were used in suitable quantities considering the atomic ratio percent (at%) of 1, 3, and 5 of [Al]/[Zn] and [Ca]/[ZnO] in 112 mL of methanol on magnetic stirring for 10 min. Subsequently, 200 mL of ethanol was added to the solution to be placed in an autoclave, maintained for 15 min under magnetic stirring, and dried in the supercritical conditions of ethyl alcohol. The obtained powders were then annealed in an oven for 2 h at 400 °C in air. The samples obtained were used for fabricating the conductometric sensors by depositing them on the interdigitated electrode platforms.

5.2.1.2.2 Characterization

Morphological analysis was carried out by SEM using a ZEISS 1540XB FE SEM instrument (Carl-Zeiss, Jena, Germany) equipped with an EDX detector. Transmission electron microscopy (TEM) was carried out with a JEOL JEM 2010 electron microscope (LaB_6 electron gun) operating at 200 kV, equipped by a Gatan 794 Multi-Scan CCD camera for digital imaging. Samples for TEM analysis were prepared by dropping a suspension of the starting powder, dispersed in isopropanol and sonicated, on a 400 mesh holey-carbon coated copper grid. An X-ray diffractometry (XRD) analysis was carried out on a Bruker AXS D8 Advance diffractometer within the 2θ range of 20 to 80° using CuKα as an X-ray source (λ = 1.5406 Å). ATR-FTIR analyses were performed using a Spectrum Two (Perkin-Elmer) FT-IR spectrometer with a diamond ATR (attenuated total reflection) single reflection accessory.

5.2.1.2.3 Sensing Tests

The sensing tests were carried out using a conductometric 3 × 6 mm ceramic platform with interdigitated contacts in Pt. Details on the conductometric ceramic platform have been reported in a previous paper [9]. Ten µL of nanomaterial dispersed in water was deposited on each device. To carry out the tests, the sensors were inserted in a holder connected to the instrumental apparatus. The instrumental apparatus consisted of a stainless-steel measuring chamber, a multimeter to acquire data Agilent 34970A, and a dual-channel power Agilent E3632A to bias the built-in heater of the device. The sensors were subjected to a flow of dry air of 100 cc (20 cc O_2 + 80 cc N_2) in relation to the flow of formaldehyde gas adopted for the sensitivity tests. The formaldehyde gas bottle used for the pulse is certified by the SOL company (www.solgroup.com (accessed on 20 August 2022)). To validate our sensor, a commercial formaldehyde sensor (SFA30 electrochemical sensor from Sensirion AG, Switzerland) was used and located near the gas flow output of our sensor. The sensor response to target gas (R) is determined as the ratio of Ra (resistance of the gas sensor in dry synthetic air) to Rg (resistance of the injected gas sensor): R = Ra/Rg. The calculation of the response and recovery time, i.e., the variation of the sensor resistance over time until it reaches 90% equilibrium after the start and the end of CH_2O detection, facilitated the study of the sensor dynamics.

5.2.1.3 Results

5.2.1.3.1 Morphological and Microstructural Characterization

The TEM images reported in Figure 5.1 highlight the differences between the pristine ZnO and the doped samples, in agreement with previous reports [11,14]. Well-shaped particles with a size range of 20–80 nm were observed on the ZnO and Ca-ZnO (see Figure 6.1a,b), whereas the presence of small particles of a few nm in size decorating the surface of the large ZnO grains was clearly noted on Al doped-ZnO and Al,Ca doped-ZnO samples (see Figure 1c) [14,15]. As these smaller particles were not found on the pure ZnO and Ca-ZnO samples, it is plausible to assume that they are related to the presence of phase(s) rich in Al, which are likely to come from a heterogeneous nucleation and successive growth on the surface of ZnO particles during synthesis in the presence of this dopant. Of course, the presence of such segregated particles on the surface, as probed by TEM, means that the local/surface composition could be very different from the theoretical one. Indeed, the at% for each dopant was theoretically calculated and based on the ratio of precursor materials. Unfortunately, at this stage we did not have the support from XPS or other techniques, which could have given us important quantitative information.

The x-ray diffraction (XRD) spectra showed the polycrystalline nature of the doped-ZnO materials, which also maintained the wurtzite structure of pure ZnO (see Figure 5.2). A detailed XRD characterization of the samples investigated has been carried out and reported separately in various papers [9,13,15]. An effect of the doping was to reduce crystallite size. This finding has been reported by other authors, even when the Al,Ca-doped ZnO composites were prepared by different synthesis methods [16]. As an explanation of this, we may focus attention on the large difference in the atomic radius between zinc (1.42 Å) and calcium (1.94 Å), leading to lattice structure distortion, which consequently limits the growth of the wurtzite grains [17].

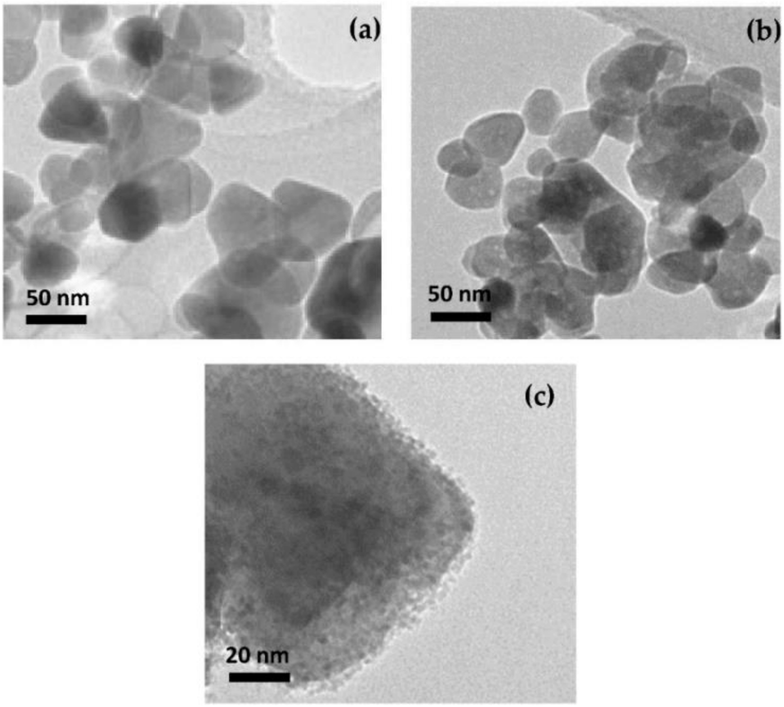

Figure 5.1. TEM images taken at the same magnification showing the particle shape and size of: (a) ZnO; (b) 1Ca-doped ZnO; and (c) Higher magnification of one particle of 3Al,3Ca-doped ZnO showing the fine particles dispersed on the surface of the bigger one (see text for the explanation).

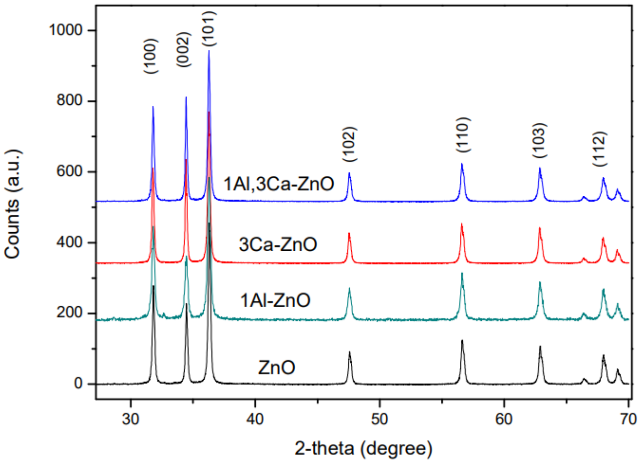

Figure 5.2. XRD of some representative samples used in this study.

In summary, the morphological and microstructural variation occurring through the doping process are expected to give large benefits in gas detection due to an enhancement of the active surface sites. Further, the formation of contact zones at different conductivity modifies the local Schottky barrier at the grain boundaries, thus creating multiple pathways for electrical conduction and helping gas-sensing detection.

5.2.1.3.2 Chemical Characterization

Additional information was acquired by a detailed ATR-FTIR characterization. In Figure 5.3a the IR spectrum of pure ZnO is reported, where the main peaks observed at 3398 cm^{-1} were relative to the O-H group, at 1513 cm^{-1} they were relative to the HC = CH group, and at 1372 cm^{-1} they were relative to the -COCH$_3$ group [18]. In the fingerprint region the presence of additional peaks were found at 829 cm^{-1}-700 cm^{-1}, relating to the Zn-OH, and at 400 cm^{-1}, relating to the Zn-O [19]. Figure 6.3b shows the characteristic ATR-FTIR obtained from Al-Ca doped/ZnO samples. Peaks were observed at 3492–3442 cm^{-1} for stretching of the $^{-}$OH group, at 1628 cm^{-1} of the C=C group, at 1440 cm^{-1} of the C-H group, at 1040 cm^{-1} of the CO-O-CO group, at 870 cm^{-1} of the Zn-OH group, at 719 cm^{-1} of the Ca-O group [20], at 555 cm^{-1} of the Al-O group [21], and stretching of the Zn-O group.

Bands associated with organic functional groups detected on the sensor layer before exposure to HCHO were due to some residues coming from the precursor materials used for the sol-gel synthesis, e.g., Zn(CH3COO)$_2$ and methanol.

Although the ATR-FTIR spectra showed that it can only give a qualitative representation of the samples investigated, this technique could be utilized to characterize the composite materials under HCHO sensing working conditions and give some information about the adsorption of formaldehyde on the surface of the sensing layer (see in the paragraph below).

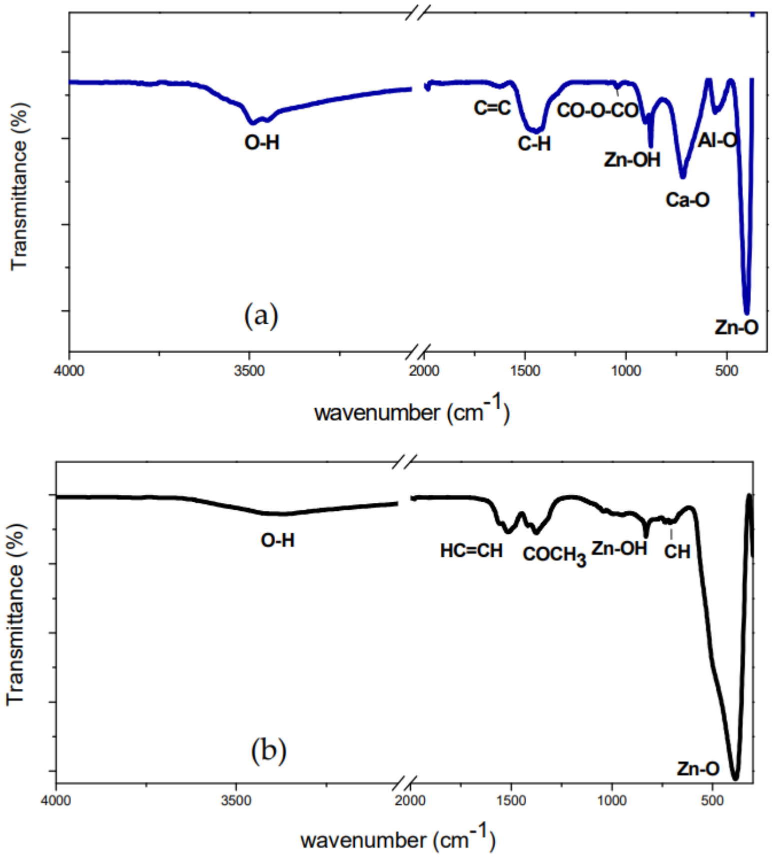

Figure 5.3. ATR-FTIR spectrum of as prepared: a) ZnO; b) 3Al,3Ca doped ZnO.

5.2.1.3.3 Electrical and Gas Sensing Characterization

The baseline resistance in dry air of the Al,Ca doped/ZnO samples was first measured at different temperatures from 100 ◦C to 400 ◦C (see Figure 5.4). Pristine ZnO shows the typical behavior of metal oxide semiconductors, i.e., as the temperature increases the baseline resistance decreases, due to the increase in the charge carriers (electrons).

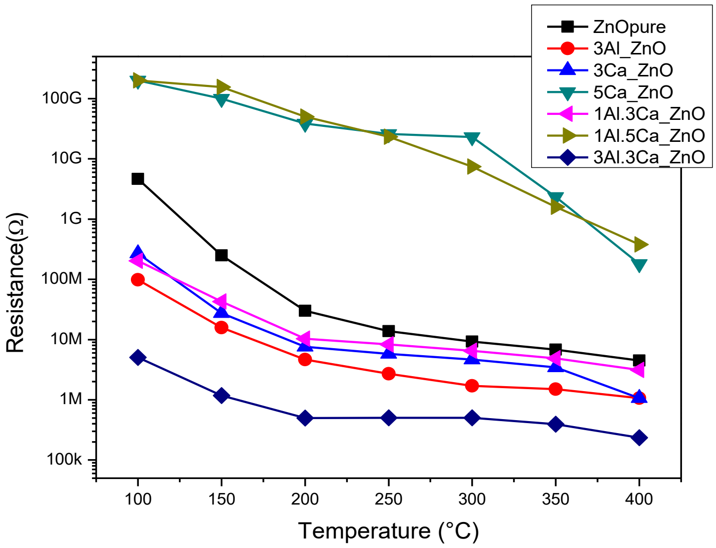

Figure 5.4. Baseline resistance in dry air of the pure and doped-ZnO sensors in the temperature range from 100 to 400 ◦C.

The results of the investigation indicated also that the Al,Ca doped/ZnO samples behaved in a similar way, i.e., the introduction of the dopants does not change the intrinsic semiconductor characteristics of the pristine ZnO. However, as clearly observed in the graph, there is a significant decrease in the resistance of the ZnO due to the doping process. This could be due to intrinsic defects that were induced during the doping process. The presence in the samples of the highest Ca loading (5at%), led to very high resistance (≥ 1 GΩ at temperature below 350°C). These observations are un agreement with previous studies, highlighting that the electrical conductivity in the Al,Ca-doped ZnO system is dependent on the loading and the ratio between the two dopants. [13,15]

To investigate the sensing performance towards the detection of formaldehyde, the sensors were tested in the same temperature interval, from 100 ◦C to 400 ◦C with a target gas concentration of 4 ppm. Figure 5.5 shows that the response of the sensors towards formaldehyde increases with the increasing temperature, except for the sensors with the highest loading of Ca (i.e., 5 at%), which did not show any response to this gas. The effect of the Al/Ca ratio on the response to HCHO suggests that the presence of Al was effective in improving the response towards the target gas, compared to the corresponding Ca-ZnO sensors. A concentration of Al between 1 and 3% appeared to be most effective in the working temperature above 300 ◦C.

Based on the electrical characterization and sensing tests at different temperatures, we selected the 3Al,3Ca doped ZnO sensor for further tests. This choice was motivated by the fact that this sensor showed a good balance of the sensing properties towards formaldehyde, e.g., a high response to the tested concentration of formaldehyde (4 ppm) and also a low baseline resistance. Figure 5.6a shows the dynamic response of this sensor towards 4 ppm HCHO at different temperatures. The highest response was found at the working temperature of 400 ◦C. Figure 5.6 b, c shows the response of the sensor registered at this temperature when subjected to a pulse of 0.125 and 4 ppm of formaldehyde in dry air, respectively. It was found that the response (τres), and also the recovery time (τ_{rec}), registered at different concentrations, became longer with an increasing HCHO concentration (from 56 s at 0.125 ppm up to 100 s at 4 ppm for τres and from 60 s at 0.125 ppm up to 150 s at 4 ppm for τ_{rec}). Following this, a transient HCHO pulse of 180 s duration and 300 s duration, respectively, for recovery in air was found.

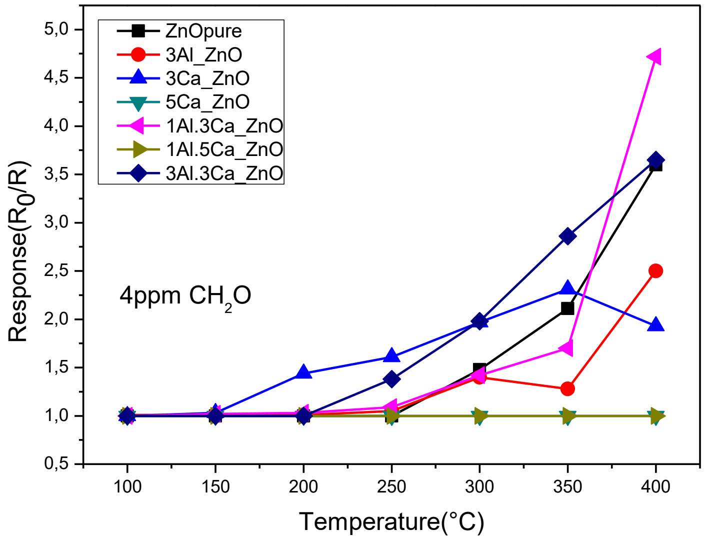

Figure 5.5. Responses to formaldehyde (4 ppm in dry air) of the pure and doped-ZnO sensors in the temperature range from 100 to 400 ◦C.

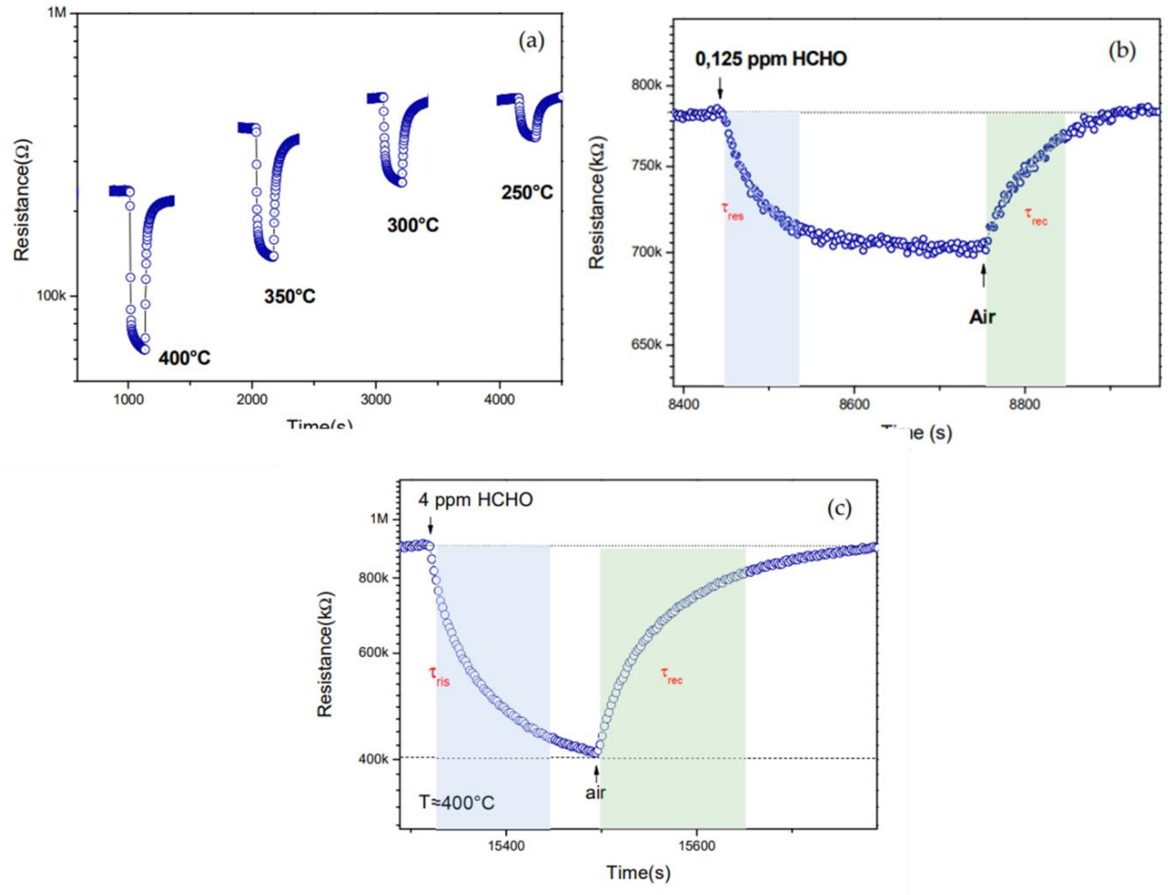

Figure 5.6. (a) Sensing tests of 3Al,3Ca-doped ZnO sensor to 4 ppm HCHO at different temperature; (b) Dynamic response of the sensor to 0.125 ppm HCHO at 400 °C, showing the response and recovery time; (c) Dynamic response of the sensor to 4 ppm.

Figure 5.7a shows the response of the 3Al,3Ca-doped ZnO sensor at different concentrations of formaldehyde, increasing the values from 0.125 ppm to 4 ppm of HCHO. Even at the lowest concentration tested, the response signal satisfied the condition S/N > 3, where S is the response signal and N is the noise level, so the experimental limit of detection (LOD) was 125 ppb HCHO/air. The related calibration curve is reported in Figure 5.7b, which highlights the linearity of the response. The data have been fitted through a linear regression model (see the red line fitting the experimental data), resulting in a coefficient of determination $R^2 = 0.9985$ which is indicative of the goodness of the linear fit.

Furthermore, the response was registered by decreasing the concentration values of HCHO, from 4 ppm to 0.500 ppm. Data, plotted in the same graph of Figure 5.7b, demonstrate the absence of any hysteresis curve, i.e., practically the sensors do not suffer from the so called "memory effect", which may invalidate the performance of the environmental sensors subjected to alternate, casual variation in the gas to be monitored.

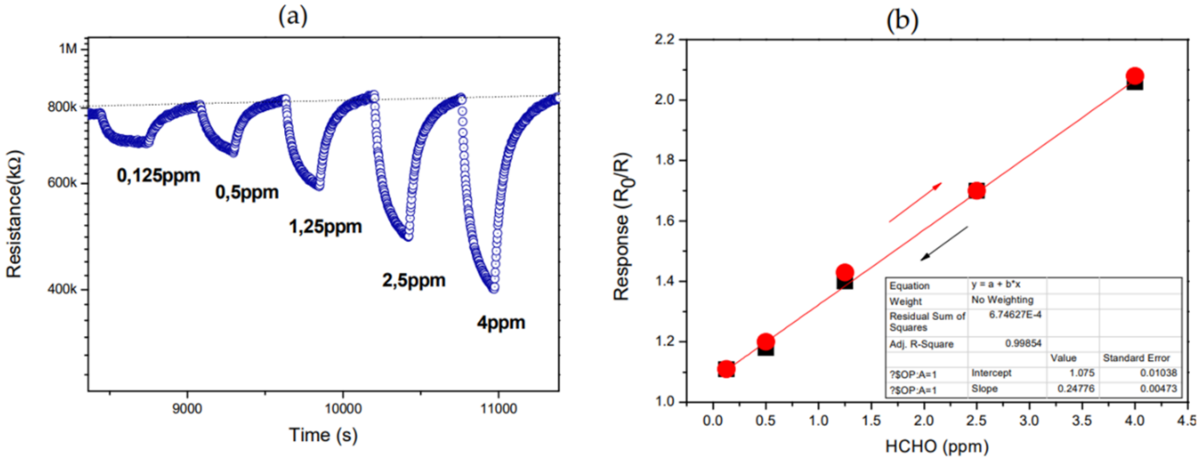

Figure 5.7. (a) Response of the 3Al,3Ca doped-ZnO sensor to different analyte concentrations, from 0.125 to 4ppm; (b) Linear fit of response registered in the function of both increasing (red point) and decreasing (black point) HCHO concentration.

To properly determine the sensor performance, the repeatability and reproducibility of the sensor are required. Repeatability is defined as the variance in the measured values of the target gas concentration upon repeated measurements. Reproducibility is the ability of the gas sensors to provide repeatability of the measurement results for prolonged usage. In Figure 5.8a the good repeatability and reproducibility of the signal is evident. The standard deviation determined from five replicates shows a low variability (<10%).

Another parameter not to be overlooked is the selectivity of the sensor to formaldehyde. Figure 5.8b reports the response of the sensor to different indoor pollutants (i.e., NO, NO_2, CO, ethanol) which can be found in indoor environments such as an office, an apartment, or a school environment. Among these gases, the sensor detects not only the formaldehyde but also the NO_2. For NO_2, an oxidizing gas, the baseline resistance variation is opposed (an increase of the resistance is found increasing the concentration) compared to HCHO, and this can be used to discriminate easily between the two gases.

Sensitivity to other gases was not relevant, which indicated that the 3Al,3Ca doped ZnO sensor had good selectivity to formaldehyde. Selectivity is an important characteristic of the sensor because its functioning can be impaired from other gases present in the same ambient environment where the sensor is positioned. Here, we reported the response to some indoor gases at the concentrations we currently have in the laboratory. In particular, the possibility to monitor formaldehyde without interference from ethanol, is highly demanding for indoor applications [22]. Ethanol vapors are, for example, common in-home environments such as the kitchen and this can cause false alarms. Usually, on metal oxide sensors, ethanol is a strong interferent, whereas the new optimized 3Al,3Ca doped ZnO sensor proposed here could overcome this limitation, being able to monitor HCHO with little or no interference from ethanol. However, we are aware that a more precise indication of the selectivity of the sensor can be acquired only by testing a larger number of different interferent gases. This is a priority of the study we plan to carry out in the future.

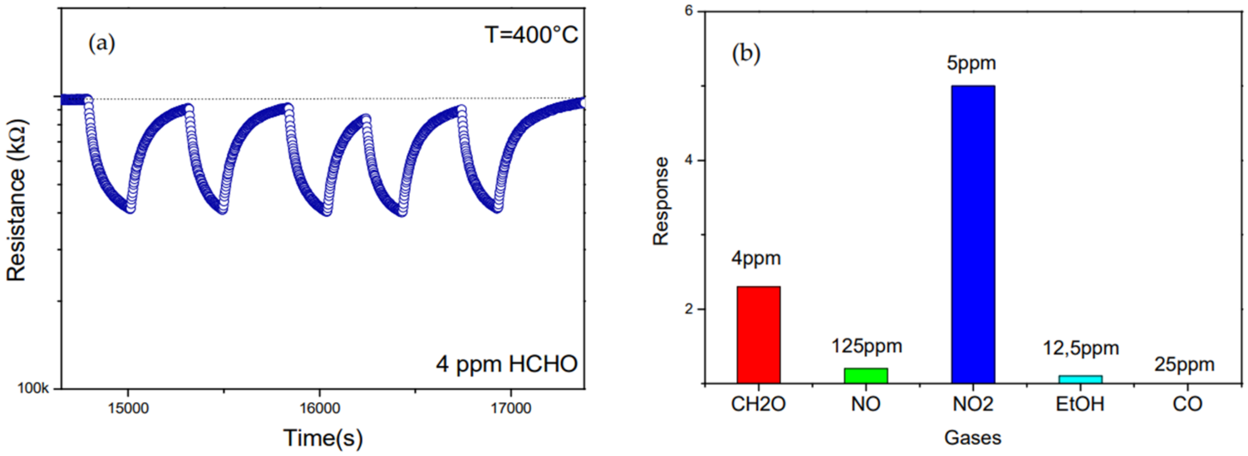

Figure 5.8. (a) Repeatability and reproducibility tests over time to 4 ppm HCHO at 400°C; (b) Signal trend considering response and recovery time. Selectivity tests of 3Al,3Ca doped ZnO sensor to different gases.

Finally, the sensing characteristics towards HCHO are compared with previous literature reports and presented in Table 5.1. This table shows some of the multitude of different materials used (single oxides, composites, amd organic/metal oxide hybrids) and the related operating conditions (temperature and HCHO concentrations, ect.) in the HCHO conductometric sensors reported previously in the literature.

Table 5.1. Sensing characteristics of 3Al,3Ca doped ZnO sensor towards HCHO compared with previous literature reports.

Sensor	Temp.°C	HCHO conc. (ppm)	Response (R_0/R)	Ref.
Au/In_2O_3	100	50	85.7	23
SWCNT@ZnO	RT	500	1.2	24
γ-Fe_2O_3	320	100	6	25
1.0 wt% MnO_2-ZnO	320	200	27	26
Ga-doped ZnO	400	205	13	27
This work	*400*	*4*	*3.5*	-

5.2.1.3.4 *Sensing Mechanism and Final Considerations*

A conductometric metal oxide gas sensor is based on the combined action of the receptor (the metal oxide sensing material) and an electrical transducer platform. The reception mechanism involves the interaction of the target gas on the surface of the metal oxide followed by the change of the sensing layer resistance (the transduction mechanism), as show in Figure 5.9.

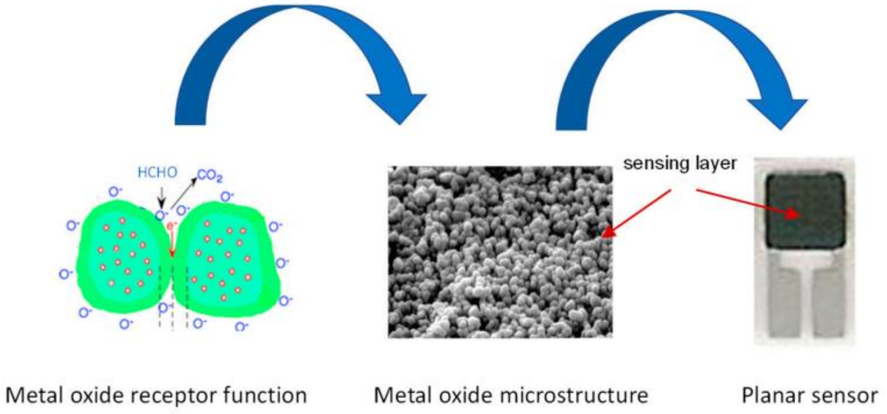

Figure 5.9. The functioning of an HCHO sensor detection.

More precisely, the sensor exposed to air interacts with oxygen molecules that adsorb on the surface of the grains. In the case of a pure ZnO-based sensor, given that this metal oxide is a n-type semiconductor, the adsorbed oxygen ions extract electrons from the conduction band, generating a charge depletion layer which results in an increase in the potential barrier at grain level and an increase in sensor resistance. The depletion layer extension depends on the amount of adsorbed oxygen and the operating temperature of the sensor. In the presence of formaldehyde, a reducing gas, the interaction with an n-type semiconductor leads to decreases in sensor resistance due to the reduction of the bridge barrier.

The presence of the Al and Ca dopants in the ZnO determines several changes (morphological, microstructural, and electrical). The changes in electrical properties were due to the modification of Schottky and Frenkel defects in the structure of the ZnO crystal lattice, leading to a decrease/increase of the baseline resistance (see above in Figure 6.4). Based on their electrical characteristics, Ca^{2+} ions were acting as electron attractors and Al^{3+} ions as electron donors. The marked differences were also related to acid-base characteristics of the two dopants, with the Ca ions having a high capacity to increase the surface basicity of the composite, while Al ions increased the amount of acid sites. This means that the interaction of the HCHO with the sensing layer was dependent on the Al and Ca loading and their ratio.

For example, the strong interaction of the 3Al,3Ca doped ZnO sensor sensing layer with the formaldehyde was monitored by the ATR-FTIR spectrum (see Figure 5.10), highlighting the presence of prominent bands associated with the formaldehyde at 2925 cm^{-1} and 2855 cm^{-1} and attributed to the O-CH2-O- and the -CHO groups, respectively.

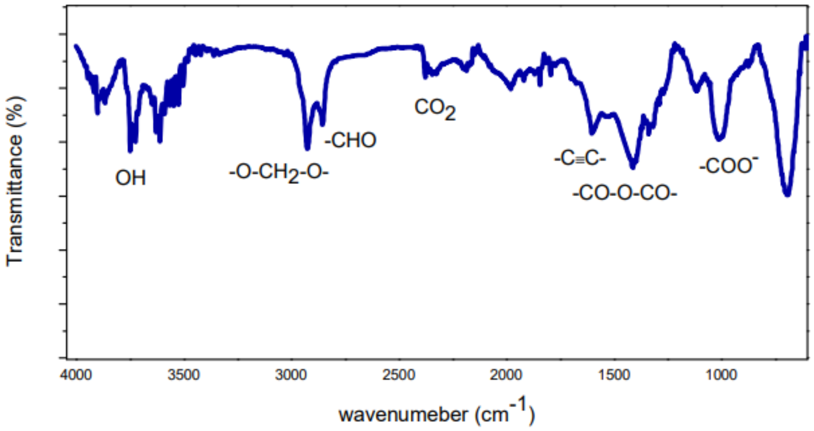

Figure 5.10. ATR-FTIR spectrum of 3Al,3Ca doped ZnO sensor after contact with HCHO.

These results concur with a computational study reporting the impact of Ca ions' doping on the enhancement of formaldehyde adsorption, as demonstrated by the increase of HCHO adsorption energy on the surface from -4.2 to -36.1 kcal/mol [28] These characteristics are the basis of the large sensing differences reported in the detection of formaldehyde with the various composite-based sensors investigated. Following on from the scope of the present paper, a deeper "in situ" AT-FTIR characterization of the composite materials under HCHO sensing in different working conditions could be of valuable interest for elucidating the HCHO sensing mechanism.

Focusing attention on practical application, the developed sensor has the advantage of a simple planar structure and can be easily fabricated for mass production by using low-cost materials and fabrication methods. Indeed, for the efficient production of gas sensors for the market, the manufacturing technology should be easy and inexpensive. [29]

Here, both the base metal oxide (ZnO) and the dopants (Al, Ca) can be considered as appropriate for the low cost of the raw materials. Also, the synthesis procedure relies on a simple, easy, solution-processable wet-chemistry method. Fabrication of the final transducer device could include acceptable sensing layer printing processes such as screen printing or spray coating on a preformed interdigitated planar ceramic platform, ensuring further outstanding advantages such as advanced mechanical and electrical characteristics [30]. By considering these characteristics, the developed sensor would be most promising as a gas sensor for formaldehyde detection in indoor and workplace environments.

5.2.1.4 Conclusions

In summary, the performances of a conductometric HCHO gas sensor based on the Al,Ca-doped zinc oxide composite have been presented. The results demonstrated that by optimizing the doping loading, a promising sensitive material showing good sensitivity, selectivity, and reproducibility for monitoring the low concentration of HCHO in air, was obtained. Thus, the developed 3Al,3Ca doped ZnO sensor could find applications in the indoor air and workplace pollution fields, due to additional advantages such as its easy fabrication and low cost.

5.2.2 Fe_2O_3-Co_3O_4 nano heterojunctions for Ethanol detection

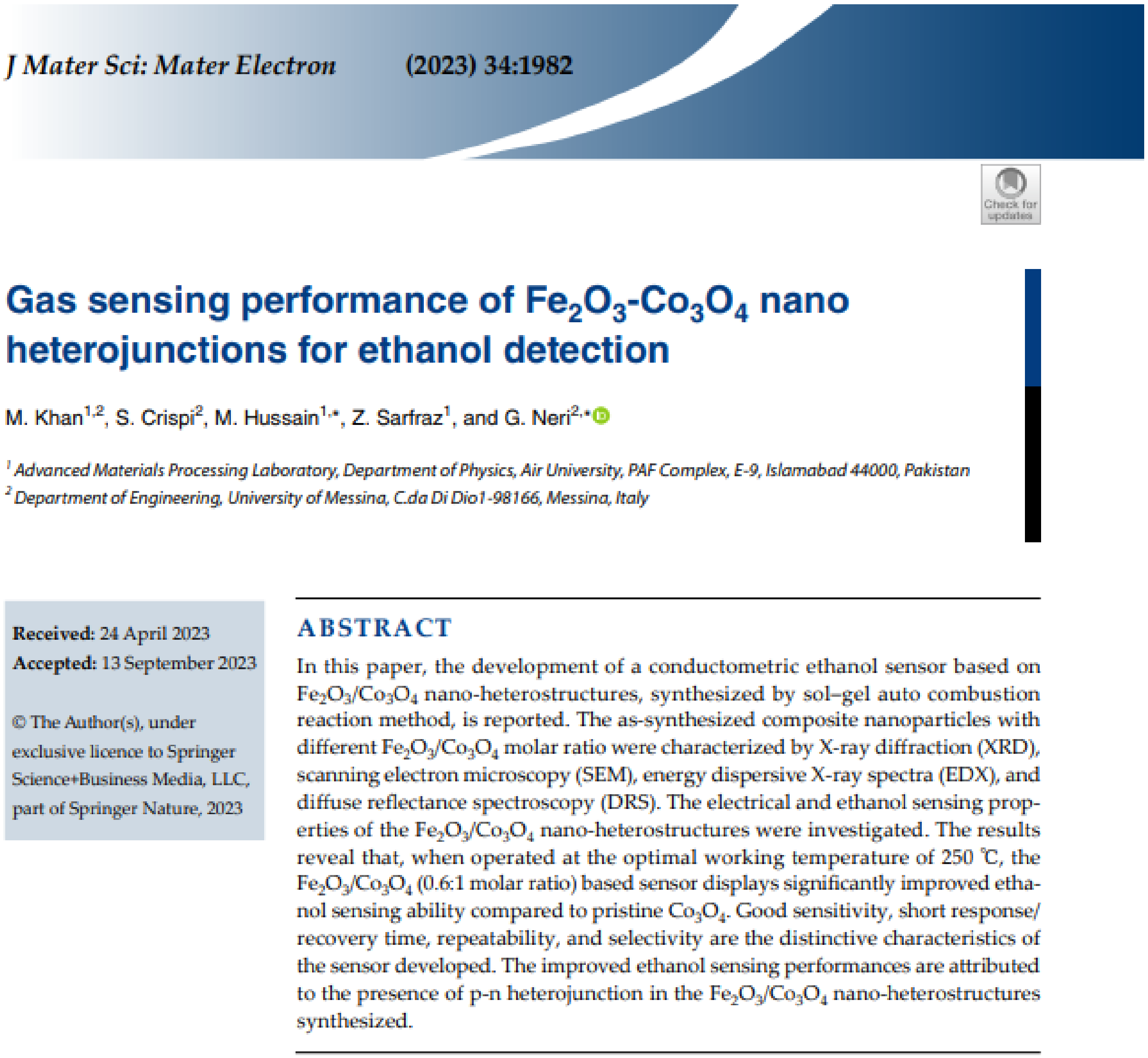

J Mater Sci: Mater Electron (2023) 34:1982

Gas sensing performance of Fe_2O_3-Co_3O_4 nano heterojunctions for ethanol detection

M. Khan[1,2], S. Crispi[2], M. Hussain[1,*], Z. Sarfraz[1], and G. Neri[2,*]

[1] Advanced Materials Processing Laboratory, Department of Physics, Air University, PAF Complex, E-9, Islamabad 44000, Pakistan
[2] Department of Engineering, University of Messina, C.da Di Dio1-98166, Messina, Italy

Received: 24 April 2023
Accepted: 13 September 2023

ABSTRACT

In this paper, the development of a conductometric ethanol sensor based on Fe_2O_3/Co_3O_4 nano-heterostructures, synthesized by sol–gel auto combustion reaction method, is reported. The as-synthesized composite nanoparticles with different Fe_2O_3/Co_3O_4 molar ratio were characterized by X-ray diffraction (XRD), scanning electron microscopy (SEM), energy dispersive X-ray spectra (EDX), and diffuse reflectance spectroscopy (DRS). The electrical and ethanol sensing properties of the Fe_2O_3/Co_3O_4 nano-heterostructures were investigated. The results reveal that, when operated at the optimal working temperature of 250 ℃, the Fe_2O_3/Co_3O_4 (0.6:1 molar ratio) based sensor displays significantly improved ethanol sensing ability compared to pristine Co_3O_4. Good sensitivity, short response/recovery time, repeatability, and selectivity are the distinctive characteristics of the sensor developed. The improved ethanol sensing performances are attributed to the presence of p-n heterojunction in the Fe_2O_3/Co_3O_4 nano-heterostructures synthesized.

Abstract: An ethanol-based conductometric sensor Fe_2O_3/Co_3O_4 nano-heterostructures, synthesized by sol-gel self-combustion reaction method, is reported. Composite nanoparticles were synthesized and characterized different Fe_2O_3/Co_3O_4 molar ratios. X-ray diffraction (XRD), the scanning electron microscopy (SEM), energy dispersive X-ray (EDX) spectra and diffuse reactance spectroscopy (DRS) have been used as techniques for characterization. By studying the electrical and sensing properties of Fe_2O_3/Co_3O_4 nano heterostructures, a sensitivity to ethanol at the optimal working temperature of 250 °C was determined. The Fe_2O_3/Co_3O_4 based sensor with 0.6:1 molar ratio shows significantly improved ethanol sensing ability

compared to pure Co_3O_4. Good sensitivity, short answer/ recovery time, repeatability and selectivity are the distinctive characteristics of the sensor has developed.

5.2.2.1 Introduction

Since their introduction, gas sensors based on conductometric transduction operation continue to represent an exciting challenge [30]. The simplicity of these devices has made them versatile for various applications, such as disease diagnosis, monitoring of gaseous pollutants in indoor and outdoor environments and so on, and many of them have reached the market and people use them in their daily lives. Further significant progress in conductometric gas sensing technology have been given by the use of sensitive materials having nanometric dimensions less than 100 nm with considerable potential to improve the gas detection performance [31]. In particular, nanomaterials based on metal oxides semiconductor (MOS) have been developed with several unique electrical characteristics [32].

The trend to improve the performance [33] of MOS has led to the development of hybrid nanomaterials [34] and heterostructures [35]. Furthermore, semiconductor metal oxide heterojunctions have assumed particular importance such that they can be adopted in optoelectronic devices [36], energy storage and environmental monitoring systems [37]. Different methods have been adopted for the synthesis of heterojunctions [32]. Sol-gel is one of the most popular methos for obtaining different MOS and heterojunctions with controllable morphologies [38].

The research carried out in the literature led to the development of this work of a Fe_2O_3/Co_3O_4 heterojunction using the sol-gel method. the developed material allows the detection of ethanol. To our knowledge, no previous research has been carried out on Fe_2O_3/Co_3O_4 composite NPs for gas sensing applications using this synthesis technique. So, a comparison of gas detection characteristics of hetojunctions based on Co_3O_4 and Fe_2O_3 has yet to be performed. In particular the Fe_2O_3/Co_3O_4 nanoparticles were prepared by sol-gel self-combustion in a single step.

A work by Liu. *et al.* [39] was found, based on a solvothermal process to prepare Co_3O_4 spinels with different morphologies such as nanoparticles, lamellar cubes and needle-shaped for ethanol gas detection. The spinels obtained were subjected to a temperature range between

100 and 300°C at a specific concentration of ethanol gas equal to 50 ppm of ethanol. A good response of 13.4 at 170°C was found for the needle-shaped spinel.

The importance of developing sensors for the detection of ethanol is given by the fact that it is a flammable chemical compound, is one of the most alcohols commonly and widely used in the food, biomedical and pharmaceutical industries chemical industries [40]. Exposure to ethanol vapor causes health problems such as such as difficulty breathing, headache, drowsiness, eyes irritation, liver damage, which explains the importance of finding a good sensor [22].

5.2.2.2 Experimental section

5.2.2.2.1 Precursors

Cobalt nitrate hexahydrate, iron nitrate monohydrate (98% purity), sodium hydroxide NaOH, hydrochloric acid (HCl), and other chemicals were of analytical grade (> 99%) were used as precursors for the synthesis of nanoparticles.

5.2.2.2.2 Fe_2O_3/Co_3O_4 composite preparation

The synthesis of Fe_2O_3/Co_3O_4 composites was carried out preparing two solutions. One with 2.40g of Co_3O_4 in 25mL of HCl and the second, different amounts of Fe_2O_3 in 5M of citric acid ($C_6H_8O_7$). Both solutions were stirred at room temperature. In the next step the two solutions were placed together in a single beaker and the final solution was placed on a heating plate at 350°C. The powders obtained were subjected to an annealing process at 400°C for 2h. Five samples were obtained indicated xFe_2O_3/yCo_3O_4, x and y are the molar ratios of compounds second the relation and named: 1/0.2 (C1); 1/0.4 (C2); 1/0.6 (C3); 1//0.8 (C4) and 1/1 (C5). The Fe_2O_3 molar % was calculated as: Fe_2O_3 (molar %) = [(mol Fe_2O_3/ (mol Fe_2O_3 + mol Co_3O_4)) × 100]. The synthesis protocol is shown in Fig. 5.11.

Figure 5.11. Synthesis procedure for the preparation of nanocomposites by auto combustion sol–gel technique.

5.2.2.2.3 Characterization

XRD analysis was performed on a D2 Phaser Bruker diffractometer operating at 30 kV in the range 10–90° (2θ), at a scanning rate of 0.02° s^{-1}. Scanning electron microscopy (SEM) images were acquired by Zeiss 1540XB FE SEM (Zeiss, Germany) instrument operating at 10 kV. Diffuse Reflectance Spectroscopy (DRS) spectra of the samples were recorded in the range from 200 to 800 nm by a facility of Perkin Elmer UV Lambda 900.

5.2.2.2.4 Sensor fabrication

Conductometric gas sensors were fabricated by depositing the synthesized composite nanomaterials on patterned alumina platform (6× 3mm) having a heating element and interdigitated Pt electrodes as follows. Typically, we disperse 1 mg of powdered material in 1mL deionized water, sonicated for 15 minutes. A drop of 10 µl was deposited on part of the device. The sensor was left to dry at room temperature to allow the water to evaporate.

5.2.2.2.5 Gas sensing tests

Sensing tests were carried out introducing the sensor device in the test chamber and measuring the resistance through a multimeter (Agilent 34970A). The sensor device is provided with a Pt heater biased by an Agilent E3632A instrument, for setting the operating temperature of the sensor.

The performances of the sensor have been evaluated measuring the response, S, defined as the ratio (R_{gas}/R_{air}), where R_{gas} is the electrical resistance at different gas concentrations and R_{air} is the baseline resistance in dry synthetic air. Additionally, we also evaluated the dynamic properties of the sensors, by measuring the response time (τ_{res}) and recovery time (τ_{rec}) characteristics, where τres is defined as the time required to reach the 90% of the resistance after injection of the target gas, whereas τ_{rec} represents the time necessary to reach 90% of the resistance baseline value in air.

5.2.2.3 Results and discussion

5.2.2.3.1 Morphological and microstructural characterization

In Figures 5.12a-c the scanning electron microscopy (SEM) images for some Fe_2O_3/Co_3O_4 composites are observed. The technique allows highlighting irregular shapes of the composites obtained through the sol-gel self-combustion process. In Figure 5.12d the EDX spectrum of the selected 0.4 Fe_2O_3/1 Co_3O_4 as an example. Second the EDX spectrum, the composite has a chemical composition of Co, Fe, O, and some impurities of Na, S and C from raw materials.

The crystalline phase and crystallinity were studied by XRD analysis. The XRD pattern in Figure 6.13 show some sharp peaks for pure cubic Co_3O_4 and rhombohedral structure of pure Fe_2O_3, confirming that the synthesized products are composed mainly of single-phase cobalt oxide and iron oxide nanoparticles. However, the considerable level of background noise makes it difficult to index the faintest peaks and they are almost indistinguishable. This does not exclude the presence of other stages but cannot be quantified. As expected, the intensity of the Co_3O_4 diffraction peaks decreases with increasing amount of Fe_2O_3. The latex parameters determined by the analysis are a = b = c = 8.1975 Å for Co_3O_4, respectively.

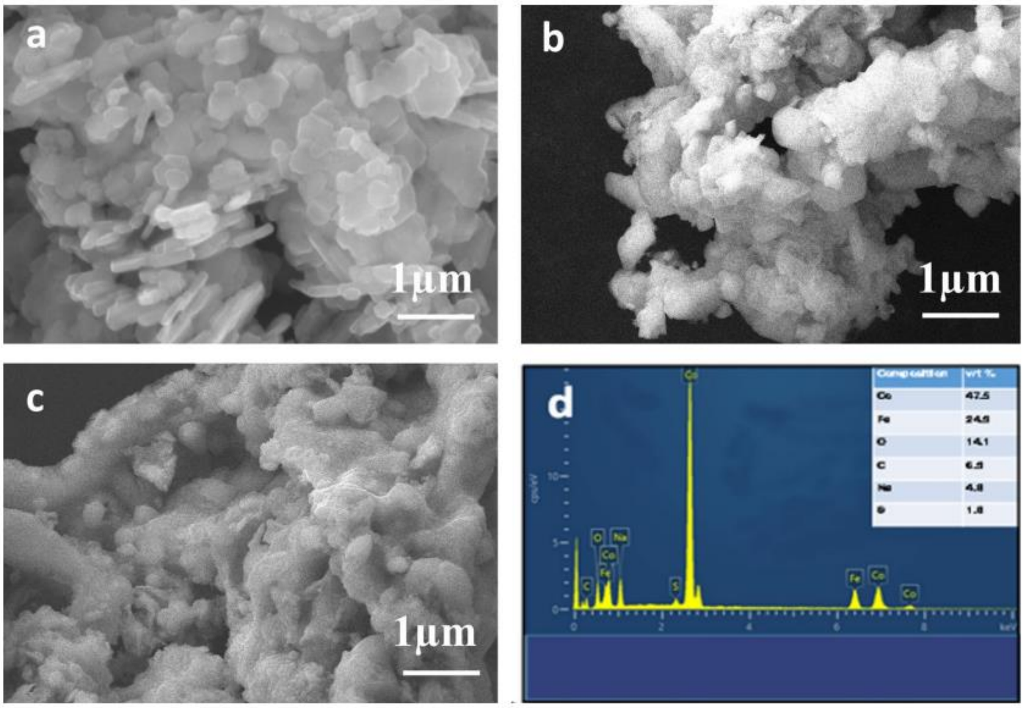

Figure 5.12. Scanning electron microscopy micrographs of SEM images of composite samples: (a) $Co_3O_{4\,pure}$; (b) $1Co_3O_4/0.4\ Fe_2O_3$; (c) $1Co_3O_4/0.8\ Fe_2O_3$; (d) EDX Pattern of $1Co_3O_4/0.4\ Fe_2O_3$ composite.

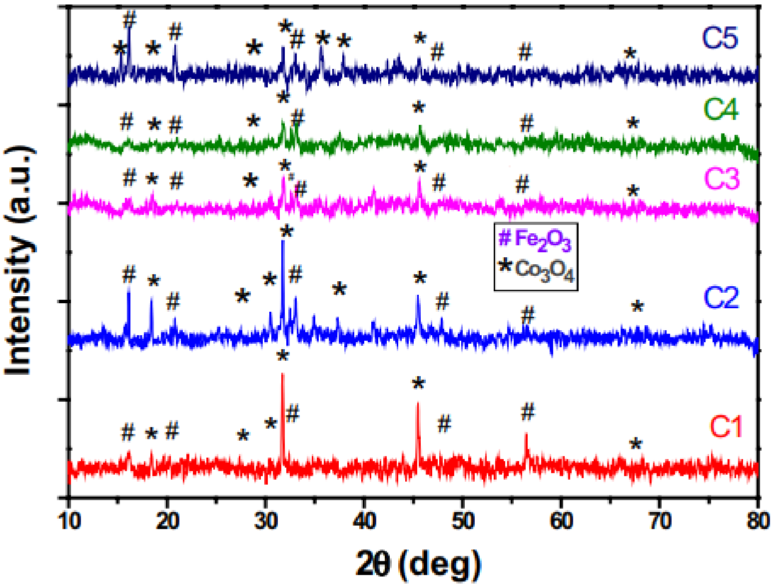

Figure 5.13. X-ray diffraction pattern of the Fe_2O_3/Co_3O_4 composites.

5.2.2.3.2 Optical properties

The Figure 5.14 (a) and (b) represents the diffuse reflectance spectroscopy (DRS) data and the reflectance spectra for the Fe_2O_3/Co_3O_4 composites. The reflectance spectra are used to estimate the Kubelka-Munk function, Equation 5.1:

$$F(R) = \frac{(1-R)^2}{2R} \tag{5.1}$$

This has resulted in the estimation of the specimen's bandgap energies as shown in Figure 5.13(a). The bandgap values estimated by these measurements are found first to decrease with the increase of Fe_2O_3 contents in Co_3O_4. An initial decrease could be attributed to suppression of oxygen vacancies due to Fe_2O_3 in long Co_3O_4 with interatomic transitions between Fe^{3+} subshells d. Further increase of hematite in the Co_3O_4 structure leads to an increase in the band gap. The phenomenon can be explained by considering the morphology, composition, crystallinity, as well as the shape and size of the particles as have an important effect optical property, so is the observed band gap trend probably the result of the concomitant effect of the above factors. This can make it difficult to isolate the most crucial variables that determine the observed optical behavior.

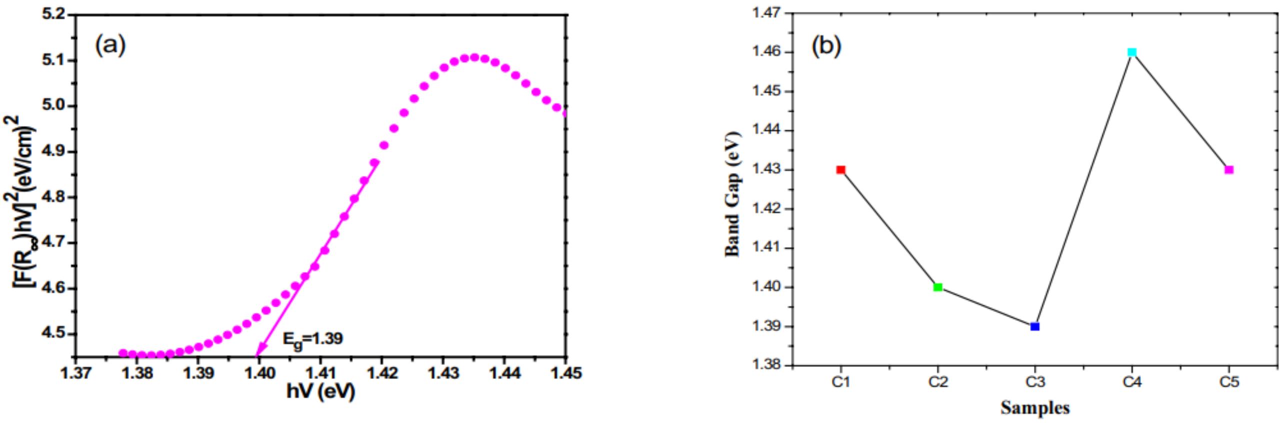

Figure 5.14. (a) DRS tecnique of Fe_2O_3/Co_3O_4 nanocomposite 0.8 Fe_2O_3/1 Co_3O_4 ; (b) Band gap vs. variation of nanocomposites samples.

5.2.2.3.3 Electrical and gas sensing properties

When designing a sensor it is necessary to reduce the energy consumption for its operation. Therefore, the choice of the best sensor operating temperature is utmost importance. The temperature also affects the basic resistance of the device, this aspect has been studied. In fact, the air resistance of a metal oxide semiconductor is strictly linked to the quantity of O_2 adsorbed on the surface [30], since the absorbed O_2 species attract electrons from Fe_2O_3/Co_3O_4 nanocomposite conduction band. This results in a decrease in the number of carriers for electrical conduction, with a consequent increase in the base resistance for those that have a greater electron depletion layer due to the greater amount of adsorbed oxygen. Furthermore, in all sensors based on nanocomposites was observed decrease in resistance with increasing temperature. This can be attributed to the increases of charge carriers for thermal excitation [40], confirming that Fe_2O_3/Co_3O_4 composites behave like semiconductor materials.

In Figure 5.15a, we observe the basic resistance of the sensors as a function of temperature, while in Figure 5.15b a comparison of the resistances of the various sensors at a certain temperature (300°C) is shown. Thus, a decrease in strength is shown of the composites compared to pure Co_3O_4.

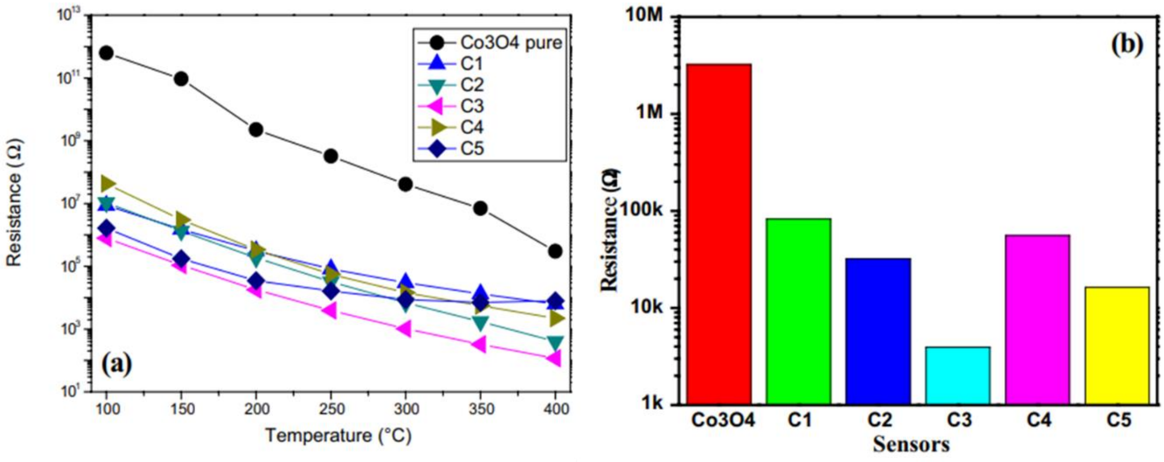

Figure 5.15 (a) Resistance in dry air of developed composite NPs vs. temperature; (b) comparison of baseline resistance in air of nanocomposite at the temperature of 300 °C.

A variation in the resistance values of the different sensors also leads to different values in the gas response. Consequently, an ethanol concentration of 100 ppm was chosen, and the sensors were studied over a temperature range of 100 to 400°C, the Figure 5.16a shows the results. Figure 5.16b shows the response of the 0.8 Fe_2O_3/1 Co_3O_4 composite as an example. The sensor response to the gas is determined by the equilibrium established between adsorption and desorption of ethanol, and reactivity of ethanol adsorbed with adsorbed oxygen species. Raising the temperature improves the absorption of ethanol and the rate of reaction that forms on the surface. The most suitable operating temperature is 250°C as the response to gas is better, as shown in the same figure. The reduction in gas response at higher temperatures is related to the desorption of ethanol. Was also observed that after each pulse the signal returns to its initial base value, indicating the reversibility of the sensor.

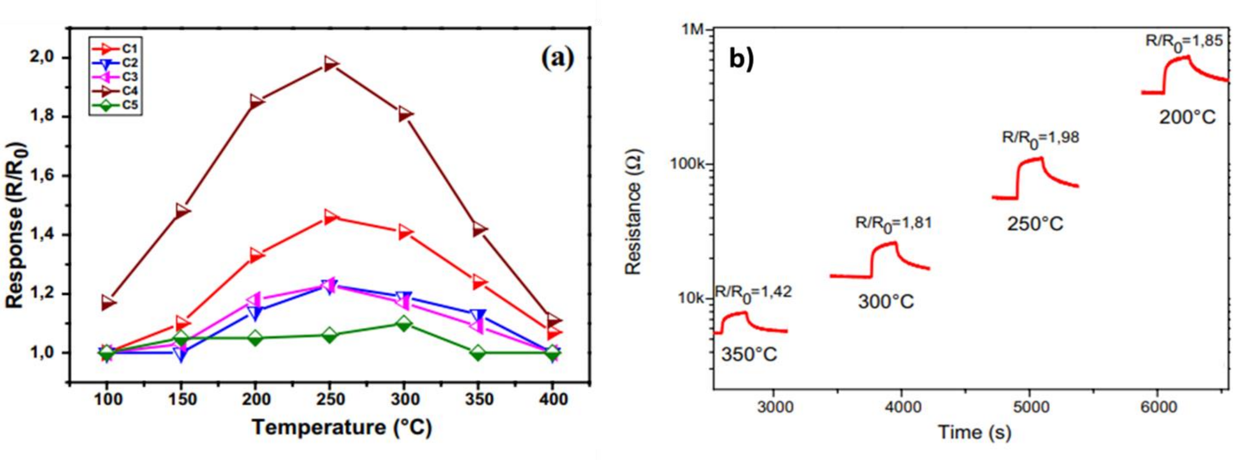

Figure 5.16. (a) Resistance vs. temperature at 100 ppm ethanol; (b)Resistance vs. time at 100 ppm ethanol for the 0.8 Fe_2O_3/1 Co_3O_4 nanocomposite.

Figure 5.17 exhibits the response of all sensors to fixed ethanol concentration. The response of pure Fe_2O_3 nanoparticles (n-type) imply a resistance decrease and do not involve any change in the p-type semiconducting properties of the pristine Co_3O_4.

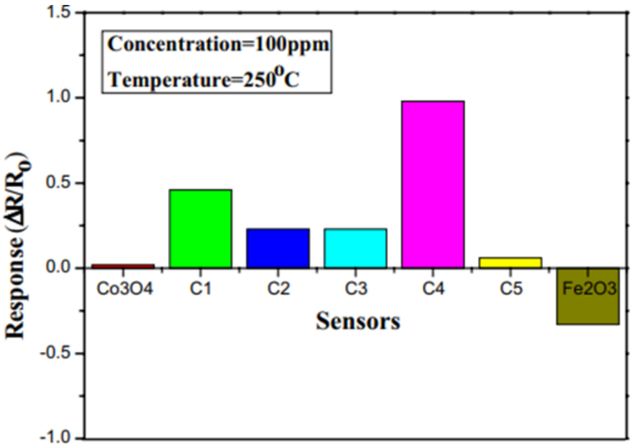

Figure 5.17. Sensor response of nanocomposites samples to the 100 ppm ethanol at the temperature of 250 °C.

Figure 5.18a show the dynamic response of ethanol concentrations of the 0.8 Fe_2O_3/1 Co_3O_4 nanocomposite, instead the Figure 5.18b shows the calibration curve of the same nanocomposite. Both tests are observed at 250°C and plotted in log-log scale. These results are helpful to derive the limit of detection (LOD) of the sensor to ethanol, which is about 1 ppm.

Response and recovery times are shown in Figure 5.18c for all nanocomposite sensors. Short times of response/recovery are observed for each sensor, indicating fast capabilities of ethanol detection, which is necessary for practical applications [22,41]. The short response can be explained by the presence of adsorbed oxygen species highly reactive on the surface of the nanocomposite sensor. Following the ethanol gas injection, these species react very quickly with ethanol, resulting in a very short response time. The slower recovery time can be explained to the sluggish surface reactions regarding the adsorption, dissociation, and ionization of oxygen [42].

The reproducibility of a sensor is the ability of that device to provide the same output signal times over time when subjected to the same quantity input [43] and it shown in Figure 6.18d. In this case, the response of sensors is constant, and the standard deviation determined from three replicates shows a very low variability (< 2%).

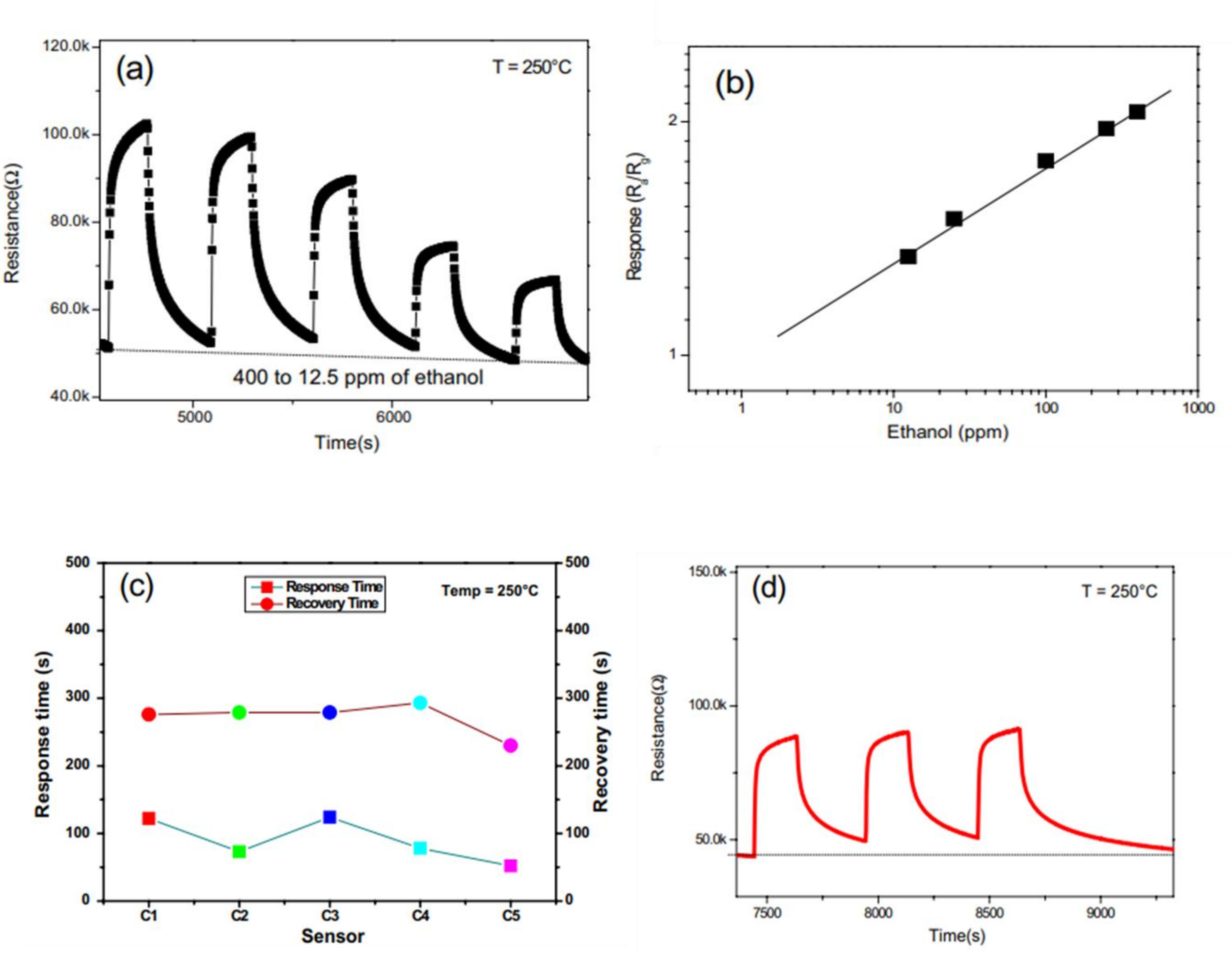

Figure 5.18. (a) Dynamics of the 0.8 Fe_2O_3/1 Co_3O_4 nanocomposite sensor in the monitoring of different ethanol concentrations; (b) Calibration curve; (c) Response and recovery time for each composite sensors; (d) Reproducibility of the sensor response to three pulses of 100 ppm of ethanol in air. All tests carried out at 250°C.

Considering the same operating temperature of 250°C, the 0.8 Fe_2O_3/1 Co_3O_4 sensors has been evaluated to possible interferent gases of the ethanol such as ammonia, hydrogen sulphide, carbon monoxide, acetone, nitrogen oxide and formaldehyde (see Figure 5.19). The sensor showed a response to formaldehyde comparable to the response of ethanol, but in many practical applications, such as breath analysis, concentration of formaldehyde in the exhaled breath is very low (in the order of ppb), therefore the interference with ethanol can be considered negligible. However, no significant responses to other gases are observed. The differences observed in the response depend on the different activation energies for the adsorption, desorption and reaction of various gases on the metal oxide surface [44]. Therefore, the sensor response is highly dependent on the gas be perceived.

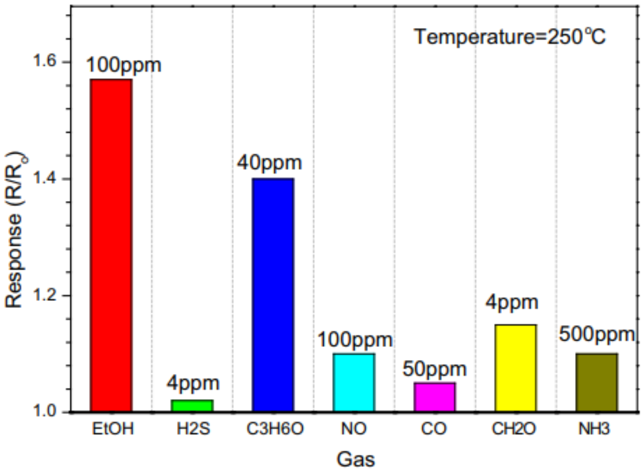

Figure 5.19. Selectivity pattern of 0.8 Fe_2O_3/1 Co_3O_4 nanocomposite sensor at 250 °C.

5.2.2.3.4 Gas sensing mechanism

It is known that a good strategy to improve the performance of a semiconductor is to integrate *p-type* and *n-type* semiconducting metal oxides. a plausible explanation has been given to the sensing mechanism of nanocomposites involved in ethanol sensing. The exposition of these sensors to air and ethanol, involves a double adsorption, one linked to the oxygen molecules and the other to the target gas (ethanol). The adsorption of O_2 on the surface causes the extraction of electrons from the conduction band [44,45]; while the adsorbed ethanol reacts with the reactive oxygen molecules to form CO_2 and H_2O as can be observed in equations 5.2-4. It gets increase in the concentration of mass electrons [46] and in a p-type semiconductor imply that the hole carriers decrease.

$$C_2H_5OH_{(ads)} + O^-_{(ads)} \rightarrow C_2H_5OH_{(ads)} + H_2O + e^- \qquad (5.2)$$

$$C_2H_5OH_{(ads)} + 5\,O^-_{(ads)} \rightarrow 2\,CO_2 + 2H_2O + 5\,e^- \qquad (5.3)$$

$$C_2H_5OH_{(ads)} + 6\,O^-_{(ads)} \rightarrow 2\,CO_2 + 3H_2O + 12e^- \qquad (5.4)$$

The reported Fe_2O_3/Co_3O_4 nanocomposites demonstrated better performance compared to pure Co_3O_4 which can be explained by evaluating:

(i) O_2 is adsorbed on the surface of p-type metal oxide semiconductors, to compensate their deficiencies [38]. Additional defects are created at the Co_3O_4/Fe_2O_3 interface, oxygen concentration on nanocomposites is expected to be significantly higher than on pure Co_3O_4.

(ii) The defects act also as preferential adsorption sites for gas target molecules. This comes likely from lattice mismatch between Co_3O_4 and Fe_2O_3 [47].

(iii) Formation of a p-n heterojunction at the interface between *p-type* Co_3O_4 and *n-type* Fe_2O_3. This is schematized in Figure 6.20 and leads to an extended modulation of the depletion layer width associated with ethanol gas adsorption and desorption [47-49].

Sensing tests demonstrated that, following exposure to ethanol, the overall resistance of the sensors increases. This result can be explained by considering that the Fe_2O_3/Co_3O_4 based p-n junction behaves as a sensitive *p-type* semiconductor material on samples with a higher load of *n-type* Fe_2O_3 component, probably due to the larger depletion width the p-side, while the n-side remains almost unchanged results. The result is opposite to what was reported other composite systems [50].

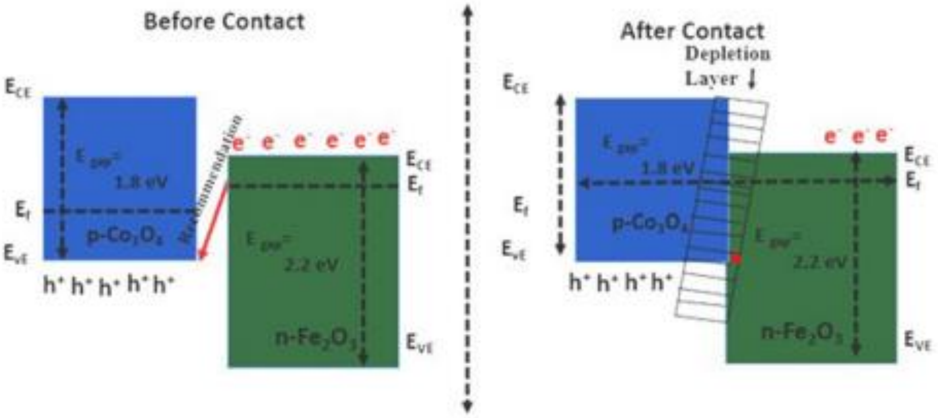

Figure 5.20. Development of heterojunction from Fe_2O_3/Co_3O_4 nanocomposites for ethanol gas sensing.

5.2.2.4. Conclusions

An auto combustion sol–gel process was used successfully to synthesize the preparation of Fe_2O_3 : Co_3O_4 (1:0.2; 1:0.4; 1:0.6; 1:0.8; 1:1) nanocomposites. SEM and XRD results have indicated the effectiveness of the auto combustion sol–gel method to synthesize Fe_2O_3 : Co_3O_4 nanocomposites. The ethanol gas sensing performance of the synthesized powders was investigated at various ethanol concentrations and temperatures. The sensing performance of the Fe_2O_3 : Co_3O_4 nanocomposite sensor was superior at the composition (1 Co_3O_4/0.8 Fe_2O_3). The response time is 50 s, and the recovery time is 300 s for 100 ppm ethanol concentration at 250 °C. The composite sensor’s improved gas sensing properties were primarily due to enhanced modulation of the conduction channel width and modulation of the potential barrier formed. Further, the difference observed in the morphology, microstructure, and optical energy band gap of composite samples are suggested also to play a determinant role in the difference observed in the gas sensing performance towards the target gas.

5.2.3. Cobalt oxide/copper oxide composites for gas sensing application

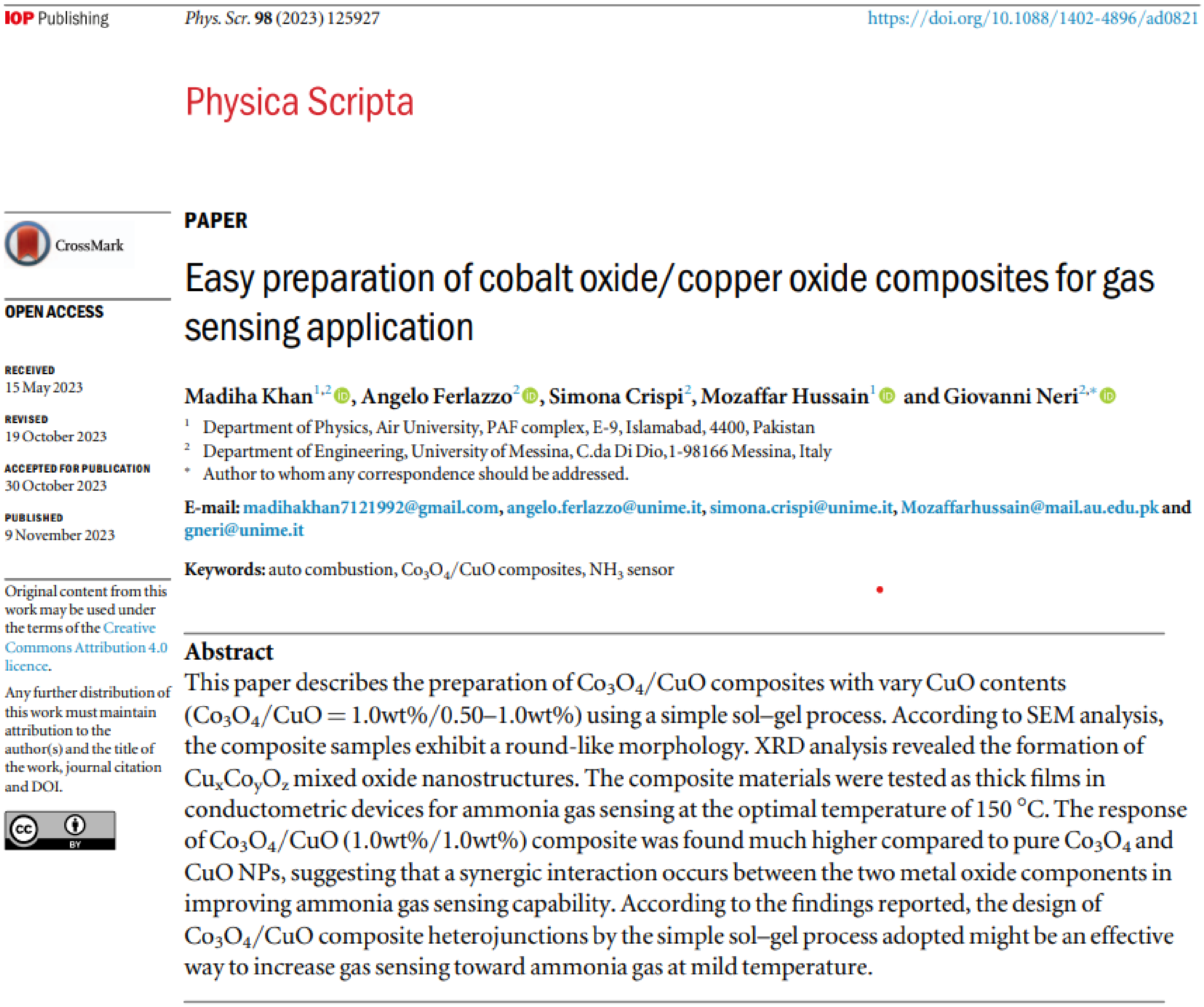

IOP Publishing Phys. Scr. **98** (2023) 125927 https://doi.org/10.1088/1402-4896/ad0821

Physica Scripta

CrossMark

OPEN ACCESS

RECEIVED
15 May 2023

REVISED
19 October 2023

ACCEPTED FOR PUBLICATION
30 October 2023

PUBLISHED
9 November 2023

PAPER

Easy preparation of cobalt oxide/copper oxide composites for gas sensing application

Madiha Khan[1,2], Angelo Ferlazzo[2], Simona Crispi[2], Mozaffar Hussain[1] and Giovanni Neri[2,*]
[1] Department of Physics, Air University, PAF complex, E-9, Islamabad, 4400, Pakistan
[2] Department of Engineering, University of Messina, C.da Di Dio,1-98166 Messina, Italy
[*] Author to whom any correspondence should be addressed.

E-mail: madihakhan7121992@gmail.com, angelo.ferlazzo@unime.it, simona.crispi@unime.it, Mozaffarhussain@mail.au.edu.pk and gneri@unime.it

Keywords: auto combustion, Co_3O_4/CuO composites, NH_3 sensor

Abstract
This paper describes the preparation of Co_3O_4/CuO composites with vary CuO contents (Co_3O_4/CuO = 1.0wt%/0.50–1.0wt%) using a simple sol–gel process. According to SEM analysis, the composite samples exhibit a round-like morphology. XRD analysis revealed the formation of $Cu_xCo_yO_z$ mixed oxide nanostructures. The composite materials were tested as thick films in conductometric devices for ammonia gas sensing at the optimal temperature of 150 °C. The response of Co_3O_4/CuO (1.0wt%/1.0wt%) composite was found much higher compared to pure Co_3O_4 and CuO NPs, suggesting that a synergic interaction occurs between the two metal oxide components in improving ammonia gas sensing capability. According to the findings reported, the design of Co_3O_4/CuO composite heterojunctions by the simple sol–gel process adopted might be an effective way to increase gas sensing toward ammonia gas at mild temperature.

Abstract: This paper describes the preparation of Co_3O_4/CuO composites with vary CuO contents (Co_3O_4/CuO = 1.0wt%/0.50–1.0wt%) using a simple sol–gel process. According to SEM analysis, the composite samples exhibit a round-like morphology. XRD analysis revealed the formation of CuxCoyOz mixed oxide nanostructures. The composite materials were tested as thick films in conductometric devices for ammonia gas sensing at the optimal temperature of 150 °C. The response of Co_3O_4/CuO (1.0wt%/1.0wt%) composite was found much higher compared to pure Co_3O_4 and CuO NPs, suggesting that a synergic interaction occurs between the two metal oxide components in improving ammonia gas sensing capability. According to the findings reported, the design of Co_3O_4/CuO composite heterojunctions by the simple sol–

gel process adopted might be an effective way to increase gas sensing toward ammonia gas at mild temperature.

5.2.3.1 Introduction

Industrialization caused air pollution, prompting the public and scientific community to seek improved detection technologies [51]. One of the primary research issues addressing industrial and environmental safety is the development of gas sensors [52]. The sensing process entails altering the characteristics of materials in response to analyte concentration [53]. This is often caused by physical or chemical adsorption [54]. Because of their enormous surface areas, nanosized materials are predicted to play an important role in both adsorption and sensor response. In general, gas sensors are based on several detecting techniques, such as chemiresistive [55] or optical [56]. Chemiresistor sensors are among the most popular due to their ease of use and inexpensive cost. The fundamental challenge for these sensors' typology is the enhancement of their sensitivity and selectivity [55, 56]. Over the last three years, a massive amount of numerous pollutants produced from various home and industrial sources have caused major difficulties for ecosystem and human health [57, 58]. Among these, ammonia (NH_3) gas is not only a widespread air contaminant, but it is also projected to play a key role in the emerging hydrogen society [59, 60]. Because of its toxicity and negative environmental consequences, ammonia gas must be monitored for leaks in applications such as industrial facilities and transportation systems [61]. Given this context, there has been an increase in demand for NH_3 gas sensors that are not only very sensitive, but also simple and low-cost [62]. Metal oxides (MOXs) are regarded as the best materials for detecting harmful gases by conductometric sensors. Spinel cobalt tetroxide (Co_3O_4) has two oxides, Co_3O_4 and CoO, with high oxygen concentrations and so exhibits p-type semiconducting properties. Co_3O_4 has been used as a cobalt-based gas sensor, and it contains Co^{3+} and Co^{2+} [63]. Stable Co_3O_4 NPs that are inexpensive in cost and thermally stable, as well as their heterostructures with CuO, have been synthesized as an efficient and environmentally friendly process Co_3O_4 NP with graphene as a support were proposed to improve gas sensing efficiency, stability, and performance for detection of ammonia [64]. Cupric oxide, on the other hand, is frequently used in environmental applications due to its exceptional gas sensing capability and small bandgap energy Co_3O_4 and CuO, both of which exhibit p-type semiconductor characteristics, were suitable for making p-p heterojunctions to be used in gas sensing applications [65]. MOX's composite heterostructures are an excellent way to improve gas sensitivity. For example, Cu^{2+} ions anchoring into octahedral sites for spinel cobaltite synthesis are intriguing due to the presence of mixed-valence metal ions, which provide better gas sensing capability and electrical conductivity compared to one-component oxides [66–68]. The interaction between support and active components is one of the most important factors in controlling gas sensing performances [69]. Based on these premises, it was thought to further improve the sensing performances by forming heterojunctions with other metal oxides. In recent years, several Co_3O_4-based gas sensors have been developed. To improve gas sensing performance and realize novel functionalities, scientists have made substantial efforts to synthesize metal oxides-based nanocomposites [30]. Because of their large surface areas, these heterostructures have gotten a lot of attention [70]. Their performances and gas detection capability depend on the synthesis method adopted. For example, Dou *et al.* synthesized Co_3O_4 nanowires for carbon monoxide (CO) detection [71], while Wang *et al.* synthesized Co_3O_4 hollow nanotubes for formaldehyde monitoring [72]. Jeong *et al.* used a p–n junction such as Co_3O_4-SnO_2, to develop a sensor for ethanol, toluene and xylene [73]. Na *et al.* also developed a sensor using Co_3O_4-ZnO for the detection of ethanol and NO_2 [74]. Li *et al.* instead considered developing a p-p junction such as Co_3O_4-SWCNT that showed good response for NOx [75], while Vishnuraj *et al.* used Co_3O_4-CNF for ammonia monitoring [76]. For these reasons, we planned to exploit the properties of Co_3O_4 to increase its performance by developing a p-p heterojunction with CuO to obtain a sensor capable of detecting ammonia. The work describes the design and manufacturing of Co_3O_4/CuO hetero-structures utilizing an effective and simple sol–gel technique. The samples nanocomposites have the same Co_3O_4 content (1.0wt %) and varying CuO contents (0.50 and 1.0wt%). The Co_3O_4/CuO hetero structures demonstrated a synergistic impact between Co_3O_4 and CuO NPs, resulting in significantly improved gas sensing capability toward ammonia (NH_3) as compared with the pure Co_3O_4. The sensing performance of the Co_3O_4/CuO (1.0wt%/1.0wt %) hetero structure was three times quicker than that of the pure Co_3O_4 NPs.

5.2.3.2 Experimental

5.2.3.2.1 Chemical reagent

All the starting ingredients were purchased from Sigma-Aldrich, including copper(II) nitrate ($Cu(NO_3)_2 \times 6H_2O$), sodium hydroxide (NaOH), and cobalt nitrate ($Co(NO_3)_2 \times 9H_2O$). Carlo Ebro Chemical Reagent Co. Ltd. supplied 98% concentrated hydrochloric acid (HCl), which was utilized as received with no additional purification.

5.2.3.2.2 Synthesis of Co_3O_4*/CuO heterostructures*

The preparation of Co_3O_4/CuO heterostructures has been reported previously [77]. Here, the preparation was carried out by using the two step-processes schematized in Figure 6.20. In the first step, pure Co_3O_4 and CuO NPs were synthesized. Co_3O_4 was prepared adding 0.2 g of $Co(NO_3)_2 \times 9H_2O$ to 200 mL of deionized H_2O and stirred for 30 min. Then, NaOH solution was added drop by drop until the pH reaches 12, and stirring continuously for 4 h, while increasing the temperature of the hot plate to 250 °C. The resulting material was washed 3–4 times with deionized water, then dried in an oven at 110 °C for the entire night and calcined for 5 h at 550 °C for Co_3O_4 phase refinement. CuO was prepared adding 15.2 g of $Cu(NO_3)_2 \times 6H_2O$ to 200 mL of deionized water, stirred at room temperature for 30 min. 5M NaOH solution was dropped into the copper nitrate solution until the pH was 9, stirred at 80 °C for 4 h and finally dried and calcinated at 550 °C for 4 h to obtain CuO NPs. To synthesize Co_3O_4/CuO hetero-structures at different CuO concentrations (0.50–1.0 wt%) and Co_3O_4 concentration (1.0 wt%), typically, 1 g of synthesized Co_3O_4 NPs were dispersed in 10 mL of concentrated HCl using ultra sonication for 15 min, and then the calculated dose of CuO was progressively added to the solution while stirring for 60 min. The resulting solution (see Figure 5.21) was then combusted at 110 °C for 4 h, until the liquid entirely dried, before being grounded.

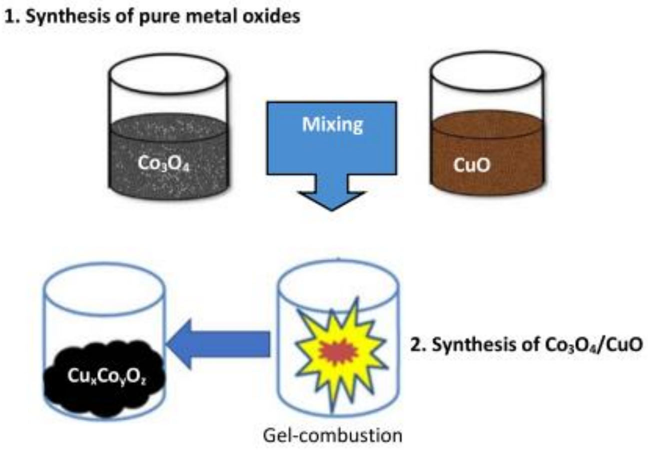

Figure 5.21. Schematic preparation of Co_3O_4/CuO heterostructures.

5.2.3.2.3 Characterization

The samples were characterized using a wide-angle XRD with Cu-Kα radiation (λ = 1.54056 Å) to investigate the crystalline phases. The XRD spectrum was collected in the 2 theta ranges of 10°–100°, at a scanning rate of 3° min^{-1} with a step of 0.03°. The materials' morphology was examined using a field emission scanning electron microscopy (FESEM). The composition of samples was determined by means of EDX analysis.

5.2.3.2.4 Sensor fabrication and gas sensing measurements

The gas sensor was manufactured by dispersing 1 mg of Co_3O_4/CuO powders, sonicated for 30 min with 1 mL of deionized water (Figure 6.22). The solution was then deposited onto the surface of ceramic substrate devices to produce a sensing layer, which was then allowed to dry at room temperature. For the electrical and sensing measurements, the sensor was mounted onto a holder with four electrical contacts, two of which regulate the sensor's working temperature, while the other two ones are used to measure the resistance. Sensing tests were performed in a home-made apparatus, inserting the sensor holder in a chamber of the volume 10 ml, where the carrier (dry air) and the gases to be tested, coming from certified bottles, were introduced at an overall flow rate of 100 mL min^{-1}. The response of the sensors is defined as R_g/R_a, where R_a and R_g are the resistances of the sensors in the dry air and target gases, respectively. The response and recovery periods are the timeframes necessary for the sensor to attain 90% of the total resistance change. Responses were collected on four identical gas sensors using the same manufacturing technique for each sample, and the findings were then averaged.

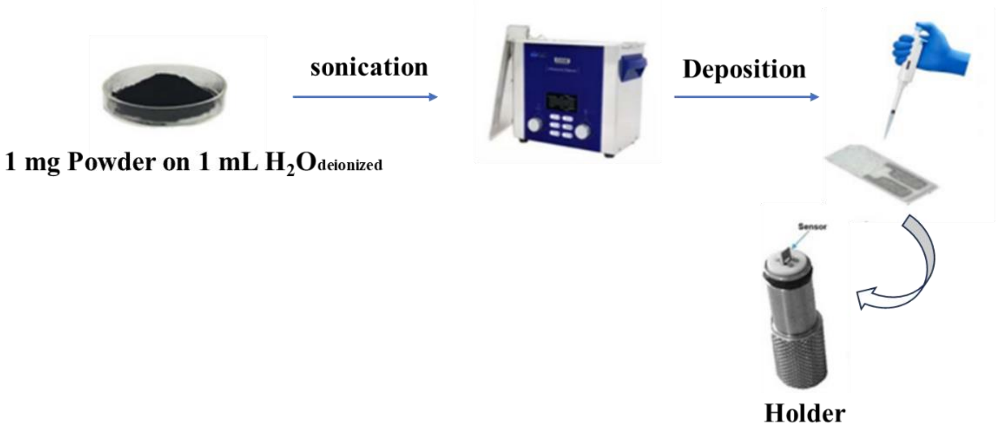

Figure 5.22. Fabrication process of the conductometric sensor by using pure Co_3O_4 and CuO, and Co_3O_4/CuO.

5.2.3.3 Results and discussions

5.2.3.3.1 Structural and morphological characteristics

SEM pictures of the synthesized pure Co_3O_4 and CuO samples, and Co_3O_4/CuO composites are shown in Figure 6.23. Co_3O_4 sample is characterized by the presence of very small and round particles, while particles with an irregular shape and larger size are observed on CuO sample. It can be noted clearly the different morphology of Co_3O_4/CuO composite particles from that of the pure metal oxides samples. The composite samples appear to be constituted by aggregated of tiny round nanoparticles. EDX spectroscopy analysis confirmed the presence of Co, O, and Cu elements in the composite samples. No other significant peaks, attributed to foreign elements, were detected and identified, suggesting that the synthesized Co_3O_4/CuO heterostructure samples were of good purity. XRD measurements were performed to identify the crystal structure of the investigated samples (Figure 6.24). XRD of pristine Co_3O_4 NPs revealed diffraction peaks at 31.27°, 36.67°, 44.68°, 59.33° and 65.25°, which corresponding to the planes of (220),(311), (400),(511) and (440), assigned to cubic spinel tricobalt tetra oxide Co_3O_4 (JCPDS card #74-2102) [78]. These peaks are of low intensity, indicating a low crystalline nature. On the other hand, the pattern of pristine CuO NPs shows high intensity peaks of well crystalline phases, which corresponds well with the standard characteristic peaks of XRD pattern for CuO (JCPDS card #89–5897). XRD patterns of Co_3O_4/CuO heterostructures with varying CuO concentrations revealed that the diffraction peaks are not coincident with those presents on pure Co_3O_4 and CuO NPs. This suggests the formation of new mixed Co-Cu oxide phases. Indeed, due to the multiple oxidation states of the two Co and Cu elements, the possibility to form mixed phases, with many Co/Cu elemental ratios, is high. The main diffraction peaks observed on the composite samples were attributed to the $CuCoO_2$ and $CuCo_2O_4$ phases. However, the presence of other CuxCoyOz mixed oxide phases, cannot be excluded. In exploring the Co_3O_4/CuO preparation in terms of alloy or composite formation it is required looking at the ionic radii. Substitutional alloys are generally formed when the two metallic components have similar ionic radii, otherwise solubility is more limited. The ionic radius of Cu^{2+} is 0.73 Å, while that of Co^{2+} is 0.65 Å [79] and these similar values would also allow forming a substitution alloys formation, as confirmed by XRD spectra above reported.

The low intensity of diffraction peaks is an indication that the composite nanoparticles are constituted of low crystallinity and/or small particle size. The decrease of the crystallinity can be due to a contraction of crystal lattice because of substitution of the cobalt ions by copper ions, considering that the ionic radius of copper and cobalt are largely different (i.e., 0.73 Å and 0.62Å for Cu^{2+} in octahedral and tetrahedral coordination, respectively, against 0.65 Å and 0.57 Å for Co^{2+} at low-spin octahedral sites and tetrahedral sites, respectively). This likely originated an elevated stress which hindered the ordered growth of the composite nanoparticles.

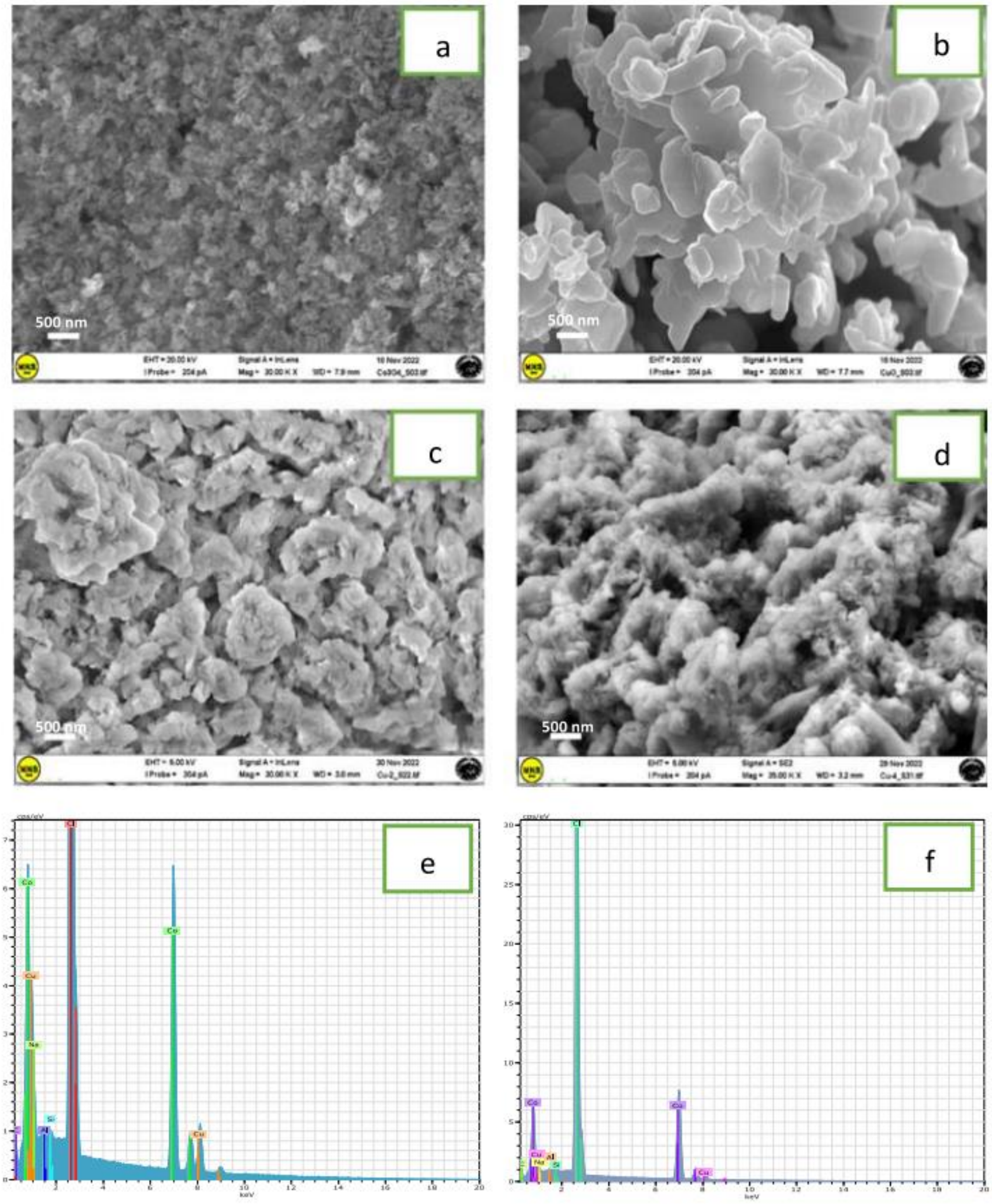

Figure 5.23. SEM images of: (a)Co_3O_4; (b)CuO; (c) Co_3O_4/CuO (1.0wt%/0.5wt%); (d) Co_3O_4/CuO (1.0wt%/1.0wt%). EDX analysis of: (e) Co_3O_4/CuO (1.0 wt%/0.5wt%); (f) Co_3O_4/CuO (1.0wt%/1.0wt%).

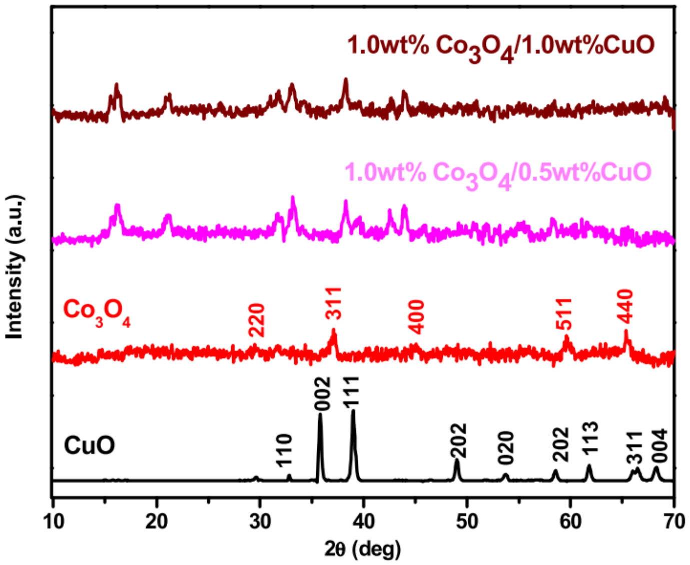

Figure 5.24. XRD patterns of the prepared Co_3O_4/CuO hetero structures with different proportions of CuO in Co_3O_4. The XRD patterns of pure CuO and Co_3O_4 are also shown.

5.2.3.3.2 Preliminary electrical and gas sensing studies

The synthesized samples of cobalt oxide, copper oxide, and copper loaded cobalt oxide nanocomposites were then used to develop conductometric sensors. First, these devices were tested evaluating their electrical baseline resistance at different temperatures. Baseline resistance is a significant parameter for evaluating the sensor's features. Data on the pure oxides have shown that Co_3O_4 is more resistive compared to CuO, at all temperatures investigated (see Figure 5.25). At the lower CuO loading, this did not modify much the resistance compared to Co_3O_4, but when the loading of CuO in Co_3O_4 was comparable (1.0wt% versus1.0wt %), a very low baseline resistance was registered, which is advantageous for sensor development. The sensor baseline decreased as the temperature rises, due to the expected influence of temperature on carrier concentration. Temperature also affects the gas sensing properties. It influences the equilibrium of gas adsorption and desorption on the surface of sensing MOX's semiconductors, as well as electron mobility between the conduction and valence bands. Preliminary tests (not shown) were designed for evaluating the operating temperature response to NH_3 of the gas sensor based on Co_3O_4 /CuO contents (1.0wt%/1.0wt %). The higher response was observed at the operating temperature of 150 °C. Figure 5.26 depicts the effect of Co_3O_4 /CuO heterostructures on NH_3 gas sensing performance when the gas concentration is 400 ppm at the optimal temperature of 150 °C. It is noteworthy that the response of Co_3O_4 /CuO heterostructures composites in various proportions are always greater than pure Co_3O_4 and CuO. It is well known that heterostructure consisting of different active materials usually exhibits enhanced reaction kinetics with respect to individual ones, which could efficiently improve the gas sensing performance. In case of the Co_3O_4/CuO heterostructure, the heterojunctions formed present strengthening effects on the gassensing response to reducing gases [77]. Further, another mechanism which can enhance the sensing performance of heterostructure is through charge carrier separation. In a n-p or p–n junction, the electric field created across the depletion region, much like, pull electrons in one direction and holes in the opposite direction. This charge 'directing' can also exist in p–p junctions, such as in Co_3O_4–CuO, through balancing of Fermi energies, and lead to enhanced sensitivity [80].

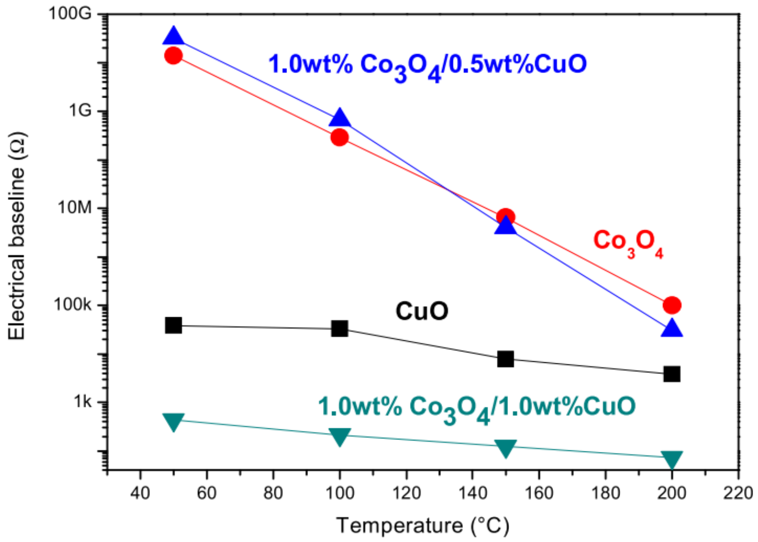

Figure 5.25. Baseline resistance of the sensors based on pure oxides and Co_3O_4/CuO composites with different Cu/Co ratios.

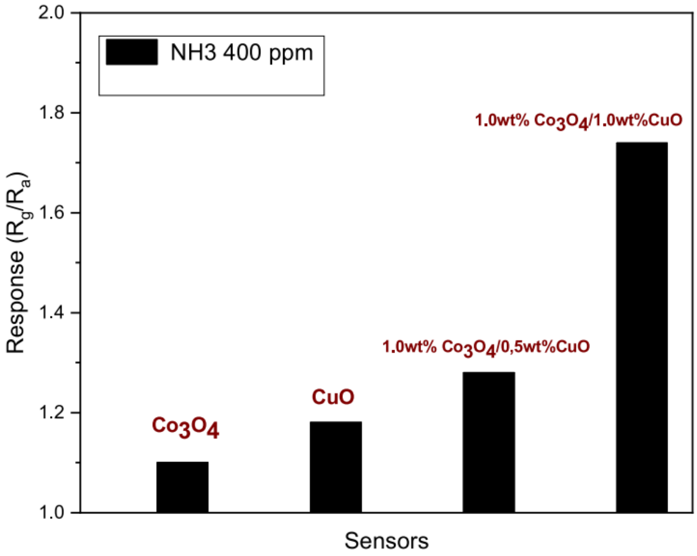

Figure 5.26. Response of the sensors to NH_3 based on Co_3O_4-CuO with different Cu/Co ratio. The concentration of NH_3 is 400 ppm. Temperature is 150 °C.

5.2.3.3.3 NH_3 sensing

After the selection of the best sensor for NH_3, we carried out a series of experiments to investigate its performances. The dynamic response characteristic curves for 1.0wt% Co_3O_4/ 1.0wt% CuO composite sensor at pulses of NH_3 gas at different concentrations (0–800 ppm), at the optimal temperature of 150 °C, are shown in Figure 5.27 (a). The response of the fabricated sensor is highly stable and reversible, i.e., the resistance increases when NH_3 is injected and decreases when the carrier gas is re-introduced. The increase in sensor response with the increase of NH_3 gas concentration is shown in figure 5.27 (b). When the concentration is increased from 0 up to 600 ppm, the trend between response and concentration appears to be highly linear (R = 0.95). When the gas concentration is increased further, the gas response starts to a plateau, indicating that the sensor reaches the saturation for this high NH_3 concentrations. Figure 5.27 (c) reports the calibration curve in the log–log plot. The linearity of the response can be used to extrapolate the limit of detection (around 50 ppm) of the developed sensor.

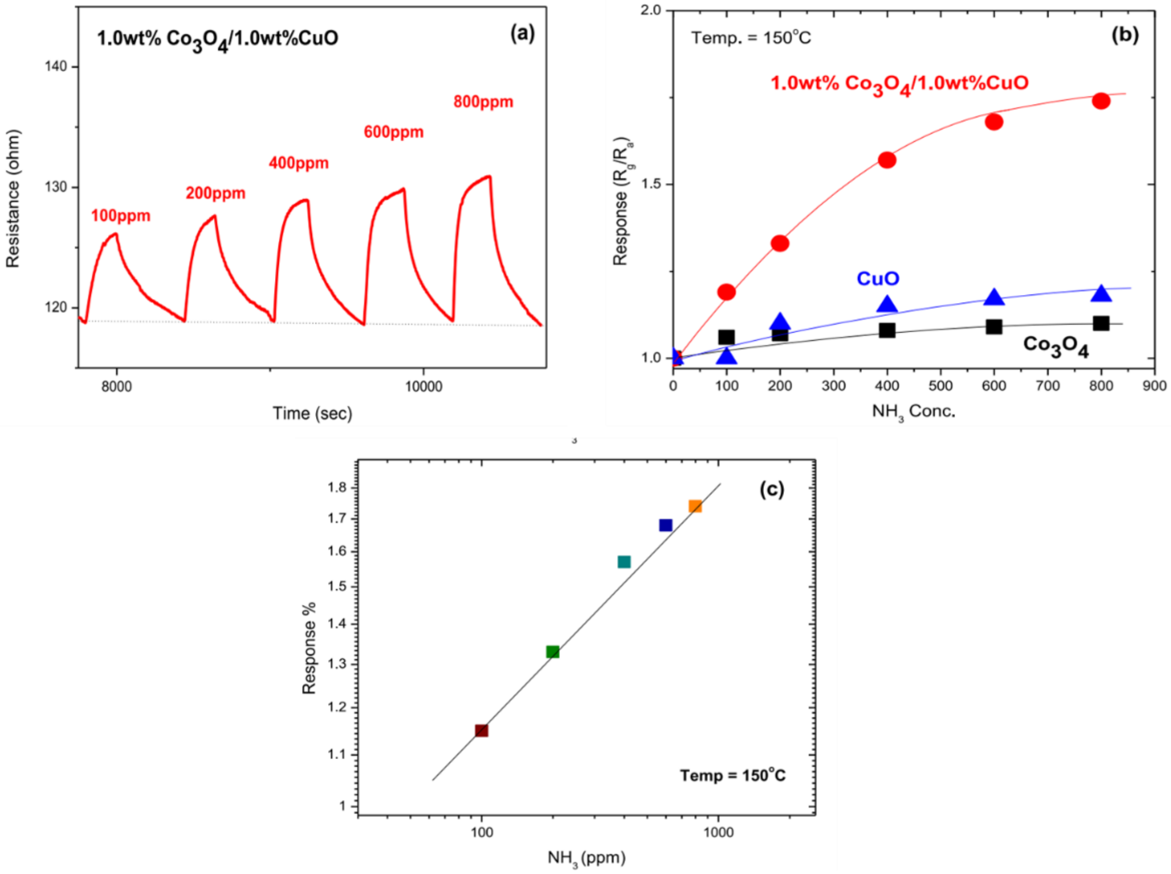

Figure 5.27. (a) Dynamic response curves to different NH_3 concentrations of the composite sensor operating at 150 °C; (b) Calibration curves of the sensors tested at different NH_3 concentrations; (c) Log-log plot of calibration curve for the composite sensor computed from results reported in the graphs(a) and (b).

The dynamics of the sensor is also evaluated. Figure 5.28 (a) depicts the response and recovery time of 1.0wt% Co_3O_4/1.0wt% CuO composite to 200 ppm NH_3. At 150 ◦C, the response time of 1.0wt% Co_3O_4/ 1.0wt% CuO sample for NH_3 gas time is 94 s, while the recovery time is 270 s. The as prepared 1.0wt% Co_3O_4/1.0wt% CuO composite performed superior NH_3 gas sensing also in terms of response and reaction time, being these values lower compared to the pure Co_3O_4-based sensor (Figure 5.28 (b)).

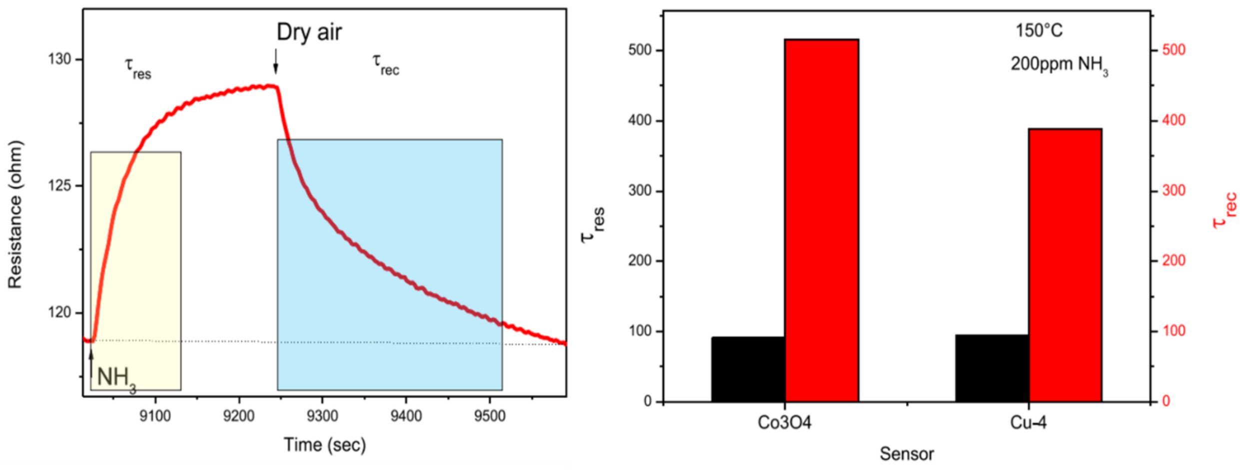

Figure 5.28.(a) Response-recovery curves of the sensor Co_3O_4/CuO (1.0wt%/1.0wt%) operating at 150 °C to 200 ppm of NH_3;(b) Comparison of the response and recovery times between the pure Co_3O_4 and the composite-based sensor, respectively.

Table 5.2 shows a comparison of the Co_3O_4/CuO composite-based sensor with previous Co_3O_4 sensors for NH_3 gas detection reported in the literature. Different forms of Co_3O_4 such as nanorods or sheets, doped or dispersed on various supports (CNTs, graphene, etc) have been considered. The sensor operating temperature, concentration of target gas, sensor response, and response and recovery time are also compared. Based on all these parameters, the performance of our composite sensor is comparable to the other cobalt oxide-based sensors developed for ammonia monitoring, with the additional advantage to be easily fabricated by a mass effective sol–gel process and avoiding expensive materials. After three test cycles, there was no discernible variation in the response to 200 ppm NH3, suggesting that the sensor has also acceptable repeatability and signal stability which are important factor for practical applications.

Table 5.2. Comparison of the performances towards NH_3 of the Co_3O_4/CuO sensor with someone found in the literature.

Material	NH_3 (ppm)	Response Rg/Ra	Temperature (°C)	τ_{res} (sec.)	τ_{rec} (sec.)	Ref.
Co_3O_4 nanorods	100	11.2	160	2	10	79
rGO-Co_3O_4	50	0.59	RT	4	300	80
Co_3O_4/CNT	1000	70.9%*	RT	8	32	81
Co_3O_4 sheets	20	2.83	RT	220	830	82
$Cu_xCo_yO_z$	100	1.1	150	94	270	This work

[a] (Ra − Rg)/Ra.

Selectivity study is shown in Figure 5.29. For this, we have compared the response to target gas, NH_3, with the one obtained by some typical interfering gases, such as H_2, NO_2 and acetone. The sensor based on the 1.0wt% Co_3O_4/1.0wt% CuO composite exhibits significantly high selectivity for NH_3 versus hydrogen and nitrogen oxide. Acetone instead give some interferences, and this will be a factor to be evaluate and overcome for practical applications.

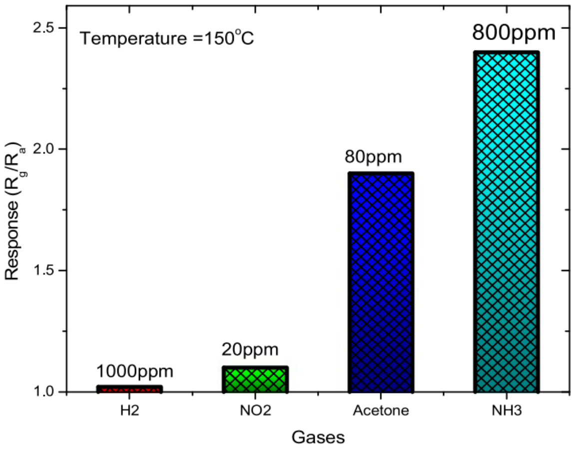

Figure 5.29. Response of the composite Co_3O_4/CuO (1.0wt%/1.0wt%) sensor versus different gases at the operating temperature of 150 °C.

5.2.3.3.4 NH_3 sensing mechanism

The NH_3 sensing mechanism of the Co_3O_4/CuO sensor can be explained as follows. When the sensor is exposed to air, O_2 molecules are adsorbed in different forms depending on the operating temperature. Physical and ionization adsorption of O_2 can occur, with the latter favored as the temperature increase [83]. Equations (5.5)–(5.7) describes the oxygen adsorption processes with increasing the temperature:

$$O_2\,(ads) + e- \Leftrightarrow O^-_2(ads) \qquad (5.5)$$

$$O^-_2\,(ads) + e^- \Leftrightarrow 2O^-\,(ads) \qquad (5.6)$$

$$O^-(ads) + e^- \Leftrightarrow O_2^-(ads) \qquad (5.7)$$

Oxygen adsorptions modulate the electronic behavior of the sensor; indeed, oxygen drain electrons from the p-semiconductor's surface (see arrows direction in Figure 5.30 (a)), increasing the holes concentration. As the electrical carrier concentrations are enhanced, the composite material is in a low-resistance condition [83]. When the composite is exposed to NH_3, it is adsorbed on the sensing layer. Due to its electron donating character and the reaction with the adsorbed oxygen (equation (5.8)),

$$4NH_3\,(ads) + 3O^-_2\,(ads) \Leftrightarrow 2N_2 + 6H_2O + 3e^- \qquad (5.8)$$

electrons are produced and returned on the surface of the composite (note the reversed direction of arrows in Figure 5.30(b)). This process led to the decrease of the resistance in n-type semiconductors [84], while for p-type ones it causes a decrease of the holes concentration and, consequently, to the increase the resistance. The response of Co_3O_4/CuO composite to NH3 gas is higher than that of pure Co_3O_4, which is ascribed to surface defects that promote gas molecules adsorption. The surface of the Co_3O_4/CuO composite contains more flaws with high adsorption energy than pure Co_3O_4. These high energy defects contain significant chemical adsorption sites for NH_3, and their response towards this gas was stronger than pure Co_3O_4. At the same time, this causes lattice oxygen enrichment. Increased lattice oxygen can boost reactivity, which may improve gas sensing characteristics.

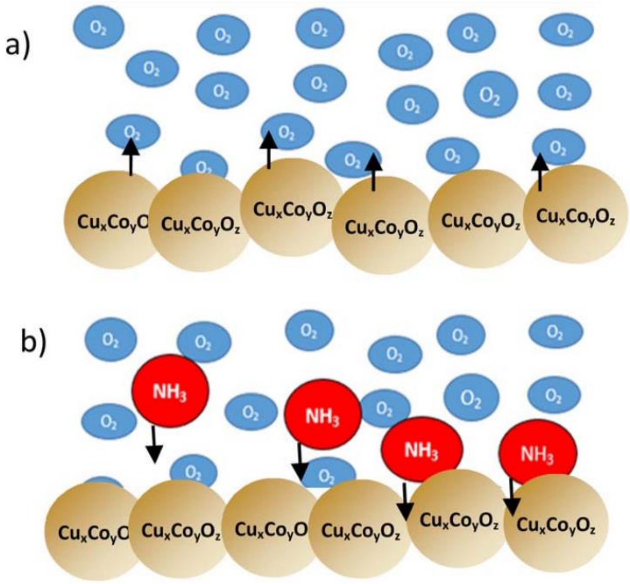

Figure 5.30. Gas sensing mechanism of Co_3O_4/CuO hetero structures in the presence of a) air and b) NH_3 gas.

As a result, the Co_3O_4/CuO nanocomposites display substantial NH_3 sensing capability. As before discussed, junctions formed when different metal oxides are mixed, are responsible of the gas sensing mechanism. However, previous research is mainly limited to p–n heterojunctions, and few studies related to p–p hetero metal oxide junctions are reported. Our data demonstrated that the formation of p–p heterojunctions in CuO-Co_3O_4 improve the response of sensors to NH_3. It can be assumed that introducing CuO, a mechanism occurs in which the majority of charge carriers come from the wide-bandgap materials to narrow-bandgap materials, establishing a low potential barrier. This also explain the increase of conductivity as CuO loading is increased. Further, CuO can capture NH_3 molecules, suggesting that CuO is the active center to improve the NH_3 sensing performance.

5.2.3.4 Conclusion

In summary, we used a sol–gel combustion approach to synthetize Co_3O_4/CuO nanocomposites. We accomplished hetero-structure modulation by altering the proportion of CuO in Co_3O_4 nanoparticles. The results demonstrate that the sensor based on Co_3O_4/CuO (1.0wt%/1.0wt%) hetero structures has good performances towards the detection of NH_3 gas. The improved sensing capabilities could be attributable to the p-p hetero junctions with abundant active sites and lattice oxygens which enhance chemical reactivity of the Co_3O_4/CuO composite.

5.3 Sensing material *via* pyrolysis method:

5.3.1 Development of a novel C-dots conductometric sensor for NO sensing

Sensors & Actuators: B. Chemical 390 (2023) 133957

Contents lists available at ScienceDirect

Sensors and Actuators: B. Chemical

journal homepage: www.elsevier.com/locate/snb

Development of a novel C-dots conductometric sensor for NO sensing

S. Crispi[a], G. Nocito[b], F. Nastasi[b], G. Condorelli[c], A.G. Ricciardulli[d], P. Samorì[d], S. Conoci[b,e,f,g], G. Neri[a,*]

[a] Department of Engineering, University of Messina, C. da Di Dio, 98158 Messina, Italy
[b] Department of Chemical, Biological, Pharmaceutical and Environmental Sciences (ChiBioFarAm), University of Messina, Viale F. Stagno d'Alcontres 31, 98166 Messina, Italy
[c] Department of Chemical Sciences, University of Catania, Viale A. Doria 6, 95125 Catania, Italy
[d] Université de Strasbourg, CNRS, Institut de Science et d'Ingénierie Supramoléculaires, 8 allée Gaspard Monge, Strasbourg 67000, France
[e] LAB Sense Beyond Nano - URT Department of Sciences Physics and Technologies of Matter, Consiglio Nazionale delle Ricerche (CNR-DSFTM), Viale F. Stagno d'Alcontres 31, 98166 Messina, Italy
[f] Istituto per la Microelettronica e Microsistemi, Consiglio Nazionale delle Ricerche (CNR-IMM), Strada VIII n. 5 Zona Industriale, 95121 Catania, Italy
[g] Department of Chemistry "G. Ciamician", University of Bologna, Via F. Selmi 2, 40126 Bologna, Italy

ARTICLE INFO

Keywords:
C-dots
NO sensor
NO_2 sensor

ABSTRACT

Carbon dots (CDs, C-dots) obtained from waste produced during the production of olive oil in Calabria (Italy) have been investigated as a gas sensing material for the sensitive and selective detection of nitric oxide (NO) in air. The obtained CDs were characterized by XPS, FT-IR and ATR-FTIR. CDs were deposited to yield a sensitive layer on a conductometric platform and tested for gas sensing, showing promising characteristics for the selective monitoring of NO in air. The response of CDs composite to NO was 1.5 @ 1250 ppm and the response and recovery times amounted to 90 and 200 s, respectively. The sensing behavior of C-dots prepared using olive waste from a different geographic location (Puglia, Italy) was also reported and compared. It has been found that the sensing behavior of the two different materials based sensors investigated towards nitrogen oxides (NO and NO_2) was completely different. On the one hand, the former exhibited selectivity towards NO. On the other, the latter showed prominent selectivity towards NO_2. This behavior can be ascribed to the different functional groups exposed on the C-dots surface undergoing non-covalent interactions with a marked specificity of the hydroxyl and ethers moieties for NO and NO_2, respectively.

Abstract: Carbon dots (CDs, C-dots) obtained from waste produced during the production of olive oil in Calabria (Italy) have been investigated as a gas sensing material for the sensitive and selective detection of nitric oxide (NO) in air. The obtained CDs were characterized by XPS, FT-IR and ATR-FTIR. CDs were deposited to yield a sensitive layer on a conductometric platform and tested for gas sensing, showing promising characteristics for the selective monitoring of NO in air. The response of CDs composite to NO was 1.5 @ 1250 ppm and the response and recovery times amounted to 90 and 200 s, respectively. The sensing behavior of C-dots prepared using olive waste from a different geographic location (Puglia, Italy) was also reported and compared. It has been found that the sensing behavior of the two different materials based sensors investigated towards nitrogen oxides (NO and NO_2) was completely different. On the one hand, the former exhibited selectivity towards NO. On the other, the latter showed prominent selectivity towards NO_2. This behavior can be ascribed to the different functional groups exposed on the C-dots surface undergoing non-covalent interactions with a marked specificity of the hydroxyl and ethers moieties for NO and NO_2, respectively.

5.3.1.1 Introduction

Gas detection using low-dimensional carbon nanomaterials, such as carbon nanotubes (CNTs), graphene (G) or graphene oxide (GO), has been largely pursued in the last decade [85]. Indeed, because of their highest surface-to-volume ratio, almost all their composing atoms are exposed to the environment to readily interact with gas molecules, yielding high sensitivity in the sensing process. By taking advantage of such a unique setting, conductometric sensors based on these 1-D or 2-D carbon nanomaterials revealed a significant capacity of detecting trace levels of gases [86]. In this regard, carbon dots (CDs) are 0-D carbon nanomaterials which display unique interesting electrical and optical properties, making them interesting components for a plethora of applications in energy, (bio)medical, and environmental technologies [87, 88].

CDs have quasi-spherical geometry with diameters below 10 nm. Its amorphous nucleus comprises sp^2 hybridized carbon and crystalline structures given by the sp^3 hybridized carbon. CDs can be synthesized by exploiting "top-down" and "bottom-up" approaches. In the top-down approach, they are obtained from large carbon structures using characteristic methods to reduce their size with control over their morphology, and purity. Powerful strategies include laser ablation, chemical and electrochemical oxidation, and ultrasound treatment. Conversely, “bottom up” protocols enable to achieve a subtle control over their size by exploiting inexpensive procedures such as microwave synthesis, thermal decomposition, and hydrothermal treatment [89].

During the last decade, much effort has been devoted to the use organic waste materials, also defined biomass, to obtain carbon nanomaterials by exploiting simple and low-cost synthesis methods [90,91]. Particularly, carbon dots produced from biomass exhibit different physical and chemical properties depending on the starting biomaterial and the preparation method adopted. Within this context, carbon dots have attracted much attention due to their unique optical, chemical, and electronic properties enabling a wide range of applications. Furthermore, CDs properties can be effectively adjusted by modifying their chemical composition.

Surface groups such as -COOH, -OH and $-NH_2$ are characteristics of these nanomaterials, and impart them excellent optical properties, so contributing to their excellent fluorescent, photoluminescent and optoelectronic properties [92]. However, little is known about the contribution of these surface groups to the optical and electronic properties of CDs [93,94]. The unique electrochemical and optical properties of CDs were largely exploited for chemical sensing [95] by focusing on their fluorescence and electrochemical characteristics for the detection of various metal ions in water (Fe^{3+}, Cu^{2+}, Hg^{2+}, etc.) and biomolecules [96].

Given their distinct properties, they could be also used as responsive materials to develop sensors capable to detect gaseous environmental pollutants. However, only a few studies have been reported so far on the application of CDs in gas sensing. In particular, previous studies used CDs as a support for the sensing phase, typically a metal oxide, and optical detection was the preferred transduction method [97,98].

In a previous introductory work, we fabricated a CDs-based conductometric sensor for NO_2 detection in air, demonstrating for the first time the use of pristine CDs in this kind of electrical solid-state device [99]. NO_2 is one among the harmful gases, which require low-cost and reliable sensors operating at room temperature and capable of detecting sub-ppm concentrations [100].

In this work we expand our endeavor to the use of CDs obtained from olive solid waste to monitor nitrogen monoxide (NO) in air by means of a conductometric sensor. The main NO emissions in the atmosphere derive from the exhaust gases of cars, in which NO is the most common form of NOx at around 93%, around 100–2000 ppm (parts per million). The Environmental Protection Agency (EPA) indicated that these emissions cause environmental problems, triggering an increase in the greenhouse effect as it exhibits 310 times greater impact than CO_2 ultimately threatening human health through the onset of serious diseases related to the respiratory system. The maximum exposure value amounts to 20 ppm. Because of these reasons, the development of gas sensors that can perceive NO in real time is highly sought after. However, previous CDs-based sensors were not able to detect NO [99]. The CDs used in the above study was obtained from the solid waste in oil production, coming from Puglia, a region of Italy. CDs produced from solid waste in oil production coming from different geographical origin, display different surface groups composition, thus we have tested another CDs obtained from the solid waste in oil production coming from a different region (Calabria, Italy), with the scope to monitor NO as target gas.

Here we report the fabrication and characterization of CD based conductometric sensors displaying high sensitivity and selectivity for NO present in the air. The comparison with the previous CDs-sensor comprising was also made, attempting to explain the different sensing behavior observed. We found that our CDs hold high potential for the development of inexpensive gas sensors to monitor selectively the targeted gases, by simply designing its surface composition.

5.3.1.2 Experimental section

5.3.1.2.1 Carbon dots preparation

Carbon dots were prepared by using a bottom-up approach starting from the discard of olive oil production, by following the synthetic procedure reported in [99]. The olive solid wastes were purified with Soxhlet extraction method by using water as a solvent. The obtained biomass was dried, pyrolyzed in absence of air (600 °C, 1 h) and subsequently ground. 100 mg of the product was suspended in 10 mL of deionized water and sonicated in an ultrasonic bath for 10 min followed by the addition of hydrogen peroxide solution (0.45% wt in 10 mL). The reaction mixture was refluxed for 90 min and after cooling to RT centrifuged for 20 min (9900 rcf,). The supernatant was filtered with a 0.2 μm microfilter and finally purified by dialysis against MilliQ-water (500–1000 Da) for 24 h. The final powders of CDs, which were adopted for the development of the gas sensor, were obtained through lyophilization. C-CDs were obtained via bottom-up approach by pyrolysis of the solid waste of olive oil production from Calabria (Italy). We also investigated carbon dots prepared with olive solid waste coming from the olive oil production process in Puglia (Italy), called P-CDs hereafter.

5.3.1.2.2 Characterization

X-ray photoelectron spectroscopy (XPS) was performed on carbon dots deposited on silicon slides using a PHI 5600 multi-technique ESCA-Auger spectrometer (Physical electronics Inc., Chanhassen, MN, USA) equipped with a monochromatic Al-K X-ray source. The XPS binding energy (BE) scale was calibrated on the C 1 s peak of adventitious carbon at 285.0 eV. Transmission Fourier Transformed Infrared (FT−IR) measurements on the silicon-deposited carbon dots were obtained using a JASCO FTIR 4600LE spectrometer (JASCO Corporation, Tokyo, Japan) in the spectral range of 560−4000 cm^{-1} (resolution 4 cm^{-1}). Attenuated Total Reflection (ATR) FTIR analyses were performed using a Spectrum Two (Perkin-Elmer) FT-IR spectrometer with a diamond ATR single reflection accessory. X-Ray powder diffraction (XRD) patterns were acquired on thin films drop-cast on silicon wafers. Measurements were carried out in air environment at room temperature by means of a Bruker D8 Advance diffractometer (Bruker Co., MA - USA) with Cu Kα radiation (λ = 1.54184 Å) and a step size of 0.05° at 40 KV and 40 mA in the range of 2θ from 2° to 60°. Thermogravimetric analysis (TGA) and Differential Scanning Calorimetry (DSC) were performed in a MettlerToledo TGA/DSC 2 STARE instrument (Mettler Toledo LLC, Columbus, OH – USA). Measurements were executed on Carbon dots powder (from 1 to 2.5 mg) both in synthetic air (Air Zero X50S, Air products, Saint Quentin Fallavier, France) and in pure nitrogen environments, starting from 25 °C to 600 °C (5 ◦C/min). Derivative Thermogravimetry (DTG) was calculated on the first derivative of the TGA curve.

5.3.1.2.3 Sensing tests

Sensor devices were fabricated by printing thick films of the C-dots dispersed in an aqueous solution on alumina substrates (6 ×3 mm^2) covered with Pt interdigitated electrodes and a Pt heater located on the backside. The sensing platform used for developing the conductometric sensors based on CDs has been reported in many previous our papers (see for example ref. [65]). The sensing tests were carried out using the data acquisition instrument Agilent 34970 A to monitor the resistance and a dual-channel power supply Agilent E3632A was used to bias the built-in heater of the sensor.

Sensing tests were performed using a homemade detection setup as follows; first, the sensor was inserted in a stainless-steel test chamber and was kept at a fixed temperature while a flow of synthetic dry air (O_2 + N_2) was passing over the sensing material to order to obtain a stable baseline resistance. Afterwards, the sensor was exposed to pulses of gas mixtures supplied from certified bottles of SOL company (www.solgroup.com). The sensor response to target gas (R) is determined as the ratio of R_a (resistance of the gas sensor in dry synthetic air) to R_g (resistance of the injected gas sensor), $R = R_a/R_g$. The calculation of the response and recovery time, i.e., the variation of the sensor resistance over time until it reaches 90% of equilibrium after the start and end of NO detection, allowed to study the sensor dynamics.

5.3.1.3 Results and discussion

5.3.1.3.1 Carbon dots material characterization

Carbon dots primarily comprise a carbon core, while their surfaces expose a large amount of reactive functional groups (such as -OH, -COOH/-COO-, etc.). Thus, a detailed characterization has been carried out for acquiring important information on the morphological, microstructural, and surface groups composition of C-CDs. In our previous study [90], transmission electron microscopy (TEM) measurements confirmed that C-CDs display quasi-spherical monodispersed carbon nanoparticles. Their diameter distribution ranged from 15 to 20 nm. We determined further the phase, structure, and crystallinity of C-CDs by X-Ray powder diffraction (XRD). As illustrated Fig.6.31 the XRD diffractogram exhibits several peaks. The broad peak from 20° to 24° (2θ) and the sharp one at $2\theta = 24.35°$ (3.7 Å d lattice spacing) can be attributed to the amorphous carbon phase and to graphitic C(002) plane [101]. The graphitic nature of CDs is confirmed by the peaks located at 40–45° and 53.80° (D-spacing 1.7 Å), which are ascribed to C(100) and C(004) planes of graphitic carbon [102].

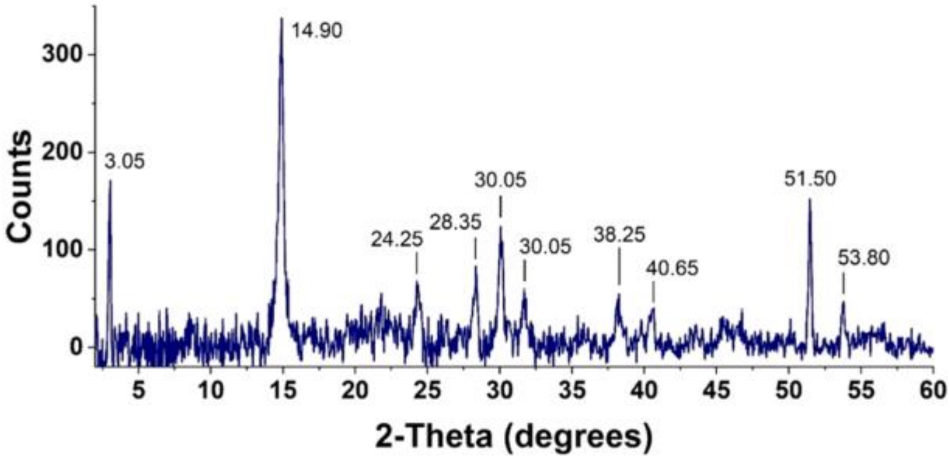

Figure 5.31. XRD pattern of C-CDs.

To characterize the groups exposed on the surface, FT-IR and XPS analyses were performed. The FT-IR spectrum of C-CDs sample is shown in Fig. 5.32a. Different vibrational signatures, due to surface groups, reveal the presence of -C=O- (carbonyl), -COO- (carboxylate), C-OH (hydroxyl), and C-O-C (ether) groups. In particular, the wide band in the 3500–3000 cm^{-1} region can be attributed to the stretching vibration of O-H groups [69-72]. The strong feature around 1600 cm^{-1} can be ascribed to convolution to the signals due to C=O stretching of carboxylic (1660 cm^{-1}) of acids or amides, to the asymmetric stretching of carboxylate (1570 cm^{-1}) and to the bending of H_2O (1620 cm^{-1}) [103–106]. The other strong features at about 1370 cm^{-1} correspond to convolution of the symmetric stretching of carboxylate groups (1450 cm^{-1}), the C-O stretches of carboxylic acids (1250 cm^{-1}) and the bending of OH groups (1350 cm^{-1}) [102–107].

XPS spectra showed the presence of C, O, N and K. Fig. 6.32b shows the C 1 s, N 1 s and O 1 s regions. The complex shape of the C 1 s signal is mainly due to the presence of C-C/C-H signal at 285.0 eV and to the signal at 289.0 eV of carboxylic groups. A component around 287.3 eV is observed which can be associated to the presence of carbons in carboxylates and amides groups [106–110]. Note a small amount of K^+ is also present.

The N 1 s band mainly reveals a peak at 400.4 eV that can be due to amines and amides (C-N containing groups) [108-110]. A small shoulder at about 399.0 eV can also be attributed to the formation of imine groups (-C=N-) [106-110]. Conversely, the O1s peak position at 532.2

eV is typical of the oxygen in organic compounds. The thermal stability study on C-CDs was performed by TGA-DSC analysis. We noticed that C-CDs, in both synthetic air and nitrogen environments, are mainly stables until 200 °C, being the weight loss in this temperature range due mainly to water desorption (Fig. 6.33). According to literature, the first decomposition stage (around 21–27% of the weight loss at 175–182 °C – Air/N_2) can be attributed to the loss of water on CDs surface [111]. The second decomposition stage (around 16–22% of total weight loss at 434–450 °C – Air/N_2) may be associated with the loss of covalently linked species to CDs surface and/or to the loss of oxygen-containing groups such as -O-C=O and C=O [112-114].

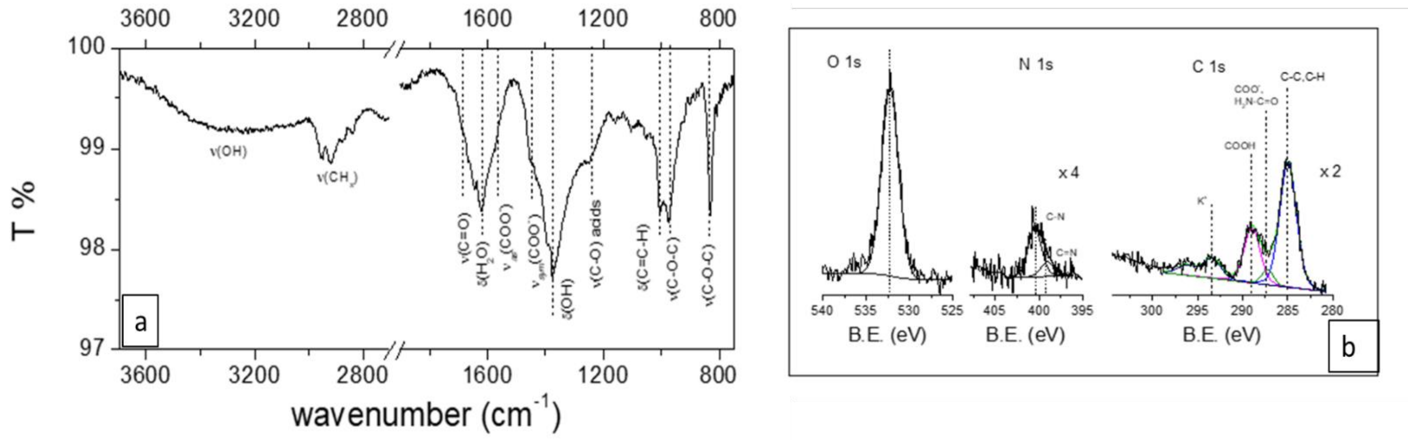

Figure 5.32. a) FT-IR and b) XPS analyses.

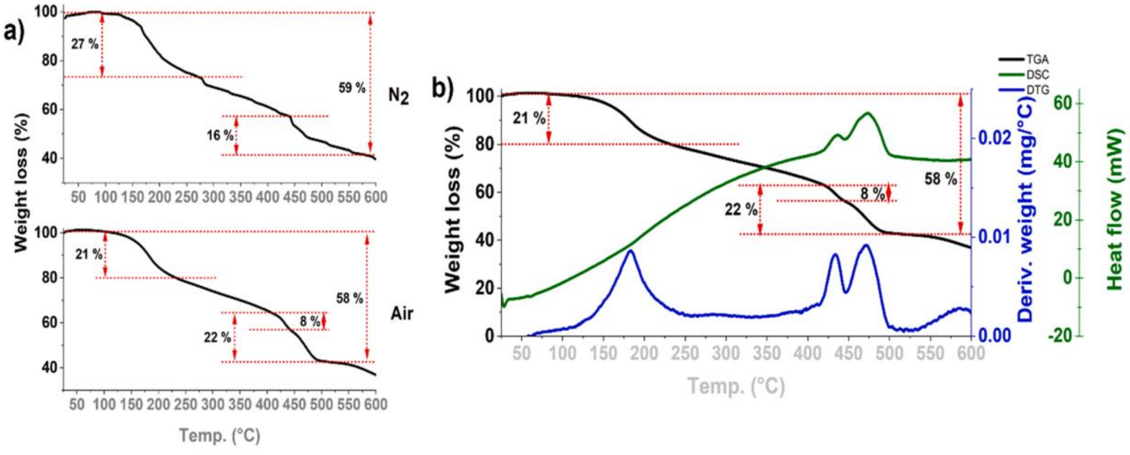

Figure 5.33. a) TGA analyses in nitrogen and synthetic air of C-CDs; b) TGA/DTG/DSC graphs in synthetic air of C-CDs

5.3.1.3.2 Electrical characterization

The electrical resistance of C-CD films in dry air as a function of temperature has been investigated. The measurements were performed with the C-dots sample deposited as a layer on the conductometric platform used for the successive sensing experiments, making it possible to use the information obtained to optimize the performances. We started our measurements at room temperature and found a very high resistance of the sample layer (Fig. 6.34). Upon increasing the temperature there is a sharp decrease of the resistance. As CDs exhibit p-type behavior, the observed resistance decrease can be attributed to holes carriers, which are activated for the conduction upon temperature increase. In contrast to n-type sensing materials, such as metal oxides, a sharp decrease in resistance occurs by increasing the temperature, as CDs require a higher activation energy for the conduction than electrons.

Subsequently, we tested the sensing characteristics of the fabricated C-CDs sensor at operating temperatures ranging from 100 °C to 250 °C. For these measurements, NO was selected as the target gas. The choice of this target gas derived by considering that carbon nanostructures are largely used for monitoring nitrogen oxides [115].

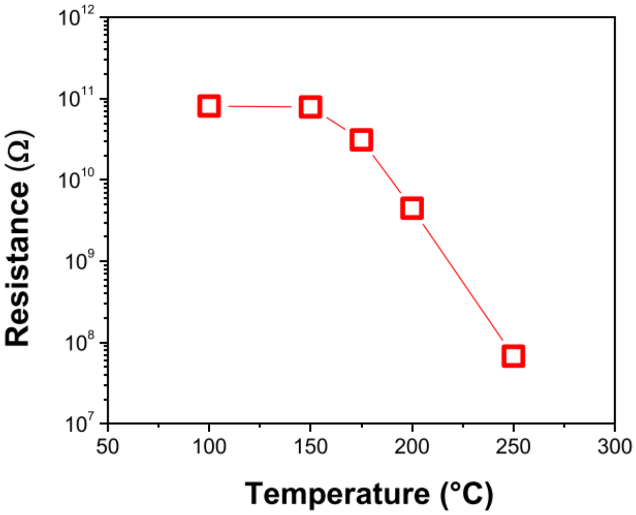

Figure 5.34. Electrical resistance of C-CDs sensor as a function of the operating temperature.

Tests were performed by using NO at a concentration of 2500 ppm. The results displayed in Fig. 5.35 revealed that starting from 150 °C, the C-CDs sensor exhibits a reversible decrease of the resistance when NO pulse was injected in the sensor chamber. An increase in temperature is accompanied by an improvement in the reaction kinetics occurring on the surface of the material yielding to an increased response. The response reached a plateau at operating temperature of 200 °C.

In view of such temperature dependent response, it was concluded that C-CDs sensors operate better for a temperature set at 200 °C. The use of higher operating temperatures revealed a strong reduction in the lifetime of the sensing layer due to the occurrence of surface oxidation [99]. As at the higher temperature tested (250 °C) surface oxidation of carbon dots may occur, the useful operating temperature "window" of the sensor was set to very narrow values, centered around 200 °C.

NO behaves as a strong π-acceptor, thus very likely yielding a strong binding between NO and the carbon dots surface the latter results in a decrease in the baseline resistance, as reported for other carbon nanomaterials [116]. We speculate that when the sensor is exposed to dry air, the oxygen molecules are adsorbed on the carbon dots surface to be ionized by electrons trapped by the semiconductor conduction band to yield oxygen ions such as O^{2-}, O^{-} or O^{2-}, depending on the operating temperature. In the presence of target gas, local doping effect occurs upon the absorption and subsequent reaction of NO with adsorbed oxygen species, ultimately leading to the observed resistance decrease.

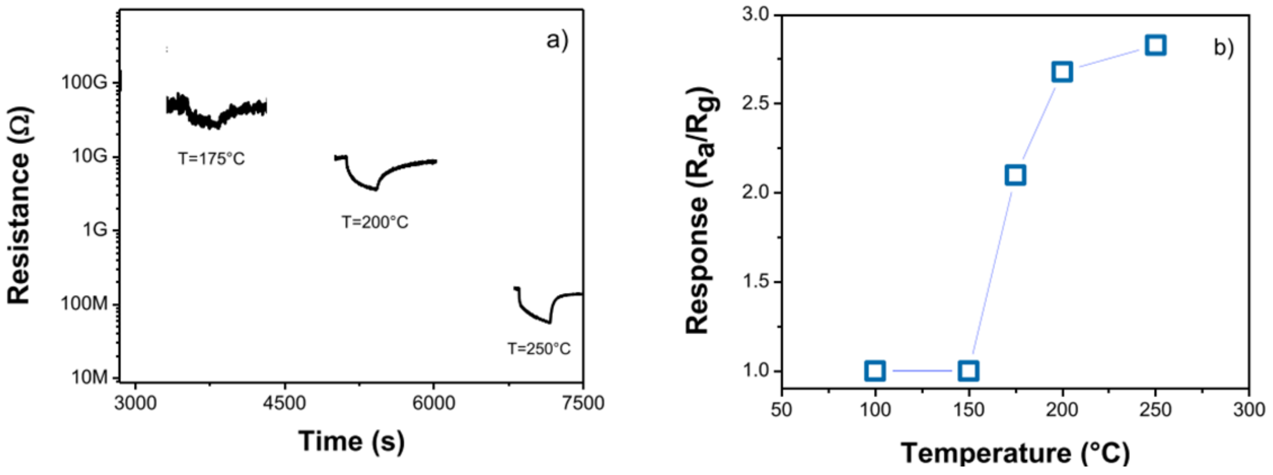

Figure 5.35 a) Response at different temperature to 2500 ppm NO of the C-CDs sensor; b) trend of the sensor response vs. the temperature.

Sensing tests were carried out to verify the performance of the C-CDs sensor towards the target gas. Therefore, the dynamics, sensitivity, reproducibility, stability over time and selectivity to the target gas in the presence of other interferent gases were also investigated. The dynamic of the C-CDs sensor was verified by testing the sensor to a concentration of 1250 ppm of NO at the operating temperature of 200 °C, as shown in Fig. 5.36. The quantified response and recovery time amount to approximatively 90 s and 200 s, respectively.

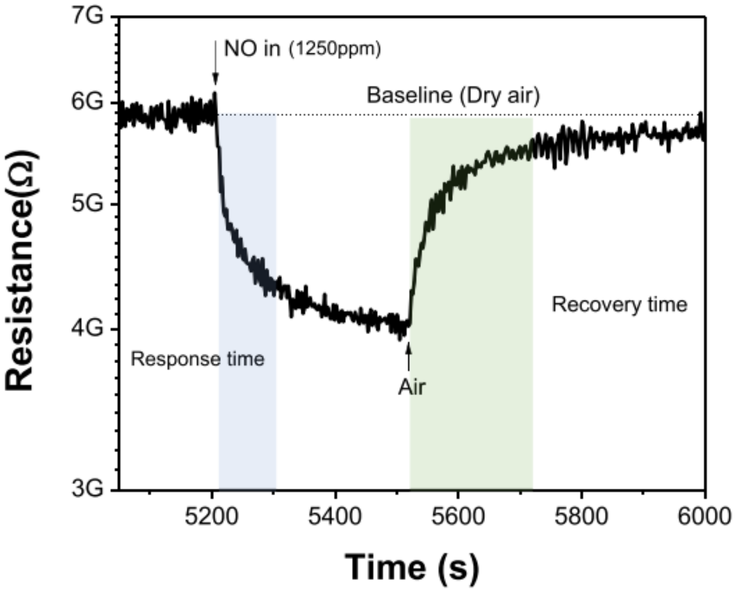

Figure 5.36. Transient response of the C-CDs sensor.

Furthermore, we have verified the response of the sensor to different concentrations of NO in the range from 125 to 4000 ppm (Fig. 5.37a). Moreover, to verify the presence of a memory effect, the sensor was tested at decreasing NO concentration (Fig. 5.37b). The response of the sensor is reproducible over time for different concentrations, and the presence of any memory effect could be excluded (Fig. 5.36c). Further, the signal revealed a good reproducibility (Fig. 5.37d).

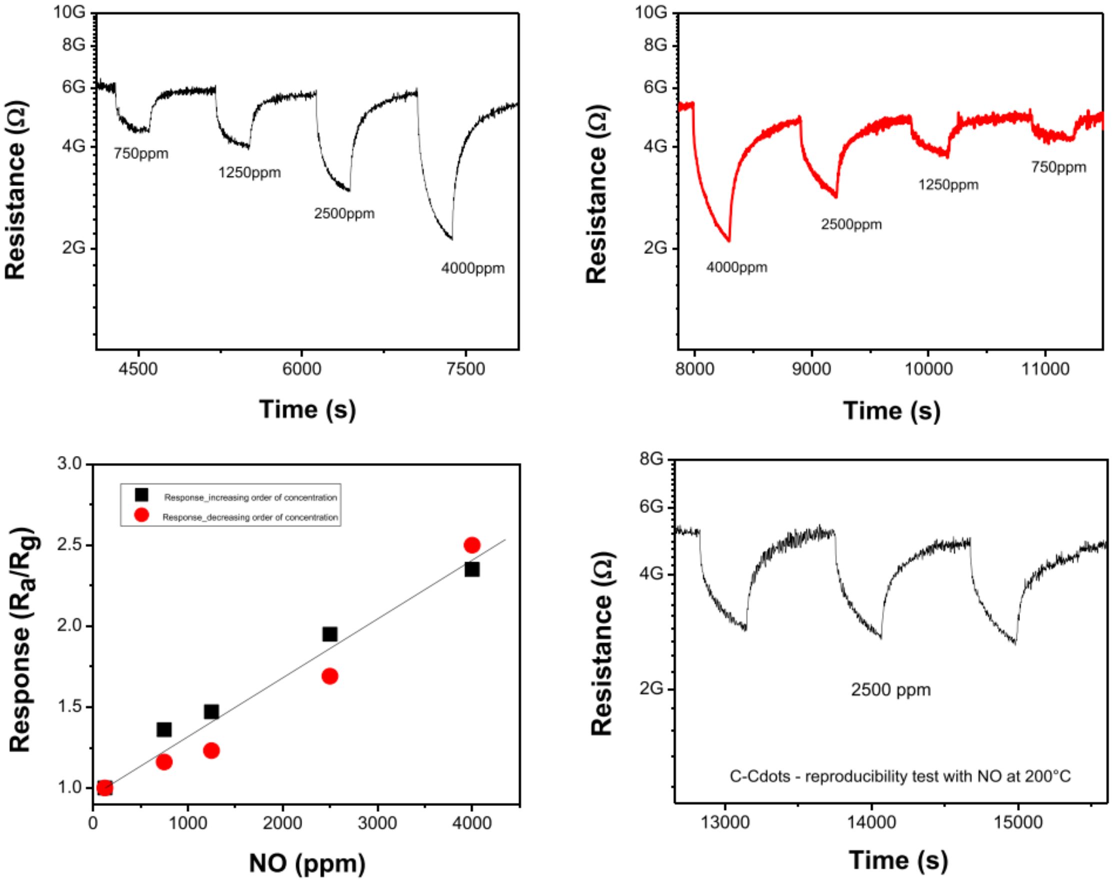

Figure 5.37. Response of the C-CDs sensor at a) increasing and b) decreasing concentrations of NO; c) Calibration curve; d) Reproducibility of the signal over time at 2500 ppm of NO.

The long-term stability is a fundamental characteristic for sensor applications. Temperature is the first factor affecting this characteristic because it can accelerate the degradation/oxidation of the most labile surface groups on the surface of CDs. From TGA/DCS study above reported, we demonstrated that C-CDs, in both dry synthetic air and nitrogen environments, are mainly stables until 200 °C, so CDs-sensors operating temperature is maintained in the range 150–200 °C. The sensor's long-term stability (as regarding both the electrical baseline in dry air and response to NO) has been tested for two months. Data (see Fig. 5.38) reveal that the baseline resistance increases a little bit, likely as a result of the slow surface oxidation of the sensing layer, but this do not appear to influence the long-term stability of C-CDs sensor response to NO in the operating conditions adopted.

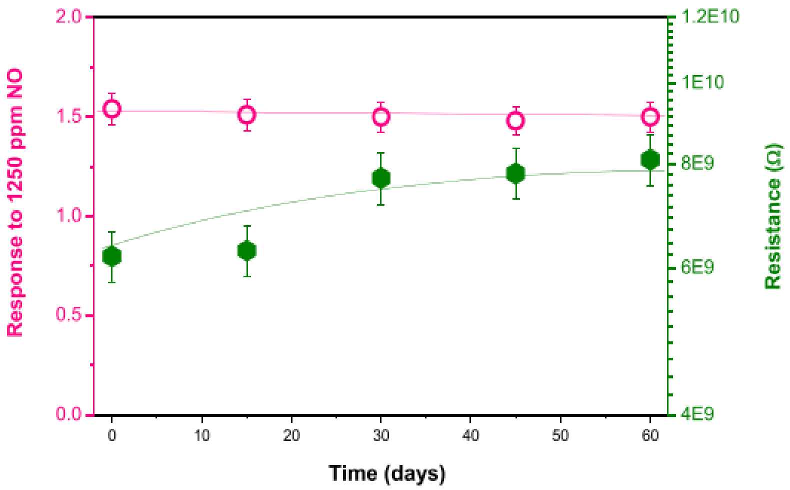

Figure 5.38. Response of the C-CDs sensor registered at various times.

Currently, we also are performing tests for acquiring information about the stability of the sensor in humid air. The effect of humidity (at rh = 50%) has been preliminary investigated. In the Fig. 5.39, is reported the effect of humidity (at rh = 50%) on pulses of NO, compared to the same in dry air. In particular, humidity increases a bit the baseline resistance and appears also to increase the noise. However, this does not influence so much the signal to NO pulses, indicating that little variations in both baseline resistance and signal response were caused by humidity.

Quantitatively, the change of 1% humidity has the same effect of less 25 ppm of NO. However, even if these preliminary results inferred that humidity do not influence remarkably the sensor performances, further investigations are necessary for assessing the effect of humidity on the long period and take the necessary action for limiting its adverse effects, if any.

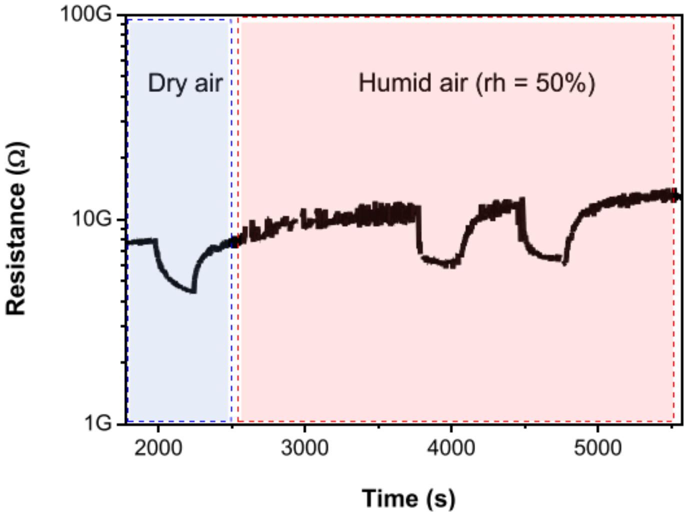

Figure 5.39. Response of the C-CDs sensor registered at different humidity levels.

The selectivity of the sensor was verified by evaluating the response to different interferent gases, i.e. CO_2, NH_3, NO_2 and CO. As displayed in Fig. 5.40, the high selectivity of the C-CDs sensor for NO over other species is confirmed.

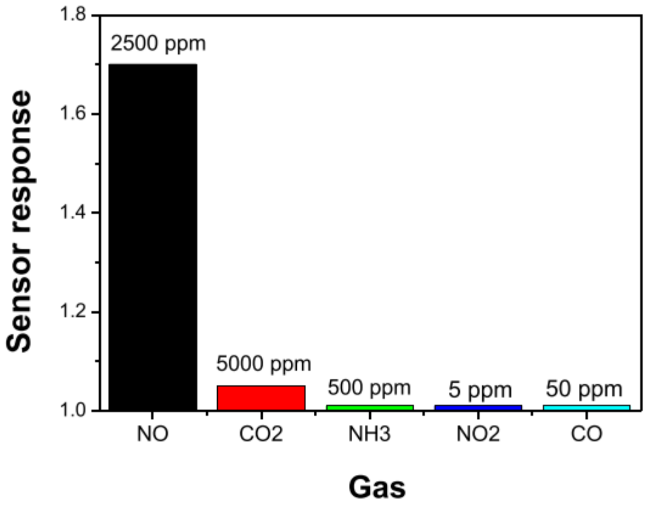

Figure 5.40. Response of the C-CDs based sensor to different gases. The high response to NO, compared with the lower response to other gases, highlights the good selectivity of this sensor towards NO.

Table 5.3 shows the comparison of our CDs sensor material with some others found in the literature. Our material exhibits performances, in terms of operating temperature, sensitivity, selectivity, and response/ recovery time, that are comparable with the state-of-the-art, being a promising alternative.

Table 5.3 - Comparison of NO sensing properties of different sensor materials.

Sensor material	Temp.(°C)	NO conc. (ppm)	Response time (s)	Recovery time (s)	Response	Ref.
C-dots	200	1250	30	200	1.50 [#]	This work
GaN	35	100	280	2300	115%*	117
Bi-SnO_2	75	5	100	120	90	118
MoO_3	200	250	600	120	80	119
WO_3	30	500	63	88	37[#]	120
ZnO	28	10	135	130	1.7[#]	121

[#] Ra/Rg or Rg/Ra;

* Ra-Rg/Ra or Rg-Ra/Ra where Ra and Rg represent the values of sensor resistance in presence of air and target gas, respectively.

5.3.1.3.3 Comparison between different CDs-based sensors and sensing mechanism

The above data unambiguously demonstrated that C-CDs sensors can detect selectively NO. In a previous paper [99] we reported a study on the sensing characteristics of a conductometric sensor based on C-dots prepared from olive oil production waste coming from a different geographic origin (Puglia, Italy). The two sensors exhibit a very different sensing behavior, presenting a large and different sensitivity and selectivity towards the nitrogen oxides, NO and NO_2. To explain this behavior, we focused our attention on the surface characteristics of the two C-dots. Surface characteristics are very important in gas sensing, because the interaction between the gas and the sensing layer surface is mediated by the surface groups. Indeed, the gas-sensing mechanism of conductometric gas sensors is well known to be primary related to the adsorption/desorption and surface reaction of gases on surface groups [122-124].

FT-IR investigation provided information on the surface groups. Indeed, FT-IR analysis showed that C-CDs have a large signature attributed to presence hydroxyl groups, while the ether one prevails on P-CDs. Obviously, the band intensity is expected to change with the temperature, which is related to the different thermal stability of the surface groups. Then, to investigate the sensor surface in the same conditions under which operate the sensor, we carried out an in-situ ATR-FTIR investigation on the sensor platform (see Fig. 5.41).

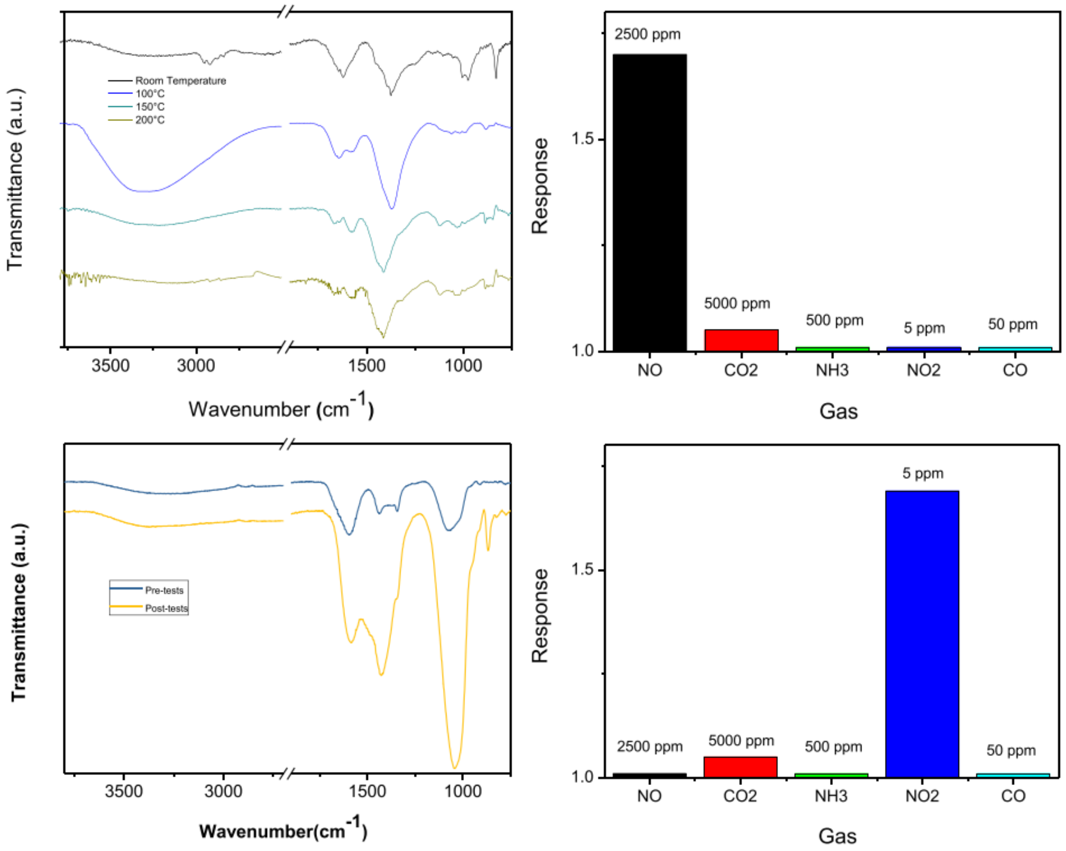

Figure 5.41. a) ATR-FTIR spectra and b) selectivity plot for the C-CDs sensor; c) ATR-FTIR spectra and d) selectivity plot for the P-CDs sensor.

By comparing the ATR-FTIR results collected at different temperatures (from room temperature to 200 °C), we could confirm that the two C-dots samples investigated show different functional groups. Interestingly, the differences noted at room temperature are retained at high temperatures (max. 200 °C). Another interesting aspect was highlighted by ATR-FTIR carried on the sensor devices after about months of functioning. Indeed, the ATR-FTIR patterns reported in Fig. 5.42 show clearly that the surface groups on CDs have undergone small changes, confirming the good stability of the sensing material in the operative conditions adopted.

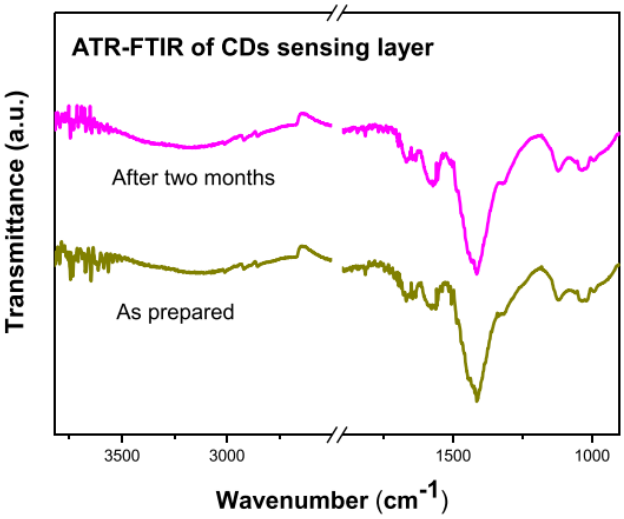

Figure 5.42. a) ATR-FTIR spectra for the C-CDs sensor as prepared and after a functioning period of about two months.

For a quantitative comparison about the sensing characteristics of the two sensors, we used the S= R_{NO}/R_{NO2} ratio, where R_{NO} and R_{NO2} is the response to NO and NO_2, respectively, at the concentration of 2500 ppm for NO and 5 ppm for NO_2. For the C-CDs sensor, the above ratio is very high (S > 23), while for sample P-CDs is around 0.1. These values clearly indicate that C-CDs sensor is selective to NO, while P-CDs is selective to NO_2.

Our data reported above indicate that ether and hydroxyl are the main functional groups presents on C-CDs and P-CDs surface, respectively. The presence of these functional groups in other carbon nanomaterials such as CNT, graphene or GO provides the active defect sites for the adsorption of nitrogen oxides, which has been related to the improvement of the binding and charge-transfer properties [125]. In a computational study, Salih *et al.* [126], explored the interaction of nitrogen oxides with graphene nanoribbons differently functionalized on the surface. The results of this study indicate that ZGNR-OH is the most selective to NO gas. Instead, ZGNR-O-OH can be considered as promising gas sensors for NO_2. Tang *et al.* reported a density functional calculations study on the adsorption of nitrogen oxides on graphene and graphene oxides [125]. These predictions are in accordance with experimental data here reported. In addition, Arunragsa *et al.* reported computational calculations which confirmed the hypothesis that the OH functional group was a major contributing factor to the

NH_3 sensitivity and selectivity on graphene quantum dots (GQDs) modified via edge functionalization [127]. Another example illustrating the structure-activity relationship of surface OH groups during NO_2 reaction on TiO_2 and the generation of nitrogen-containing species has been reported by Liu *et al.* [128].

Based on the above literature reports and our gas sensing results, a schematic representation of the gas sensing mechanism in these CDs sensors is illustrated in Fig. 5.43.

The main pathway to be highlighted is the chemisorption of target gaseous molecules (NO, NO_2) on CDs and the subsequent interaction with the surface groups. Indeed, the interaction of nitrogen oxides with these functional groups results in the formation of different chemisorbed species. These intermediates can further react with the adsorbed oxygen species, explicating the transduction function. Based on the previous computational studies, the charge transfer per NO_2 increases as the number of hydroxyl group decrease, suggesting that the P-CDs sensor will increase the sensor response to this gas, as observed experimentally. The opposite behavior observed on C-CDs sensor, leading to prominent NO selectivity, agree with this view.

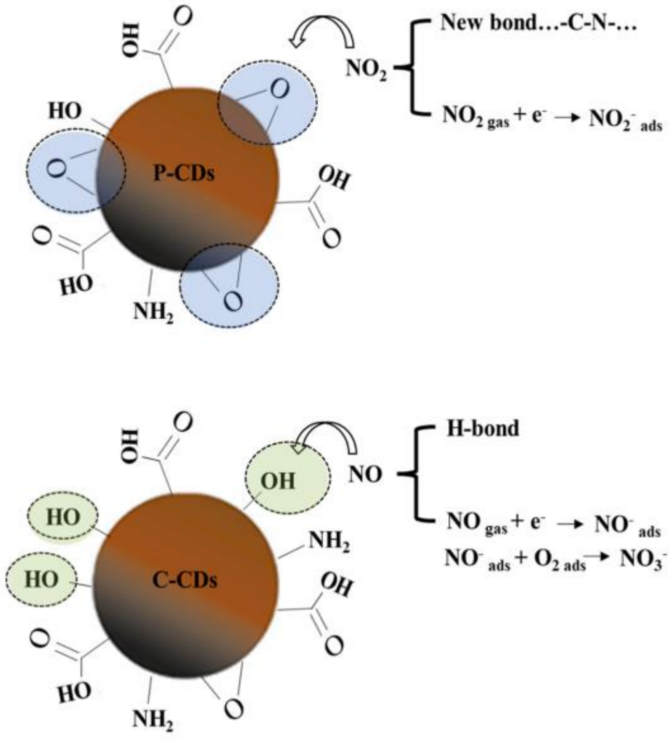

Figure 5.43. Schematic representation of the NO and NO_2 sensing mechanism on C-dots sensors.

5.3.1.4 Conclusion and final remarks

In this work, we focused our attention on the sensing properties of conductometric platforms based on C-dots, acting as sensing layer for common gas pollutants, such as NO and NO_2. Comparing the sensing properties of C-dots coming from olive waste of different geographic origins, we observed opposite sensitivity and selectivity towards these gases, which has been explained by the presence of different functional groups on the surface of these CDs. We believe that developing controllable synthetic and production methods, will greatly extend the application of CDs-sensors for other target gases. Establishing structure to property relationships in CDs will enhance understanding the gas sensing mechanism of CDs-based materials. For the practical application of these sensors, however, some issues need to be still addressed, such as the effect of humidity on the long-term affordability and stability.

5.4 Sensing material *via* Atomic Layer Deposition (ALD) method:

5.4.1 Gas sensing properties of CNT/WS_2 Core-shell Heterostructures

Overview: The report is a part of one of the applications of the CNT/WS_2 core-shell heterostructures relative to the gas sensing. The complete work is **under review:**

R. Zribi, Simona Crispi, Daniele Giusi, Medet Zhukush, Claudio Ampelli, Chengxu Shen, Muhammad Hamid Raza, Nicola Pinna, Giovanni Neri, *Gas Sensing and Electrochemical Properties of CNT/WS_2 Core-shell Heterostructures.*

Abstract: A CNT/WS_2 core-shell heterojunction was obtained by atomic layer deposition (ALD) through the growth of tungsten disulfide (WS_2) layers with different thicknesses on carbon nanotubes (CNTs). The deposition of different layers of WS_2 was followed with transmission microscopy (TEM). Characterization demonstrated conformal growth as small platelet flakes on CNTs at low ALD cycles while, with increasing number of ALD cycles, WS_2 platelets grow further to form a continuous film. The electrical properties of the synthesized CNT/WS_2 heterostructures were evaluated for sensing applications. A CNT/WS_2 conductometric sensor was developed for nitrogen dioxide (NO_2) gas sensing monitoring. The gas sensing results were correlated to the morphology and surface coverage of the WS_2 shell on the core of the CNTs. CNT/WS_2 with 200-300 cycles ALD demonstrated the best performance due to the optimal catalytic properties of WS_2 and the formation of CNT/WS_2 junctions, enabling sensitive and selective gas detection with a minimum limit of detection 70 ppb (LOD) at an operating temperature of 150°C.

5.4.1.1 Introduction

Carbon nanotubes (CNTs) have emerged in recent years as an extraordinary class of nanomaterials due to their unique physical, chemical, optical, electrical, electrochemical and magnetic properties [129]. In many applications, they are also used to support the active phase(s), dispersed/coated on them, or typically form a shell layer [130-135]. The functional properties of the shell layer depend on the shape and morphology of the active phase, as well as the thickness and distribution of the substrate play a fundamental role [136]. The properties of CNTs are closely related to the coating method used, therefore studies are focused on the development of methods for the preparation of CNT/shell layers [137,138]. Among the reported chemical-physical methods, atomic layer deposition (ALD) is a method that allows obtaining compliant and homogeneous coatings of CNTs with high control over the thickness of the deposited layers [139,140]. Adjusting the thickness of the active shell layer gave the possibility to verify a clear structure-property relationship [133,137].

In this study, CNT/WS_2 core–shell heterostructures were synthesized by ALD, depositing different thicknesses and obtaining different WS_2 shell morphologies. Tungsten disulfide (WS_2) belongs to the class of 2D-TMD nanomaterials (transition metal dichalcogenides), characterized by a large surface-to-volume ratio, confined atomic thickness and peculiar electronic properties [141]. Functionalizing/coating the surface of CNTs with active layers of WS_2 has proven to be a promising way to improve performance [142]. It has shown great promise as a sensing material for the development of conductometric sensors [143,144]. The gas sensing properties of core CNTs/shell metal oxides have been extensively studied in the past by our group, and the performance is very relevant to the thickness of the shell layers [131-135].

Therefore, in this work, the sensing characteristics of the new CNT/WS_2(X) nanostructures on NO_2 detection were first performed by evaluating the conductometric platforms at the operating temperature of 150 °C. Gas sensing properties on carbon-based nanostructures are enhanced by the presence of WS_2 layers due to the ability to charge carrier concentration on the adsorption of gaseous molecules [145]. In literature, a particular sensitivity of heterojunction for NO_2 is demonstrated. NO_2 is a toxic gas produced by industrial plants, house boilers, and auto vehicles. Therefore, NO_2 is mainly found in the ambient city air and harms the environment and people. Thus, monitoring NO_2 at ppb levels is highly demanding [146].

In the literature, there are no CNT/ WS_2 core-shell heterostructures with different WS_2 layer thicknesses prepared by ALD that have been applied to study their electrical characteristics. By changing the thickness of the WS_2 layer, the performance in applications was optimized, shedding light on the effect of the thickness of the WS_2shell on the electrical properties of CNT/ WS_2 core/shell heterostructures.

5.4.1.2 Experimental section

5.4.1.2.1 Chemical

Carbon nanotubes were purchased from Applied Science Inc. All gases of 99.99% purity used in the ALD process were supplied by Air Liquide. The bis(t-butylimido)bis(dimethylamino) tungsten(VI) precursor (BTBMW, >97%) was supplied by Strem Chemicals, and the H_2S precursor (>99.5%) was purchased from Air Liquide. Phosphate buffer solution, PBS pH 7.4, was used. All chemicals and reagents were used without further purification.

5.4.1.2.2 Synthesis of CNT/WS_2 nanostructures by ALD

Carbon nanotubes (CNTs) were functionalized as described in previous work [131-133, 138, 139]. 10 mg of dried powder (80 ºC overnight) was dispersed in 2 mL of ethanol by ultrasonication (30 minutes) and drop-cast onto aluminum foil for deposition of ALD-WS_2. The WS_2 films were deposited in our home-made ALD system at 300 ºC with the established process [146]. The precursor BTBMW (maintained at 80 ºC) and H_2S were the precursors [147]. The thickness of the WS_2 layer was controlled by changing the number of ALD cycles, and the samples were named CNT/WS_2(X), where X represents the number of ALD cycles.

5.4.1.2.3 Physical characterization

High-resolution transmission electron microscopy (HRTEM) was carried out at an operation voltage of 200 kV on a FEI Talos F200S. X-ray diffraction (XRD) patterns were recorded on a STOE Stadi MP Diffractometer with Mo Kα1 radiation source (λ = 0.7093 Å).

5.4.1.2.4 Gas sensing tests

Sensing tests were performed with sensors fabricated by printing a layer (10–30 μm thick) of the 1 mg CNT/WS_2 sample dispersed in water on alumina substrates (6 mm × 3 mm) with a heating element and interdigitated Pt electrodes. The sensor devices were introduced in the test chamber, measuring the resistance through a multimeter (Agilent 34970A). An Agilent E3632A instrument was employed to bias the Pt heater of the sensor for measurements at high temperatures. The gas response, S, is defined as the ratio R/R_0 (for p-type behavior) and the ratio R_0/R (for n-type behavior), where R is the electrical resistance measured at different gas concentrations, and R_0 is the baseline resistance in dry synthetic air. To further investigate, the typical dynamic response time, τ_{res}, and recovery time, τ_{rec}, characteristics were measured according to their resistance. Response time, τ_{res}, i. e. the time required for the sensor to reach 90% of the saturation resistance after injection of the target gas, and recovery time, τ_{rec}, i. e. the time necessary for the sensor to reach 90% of the resistance baseline value in air, were also evaluated.

5.4.1.3 Results and discussion

5.4.1.3.1. Morphological and structural characterization

The morphological and structural characteristics of CNT/WS_2 composites were studied. The microstructure of the WS_2 shell was studied by X-ray diffraction (XRD). In Figure 6.44 we observe the peaks at 6.50°, 15.28°, 17.92°, 22.09°, 26.24° attributed to the (002), (101), (013), (015), (008) planes of the hexagonal phase of WS_2 based on the reference sheet COD 96-900-9146. The peak at 12° is attributed to the diffraction of the (002) plane of graphite carbon in CNTs (COD 96-101-1061). Furthermore, the diffraction peaks become sharper and more intense with the increase in the number of ALD cycles, indicating an increase in the amount of crystalline WS_2 deposited on the CNT substrates. This is also confirmed by the relatively intense ratio of reflection peaks between CNT and WS_2.

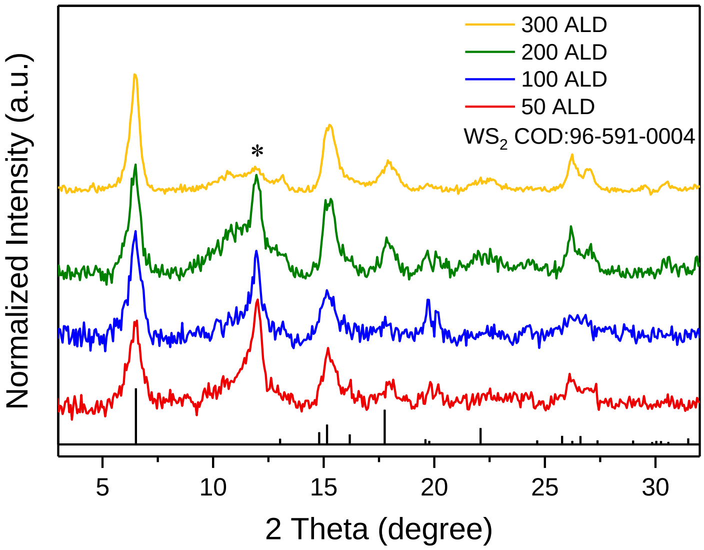

Figure 5.44. X-ray diffraction (XRD) patterns of CNTs/WS$_2$(X) composites with varying WS$_2$ ALD cycles from 50 to 300. Asterisks reflect the diffraction of the graphite carbon from the CNTs substrates.

The prepared CNTs/WS$_2$ (X) were characterized by high-resolution transmission electron microscopy (HR-TEM). In Figure 6.45 we observe a morphology characterized by a few flakes with a length of ~ 30 nm and a thickness of ~ 6 nm grown on the CNTs in the CNT/ WS$_2$ (50) sample (Figure 5.45a). However, these flakes are individual and distant from each other, exposing some surfaces that are not completely covered. With more ALD cycles increased to 100, the size of the flakes also increases, indicating a length of approximately 50 nm and a thickness of 10 nm (Figure 6.45a, b). Some of the flakes increased in size by incorporating those nearby. Instead, composites with more than 200 ALD deposition cycles depict a continuous WS$_2$ layer on the CNTs, showing a film thickness of ~10 nm for CNT/ WS$_2$ (200) and ~15 nm for CNT/WS2 (300) (Figure 5.45 c,d). In Figure 6.44e, clear lattice fringes are observed in HRTEM with a d spacing of approx. 0.7 nm is attributed to the (002) lattice plane WS$_2$.

According to the selected area electron diffraction (SAED) pattern is recorded from CNT/WS2 (200), suggesting that the deposited WS2 is polycrystalline (Figure 5.45f). A more detailed characterization of the heterostructures is already reported [146].

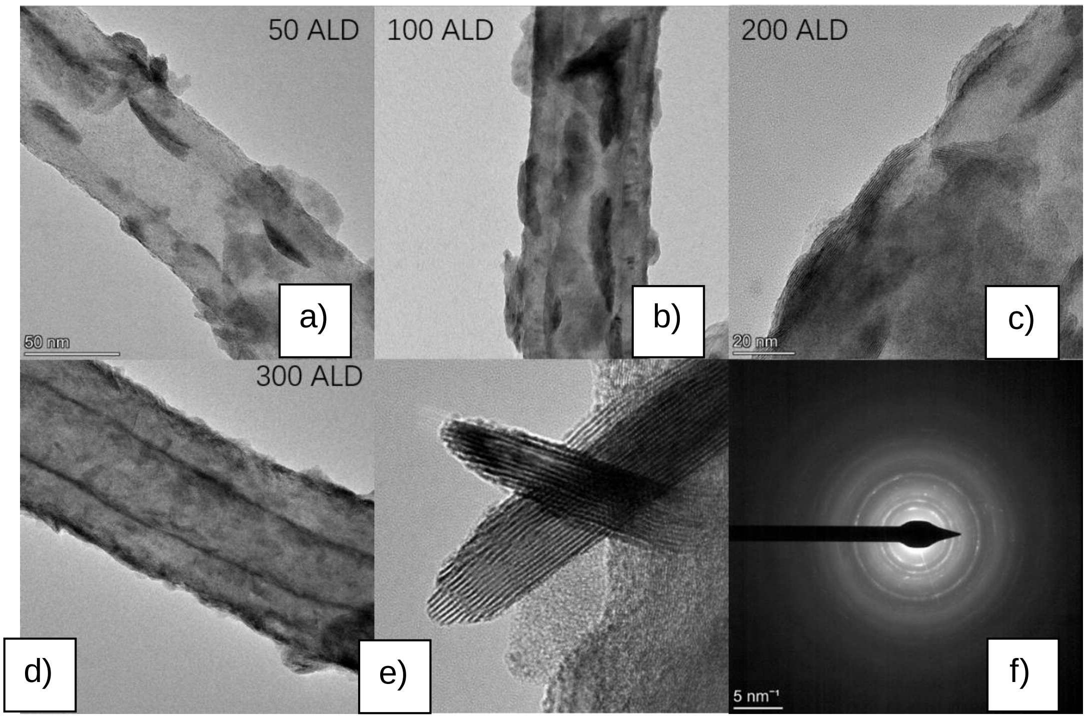

Figure 5.45. TEM images of CNTs/WS_2(X) composites with (a) 50, (b) 100, (c) 200 and (d) 300 ALD cycles of WS_2. (e) HR-TEM image of the grown WS_2 flakes and (f) SAED pattern of the prepared CNTs/WS_2(X) sample.

5.4.1.3.2 Electrical characterization

The prepared CNT/WS_2(X) nanocomposite samples were evaluated to assess their electrical characteristics. Tests were performed with the conductometric platform used for the successive sensing experiments, so the information obtained could be directly used for optimizing their performances. The electrical properties of samples have been evaluated in the range of 50-150 °C (Figure 6.46). CNTs used show resistance in the range of 80-100 ohm and as expected for its semiconductor behavior, the electrical resistance decreases with increasing the temperature.

Usually, the resistance of CNT/WS_2(X) sensors should increase compared to the bare CNTs due to the low intrinsic conductivity of WS_2 and the formation of WS_2-WS_2 contacts. However, the prepared CNTs/WS_2(X) resistance values are almost like those measured for bare CNTs. This finding can be explained by considering that the shell layer is not homogeneous, so CNT-CNT contacts of high conductivity are still present, as confirmed by transmission electron microscopy images (Figure 5.44, HRTEM).

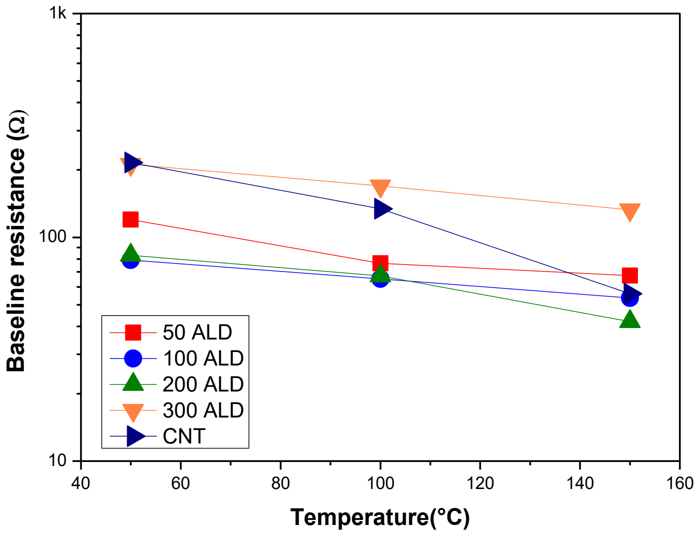

Figure 5.46. Electrical resistance of the samples in nitrogen as a function of temperature.

5.4.1.3.3. Gas sensing behavior

For the gas sensing tests of CNT/WS_2(X) sensors, NO_2 was selected as the target gas. The dynamic of the sensor signal over time of the CNT/WS_2(X) sensors to the target gas at the temperature of 150 °C is highlighted in Figure 5.47 a,b. The sensors exhibit an acceptable recovery time and a reversible decrease of the resistance when the NO_2 pulse was pulsed in the measurement chamber (Figure 5.46a). In particular, the response and recovery time calculated is approximately 300 s and 800 s, respectively, measured at a concentration of 2.5 ppm. The baseline has been found relatively stable at the operating temperature of 150 °C and the signal response. Moreover, CNT/WS_2(X) sensors exhibit typical *p-type* behavior, as reported for different WS_2 sensors in the literature [148]. The sensor calibration, reporting the response of the CNT/WS_2(100) sensor at different NO_2 concentrations in a log-log plot, is shown in Figure 5.47c. By extrapolating data at NO_2 concentration from 500 ppb to 8 ppm, a limit of detection of about 70 ppb has been proposed. The selectivity of the sensor was at last verified by evaluating the response to different interferent environmental gases, i.e. CO_2, NH_3, NO_2, and CO. The sensor shows a high response to NO_2 compared to other gases (see Figure 5.47d).

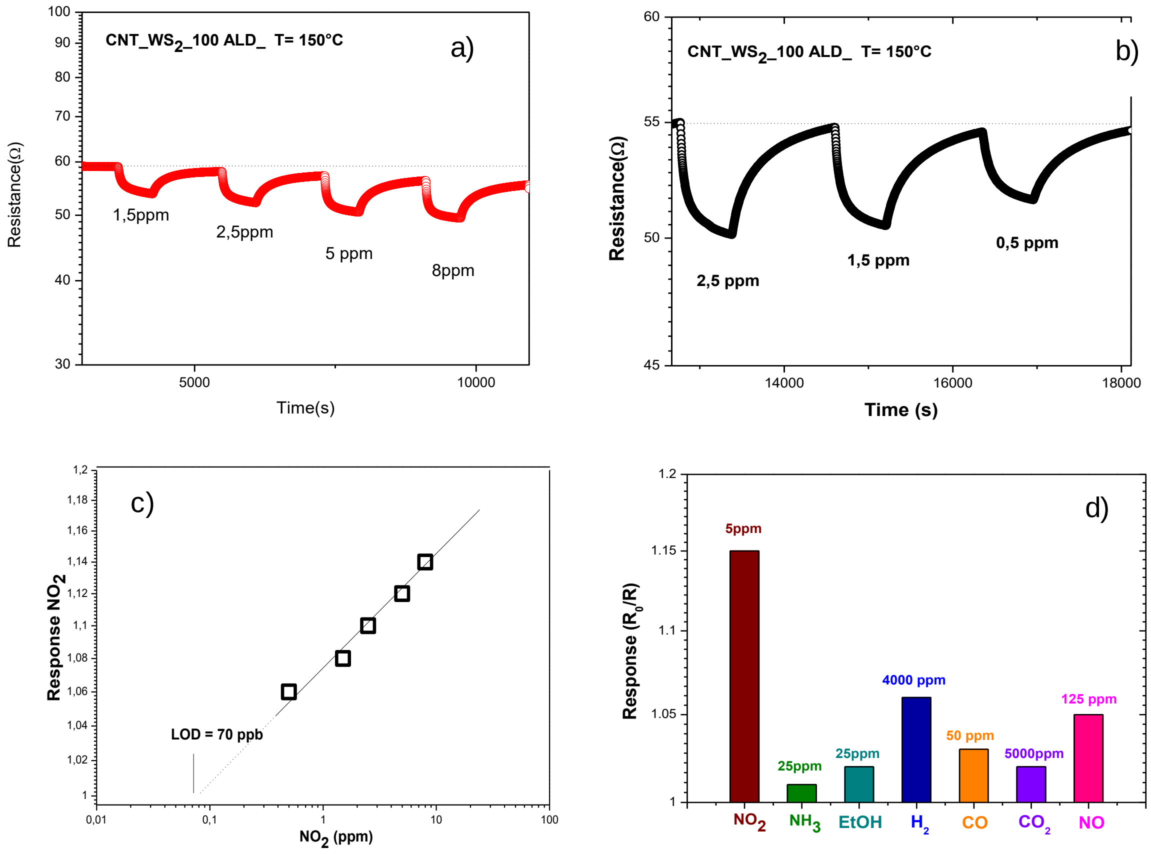

Figure 5.47. (a, b) Response at different concentrations of NO_2 of the CNT/WS_2(100) sensor at the operating temperature of 150 °C; (c) Calibration curve in log-log scale; (d) Response of the CNT/WS_2(100) sensor to different gases.

Figure 5.48 compares the response of the sensors fabricated with pristine CNTs and the CNT/WS_2(X) heterostructures with varying thicknesses of the WS_2-shell layer toward NO_2 (5 ppm). The trend observed shows the typical behavior previously reported by us for CNTs/metal oxide-based sensors [131, 133], irrespective of the metal oxide (SnO_2, TiO_2, NiO) or target gas (H_2, ethanol, acetone) used. The response increased as the ALD cycles increased up to 300 cycles (about 15 nm WS_2 shell thickness) The results reported here confirm that the metal disulfide shell thickness is a critical parameter for the design of the core-shell heterostructures-based conductometric sensors.

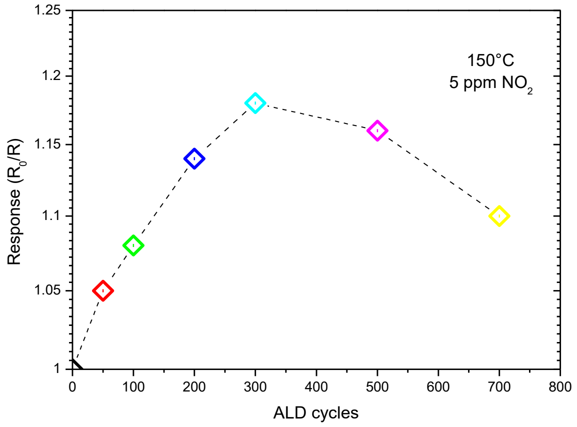

Figure 5.48. Sensing response to 5 ppm of NO_2 in air of the CNT/WS_2 nanostructures towards NO_2 as a function of the ALD cycles.

Results can be explained, considering that, initially, WS_2 grows on the CNTs like small platelets/flakes, and CNTs are not fully covered with WS_2. With increasing the number of ALD cycles, WS_2 platelets/flakes grow in size, and covering density and the coverage of the CNT surfaces increase. The full coverage of CNTs with a continuous film of WS_2 started occurring at approximately greater than equal to 200 ALD cycles and continued on the samples with the larger ALD cycles (CNT/WS_2(700)).

5.4.1.3.4 Effect of WS_2 shell layer on electrical performances

In this section, we try to give an overall explanation of the electrical behavior observed. In fact, many studies reported improved responses of metal oxides (MOX) gas sensors by preparing CNTs/metal oxides heterostructures. The experimental results show that there is a correlation between the metal oxide shell thickness (i.e., the number of ALD cycles) and their gas sensing response. Specifically, a volcano curve with a well-defined maximum has been observed, plotting the sensor response vs. the shell thickness. This behavior was explained to be linked to the width of the depletion layer [149]. Indeed, the highest sensing response of the core-shell metal oxide/CNTs sensor was observed when the thickness of the MOX layer was comparable to the thickness of the depletion layer, i.e., a few times the Debye length (λD). In these conditions, the shell layer is in the space-charge-region, and the charge conduction in the metal oxide shell layer is dominantly perturbed by the oxygen species and/or target gas chemisorbed at the surface, leading to a large resistance (conductance) variation. We believe that the same mechanism occurs with the new CNT/WS_2(X) composites investigated in this study. Tests are planned with CNT/WS_2(X) composites having a larger number of WS_2 ALD cycles, to determine the optimal thickness of the WS_2 layer at which the large resistance (conductance) variation occurs.

5.4.1.4 Conclusions

CNT/WS_2 core-shell heterostructures were prepared by atomic layer deposition (ALD) of tungsten disulfide (WS_2) on carbon nanotubes (CNTs). The WS_2 shell layers showed different thicknesses and morphology depending on the number of ALD cycles. The ALD-fabricated CNT/WS_2 core-shell heterostructures have performed in gas sensing application. Their gas-sensing behavior was tested for the monitoring of NO_2. The tests made it possible to demonstrate that the electrical properties of CNT/WS_2 core-shell heterostructures are strongly dependent on the thickness of the WS_2 shell layer. Among CNT/WS_2 core-shell heterostructures, those having a WS_2-shell thickness in the range from 10 to 15 nm showed superior electrical capabilities.

5.4.2 Gas sensors of mesoporous $NbTiO_2$ thin film modified by NiO shell-layer

Abstract: Mesoporous titania (M-TiO_2) was synthesized as pure and Nb-modified thin film. The core mesoporous structure was also coated with a NiO shell layer through Atomic Layer Deposition (ALD). A detailed morphological and microstructural characterization of the films was carried out by TEM analysis. Gas sensors based on the pure M-TiO_2 and modified Nb-TiOx/NiO Nb-TiOx/NiO layers, were developed using a conductometric platform with interdigitated Pt electrodes. The sensors with modified layers demonstrated improved sensitivity to reducing gases, specifically to acetone and ethanol, compared to pure M-TiO_2.

5.4.2.1 Introduction

Although in recent years many different semiconductor nanomaterials have been proposed as sensitive material for gas sensors, metal oxides remain the most investigated because of the low cost and excellent performances. Titania (TiO_2) is n-type semiconductor with a wide-band gap of 3.0-3.2 and excellent photocatalytic and sensing performances, such as good sensitivity, short response/recovery time, good chemical stability, in addition to the low cost [150,151]. The gas sensing properties of TiO_2 are largely recognized [152-155].

The structure of the sensing layer is an important factor affecting the sensing properties. The mesoporous structure allows for a high surface area/volume ratio [156] and greater ability to promote mass transfer kinetics [157]. Mesoporous TiO_2 architectures have recently attracted a renewed interest in both fundamental and applied materials research [158].

To improve the characteristics of metal oxides, doping and/or addition of another metal oxide, forming a binary or ternary composite, have been proposed. In this paper we have investigated mesoporous titania (M-TiO_2) films. The M-TiO_2 films were modified doping it with niobium (Nb) and coating the mesoporous structures with nickel oxide (NiO) to form core/shell structures.

Incorporating the aliovalent ions (such as Nb^{5+}) into the TiO_2 structure, is a way to enhance the conductivity which is attributed to an increase in donor density. Substitution of Nb^{5+} for Ti^{4+} introduces additional charge carriers, which increase the low bulk conductivity of

TiO_2. Wang *et al.* reported that the conductivity of Nb-doped mesoporous TiO_2 was more than two orders of magnitude higher than that of undoped TiO_2 [159].

To permit a facile fabrication and reproducibility of the sensor, M-TiO_2 and Nb-doped M-TiO_2 films have been synthesized *via* dip-coating method directly on the conductometric platform having a heating element and a pair of Pt interdigitated electrodes. [153]. Nb-doped M-TiO_2/NiO core-shell layers have been also formed *via* Atomic Layer Deposition (ALD) on the sensor platform. The developed sensors were tested for gas sensing of reducing gases.

The nanomaterials obtained exhibited a high selectivity to acetone. Acetone is a widely used chemical compound belonging to the class of Volatile Organic Compounds (VOC) as it is composed of a carbon atone (C) and hydrogens (H), the correct IUPAC name is propanone. Acetone is a solvent widely used in industry and is found in many household products. It has a molecular weight of 58.08 g/mol, a density of 0.79 g/cm^3 at 20 °C and an odor intense. However, it can be easily inhaled, causing serious effects on human health. In fact, it is estimated that concentrations of acetone above 173 ppm can seriously affect the central nervous system and damage important organs of the body [160]. Instead, long-term exposure causes damage to the eyes and nose [161]. For these reasons, a professional threshold limit value for acetone was defined as 250 ppm, considering a time-weighted average of 8 hours [162]. In addition to the negative effects on the human body, it is a flammable substance with a low explosive limit (LEL) of 2.6% and an upper explosive limit (UEL) of 12.8%. The human body itself generates VOCs due to ingestion of food and/or environmental exposure. In fact, exhaled human breath includes approximately 3500 different VOCs [163] and the analysis of VOCs in breath gas can be used as a non-invasive tool for a simple health check that can be conducted both at home and in a medical facility for medical diagnoses and to monitor the success of a therapy [164,165].

In this specific case, acetone is considered an important biomarker of type 1 diabetes. It has been reported that the exhaled breath of diabetic people contains an acetone concentration value > 1.8 ppm compared to healthy people (0.3-0 .9 ppm) [166]. Therefore, monitoring breath acetone can be considered a useful way to monitor diabetic patients [167]. Furthermore, its monitoring can be used for insulin management as there is a correlation between acetone and blood glucose level. As discussed, it explains the importance of developing gas sensors for acetone.

Designing a specific sensor for acetone is not easy as there can be various interfering gases, one of these is ethanol. Therefore, the nanomaterials discussed in this work allow us to explain the possibility of making a sensor more selective to acetone rather than ethanol.

5.4.2.2 Experimental section

5.4.2.2.1 Synthesis of $NbTiO_2$ mesoporous

$NbTiO_2$ mesoporous have been synthesized by according to the procedure described by Marvin *Frisch et al.* [153]. In brief, the precursors $TiCl_3$ and $NbCl_5$ (molar ratio of 35% Nb) were dissolved in EtOH with the formation of metal ethoxides, and a tri-block copolymer PEO-PPO-PEO was used a soft-template to obtain the porosity. The growth of film was obtained *via* dip-coating method on the conductometric platform in air at 45°C. Afterwards, it was calcined at 600°C for 30 minutes. In Figure 5.49 the diagram of the procedure.

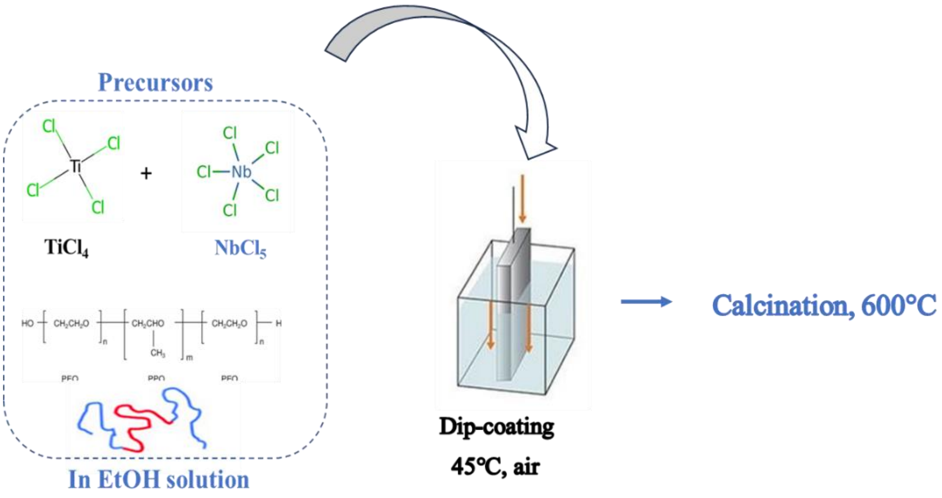

Figure 5.49. Schematic synthesis of $NbTiO_2$ mesoporous.

5.4.2.2.2 Synthesis of $NbTiO_2$/NiO nanostructures by ALD

The deposition of NiO films of different thicknesses on the conductimetric platform (with $NbTiO_2$ mesoporous deposited) were obtained by a commercial thermal ALD system by ARRADIANCE, GEMSTAR-6. Before the ALD process, the instrument was set. The baseline pressure was maintained at approximately $2,17x10^{-2}$ mbar and a 10 sccm of argon mass flow. Si wafers (Siegert wafer B014002, single side polished) were put into the ALD chamber with the sensors as reference to see the thickness. Before to put into the chamber, the Si wafers were cleaned in piranha solution, ethanol, isopropanol, and deionized water followed by nitrogen blow drying and the thickness were calibrated by spectroscopic ellipsometry (SENpro SENTECH) of 70° incidence's angle.

The NiO was obtained using bis-(cyclopentadienyl) nickel, nickelocene [Ni(Cp)$_2$], and 20% ozone (O$_3$) as metal precursor and oxygen source. The temperature of the Ni (Cp)$_2$ container was maintained at 90 °C for the low vapor pressure of nickelocene and 200 °C for the reaction chamber. According to the instrument mechanism of pulsed-vapor-push (PVP) technique to boost the precursor into the chamber, the pulsing/exposure/purge time for nickelocene and ozone was adjusted to 2 s/30 s/20 s and 0.5 s/20 s/30 s, respectively. The thicknesses of the NiO deposited layers were controlled by varying the number of ALD cycles as 5-50-100-150-200 cycles.

5.4.2.2.3 Physical Characterization

High-resolution transmission electron microscopy (HRTEM) was carried out at an operation voltage of 200 kV on a FEI Talos F200S. X-ray diffraction (XRD) patterns were recorded on a STOE Stadi MP Diffractometer with Mo Kα_1 radiation source (λ= 0.7093).

5.4.2.2.4 Gas sensing tests

The gas sensing tests were carried out with sensors fabricated by ALD of the nanomaterials is deposited directly on device that had a heating element and Pt electrodes. In the tests, the sensor devices were introduced in the test chamber and the resistance was measured with a multimeter (Agilent 34970A). An Agilent E3632A instrument was employed for measurements at high temperatures. The gas response, S, is defined as the ratio R_0/R for n-type behavior, where R_0 is the baseline resistance in dry synthetic air and R is the electrical resistance measured at different gas concentrations. Typical dynamic response time, τ_{res}, and recovery time, τ_{rec}, characteristics were measured according to their resistance. Response time, τ_{res}, i. e. the time required for the sensor to reach 90% of the saturation resistance after injection of the target gas and recovery time, τ_{rec}, i. e. the time necessary for the sensor to reach 90% of the resistance baseline value in air, were also evaluated.

5.4.2.3 Results and discussion

5.4.2.3.1 Morphological and structural characterization

SEM and TEM characterization have been carried out for NbTiOx samples. In Figure 5.50 is shown the mesoporous morphology.

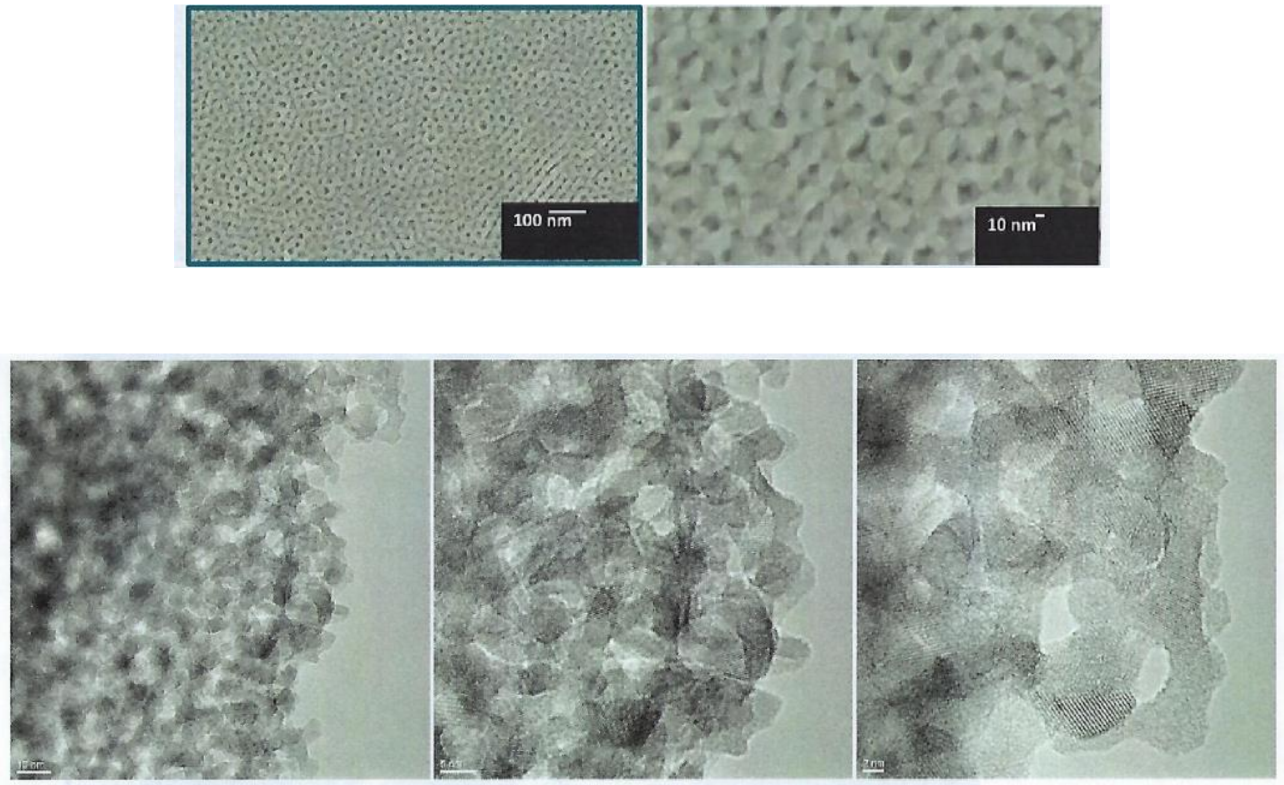

Figure 5.50. SEM and TEM analysis of the synthesized mesoporous titania.

5.4.2.3.2 Electrical characterization

The electrical properties of the sensors developed by the ALD method were verified evaluating the baseline resistance in dry air at different temperatures. In Figure 5.51, the electrical properties of pure m-TiO_2 and that Nb-doped are compared. Tests have confirmed that the addition of the dopant decrease the baseline resistance compared to the pure M-TiO_2. The results agree with computational studies found in the literature, which demonstrate an increase of the conductivity of more than three orders of magnitude. Mulliken population analyses have demonstrated an increasing occupation of Ti 3d-orbitals resulting in an increase in crystallinity. Also, the presence of Nb ions into the titania lattice enhances the stability of the porous network [153].

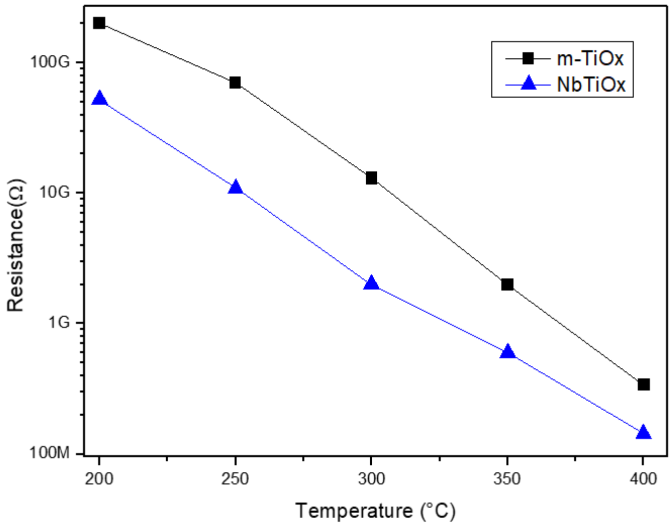

Figure 5.51. Baseline resistance in dry air of m-TiO_2 pure and $NbTiO_2$ sensors in a range of temperatures from 200 to 400°C.

Subsequent tests were carried out on core-shell Nb-M-TiO_2/NiO sensors to investigate the baseline resistance change with the addition of NiO layer. As expected, NiO thickness influence the baseline resistance (Figure 5.52). First, a strong decrease was observed for a very low thickness (2.60 nm) of NiO shell obtained with only 5 ALD cycles. A further increase of resistance is observed with the increase of the NiO shell thickness.

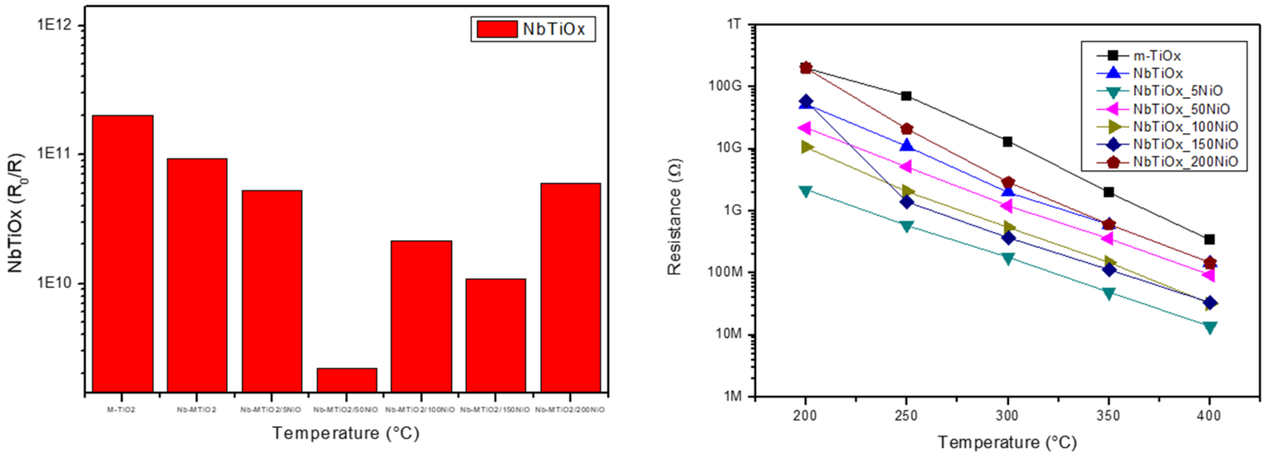

Figure 5.52. Comparison of baseline resistance in dry air of all sensors: m-TiO_2 pure, NbTiOx, NbTiOx_5NiO, NbTiOx_50NiO, NbTiOx_100NiO, NbTiOx_150NiO and NbTiOx_200NiO in a range of temperatures from 200 to 400°C.

NiO is a p-type semiconductor with a bad gap of 3.50 eV [168] with high bonding strength holding the ions [169], and this determines its high electrical resistance. Literature data report that on NiO thin films, having a thickness comparable to Debye length, low resistance is observed, given by a high contribution of holes as charge carriers in contrast to NiO thicknesses greater than Debye's length [170]. The phenomenon, shown in Figure 5.53, helped to explain why low resistances are observed at low NiO thicknesses in contrast to high thicknesses where resistance increases with increasing thickness.

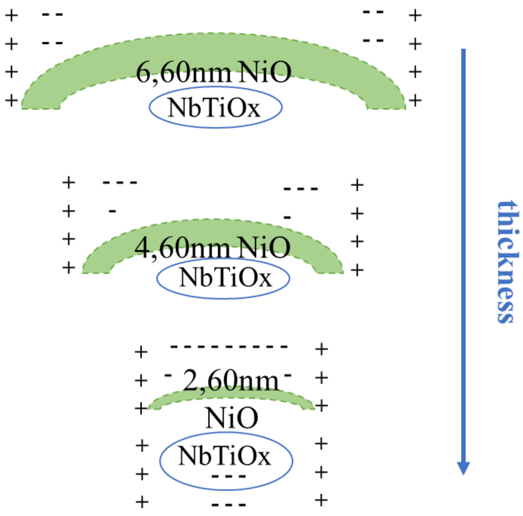

Figure 5.53. Debay mechanism as a function of the NiO thickness.

5.4.2.3.3 Gas sensing behavior

Subsequent tests were then devoted to investigating the behavior of the sensors exposed to various gases. Preliminary, was ascertained the greater sensitivity of sensors to reducing gases respect to oxidizing ones. So, the sensitivity to ammonia (NH_3), formaldehyde (HCHO), ethanol (EtOH) and acetone (C_3H_6O) chosen as representative reducing gases was tested at the operating temperature of 400°C and to the same concentration of 40 ppm is observed in Figure 6.54. Aggregated data obtained from the sensing tests indicate some interesting features: 1) the modified sensors display larger response compared to pure M-TiO_2 sensor; 2) the sensor response to the different gases for the Nb-M-TiO_2/NiO is core-shell sensor is a function of the thickness of NiO shell layer; 3) acetone gas shows the higher response compared to the other investigated gases. These findings are important because give us the opportunity to modulate the sensing performances of the sensor towards the desired gas to detect and also to obtain the better conditions for a selective sensing.

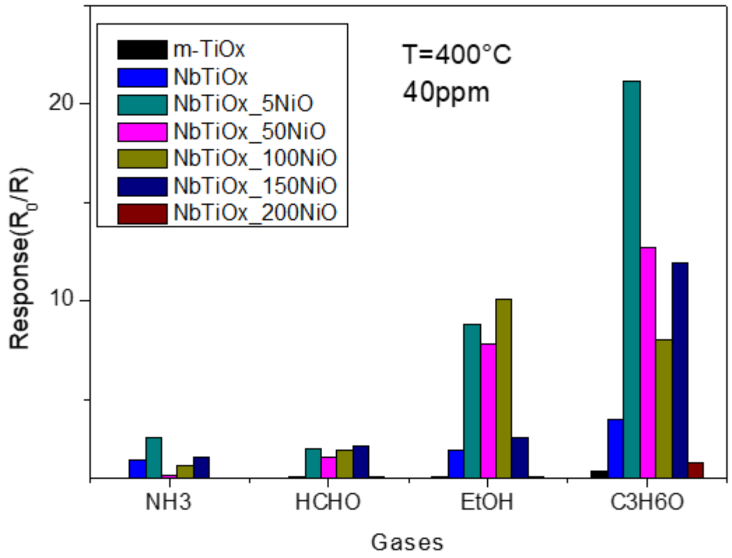

Figure 5.54. Sensitivity of sensors to 40ppm of the reducing gases as NH_3, HCHO, EtOH and C_3H_6O, at 400°C.

The increased performances of mesoporous titania due to Nb and NiO allow to modulate the selectivity to the observed gases, in fact greater sensitivities are observed for ethanol and acetone compared to ammonia and formaldehyde. The increased sensitivity to

EtOH and Acetone is closely related to the charge carriers of the nanocomposite and to the charge transfer of the gases. The Nb/TiOx/NiO composite is an n-type semiconductor, interaction with reducing gases results in a decrease in resistance followed by an increase in conductivity. In the specific case, the interaction of gases such as EtOH and Acetone with the surface favor a greater electron transfer and increases the number of free electrons on semiconductor surface. Other tests in Figure 6.55a and b have concentrated on verifying the sensitivity of the sensors to EtOH and Acetone when subjected to a temperature range from 200 to 400°C in dry air. According to the data found, the presence of Nb, the thickness of the NiO and the temperature influence the selectivity to the two gases. Evaluating the reference sensors, uncoated m-TiOx and NbTiOx, a higher sensitivity to Acetone is observed in both, which increases with the presence of the Nb dopant. A greater selectivity to Acetone is observed for the sensor NbTiOx at low NiO cycles (5 cycles of 2.60 nm thickness) at the operating temperature of 300°C.

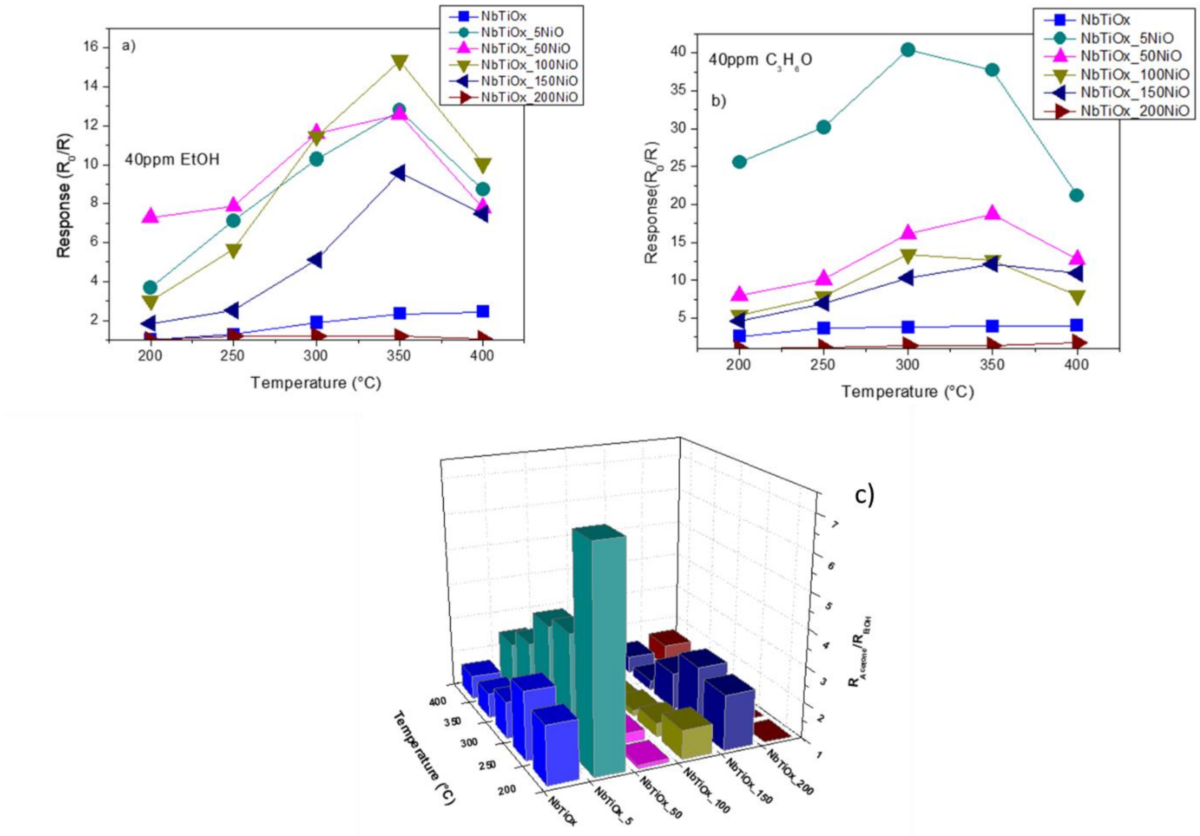

Figure 5.55. Response of the tested sensors to a) ethanol and b) acetone at different temperatures. C) 3-D graph summarizing the relative response $R_{Acetone}/R_{Ethanol}$ vs. the temperature for all tested sensors.

Focusing on the NbTiOx/5NiO sensor, the dynamic response to different concentration of Acetone and EtOH is shown in Figure 5.56 a, b). The sensor shows similar dynamic characteristics for both gases, i.e. 28s/170s for Acetone and 33s/175s for EtOH as response/recovery time, respectively. Figure 5.55c reports the response *vs* concentrations curves for both gases, showing the higher sensitivity of the sensor for Acetone.

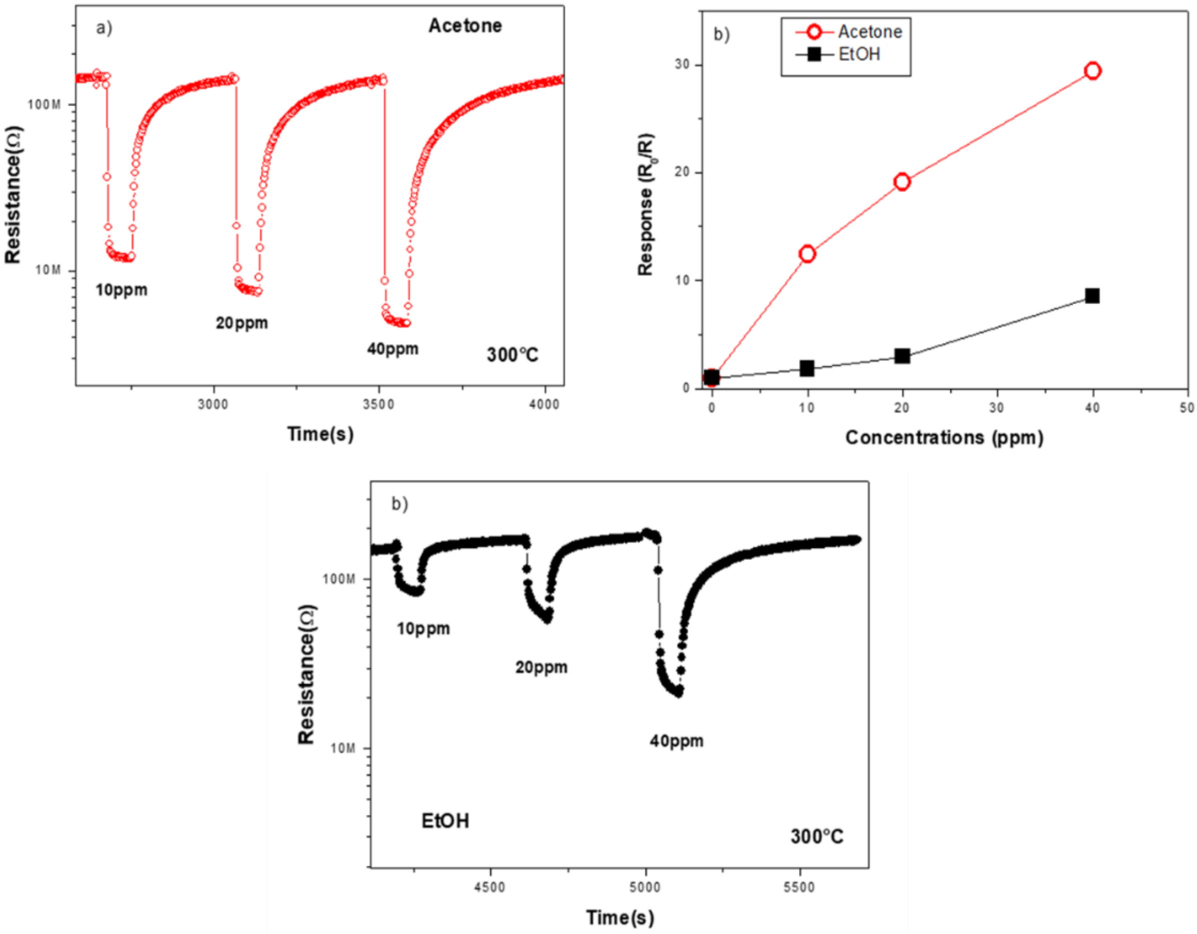

Figure 5.56. NbTiOx_5NiO sensor: a) dynamic response with Acetone and EtOH like gases at different concentration; b) calibration curve at 300°C; c) calibration curves for Acetone and ethanol at 300°C.

The signal stability, memory effects, long term stability are all parameters to be take into account for the practical applications of the sensors. In Figure 5.57, the memory effect of the NbTiOx sensor was tested performing measurements at different increasing/decreasing concentrations of ethanol.

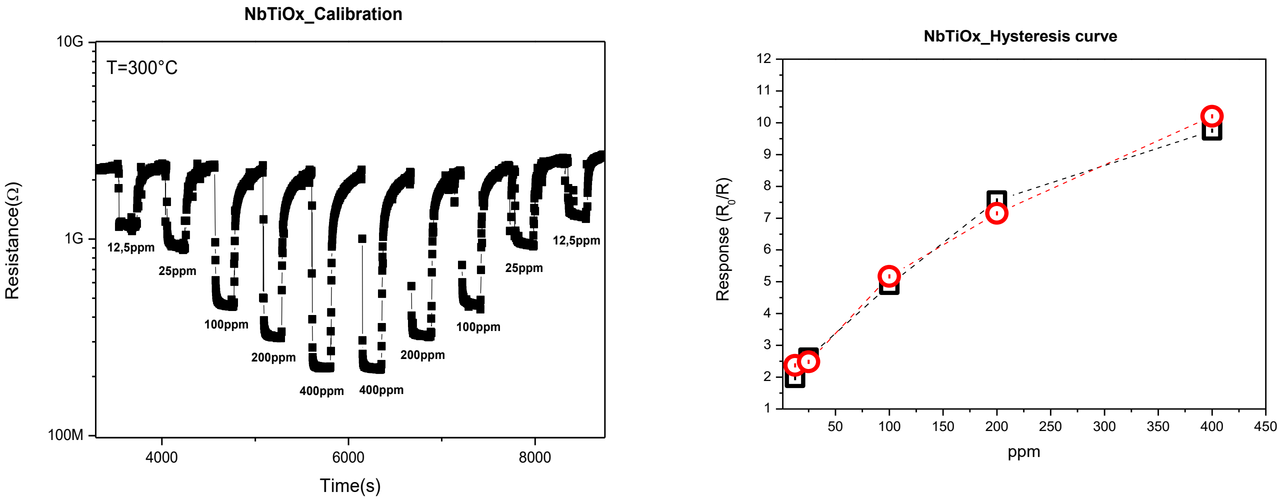

Figure 5.57. a) Dynamic response of NbTiOx sensor at different increasing/decreasing concentrations of EtOH; b) calibration curves.

The signal reproducibility is very good (Figure 5.58a). The sensor was also tested for a period of one month, and no drift phenomenon is observed (Figure 5.58b), indicating the good stability of the sensing layer.

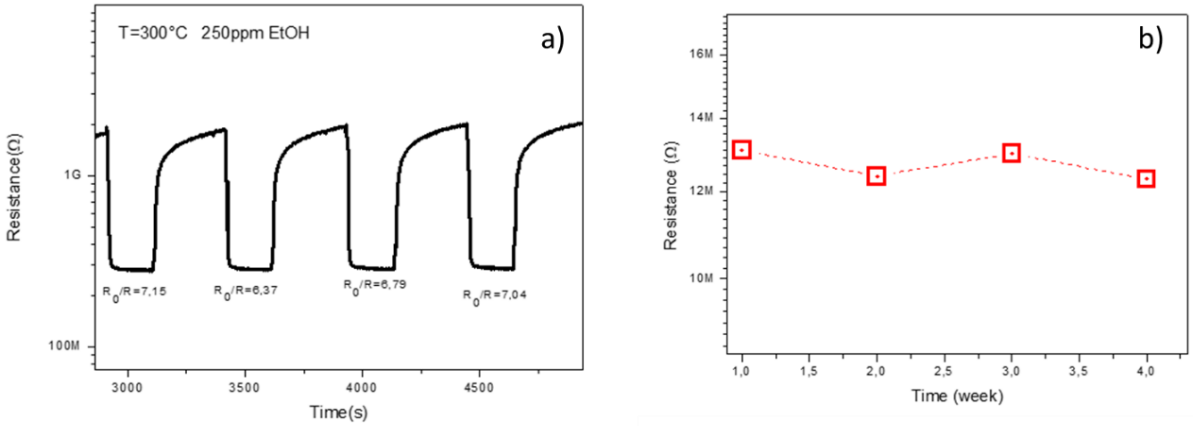

Figure 5.58. Stability of NbTiOx_5NiO sensor on time at 300° C.

Selectivity is another parameter that should not be neglected; an excellent selectivity of the sensor for acetone at 300°C is observed in the graph in Figure 5.59 when the sensor has been subjected to a mixture of gases of different concentrations.

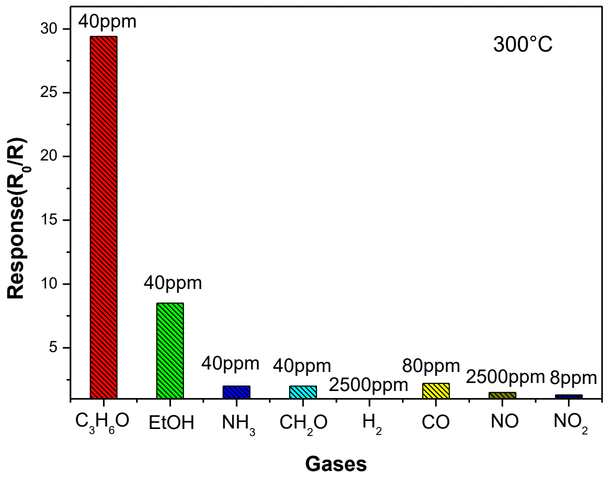

Figure 5.59. Selectivity tests of NbTiOx_5cNiO to different gases at 300°C.

To compare sensing data at all temperature for both acetone and ethanol is a way to define the best sensor and conditions with the highest selectivity towards acetone. NbTiOx_5cNiO sensor display a higher response towards acetone compared to ethanol, as demonstrated by the highest value of the R_{acet}/R_{eth}, at the temperature of 300 °C.

The sensitivity to gases mirrors what has been said for the electrical properties, a composite of NbTiOx with a thin coating of NiO in the interaction with gases an influence of the core and of the coating is observed favoring the interaction with acetone, a strongly reducing gas. A composite with high NiO thicknesses has a lower electronic contribution from the core and the interaction with the gas is closely linked to the thickness of the NiO, as an increase in thickness to 6.60 nm causes a decrease in sensitivity to the gases tested.

The mechanisms described have been confirmed by studies in the literature, where NiO thickness and core affect sensitivity to gases, in fact in a sensors NiO/SCCNTs the sensitivity to Acetone and EtOH is linked to the thickness and core and the response, respect this work, changes the direction because the heterojuction formed is p-p type [171]. Another comparison is observed with CNTs/SnO_2/NiO heterostructures, obtained by adopting the same ALD method, in which the variation of NiO thickness varies the response of the sensors to hydrogen and varies the electrical properties. A CNTs/SnO_2 50 cycles/ NiO 200 cycles heterostructure was observed to have n-type semiconductor behavior in contrast to a CNTs/SnO_2 50 cycles/ NiO 350 cycles heterostructure that showed p-type semiconductor behavior [172].

Same behavior was observed by J. Fang *et al.* in a SnO_2/NiO heterojunction obtained by a synthesis method other than ALD. SnO_2 was prepared by radio frequency (RF) magnetron sputtering and the different NiO thicknesses were obtained by electron beam evaporation. The SnO_2/NiO heterojunction behaves as an EtOH-sensitive n-type semiconductor. The gas sensitivity is higher for low NiO thicknesses and decreases with increasing thickness [173].

Gun-Joo *et al.* studied TiO_2 nanorods and TiO_2-core/NiO-shell nanorods synthesized by hydrothermal techniques and their acetone sensing properties. The TiO_2-core/NiO-shell nanorod sensor showed a stronger response to acetone than the pristine TiO_2 nanorod sensor. The response of the core—shell nanorod sensor to 200 ppm of acetone at 400 °C was 9.81, whereas that of the pristine nanorod sensor was 5.76 under the same conditions. Furthermore, under these conditions, the recovery time of the core-shell nanorod sensor was 136 s, which was much shorter than that of the pristine nanorod sensor (498 s), even though the response time of the former (14.6 s) was slightly longer than that of the latter (5.2 s). The core-shell nanorod sensor showed excellent selectivity to acetone over other volatile organic compound gases including ethanol, methanol, benzene, and toluene. The improved sensing performance of the core-shell nanorod sensor is attributed to modulation of the conduction channel width at the TiO_2-NiO interface accompanying the adsorption and desorption of acetone gas as well as preferential adsorption and diffusion for oxygen and acetone molecules at the TiO_2-NiO interface [174].

6.4.2.4 Conclusions

A mesoporous titania compound was modified by doping with 35 percent in mol Nb and deposition of NiO layers via ALD. The composite was deposited directly onto the resistive device by the same ALD technique. Different sensors were obtained starting from m-TiOx and NbTiOx as reference to deposit different thicknesses of NiO. The NbTiOx sensor having a thickness of 2.60 nm (5 cycles of ALD reaction) showed performance such that it could have very good selectivity to acetone over ethanol. The surface reaction mechanism verified computational studies and confirmed the influence of NiO on the composite in comparison with other heterojunctions. The sensing mechanism is closely related to the presence of the dopant in the crystal structure and the presence of a thin NiO layer. A thin NiO thickness results in a shorter Debye length and thus a greater contribution of holes as charge carriers in the conduction process and interaction with acetone, a strongly reducing gas.

5.4.2.5 Additional information

The work was carried out during the European PhD period in Berlin at Humboldt University, as a Guest researcher in the laboratory of Prof. Nicola Pinna.

Additional characterizations are in progress and will be added at the time of review and submission of the work.

5.5 New Plants-assisted synthesis:

5.5.1 Gas sensors based Nickel ferrite ($NiFe_2O_4$)

Abstract: $NiFe_2O_4$ spinel samples were obtained from a new synthesis using the hibiscus flower as a precursor. The basic solution was treated with different solvents and additives resulting in the formation of three different nickel ferrites. The sensing tests verified sensitivity to NO_2 gas with distinct performances for each sensor. The NiF1 sensor showed low resistances and short response/recovery times, while higher sensitivity and response was found for the NiF4 sensor, response of 4.5 for 5ppm NO_2 at an operating temperature of 150°C. SEM/EDAX and XRD characterizations were carried out which allowed us to explain the different behaviors of the nanomaterials obtained.

5.5.1.1 Introduction

Nanomaterials exhibit optical, electrical, mechanical and quantum properties according to particles size (range 1-100nm), grain size, surface area, crystallinity and so on. Nowadays, there are several nanomaterials, such as metal oxides, organometallic compounds, organic-inorganic composites, developed for different applications from the biomedical to the industrial field. The trend is to improve the performance of already known nanomaterials also through combinations with other nanomaterials.

Among the nanomaterials of interest, we find ferrites. Ferrites are ferromagnetic materials whose general formula is $Me^{2+}Fe_2^{3+}O_4^{2-}$, Me is bivalent metal ion (as Ni, Cu, Mn, Zn and so on). The spatial arrangement of metal cations and oxygen anions in the lattice allows to obtain different geometrical configurations [175]. In fact, it is possible to obtain spinal ferrite ($MeFe_2O_4$), garnet ferrite ($Me_3Fe_5O_{12}$) and ortho- or hexagonal ferrite ($MeFeO_3$) that depending on the synthesis process [176]

In this work, more attention has been paid to the development of a nickel ferrite, because has low magnetic anisotropy, low curie temperature, good electrical stability and on particularly a high electrical conductivity [177]. Nickel ferrites evince an inverse spinel structure which M^{2+} is a divalent cation, Fe^{3+} ions fill into 8 tetrahedral cations and 16 octahedral cations are filled by Fe^{3+} and Ni^{2+} ions. [178] Such atomic arrangement in the crystalline structure makes it a magnetic and electrical material since the inversion degree of parameters is closely related to the size. More properties were observed for nano-scale dimensions than for bulk [179]. Properties that allow the material to be adopted in different fields, from biomedical to industrial, specifically as solid oxide fuel cells [180], antenna fabrication [181], catalysts [182], electrical and electronic device [183,184], gas sensors [185], magnetic sensors, [186] radio frequency circuit [187] and so on.

There are several synthesis methods for nickel ferrite, as hydrothermal [188], co-precipitation [189], sol-gel [190], microwave-assisted [191], solvo-thermal [192], combustion [193] and mechanical milling [194]. In addition to the classical synthesis methods, new syntheses and new morphologies are being developed for $NiFe_2O_4$. Precursors that are generally used for synthesis are reacted with new precursors. S.I.H. Taqvi *et al.* [195] demonstrated the possibility of obtaining a $NiFe_2O_4$ spinel through the addition of the extract of the Ixora coccinea plant and good performances were found for the detection of pentachlorophenol. Instead, N. Janudin *et al.* [196] a nanocellulose as a substrate to improve the performance of $NiFe_2O_3$ pristine in chlorine detection. The choice of the method to be used is determined by the yield of the nanoparticles (NPs), i.e. it is linked to their morphology, the operating conditions, the dimensions and the shape of the NPs, moreover the times, the costs and the use of solvents and surfactants are factors which should not be neglected for an experiment.

In this regard, the work reports a different synthesis method which three different spinels of nickel ferrite are developed adopting a plant extract of Hibiscus flowers to different conditions to develop a conductometric gas sensor. A change in the electrical properties of the developed gas sensors linked to the different synthesis conditions has been demonstrated.

5.5.1.2. Experimental section

5.5.1.2.1 Preparation of $NiFe_2O_4$ nanoparticles

A new synthesis has been developed using hibiscus flowers as precursors. The initial procedure consisted of cutting and finely grinding the flowers. The powder produced was washed with distilled water to remove impurities. The plant extract solution was prepared by boiling 10 g of the powder obtained in 100 mL of distilled water, at 70°C for approximately 30 minutes, until the color of the solution changed. A second solution was prepared with 25% $NiCl_2$ (Ni source) and $FeCl_3$ (Fe source) as precursors in 90 mL of distilled water. Then, 10 mL of hibiscus extract was added to the second solution. The solution is 0.1 M. This solution was used as a starting solution to develop three different ferrites named NiF1, NiF2 and NiF4.

For the NIF1 sample, 1 mL of ammonia was added to the solution. For NIF2, in addition to 1 mL of ammonia, 0.1 M of hexamethylenetetramine (HTMA C6H12N4) was added. Finally, NIF4 was prepared by adding 0.1 M hexamethylenetetramine (HTMA C6H12N4) and 0.24 g NaOH without ammonia. All samples were kept for 24 hours at room temperature, then filtered, dried at 80°C for 2 hours and finally calcined at 500°C for 2 hours. The complete procedure is shown in Figure 5.60.

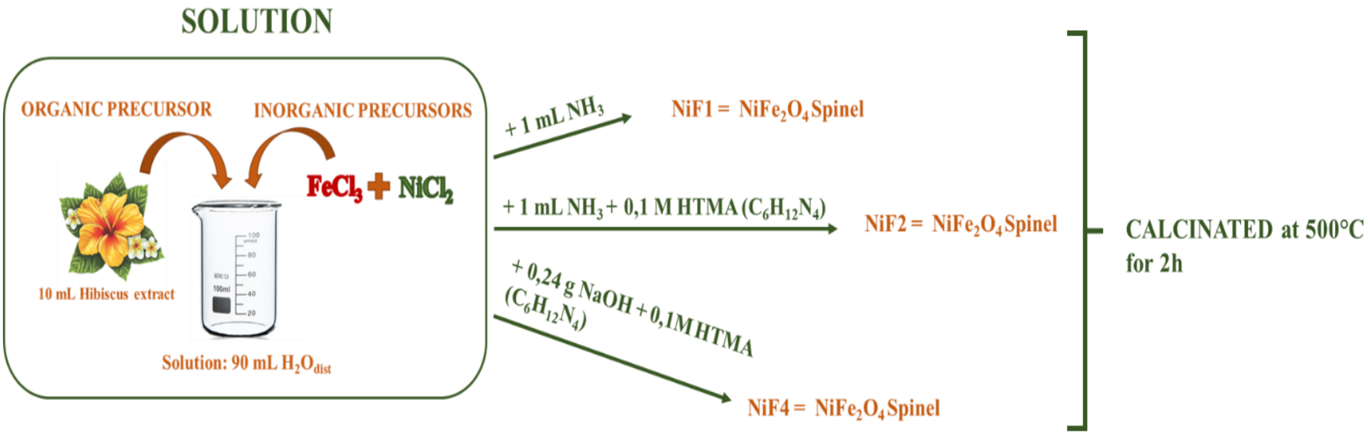

Figure 5.60. Preparation of $NiFe_2O_4$ spinels.

5.5.1.2.2 Characterization

SEM/ EDAX-APEX microscopy was used to investigate the morphology and chemical composition in our different spinel ferrite samples. The X-ray Diffraction (XRD) analysis was adopting to verify the structures and crystallinity of samples.

5.5.1.2.3 Gas sensing measurements

A resistive device in alumina with interdigitated Pt contacts of the dimensions of 6x3 mm has been adopted to develop the gas sensors. A dispersion solution of 1 mg of nanomaterial on

1mL of distilled water sonicated for 15 min was used to drop 10 µL on surface on device. The sensors obtained were left to dry at room temperature. After, each sensor was connected to the instrument through a holder and was introduced in a test chamber subjected to different gases and different temperatures. The Agilent 34970A multimeter was used to check the resistance and Agilent E3632A instrument was employed for measurements at different temperatures.

The calculation of the gas response, S, is defined as the ratio R_{gas}/R_{air} (for *p-type* behavior) and the ratio R_{air}/R_{gas} (for *n-type* behavior), where R_{gas} is the electrical resistance measured at different gas concentrations, and R_{air} is the baseline resistance in dry air. The dynamic response time, τ_{res}, and recovery time, τ_{rec} characteristics were measured according to their resistance. Response time, τ_{res}, i. e. the time required for the sensor to reach 90% of the saturation resistance after injection of the target gas, and recovery time, τ_{rec}, i. e. the time necessary for the sensor to reach 90% of the resistance baseline value in air, were also evaluated.

5.5.1.3 Results and Discussion

5.5.1.3.1 Structural and Morphological Analysis

The prepared nanomaterials were characterized by SEM-EDX and XRD microscopy. SEM images of the samples (NiF1, NiF2 and NiF4) at different magnifications are shown in the following Figures 5.61 a, b and c. The characteristic regular morphology of iron is observed in the three samples. The real atomic composition of the samples was carried out through an EDAX analysis, in Figures 5.62 a, b and c the percentages of atoms, the spectra and the image corresponding to the analysis for each sample are shown. The constant high percentage of iron contained in the three samples is evident, while the percentage of nickel decrease from NiF1 (12% Atomic) to NiF4 (1% Atomic).

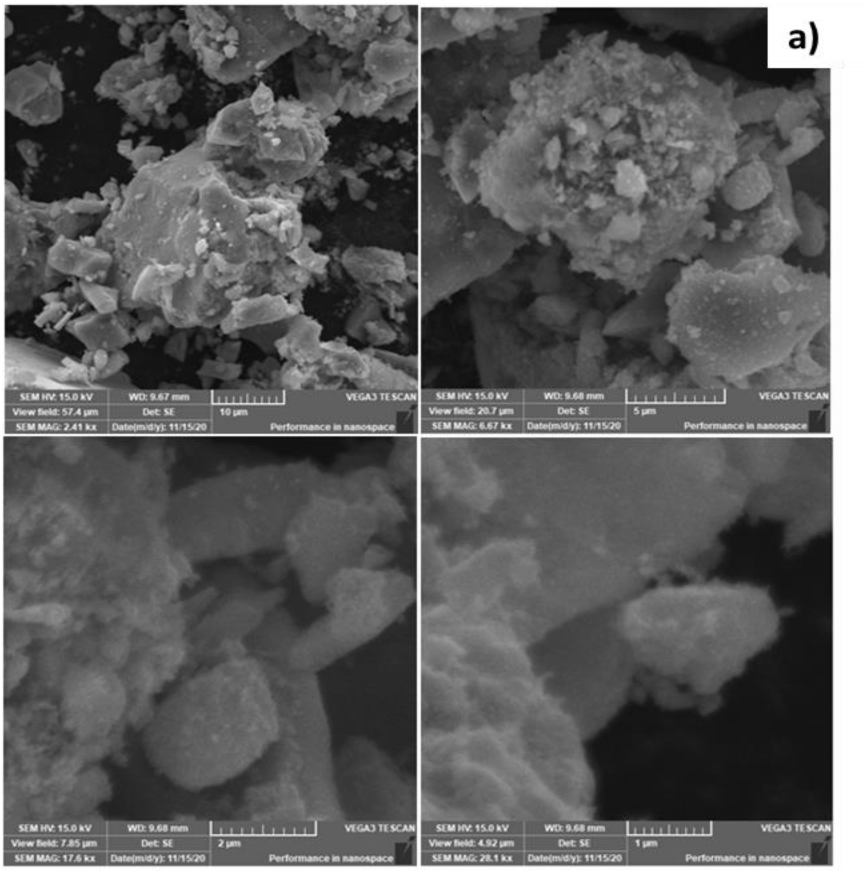
a)
SEM HV: 15.0 kV
WD: 9.67 mm
View field: 57.4 μm
Det: SE
10 μm
SEM MAG: 2.41 kx
Date(m/d/y): 11/15/20
VEGA3 TESCAN
Performance in nanospace
SEM HV: 15.0 kV
WD: 9.68 mm
View field: 20.7 μm
Det: SE
5 μm
SEM MAG: 6.67 kx
Date(m/d/y): 11/15/20
VEGA3 TESCAN
Performance in nanospace
SEM HV: 15.0 kV
WD: 9.68 mm
View field: 7.85 μm
Det: SE
2 μm
SEM MAG: 17.6 kx
Date(m/d/y): 11/15/20
VEGA3 TESCAN
Performance in nanospace
SEM HV: 15.0 kV
WD: 9.68 mm
View field: 4.92 μm
Det: SE
1 μm
SEM MAG: 28.1 kx
Date(m/d/y): 11/15/20
VEGA3 TESCAN
Performance in nanospace

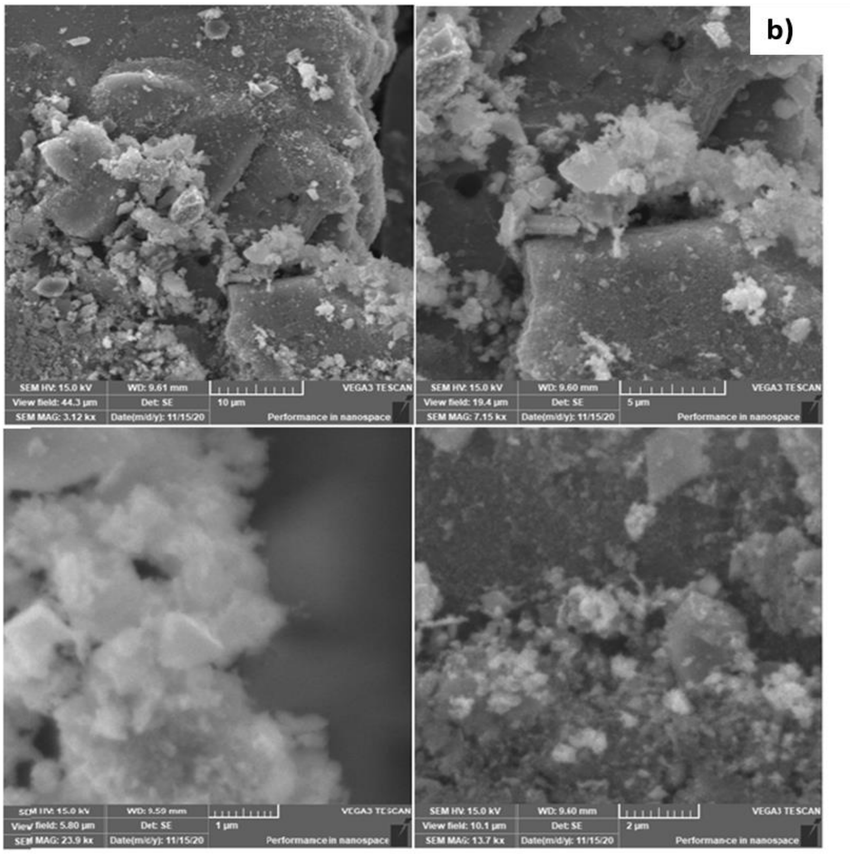
b)
SEM HV: 15.0 kV
WD: 9.61 mm
View field: 44.3 μm
Det: SE
10 μm
SEM MAG: 3.12 kx
Date(m/d/y): 11/15/20
VEGA3 TESCAN
Performance in nanospace
SEM HV: 15.0 kV
WD: 9.60 mm
View field: 19.4 μm
Det: SE
5 μm
SEM MAG: 7.15 kx
Date(m/d/y): 11/15/20
VEGA3 TESCAN
Performance in nanospace
SEM HV: 15.0 kV
WD: 9.59 mm
View field: 5.80 μm
Det: SE
1 μm
SEM MAG: 23.9 kx
Date(m/d/y): 11/15/20
VEGA3 TESCAN
Performance in nanospace
SEM HV: 15.0 kV
WD: 9.60 mm
View field: 10.1 μm
Det: SE
2 μm
SEM MAG: 13.7 kx
Date(m/d/y): 11/15/20
VEGA3 TESCAN
Performance in nanospace

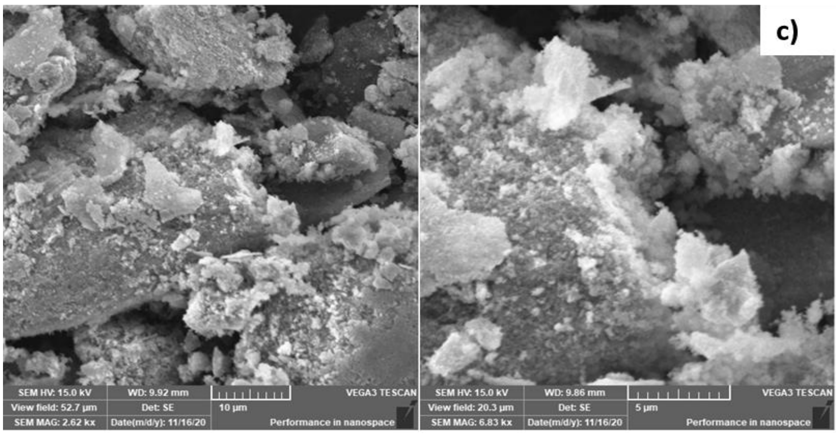

Figure 5.61. SEM imagines: (a) four imagines at different magnification of NiF1 sample; (b) four imagines at different magnification of NiF2 sample and (c) two imagines at different magnification of NiF4 sample.

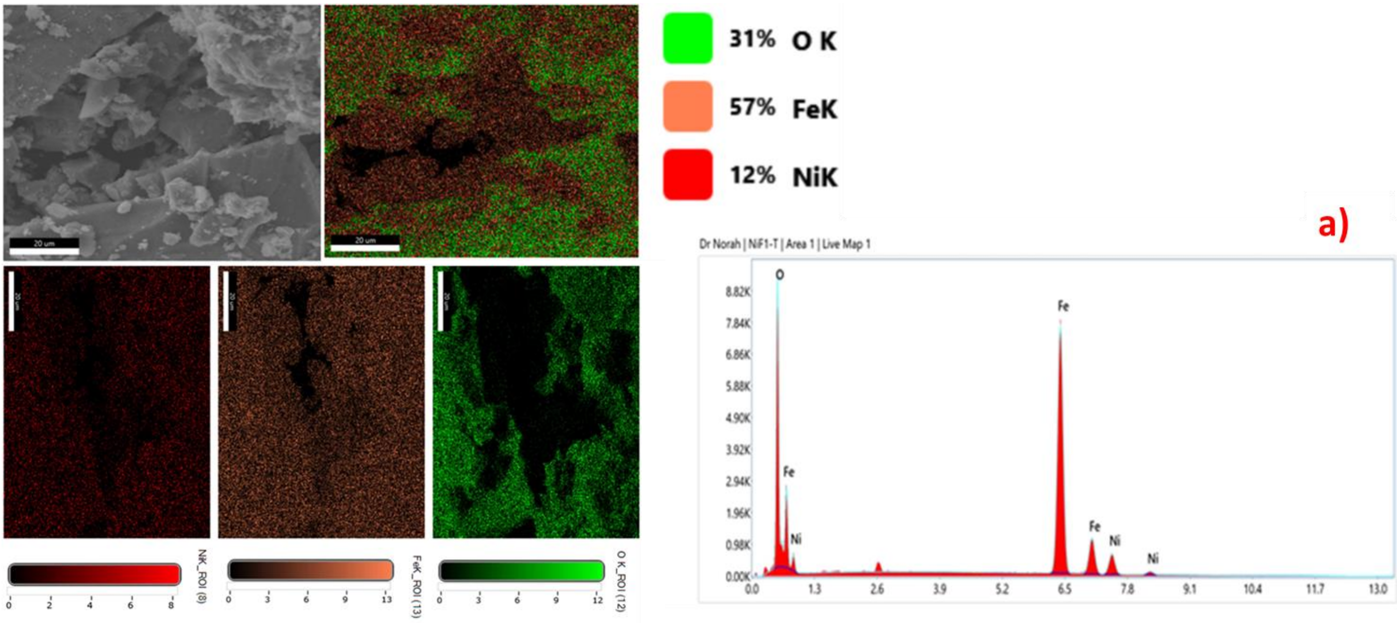

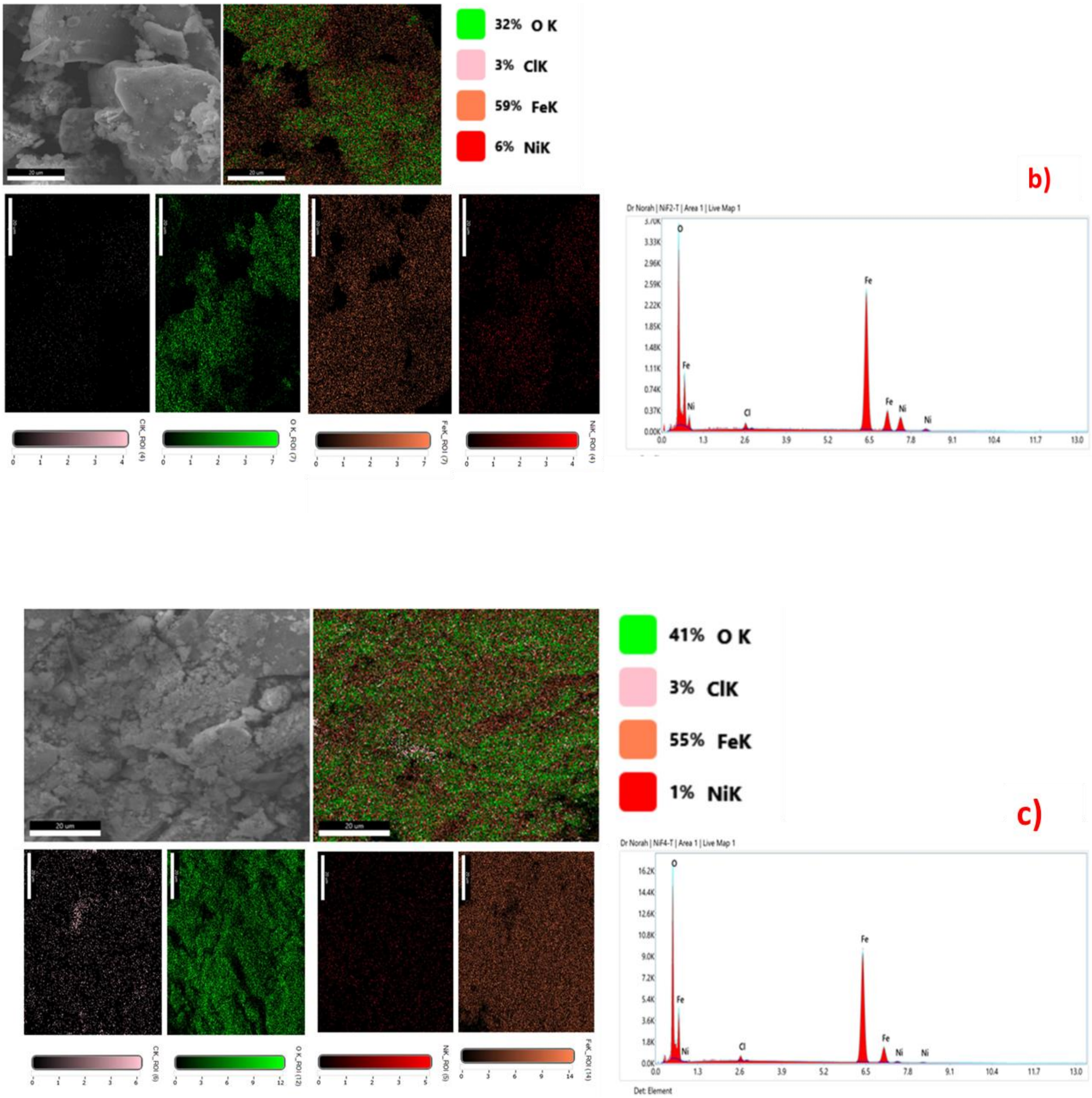

Figure 5.62. EDAX/APAX analysis of each sample: (a) mapping and spectrum of NiF1 sample; (b) mapping and spectrum of NiF2 sample and (c) mapping and spectrum of NiF4 sample.

The different solvent used and the presence of HTMA in the structure resulted in the formation of three different nickel ferrites spinels. The structures and phases composition of the compounds were exploited adopting XRD technique. The diffraction peak, in Figure 5.64

at 30°, 35°, 45°, 54° 58°, 64°, 73° and 75° are attributed to the phases (220), (311), (400), (422), (511), (440), (620) and (533) observed for the NiF1 sample, based on the reference card of COD 96-591-005 for $NiFe_2O_4$. In addition to the ferrite phase, an hematite (Fe_2O_3) phases in the peaks at 33° (104), 36° (110), 42° (113), 59° (024) and 63° (300) were found in the samples NiF2 and NiF4 (reference COD 96-900-0140).

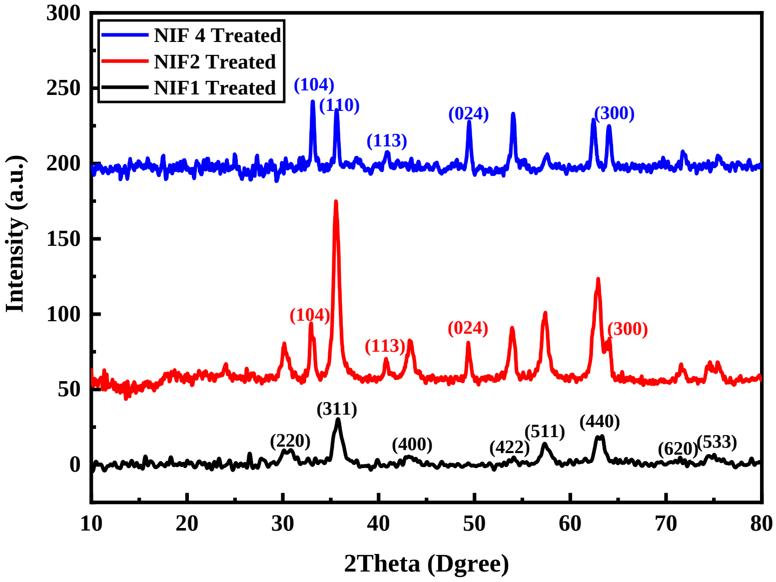

Figure 5.64. XRD patterns of NIF1, NIF2, and NIF4 samples.

The obtained average crystallite size is 8.37 nm, 9.12 nm, and 11.92 nm for the NIF1, NIF2, and NIF4 samples, respectively. The broadening of peaks in the NIF1 and NIF2 samples compared to the NIF4 sample suggests that the higher presence of the $NiFe_2O_4$ phase in the former samples leads to a reduction in crystallite size.

5.5.1.3.2 Electrical characterization

The three compounds (NiF1, NiF2 and NiF4) were evaluated from the point of view electrical adopting the devices used for the successive sensing experiments, the information obtained could be directly used for optimizing their performances.

The electrical properties of compounds have been verified in range of the 100-400°C in dry air conditions (Figure 5.64). The classic semiconductor behaviour was observed, so an increase in temperature causes a decrease in the resistance of the sensors. High resistance was observed for NiF4 sensor respect the other two sensors that were shown similar behaviour. The electrical characteristic of NiF4 could be explained by presence of greater amount of oxygen and less amount of nickel respect other compounds, such as found in EDAX analysis (Figure 5.62c).

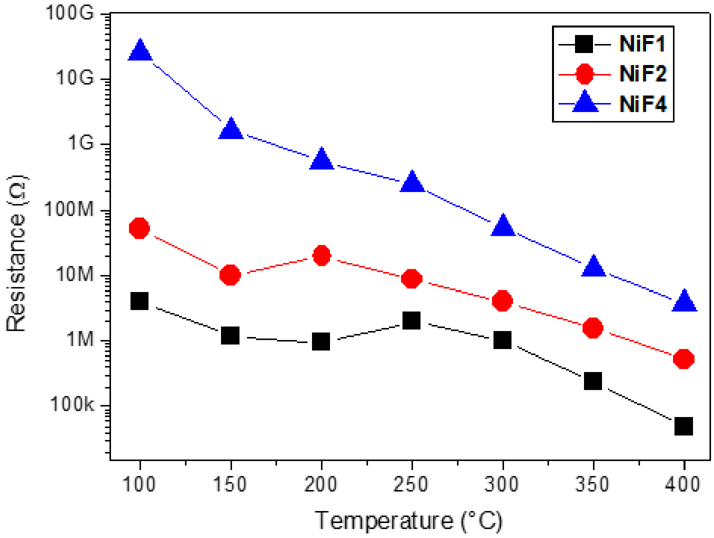

Figure 5.64. Electrical properties of samples: Resistance vs Temperature.

5.5.1.3.3 Gas sensing behaviour

In the preliminary tests NO_2 was selected as the target gas for the three materials. The calibration curves at 150°C are shown in Figure 6.65. Greater gas response and high resistance is observed for the NiF4 sensor, instead low response, good resistance and good dynamic signal trend was observed for NiF1 sensor (see Figure 6.66a) respect other samples as shown in Figure 5.66 b and c. The response and recovery time verified corresponding to sensors are 40 and 140 sec for NiF1; 60 and 190 sec for NiF2; 55 and 160 sec for NiF4 respectively, measured at a concentration of 5 ppm (see Figure 6.67).

The sensors exhibit a *n-type* behaviour, as the resistance increase with the adsorption of the oxidant gas on the semiconductor surface.

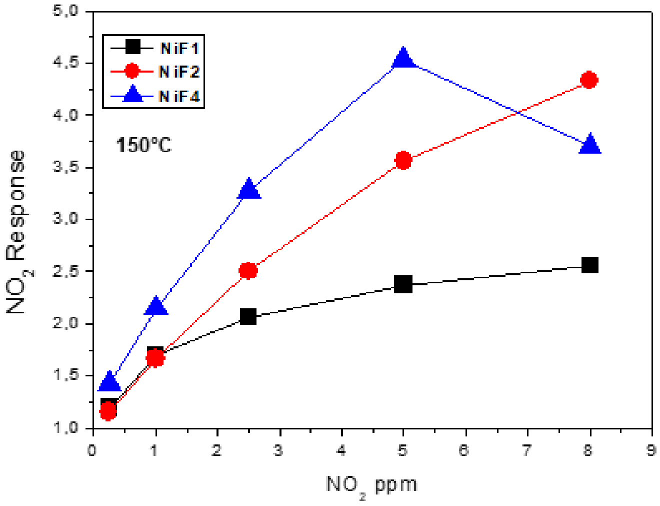

Figure 5.65. Calibration curves of the sensors at 150°C in a specific range of concentration.

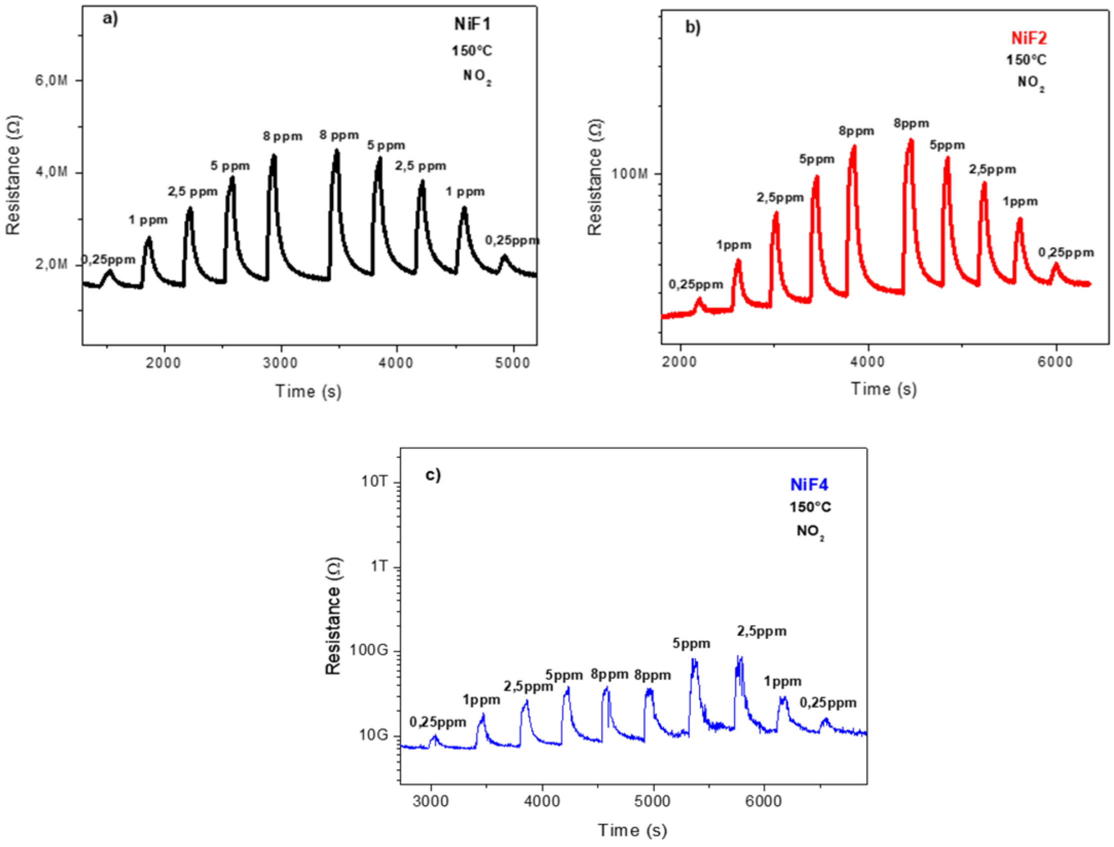

Figure 5.66. (a, b and c) Dynamic signal trend of sensors NiF1, NiF2 and NiF4 at 150°C.

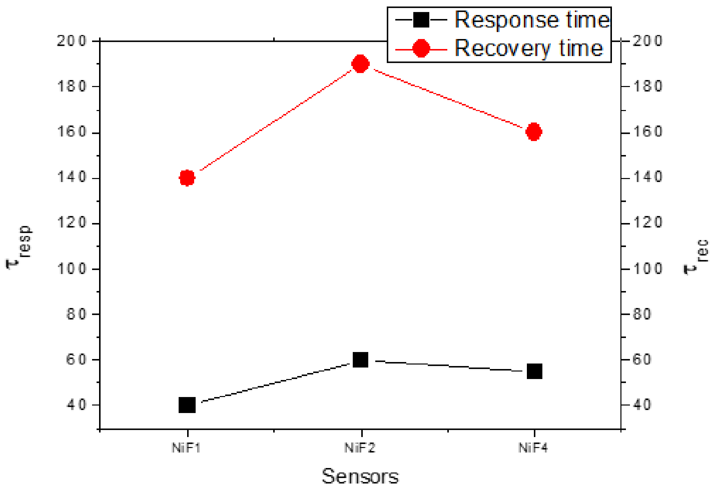

Figure 5.67. Response and Recovery time of samples.

The Figure 5.68 (a, b and c) exhibit the reproducibility tests over time at 150°C to 5ppm NO_2. The NF4 is the sample with good reproducibility of the signal.

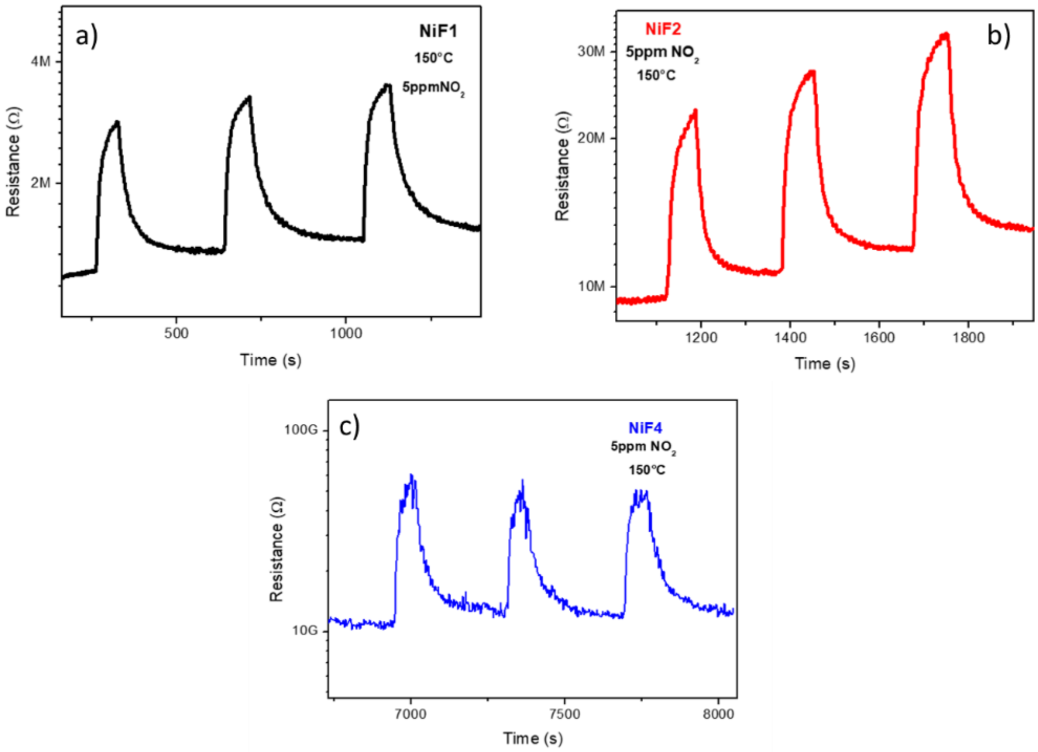

Figure 5.68. (a, b and c) Reproducibility tests of NiF1, NiF2 and NiF4 sensors to 5ppm NO_2 at operating temperature of 150°C.

Final tests allowed to verify the selectivity of the sensors to a mixture of different gases of different concentration (see Figure 5.69 a, b and c). The sensors were subjected to gases such as formaldehyde (CH_2O), ammonia (NH_3), ethanol (EtOH), nitric oxide (NO) and hydrogen sulphide (H_2S). Subjecting the sensors to different gases made it possible to evaluate the sensitivities and the different behaviors. Other than the response variation, no semiconductor behavior variation in NO_2 sensitivity is observed and they continue to exhibit the properties of an *n-type* semiconductor. A variation in the interaction with formaldehyde exhibit the NiF2 sensor with a *p-type* behavior, probably due to the presence of a variation in the sensor surface.

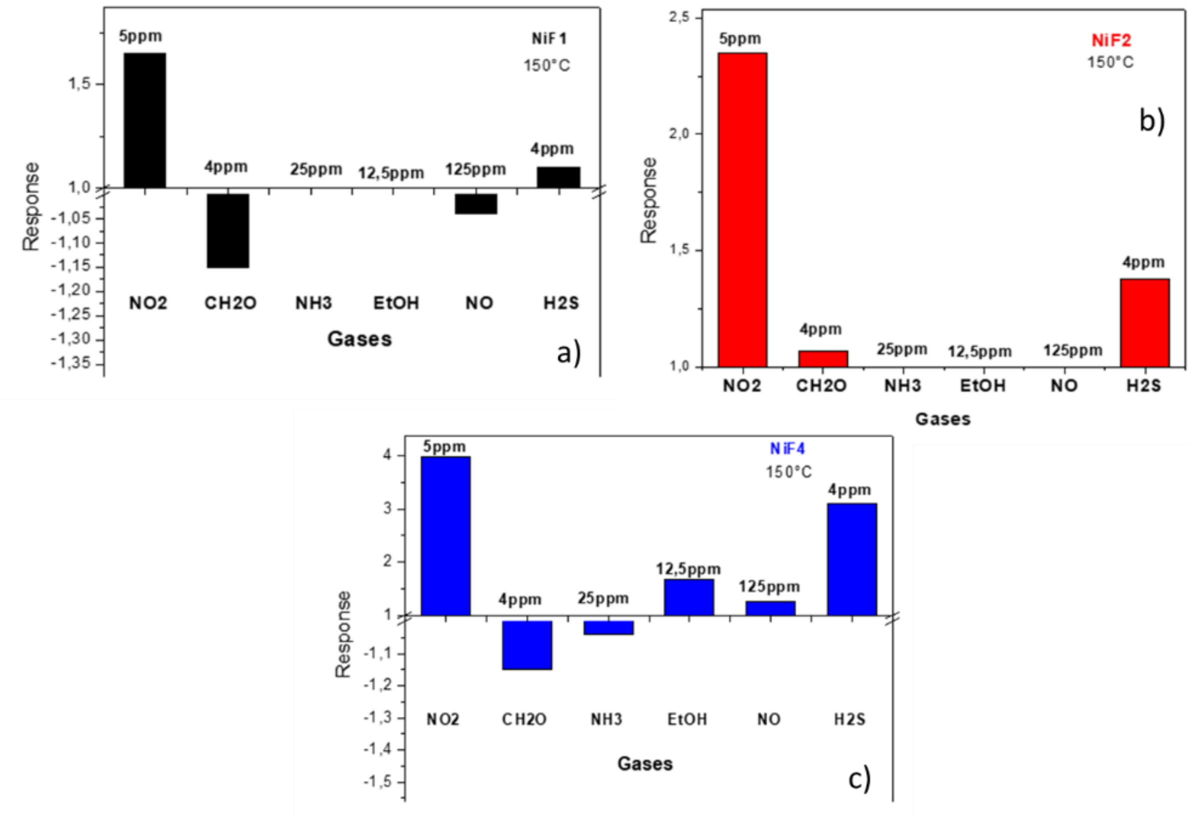

Figure 5.69. (a, b and c) selectivity tests of sensors NiF1, NiF2 and NiF4 at 150°C in different gases such as 4ppm CH_2O, 25ppm NH_3, 12,5ppm EtOH, 125ppm NO and 4ppm H_2S.

Previously we discussed the importance of the influence of the synthesis of a nickel ferrite. The synthesis influences the morphology and chemical-physical properties of the spinel. In the case of these materials the synthesis does not change but the solvent and the presence of

HTMA, which made them spinels with different sensitivities. In detail, different sensitivities were verified for NO_2 with almost opposite performances for NiF1 and NiF4. NiF1 showed a low resistance, stable and reproducible signal, behavior which could be explained through the result found from the characterizations. Compared to the other samples, NiF1 has a higher atomic percentage of nickel and a lower percentage of oxygen, which could give it low resistance, furthermore it does not have possible amino groups on the surface due to the absence of HTMA, which could explain a low response to NO_2. Hence, low response and low interaction with surface explain the high response/recovery time. Different behavior is observed for NiF4. This sensor showed greater sensitivity and reproducibility to NO_2 which can be explained by the possible presence of amine groups on the surface favouring the adsorption of NO_2. Instead, high resistance, as already discussed, could be caused by a higher percentage of oxygen. The performance of NiF4 could also be given by the coexistence of two phases ($NiFe_2O4$ and Fe_2O_3) in the crystalline structure.

5.5.1.4 Conclusion

A new synthesis method was reported in this work. A hibiscus flower extract was used as a precursor to develop nickel ferrites ($NiFe_2O_3$). The solution containing the precursors was treated in three different ways: one by adding only a quantity of NH_3 from which the NiF1 sample was obtained; the second with the same quantity of NH_3 and the addition of an amine (HTMA) for NiF2; the third, with the addition of a quantity of NaOH and HTMA without NH_3 for NiF4. Different behaviors were observed for the samples. The EDAX and XRD characterizations allowed explanations to be given. In particular, different structures have been obtained with different chemical composition. The different phases coexisting in the NiF4 sample made it better performing in the detection of NO_2; low resistances were observed for NiF1 given the correct atomic balance found. More synthesis studies could generate nickel ferrites with higher performance.

5.5.1.5. Additional information

In paragraph 5.5.1., only the part of the work regarding the development of a gas sensor using nickel ferrites is discussed. The development of an electrochemical sensor using this nanomaterial is discussed in the "side work" section.

5.6. Synthesis *via* co-precipitation method:

5.6.1 Innovative Materials based on Mn-Zn-ZIF for gas monitoring

Overview: The following work is part of the **Italian Patent n° 102022000006857:** *Innovative nanostructured materials based on ZIF including Manganese for gas monitoring.*

Inventors: Conoci S., Neri G., Donato N., Moulaee K., Petralia S., Condorelli G.G., Monforte F., Crispi S..

5.6.1.1 Introduction

Twentieth century technology has moved towards the development and miniaturization of new devices. Among these are the sensors. The sensors are experiencing great success especially due to the possibility of being able to adopt them in various applications, such as the detection of polluting gases for environmental monitoring. Current methodologies for gas detection are divided into laboratory analytical methodologies which are based on optical and spectrometric methods as chromatographic separation, and in sensorial methodologies based on materials sensitive to the presence of a species gaseous with electrical or optical transduction. The second method, compared to the first, in addition to miniaturization, makes the measurement simpler and reduces costs. Sensitive materials are nanomaterials ranging in size from 1-100 nm and metal oxides are generally the most synthesized. Nanomaterials based metal oxide semiconductor as ZnO, SnO_2, TiO_2, NiO ,[197] polymers, organic compounds such as calixarenes and calix-pyrroles .

Only a limited number of nanomaterials are currently used in gas sensing mainly due to their poor thermal resistance to temperatures usually used. The main technical problems that currently exist are since these materials they are often characterized by good sensitivity but poor selectivity or vice versa e however, it has poor resistance to high temperatures. As for the sensitivity, this is appropriately optimized by selecting the working temperature of the sensor (typically high temperatures 300°C-500°C). The selectivity problem is instead addressed by using appropriate membranes semi-permeable capable of preferably selecting a gaseous species compared to others depending on its properties such as generally size and polarity. Both solutions are very often incompatible with both the platform (smartphones, implantable devices, wearables, etc.) on which the sensitive material must be integrated, both with the material itself, when this is thermally not very stable, drastically impacting the life of the sensor.

The problem addressed by this work is therefore that of providing efficient materials for the creation of sensors suitable for detecting and/or monitoring gaseous species that resolves the above-listed problems or inconveniences. Specifically, the problem addressed is to develop very sensitive sensors for gaseous species and which, secondly, they are able to operate at temperatures lower than those used today from other known sensors. This problem is solved by materials for the detection and/or monitoring of species gaseous materials of the present work which are the nanostructured materials based on ZIF (short for Zeolitic Imidazolate Frameworks) to different manganese dopings, in particular, comprising from 0.3% to 10% by weight of manganese. The value of percentage by weight of Manganese expresses the weight of manganese compared to the weight of zinc, i.e. it is the ratio between the weight of manganese and the weight of zinc, multiplied by one hundred.

The project also concerns a new method of preparing a material based on nanostructured Zn-ZIF (Zeolitic Imidazolate Frameworks). appropriately doped with different amounts of Manganese and its application in the gas sensing for monitoring gaseous species using resistive sensors. In particular, it concerns a nanostructured material with a high surface area active, based on Zn-ZIF with different manganese doping (0.3 - 3%) (Mnx-Zn-ZIF), and its use in an electrical transduction platform for species detection gases such as NO_2, ethanol, acetone, CO, etc., with high specificity. Modulation of sensitivity and selectivity to the specific gases of interest is obtained by means of the optimization of the sensor's working temperature.

5.6.1.2 Experimental section

5.6.1.2.1 Mnx-Zn-ZIF Synthesis

The synthesis of MnxZn-ZIF nanostructures (with x from 0.3% to 10%) can be achieved carried out through the following preparation procedures. All materials and compounds are commercially available.

An aliquot of 20 mL of aqueous solution containing $Zn(NO_3)_2 \times 6H_2O$ (0.7g) (MW=297.39; 2.35 mmol) and $Mn(acetate)_2$ (0.0018 g. 0.37% by weight) (MW=172.94; 0.010 mmol) were mixed with a volume of 90 mL of methyl imidazole (1.664 M) (MW=82.1; d=1.03; 1130.5 mmol). The solution was left to react for 4 hours at room temperature. After 4 hours, the solid obtained was separated from the solution (part of the suspension) by centrifugation. The product has been washed with deionized water and dried for 24 hours in an oven at 50°C.

5.6.1.2.2 Growth of the nanomaterial via spotting on pre-treated substrates

SiO_2 and Pt substrates for Mnx-Zn-ZIF deposition were adopted. Substrates were chosen to test the interaction of the material with the substrate and find suitable deposition methods, furthermore the idea is to develop a gas sensor to be integrated into MEMS and VLSI technologies. The method involves depositing reaction aliquots with a volume of 2 or 4 µL on the surface of suitably pre-treated solid substrates (Si/SiO_2 or Si/Pt). The substrate is activated with an O_2 plasma treatment for 10 min at 100W, x µL of $Zn(NO_3)_2 \times 6H_2O$ solution (0.7g) and $Mn(acetate)_2$ (0.0018 g). On top of the previous solution, xx µL of methyl imidazole solution are added (1.664 M) and left to incubate for 4 hours in a room at room temperature and humidity relative about 90%, after it is washed with deionized water and dried with a nitrogen flow.

5.6.1.2.3 Structural and Chemical Characterization

The morphology and structure of Mnx-Zn-ZIF have been observed using techniques such as SEM and XRD (Figure 5.70). The SEM characterization allowed the observation of particle agglomerates. Given the quantity of material and being in the form of powder, therefore a dense packing of grains, it is possible to distinguish the hexagonal morphology, and it is possible to notice the presence of more isolated and brighter crystals, with a hexagonal shape and dimensions between 150 and 200 nm. The comparison of the XRD diffractograms unequivocally confirms, the actual doping of ZIF with Manganese within the ZIF structure.

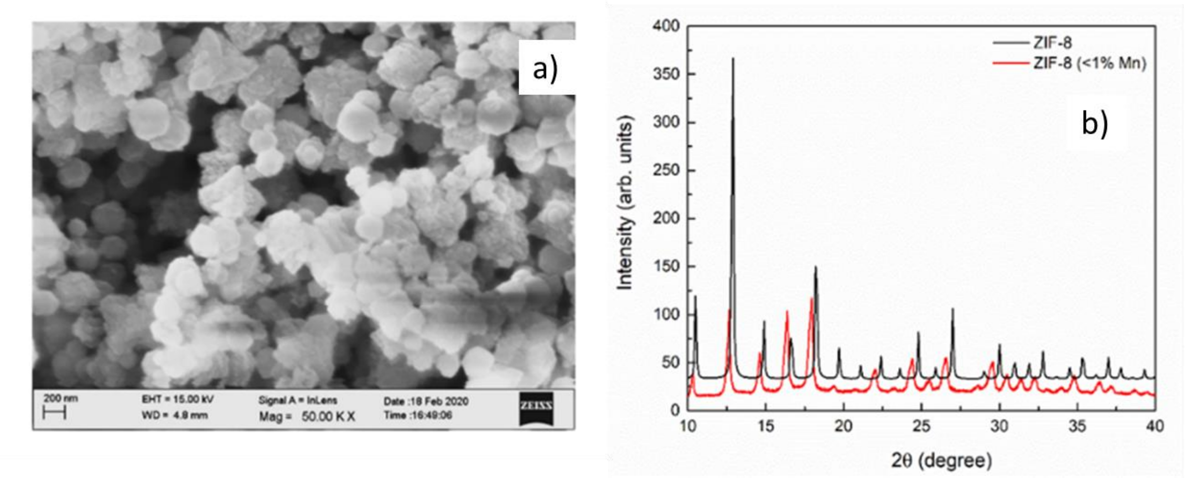

Figure 5.70. (a) SEM characterization; (b) XRD pattern. Both of Mnx-Zn-ZIF sample.

FT-IR spectra are shown in Figure 5.71 of the Mnx-Zn-ZIF product at different concentrations of Manganese with x from 0% to 10% by weight, while in Figure 5.72, of the nanomaterial on Si/Pt (left) and Si/Pt-plasma-O_2 (right).

Oxygen plasma treatment is essential as it allows the increase of the density of the surface hydroxyl groups, increasing the growth efficiency of the nanomaterial itself. In fact, as can be clearly seen from the FTIR spectra reported in Figure, the Plasma treatment involves a clear increase in the following peaks: 1590 cm^{-1}, stretching C=N; 1150 cm^{-1}, C-N stretching; and 420 cm^{-1}, Zn-N stretching.

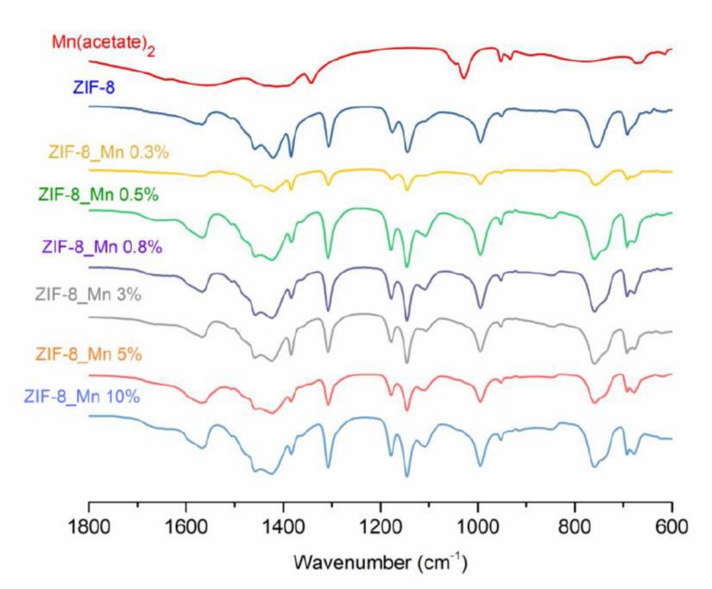

Figure 5.71 Mnx-Zn-ZIF FT-IR spectra.

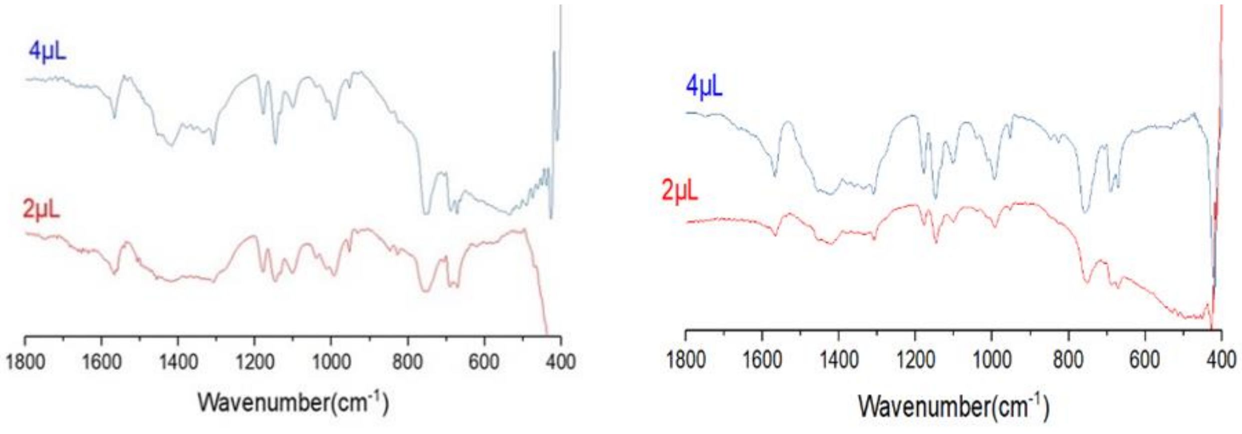

Figure 5.72. FT-IR spectra of Mnx-Zn-ZIF on Si/Pt (left) and Si/Pt-plasma-O_2 (right).

5.6.1.2.4 Gas sensing tests

In the first experimental tests we turned our attention to the preparation of Mnx-Zn-ZIF both as films on Pt and SiO_2 substrates and in powder form, in this second part, our study focused on the gas-sensing tests of Mnx-Zn-ZIF on a sensor resistive. For this purpose, a paste was prepared by mixing the Mnx-Zn-ZIF powders with small quantities of milli-Q H_2O on the surface of the electrode consisting of an alumina support (3 mm × 6 mm), equipped with interdigitated Pt electrodes and of heating elements (Figure 5.73). The Agilent 34970A multimeter was used to check the resistance and Agilent E3632A instrument was employed for measurements at different temperatures.

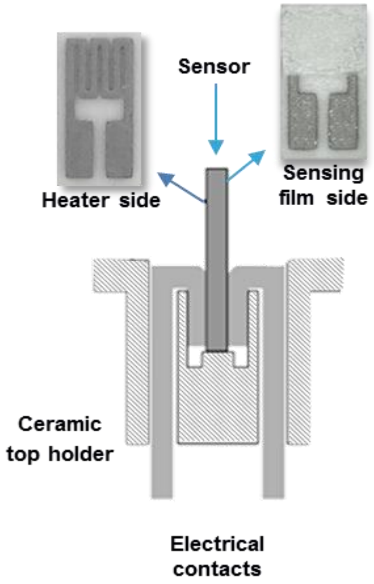

Figure 5.73. Sensor structure and schematic representation of a holder.

Subjecting the Mnx-Zn-ZIF sensor to different concentrations of different gases showed increased sensitivity to NO_2 and EtOH. The treatment of the same at different temperatures made it possible to verify a selectivity linked to the temperature. Figure 5.74 a, b and c shows the trend of the signals. It has been demonstrated that if the sensor operates at a temperature of 350°C, the greater the selectivity for ethanol (EtOH) while an operating temperature of 200°C allows better detection of NO_2. Concentrations of 20 ppm and 2 ppm were used for EtOH and NO_2.

The observation found is linked to the reaction mechanisms that occurred on the surface of the nanomaterial and to the activation processes. Therefore, at 350°C the reactions with EtOH are favored and at 200°C with NO_2. Furthermore, a typical trend of an *n-type* semiconductor was observed, i.e. a decrease in resistance in the interaction with EtOH (reducing gas) and an increase with NO_2 (oxidizing gas).

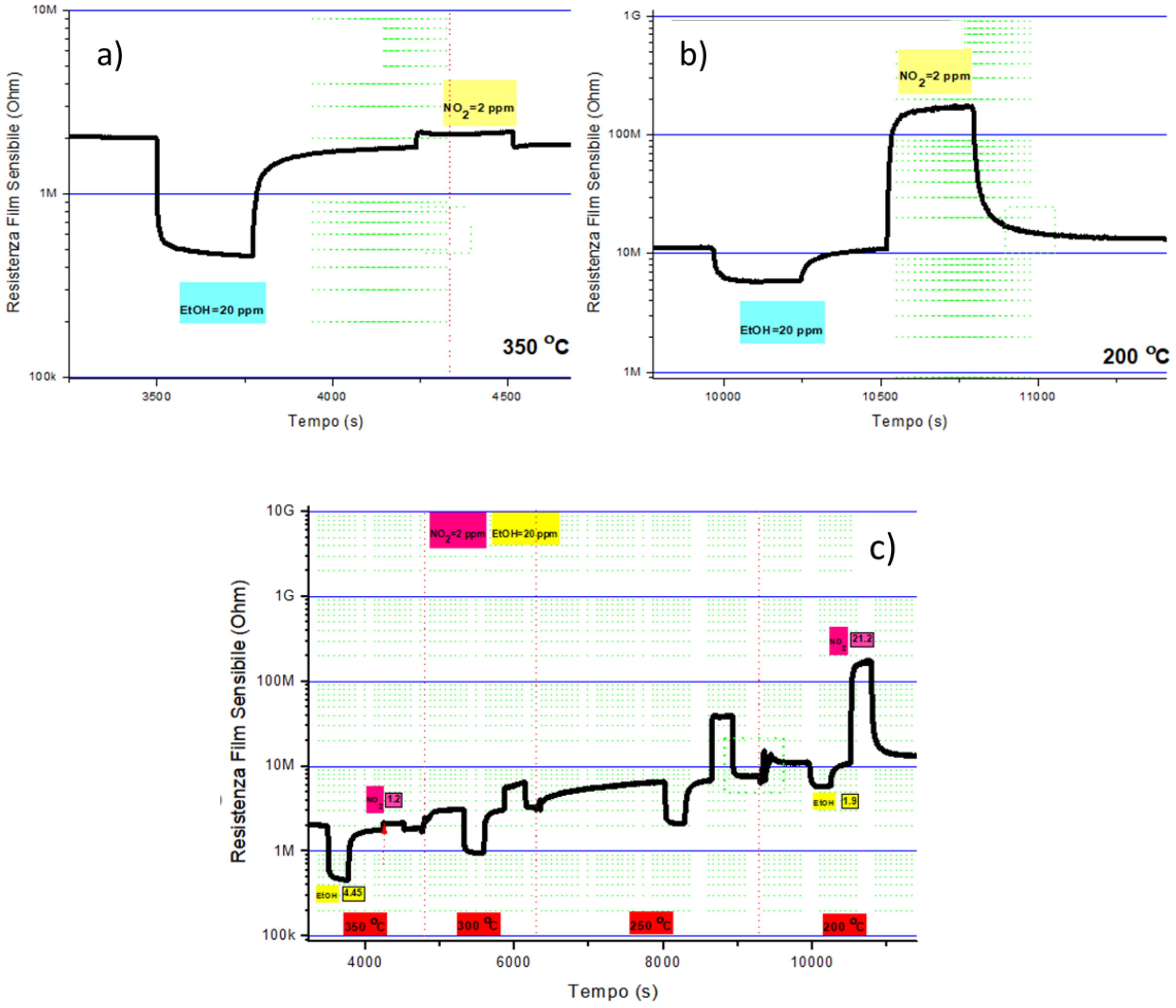

Figure 5.74. Response vs time: a) tests at 350°C with 20 ppm EtOH and 2 ppm NO_2; b) tests at 200°C with 20 ppm EtOH and 2 ppm NO_2; c) Tests at temperature range of 350-200 °C.

Having verified the low operating temperatures and low NO_2 concentrations, it was decided to focus on the interaction with this gas. The sensor was also tested at lower concentrations (range of 0.14 ppm – 4.2 ppm) at the same temperature (200 °C), shown in Figure 5.75a and calibration curve in Figure 5.75b. The responses at low concentrations allow us to define an LOD of 0.14 ppm. Good reproducibility was found in Figure 5.76.

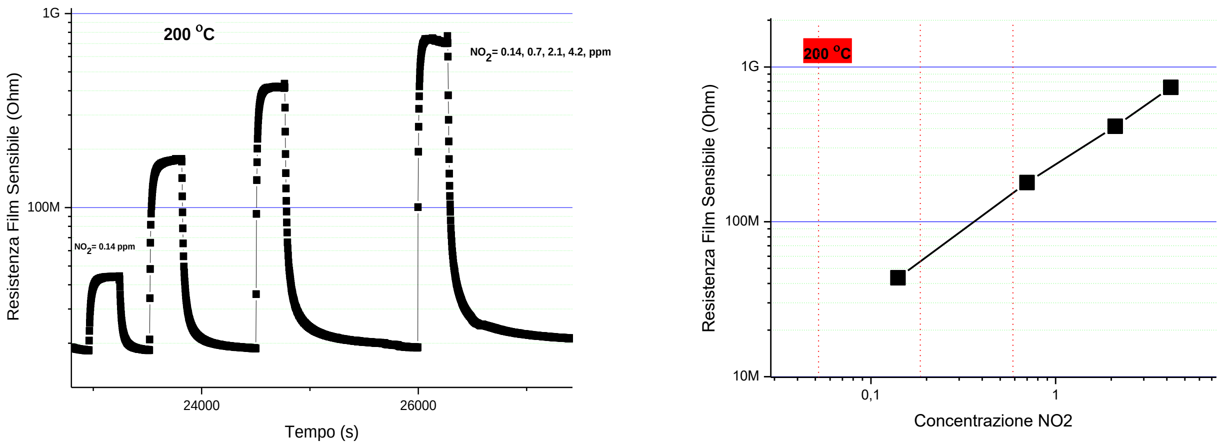

Figure 5.75. a) Variation in resistance over time following an increase in NO_2 concentration at 200°C; b) Calibration curve.

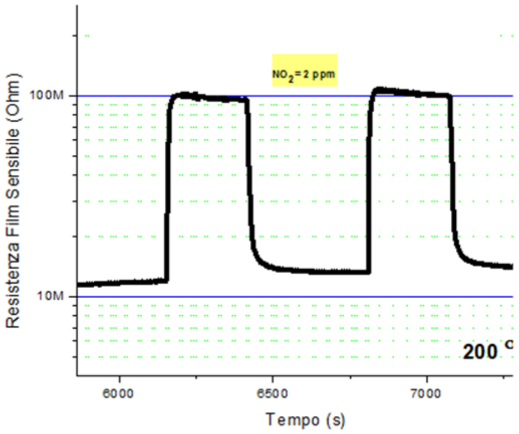

Figure 5.76. Reproducibility of two pulse to 2 ppm NO_2 at 200°C.

5.6.1.3 Conclusions

The objective of this work was to prepare an innovative nanostructured material and develop different methods for integration into a miniaturized sensor for the electrical detection of gaseous species. We have succeeded in developing a highly selective resistive sensor for the gaseous chemical species NO_2 and ethanol operating at different temperatures. The main novelty of this work concerned the preparation of a new Zn-ZIF-based material suitably doped with various concentrations of Mn, exploiting a co-precipitation method never before adopted for the ZIF system. This invention is in fact the subject of a patent filing. The main advantages of this new material compared to the common ZIF-8 concern the increase in thermal stability, high sensitivity at low temperatures and good selectivity. All these advantages make this material interesting for future applications in the sensor sector for environmental and industrial monitoring.

5.7 References

1. Indoor Air Quality. Available online: https://www.epa.gov/indoor-air-quality-iaq/introduction-indoor-air-quality (accessed on 20 August 2022).
2. D. Norbäck, R . Kishi, A. Araki, *Indoor Environmental Quality and Health Risk toward Healthier Environment for All*, Springer: Singapore (2020).
3. S. Dugheri, D. Massi, N. Mucci, G. Marrubini, G. Cappelli, A. Speltini, M.C. Bonferoni, G. Arcangeli, *Exposure to airborne formaldehyde: Sampling and analytical methods—A review*, Trends Environ. Anal. Chem. 29 (2021) 00116.
4. J.R.Hottle, A.J. Huisman, J.P. DiGangi, A. Kammrath, M.M. Galloway, K.L. Coens, F.N. Keutsch, *A laser induced fluorescence-based instrument for in-situ measurements of atmospheric formaldehyde*, Environ. Sci. Technol 43 (2009) 790–795.
5. U. Cindemir, M. Trawka, J. Smulko, C.G. Granqvist, L. Österlunda, G.A. Niklasson, *Fluctuation-enhanced and conductometric gas sensing with nanocrystalline NiO thin films: A comparison*, Sens. Actuators B 242 (2017) 132–139.
6. J.Liu, L. Zhang, B.Cheng, J. Fan, J. Yu, *A high-response formaldehyde sensor based on fibrous Ag-ZnO/*In_2O_3 *with multi-level heterojunctions*, J. Hazard. Mater. 413 (2021) 125352.
7. R.K. Kampara, T. Sonia, D. Balamurugan, B.G. Jeyaprakash, *Formaldehyde vapour sensing property of electrospun NiO nanograins*, Front. Mater. Sci. 15 (2021) 416–430.
8. D. Wang, L. Tian, H. Li, K. Wan, X. Yu, P. Wang, A. Chen, X. Wang, J. Yang, *Mesoporous Ultrathin* SnO_2 *Nanosheets In-situ Modified by Graphene Oxide for Extraordinary Formaldehyde Detection at Low Temperature*, ACS Appl. Mater. Interfaces 11 (2019) 12808–12818.
9. S. Jaballah, M. Benamara, H. Dahman, D. Lahem, M. Debliquy, L. El Mir, *Formaldehyde sensing characteristics of calcium-doped zinc oxide nanoparticles-based gas sensor,* J. Mater. Sci. Mater. Electron 31 (2020) 8230–8239.
10. C.L. Hsua, L.F. Changa, T.J Hsueh, *Light-activated humidity and gas sensing by ZnO nanowires grown on LED at room temperature*, Sens. Actuators B 249 (2017) 265–277.
11. Y.Wang, M.S. Ghamsari, S. Dhara, *ZnO Nanorods for Gas Sensors. In Nanorods and Nanocomposites*, Eds.; IntechOpen: London, UK, (2018).

12. Y.Kang, F. Yu, L. Zhang, W. Wang, L. Chen, Y. Li, *Review of ZnO-based nanomaterials in gas sensors*, Solid State Ion. 360 (2021) 115544.
13. R. Dhahri, S.G. Leonardi, M. Hjiri, L. El Mir, A. Bonavita, N. Donato, D. Iannazzo, G. Neri, *Enhanced performance of novel calcium/aluminum co-doped zinc oxide for* CO_2 *sensors*, Sens. Actuators B 239 (2017) 36–44.
14. C.L. Hsua, L.F. Changa, T.J. Hsueh, *Light-activated humidity and gas sensing by ZnO nanowires grown on LED at room temperature*, Sens. Actuators B 249 (2017) 265–277.
15. M. Hjiri, L. El Mir, S.G. Leonardi, A. Pistone, L. Mavilia, G. Neri, *Al-doped ZnO for highly sensitive CO gas sensors,* Sens. Actuators B Chem. 196 (2014) 413–420.
16. Y. Kang, F. Yu, L. Zhang, W. Wang, L. Chen, Y. Li, *Review of ZnO-based nanomaterials in gas sensors.* Solid State Ion, 360 (2021) 115544.
17. A.I. Istrate, I. Mihalache, C. Romanitan, O. Tutunaru, S. Vulpe, F. Nastase, L.M. Veca, *Ca-Doped ZnO:Al Thin Films: Synthesis and Characterization. Coatings* 11 (2021) 1023.
18. Sigma Aldrich. Available online: https://www.sigmaaldrich.com/IT/it/technical-documents/technicalarticle/analytical-chemistry/photometry-and-reflectometry/ir spectrum-table (accessed on 20 August 2022.
19. A. Taufiq, H.N. Ulya, J. Utomo, N. Hidayat, H. Susanto, N. Mufti, S. Soontaranon, *Structural, Optical, and Antifungal Characters of Zinc Oxide Nanoparticles Prepared by Sol-gel Method,* J. Phys. Conf. Ser. 1093 (2018) 012001.
20. D. Kudasova, B. Mutaliyeva, K. Vlahovˇıcek-Kahlina, S. Juri, M. Marijan, S.V. Khalus, A.V. Prosyanik, S. Šegota, N. Špani, M. Vincekovi, *Encapsulation of Synthesized Plant Growth Regulator Based on Copper(II) Complex in Chitosan/Alginate Microcapsules,* Int. J. Mol. Sci.22 (2021) 2663.
21. M. Khitous, Z. Salem, D. Halliche, *Removal of phosphate from industrial wastewater using uncalcined MgAl-*NO_3 *layered double hydroxide: Batch study and modeling Desalinate Water,* Treat. 57 (2016) 15920–15931.
22. A. Mirzaei, S.G. Leonardi, G. Neri, *Detection of hazardous volatile organic compounds (VOCs) by metal oxide nanostructures-based gas sensors: A review.* Ceram. Int. 42 (2016) 15119–15141.

23. F. Gu, M. Di, D. Han, S. Hong, Z. Wang, *Atomically Dispersed Au on* In_2O_3 *Nanosheets for Highly Sensitive and Selective Detection of Formaldehyde*, ACS Sens. 5 (2020) 2611–2619.
24. Z. Gao, Z. Lou, S. Chen, L. Li, K. Jiang, Z. Fu, W. Han, G. Shen, *Fiber gas sensor-integrated smart face mask for room temperature distinguishing of target gases.* Nano Res. 11 (2018) 511–519.
25. K. Huang, L. Kong, F. Yuan, C. Xie, *In situ diffuse reflectance infrared Fourier transform spectroscopy study of formaldehyde adsorption and reactions on nano* γ-Fe_2O_3 *films*, Appl. Surf. Sci. 270 (2013) 405–410.
26. C. Xie, L. Xiao, M. Hu, Z. Bai, X. Xia, D. Zeng, *Fabrication and formaldehyde gas-sensing property of ZnO–*MnO_2 *coplanar gas sensor arrays*, Sens. Actuators B 145 (2010) 457–463.
27. N. Han, Y. Tian, X. Wu, Y. Chen, *Improving humidity selectivity in formaldehyde gas sensing by a two-sensor array made of Ga-doped ZnO*, Sens. Actuators B 138 (2009) 228–235.
28. J. J-Zhou, L. Zou, X. Zhang, L. Ji, P. Delir, K. Nezhad, *Computational investigation of sensing properties of Ca-doped zinc oxide nanotube toward formaldehyde*, J. Mol. Model. 27 (2021) 303.
29. V. Goletto, G. Mialon, T. Faivre, Y. Wang, I. Lesieur, N. Petigny, S.S. Vijapurapu, *Formaldehyde and total VOC (TVOC) commercial low-cost monitoring devices: From an evaluation in controlled conditions to a use case application in a real building*, Chemosensors 8 (2020) 8.
30. G. Neri, *First fifty years of chemoresistive gas sensors*, Chemosensors 3 (2015) 1–20.
31. Y. Zeng, S. Lin, Gu. Ding, X. Li, *Two-dimensional nanomaterials for gas sensing applications: the role of theoretical calculations*, Nanomaterials 8(10) (2018) 851.
32. N. Van Hoang, L.M. Duc, N.T. Hiep, N.M. Hung, C.V. Nguyen, P.T. Hung, P.D. Hoat, V.K. Vo, Y.-W. Heo, *Comparative study on the gas-sensing performance of ZnO/*SnO_2 *external and ZnO–*SnO_2 *internal heterojunctions for ppb* H_2S *and* NO_2 *gases detection*, Sens. Actuators B: Chem, 334 (2021)129606.
33. M. Bhati, M. Kumar, R. Banerjee, *Gas sensing performance of 2D nanomaterials/metal oxide nanocomposites: a review*, J. Mater. Chem. C 9 (2021) 8776–8808.

34. W. Xiaonan, Y. S. Xiong, Y.G. Gong, Wu. Weiwei, Z. Mao, Q. Liu, Hu. Sheng, X. Long, *MOF-SMO hybrids as a H_2S sensor with superior sensitivity and selectivity,* Sens. Actuators B Chem. 292 (2019) 32–39.
35. M.Y. Lin, C.E. Chang, C.H. Wang, Su. Chen-Fung, C. Chen, S.C. Lee, S.Y. Lin, *Toward epitaxially grown twodimensional crystal hetero-structures: Single and double MoS_2/graphene hetero-structures by chemical vapor depositions*, Appl. Phys. Lett. 105(7) (2014) 073501.
36. F. Liao, B.T. Lo, E. Tsang, *The applications of nano-hetero-junction in optical and thermal catalysis*, Eur. J. Inorg. Chem. 13 (2016)1924–1938.
37. M.H. Balali, N. Nouri, E. Omrani, A. Nasiri, W. Otieno, *An overview of the environmental, economic, and material developments of the solar and wind sources coupled with the energy storage systems*, Int. J. Energy Res. 41 (2017) 1948–1962.
38. B. Nam, T.K. Ko, S.K. Lee, *NO_2 sensing properties of WO3-decorated In2O3 nanorods and In2O3-decorated WO3 nanorods*, Nano Converg. 6 (2019) 1–10.
39. T. Liu, J. Liu, Qi. Liu, Y. Sun, X. Jing, H. Zhang, J. Wang, *Three-dimensional hierarchical Co_3O_4 nano/micro-architecture: synthesis and ethanol sensing properties*, Cryst. Eng. Commun. 18 (2016)5728–5735.
40. F.R. Juang, W.Y. Wang*, Ethanol gas sensors with nanocomposite of nickel oxide and Tungsten oxide,* IEEE Sensors J. 21 (2021) 19740–19752.
41. A. Mirzaei, K. Janghorban, B. Hashemi, M. Bonyani, S.G. Leonardi, G. Neri, Highly stable and selective ethanol sensor based on α-Fe2O3 nanoparticles prepared by Pechini sol–gel method. Ceram. Int. 42, 6136–6144 (2016).
42. M. Al.Hashem, S. Akbar, P. Morris, *Role of oxygen vacancies in nanostructured metal-oxide gas sensors: a review,* Sens. Actuators B Chem. 301 (2019) 126845.
43. A. D'Amico, C. Di Natale*, Introsuction to sensors*, ARACNE editor (2008).
44. Korotcenkov, *The role of morphology and crystallographic structure of metal oxides in response of conductometric-type gas sensors*. Mater. Sci. Eng. R 61 (2008)1–39.
45. N. Al. Hardan, M. Abdullah, A.A. Aziz, *Performance of Cr-doped ZnO for acetone sensing*, Appl. Surf. Sci. 270 (2013) 480–485.

46. P. Rai, Y.S. Kim, H.M. Song, M. K. Song, Y.-T. Yu, *The role of gold catalyst on the sensing behavior of ZnO nanorods for CO and* NO_2 *gases*, Sens. Actuators, B Chem. 165 (2012) 133–142.
47. H. Zhang, J. Feng, T. Fei, S. Liu, T. Zhang, SnO_2 *nanoparticles-reduced graphene oxide nanocomposites for NO2 sensing at low operating temperature*, Sens. Actuators B: Chem. 190 (2014)472–478.
48. D. Jua, H. Xua, Z. Qiua, J. Guoa, J. Zhanga, B. Cao, *Highly sensitive and selective triethylamine-sensing properties of nanosheets directly grown on ceramic tube by forming NiO/ZnO PN heterojunction*, Sens. Actuators B: Chem. 200 (2014) 288–296.
49. Z. Hua, Y. Li, Y. Zeng, Yi. Wi, *A theoretical investigation of the power-law response of metal oxide semiconductor gas sensors I: Schottky barrier control*, Sens. Actuators, B Chem. 255 (2018)1911–1919.
50. B. Bhowmik, K. Dutta, P. Bhattacharyya, *An Efficient Room Temperature Ethanol Sensor Device Based on p-n Homojunction of* TiO_2 *Nanostructures*, IEEE Trans. Electron Dev. 66(2) (2019)1063–1068.
51. N. Itoh, A. Oshima, E. Suga, T. Sato, *Kinetic enhancement of ammonia decomposition as a chemical hydrogen carrier in palladium membrane reactor*, Catalysis Today 236 (2014) 70-76.
52. T. Hejze, J.O. Besenhard, K. Kordesch, M. Cifrain, R.R. & Aronsson, *Current status of combined systems using alkaline fuel cells and ammonia as a hydrogen carrier*, Journal of Power Sources 176(2) (2008) 490-493.
53. R. Nayak-Luke, R. Bañares-Alcántara and I. Wilkinson, *"Green" Ammonia: Impact of Renewable Energy Intermittency on Plant Sizing and Levelized Cost of Ammonia,* Industrial & Engineering *Chemistry Research* **57**(43)(2018) 14607-14616.
54. M. Righettoni, A. Amann, and S.E. Pratsinis, *Breath analysis by nanostructured metal oxides as chemo-resistive gas sensors,* Materials Today **18**(3) (2015)163-171.
55. F. Meng, X. Li, Z. Yuan, Y. Lei, T. Qi and J. Li , *Ppb-Level Xylene Gas Sensors Based on* Co_3O_4 *Nanoparticle-Coated Reduced Graphene Oxide(rGO) Nanosheets Operating at Low Temperature,* IEEE Trans. Instrum. Meas. 70 (2021) 9511510.

56. Y. Liu, H. Ji, Z. Yuan and F. Meng, *Conductometric butanone gas sensor based on* Co_3O_4 *modified* SnO_2 *hollow spheres with ppb-level detection limit,* Sensors Actuators B 374 (2023) 132787.
57. S. Abdulla, T.L. Mathew and B. Pullithadathil, *highly sensitive, room temperature gas sensor based on polyaniline-multiwalled carbon nanotubes (PANI/MWCNTs) nanocomposite for trace-level ammonia detection*, Sensors Actuators B 221 (2015) 1523–34.
58. I. Manisalidis, E. Stavropoulou, A. Stavropoulos and E. Bezirtzoglou, *Environmental and Health Impacts of Air Pollution: A Review*, Front Public Health 8 (2020) 14.
59. L. Wang, M. Xia, H. Wang, K. Huang, C. Qian, C.T. Maravelias and G.A. Ozin, *Greening Ammonia toward the Solar Ammonia Refinery*, Joule 2 (2018) 1055–74.
60. D. Angeles, K. Are, L. Razon and R. Tan, *Twenty-Four Years of PRES Conferences: Recent Past, Present and Future-Process Integration Towards Sustainability*, Chemical Engineering Transactions 61 (2017) 271–6.
61. Y. Zhang, J. Zhang, Y. Jiang, Z. Duan, B. Liu, Q. Zhao, S. Wang, Z. Yuan and H. Tai, *Ultrasensitive flexible* NH_3 *gas sensor based on polyaniline/*$SrGe_4O_9$ *nanocomposite with ppt-level detection ability at room temperature*, Sensors Actuators B 319 (2020) 128293.
62. V. Modafferi, G. Panzera, A. Donato, P.L. Antonucci, C. Cannilla, N. Donato, D. Spadaro and G. Neri, *Highly sensitive ammonia resistive sensor based on electrospun* V_2O_5 *fibers,* Sensors Actuators B 163 (2012) 61–8.
63. Y. Sharma, N. Sharma, G.S. Rao and B.V.R. Chowdari, *Lithium recycling behaviour of nano-phase-*$CuCo_2O_4$ *as anode for lithium-ion batteries*, J. Power Sources 173 (2007) 495.
64. Q. Feng, X. Li, J. Wang and A.M. Gaskov, *Reduced graphene oxide (rGO) encapsulated* Co_3O_4 *composite nanofibers for highly selective ammonia sensors*, Sensors and Actuators B 222 (2016) 864–70.
65. M. Xu and J.P. Cheng, *The advances of* Co_3O_4 *as gas sensing materials: A review,* J. of Alloys and Compounds 686 (2016) 753–68.
66. Y. Wang, W. Wang and W. Song, *Binary CuO/*Co_3O_4 *nanofibers for ultrafast and amplified electrochemical sensing of fructose*, Electrochim. Acta 56 (2011) 10191–6.

67. A. Al-Sarraj, B. Salah, A.I. Ayesh, K.M. Saoud, A.A. El Mel, A. Rehman, A. Bermak and Y. Haik, *Fabrication of Ag_2O/WO_3 based sensors for detection of hydrogen sulfide,* Sens. Actuators, A333 (2022) 113256.

68. S. Jain, A. Patrike, S.S. Badadhe, M. Bhardwaj and S. Ogale, *Room-Temperature Ammonia Gas Sensing Using Mixed-Valent $CuCo_2O_4$ Nanoplatelets: Performance Enhancement through Stoichiometry Control*, ACS Omega 3 (2018) 1977–82.

69. M. Matsuguchi, T. Nakamae, R. Fujisada and S. Shiba, *A Highly Sensitive Ammonia Gas Sensor Using Micrometer-Sized Core–Shell-Type Spherical Polyaniline Particles*, Sensors 21 (2021) 7522.

70. M. Wojciechowska, M. Zieliński, A. Malczewska, W. Przystajko and M. Pietrowski, *Copper–cobalt oxide catalysts supported on MgF_2 or Al_2O_3—their structure and catalytic performance*, Appl. Catal., A 298 (2006) 225–31.

71. Z. Dou, C. Cao, Y. Chena and W. Song, *Fabrication of porous Co_3O_4 nanowires with high CO sensing performance at a low operating temperature,* Chem. Commun. 50 (2014) 14889–91.

72. S. Wang, C. Xiao, P. Wang, Z. Li, B. Xiao, R. Zhao, T. Yang and M. Zhang, *Co_3O_4 hollow nanotubes: Facile synthesis and gas sensing properties*, Mater. Lett. 137 (2014) 289–92.

73. H.-M. Jeong, J.-H. Kim, S.-Y. Jeong, C.-H. Kwak and J.-H. Lee, *Co_3O_4–SnO_2 Hollow Heteronanostructures: Facile Control of Gas Selectivity by Compositional Tuning of Sensing Materials via Galvanic Replacement*, ACS Appl. Mater. Interfaces 8 (2016) 7877–83.

74. C. W. Na, H.-S. Woo, I.-D. Kimb and J.-H. Lee, *Selective, sensitive, and reversible detection of H_2S using Mo-doped ZnO nanowire network sensors,* Chem. Commun. 47 (2011) 5148–50.

75. W. Li, H. Jung, N.D. Hoa, D. Kim, S.K. Hong and H. Kim, *Nanocomposite of cobalt oxide nanocrystals and single-walled carbon nanotubes for a gas sensor application,* Sensors and Actuators B 150 (2010) 160–166.

76. R. Vishnuraj, R. Unnathpadi and B. Pullithadathil, p-*Co_3O_4 supported heterojunction Carbon Nanofibers for Ammonia gas sensor applications,* J. Mater. NanoSci. 9 (2022) 61–67.

77. P.H. Phuoc, N.N. Viet, N.V. Chien, N.V. Hoang, C.M. Hung, N.D. Hoa c, Nguyen Van Duy , H.S. Hong, D.D. Trung, N.V. Hieu ,*Comparative study of CuO/*Co_3O_4 *external and CuO-*Co_3O_4 *internal heterojunctions: Do these factors always enhance gas-sensing performance?*, Sens. Actuators B 384 (2023) 133620.
78. R. Mohandoss, S. Dhanuskodi, B. Renganathan and D. Sastikumar, *Gas sensing property of lithium tetraborate clad modified fiber optic sensor*, Curr. Appl Phys. 13 (2013) 957–63.
79. A. Azam, *Microwave assisted synthesis and characterization of Co doped Cu ferrite nanoparticles,* J. of Alloys and Compounds 540 (2012) 145–53.
80. J.M. Walker, S.A. Akbar and P.A. Morris, *Synergistic effects in gas sensing semiconducting oxide nano-heterostructures: A review,* Sens. Actuators B 286 (2019) 624–40.
81. Y.Lin, K.Kan, W.Song, G. Zhang, L. Dang, Y. Xie, P. Shen, L. Li, K. Shi, *Controllable synthesis of* Co_3O_4*/polyethyleneimine-carbon nanotubes nanocomposites for CO and* NH_3 *gas sensing at room temperature,* J. Alloys Compd. 639 (2015) 187–196.
82. Z. Li, Z. Lin, N. Wang, J. Wang , W. Liu, K. Sun and Z. Wang, High precision NH_3 sensing using network nano-sheet Co_3O_4 arrays based sensor at room temperature, Sensors Actuators B 235 (2016) 222–31.
83. E. Fazio, S. Spadaro, C. Corsaro, G. Neri, S.G. Leonardi, F. Neri, N. Lavanya, C. Sekar, N. Donato and G. Neri, *Metal-Oxide Based Nanomaterials: Synthesis, Characterization and Their Applications in Electrical and Electrochemical Sensors,* Sensors 21 (2021) 2494.
84. V. Modafferi, S. Trocino, A. Donato, G. Panzera and G. Neri, *Electrospun* V_2O_5 *composite fibers: Synthesis, characterization and ammonia sensing properties*, Thin Solid Films 548 (2013) 689–694.
85. E. Llobet, *Gas sensors using carbon nanomaterials: a review*, Sens. Actuators B Chem. 179 (2013) 32–45.
86. P. Dariyal, S. Sharma, G.S. Chauhan, B.P. Singh, S.R. Dhakate, *Recent trends in gas sensing via carbon nanomaterials: outlook and challenges*, Nanoscale Adv. 3 (2021) 6514–6544.

87. P. Kumar, S. Dua, R. Kaur, M. Kumar, G. Bhatt, *A review on advancements in carbon quantum dots and their application in photovoltaics*, RSC Adv. 12 (2022) 4714–4759.
88. G. Nocito, G. Calabrese, S. Forte, S. Petralia, C. Puglisi, M. Campolo, E. Esposito, S. Conoci, *Carbon dots as promising tools for cancer diagnosis and therapy*, Cancers 13 (9) (2021) 1991.
89. R. Wang, K.Q. Lu, Z.R. Tang, Y.J. Xu, *Recent progress in carbon quantum dots: synthesis properties and applications in photocatalysis*, J. Mater. Chem. A 5 (2017) 3717–3734.
90. Y. Zhou, J. He, R. Chen, X. Li*, Recent advances in biomass-derived graphene and carbon nanotubes*, Mater. Today Sustain. 18 (2022), 100138.
91. G. Nocito, E.L. Sciuto, D. Franco, F. Nastasi, L. Pulvirenti, S. Petralia, C. Spinella, G. Calabrese, S. Guglielmino, S. Conoci, *Physicochemical characterization and antibacterial properties of carbon dots from two mediterranean olive solid waste cultivars*, Nanomaterials 12 (5) (2022) 885.
92. C. Long, Z. Jiang, J. Shangguan, T. Qing, P. Zhang, B. Feng, *Applications of carbon dots in environmental pollution control: a review*, Chem. Eng. J. 406 (2021), 126848.
93. J. Liu, R. Li, B. Yang, *Carbon dots: a new type of carbon-based nanomaterial with wide applications*, ACS Cent. Sci. 6 (12) (2020) 2179–2195,
94. C. Kang, Y. Huang, H. Yang, X.F. Yan, Z.P. Chen, *A review of carbon dots produced from biomass wastes*, Nanomaterials 10 (11) (2020) 2316.
95. X. Sun, Y. Lei, *Fluorescent carbon dots and their sensing applications*, Trends Anal. Chem. 89 (2017) 163–180.
96. H. Li, Z. Kang, Y. Liu, S.T. Lee, *Carbon nanodots: synthesis properties and applications,* J. Mater. Chem.. 22 (2012) 24230–24253.
97. Y. Sun, J. Li, D. He, X. Wang, Y. Shi, L. Pan*, Recent progress on performances and mechanisms of carbon dots for gas sensing*, Luminescence (2022) 1–13.
98. Z. Yu, L. Zhang, X. Wang, D. He, H. Suo, C. Zhao, *Fabrication of ZnO/Carbon quantum dots composite sensor for detecting NO gas*, Sensors 20 (17) (2020) 4961.
99. Sawalha, K. Moulaee, G. Nocito, A. Silvestri, S. Petralia, M. Prato, S. Bettini, L. Valli, S. Conoci, G. Neri, *Carbon-dots conductometric sensor for high performance gas sensing*, Carbon Trends 5 (2021), 100105.

100. M. Urso, S.G. Leonardi, G. Neri, S. Petralia, S. Conoci, F. Priolo, S. Mirabella, *Room temperature detection and modelling of sum-ppm NO_2 by low-cost nanoporous NiO film*, Sens. Actuators B Chem. 305 (2020), 127481.

101. S.S. Jones, P. Sahatiya, S. Badhulika, *One step high yield synthesis of amphiphilic carbon quantum dots derived from chia seeds: a solvatochromic study*, New J. Chem. 41 (2017) 13130–13139.

102. R. Atchudan, T.N.J.I. Edison, Y.R. Lee, *Nitrogen-doped carbon dots originating from unripe peach for fluorescent bioimaging and electrocatalytic oxygen reduction reaction,* J. Colloid Interface Sci. 482 (2016) 8–18.

103. K. Nakamoto, *Infrared and Raman Spectra of Inorganic and Coordination Compounds,* John Wiley & Sons, Inc,, New York, USA (1978).

104. Y.T. Yen, Y.S. Lin, T.Y. Chen, S.C. Chyueh, H.T. Chang, *Carbon dots functionalized papers for high-throughput sensing of 4-chloroethcathinone and its analogues in crime sites*, R. Soc. Open Sci. 6 (2019), 191017.

105. N.A. Alarfaj, M.F. El.Tohamy, H.F. Oraby, *CA 19-9 pancreatic tumor marker fluorescence immunosensing detection via immobilized carbon quantum dots conjugated gold nanocomposite*, Int. J. Mol. Sci. 19 (4) (2018) 1162.

106. S. Sawalha, A. Silvestri, A. Criado, S. Bettini, M. Prato, S. Bettini, L. Valli, *Tailoring the sensing abilities of carbon nanodots obtained from olive solid wastes*, Carbon 167 (2020) 696–708.

107. C. Tudisco, V. Oliveri, M. Cantarella, G. Vecchio, G.G. Condorelli, *Cyclodextrin anchoring on magnetic Fe3O4 nanoparticles modified with phosphonic linkers,* Eur. J. Inorg. Chem. (2012) 5323–5331

108. E. Smecca, A. Motta, M.E. Fragala, ` Y. Aleeva, G.G. Condorelli, *Spectroscopic and theoretical study of the grafting modes of phosphonic acids on ZnO nanorods*, J. Phys. Chem. C 117 (2013) 5364–5372.

109. C. Tudisco, M.T. Cambria, F. Sinatra, F. Bertani, A. Alba, A.E. Giuffrida, S. Saccone, E. Fantechi, C. Innocenti, C. Sangregorio, E. Dalcanale, G.G. Condorelli, *Multifunctional magnetic nanoparticles for enhanced intracellular drug transport*, J. Mater. Chem. B 3 (2015) 4134–4145.

110. D. Briggs, G. Beamson, *Primary and secondary oxygen-induced C1s binding energy shifts in X-ray photoelectron spectroscopy of polymers*, Anal. Chem. 64 (1992) 1729–1736.

111. X. C. G. Huang, H. Z. C. Wang, D. C. Z. Huang, H. Xie, *Photoluminescent carbon dots derived from sugarcane molasses: synthesis properties and applications*, RSC Adv. 7 (2017) 47840–47847.

112. S. P. A. Mewada, N. M. S. Shinde, M. T. G. Oza, M. S. M. Sharon, *Green synthesis of biocompatible carbon dots using aqueous extract of Trapa bispinosa peel*, Mater. Sci. Eng. C 33 (2013) 2914–2917.

113. D. Wang, Z. Wang, Q. Zhan, Y. Pu, J.X. Wang, N. R. Foster, L. Dai, *Facile and scalable preparation of fluorescent carbon dots for multifunctional applications*, Engineering 3 (2017) 402–408.

114. K. J. Mintz, M. Bartoli, M. Rovere, Y. Zhou, S. D. Hettiarachchi, S. Paudyal, J. Chen, J. B. Domena, P. Y. Liyanage, R. Sampson, D. Khadka, R. R. Pandey, S. Huang, C. C. Chusuei, A. Tagliaferro, R. M. Leblanc*, A deep investigation into the structure of carbon dot*s, Carbon 173 (2021) 433–447.

115. D.W. Jeong, K.H. Kim, B.S. Kim, Y.T. Byun, *Characteristics of highly sensitive and selective nitric oxide gas sensors using defect-functionalized single-walled carbon nanotubes at room temperature*, Appl. Surf. Sci. 550 (2021), 149250.

116. J. Maklin, T. Mustonen, K. Kordas, S. Saukko, G. Toth, J. Vah akangas, *Nitric oxide gas sensors with functionalized carbon nanotubes*, Phys. Stat. Sol. b 244 (2007) 4298–4302.

117. M. Reddeppa, B.G. Park, N.D. Chinh, D. Kim, J.E. Oh, T.G. Kim, M.D. Kim, *A novel low-temperature resistive NO gas sensor based on InGaN/GaN multi-quantum wellembedded p-i-n GaN nanorods*, Dalton Trans. 48 (2019) 1367–1375.

118. Z. Ma, K. Yang, C. Xiao, L. Jia, *Electrospun Bi-doped SnO_2 porous nanosheets for highly sensitive nitric oxide detection*, J. Hazard. Mater. 416 (2021), 126118.

119. S. Barazzouk, R.P. Tandon, S. Hotchandani, *MoO_3-based sensor for NO, NO_2 and CH_4 detection*, Sens. Actuators B: Chem. 119 (2006) 691–694.

120. Z.X. Cai, H.Y. Li, X.N. Yang, X. Guo, *NO sensing by single crystalline WO_3 nanowires*, Sens. Actuators B: Chem. 219 (2015) 346–353.

121. M. Kaur, S. Kailasaganapathi, N. Ramgir, N. Datta, S. Kumar, A.K. Debnath, D. K. Aswal, S.K. Gupta, *Gas dependent sensing mechanism in ZnO nanobelt sensor*, Appl. Surf. Sci. 394 (2017) 258–266.

122. R. Leturca, R. Bhusari, E. Barborini, *Physical mechanisms underpinning conductometric gas sensing properties of metal oxide nanostructures*, Adv. Phys. X 7 (2022) 2044904.

123. N.K. Chowdhury, B. Bhowmik, *Micro/nanostructured gas sensors: the physics behind the nanostructure growth sensing and selectivity mechanisms*, Nanoscale Adv. 3 (2021) 73–9.

124. N. Barsan, U. Weimar, *Conduction model of metal oxide gas sensors, J. Electroceram*, 7 (2001) 143–167.

125. Tang, Z. Cao, *Adsorption of nitrogen oxides on graphene and graphene oxides: insights from density functional calculations*, J. Chem. Phys. 134 (2011), 044710.

126. E. Salih, A.I. Ayesh, *Enhancing the sensing performance of zigzag graphene nanoribbon to detect NO, NO_2, and NH_3 gases*, Sensors 20 (14) (2020) 3932.

127. S. Arunragsa, Y. Seekaew, W. Pon-On, C. Wongchoosuk, *Hydroxyl edge-functionalized graphene quantum dots for gas-sensing applications*, Diam. Relat. Mater. 105 (2020), 107790.

128. C. Liu, Q. Ma, H. He, G. He, J. Ma, Y. Liu, Y. Wu, *Structure-activity relationship of surface hydroxyl groups during NO_2 adsorption and transformation on TiO_2 nanoparticles*, Environ. Sci. Nano 4 (2017) 2388–2394.

129. S. Rathinavel, K. Priyadharshini, D. Panda, *A review on carbon nanotube: An overview of synthesis, properties, functionalization, characterization, and the application, Mater.Sci. Eng B. 268* (2021) 115095.

130. M. Chunrong, L. Xiang, L. Deng, H. Yan-Yan, L. Sungsik, L. Xiao-Zhen, H. Yu-Shi, M. Zi-Feng, X. Hui, *Coaxial Carbon Nanotube Supported TiO_2@MoO_2@Carbon Core–Shell Anode for Ultrafast and High-Capacity Sodium Ion Storage*, ACS Nano 13(1) (2019) 671-680.

131. M.H. Raza, R. Di Chio, K. Movlaee, P. Amsalem, N. Koch, N. Barsan, G. Neri, N. Pinna, *Role of Heterojunctions of Core−Shell Heterostructures in Gas Sensing*, ACS. Appl. Mater. Interfaces, 14 (2022) 22041-22052.

132. K. Moulaee, M.H. Raza, N. Pinna, N. Donato, G. Neri, *CNT/Al_2O_3 core-shell nanostructures for the electrochemical detection of dihydroxybenzene isomers*, Phys. Chem. Chem. 23 (2021) 14064–14074.

133. M.H. Raza, K. Movlaee, S.G. Leonardi, N. Barsan, G. Neri, N. Pinna, *Gas Sensing of NiO-SCCNT Core-Shell Heterostructures: Optimization by Radial Modulation of the Hole-Accumulation*, Lay, Adv. Funct. Mater., 30 (2020) 1906874.

134. M.H. Raza, K. Movlaee, Y. Wu, S.M. El-Refaei, M. Karg, S.G. Leonardi, G. Neri, N. Pinna, *Tuning the NiO Thin Film Morphology on Carbon Nanotubes by Atomic Layer Deposition for Enzyme-Free Glucose Sensing*, ChemElectroChem.6 (2019) 383–392.

135. Y. Fan, Y. Wu, G. Clavel, M.H. Raza, P. Amsalem, N. Koch, N. Pinna, *Optimization of the Activity of Ni-Based Nanostructures for the Oxygen Evolution Reaction.* ACS Appl. Energy Mater., 1 (2018) 4554−4563.

136. A. Staerz, X. Gao, F. Cetmi, Z. Ming, U. Weimar, T. Zhang, N. Barsan, *Dominant Role of Heterojunctions in Gas Sensing with Composite Materials*, ACSAppl.Mater.Interfaces 12 (2020) 21127−21132.

137. H. Y. Si, C.H. Liu, H. Xu, T.M. Wang, H.L Zhang, *Shell-Controlled Photoluminescence in CdSe/CNT Nanohybrids*, Nanoscale Res Lett. 4 (2009) 1146.

138. Y. Zhang, C. Guerra-Nuñez, M. Li, J. Michler, H.G. Park, M.D. Rossell, R. Erni, I. Utke, *High Conformity and Large Domain Monocrystalline Anatase on Multiwall Carbon Nanotube Core-Shell Nanostructure: Synthesis, Structure, and Interface.* Chem. Mater. 28 (10) (2016) 3488-3496.

139. C. Marichy, M. Bechelany, N. Pinna, *Atomic Layer Deposition of Nanostructured Materials for Energy and Environmental Applications,* Adv. Mater.,24 (2012) 1017-1032.

140. N. Pinna, M. Knez, Atomic *layer deposition of nanostructured materials.* Wiley-VCH.(2011), ISBN: 978-3-527-32797-3.

141. H.C. Kim, H. Kim, J.U. Lee, H.B. Lee, D.H. Choi, J.H. Lee, W.H. Lee, S.H. Jhang, B.H. Park, H. Cheong, S.W. Lee, H.J. Chung, *Engineering Optical and Electronic Properties of WS_2 by Varying the Number of Layers*, ACS Nano.9,7, (2015) 6854–6860.

142. A.J. Saleh Ahammad, J.J. Lee, Md. Aminur Rahman*, Electrochemical Sensors Based on Carbon Nanotubes,* Sensor, 9 (2009) 2289-2319.

143. S. G. Leonardi, W. Wlodarski, Y. Li, N. Donato, Z. Sofer, M. Pumera, G. Neri, *A highly sensitive room temperature humidity sensor based on 2D-*WS_2 *nanosheets,* FlatChem. 9 (2018) 21-26.

144. T. Järvinen, G.S. Lorite, J. Peräntie, G. Toth, S. Saarakkala, V.K. Virtanen, K. Kordas, WS_2 *and* MoS_2 *thin film gas sensors with high response to* NH_3 *in air at low temperature,* Nanotechnol. 30 (2019) 405501.

145. Y. Xu, J. Xie, Y. Zhang, F. Tian, C. Yang, W. Zheng, X. Liu, J. Zhang, N. Pinna, Edge*-enriched* WS_2 *nanosheets on carbon nanofibers boosts* NO_2 *detection at room temperature,* J. Hazard. Mater. 411 (2021) 125120.

146. J.H. Cha, S.J. Choi, S. Yu, I.D. Kim, *2D* WS_2*-edge functionalized multi-channel carbon nanofibers: effect of* WS_2 *edge-abundant structure on room temperature* NO_2 *sensing,* J. Mater. Chem. A. 5 (2017) 8725–8732.

147. Y. Wu, M.H. Raza, Y.C. Chen, P. Amsalem, S. Wahl, K. Skrodczky, X. Xu, K. Shyam Lokare, M. Zhukush, P. Gaval, N. Koch, E. A. Quadrelli, N. Pinna, *Self-Limited Atomic Layer Deposition of WS2 Based on the Chemisorption and Reduction of Bis(t-butylimino)bis(dimethylamino) Complexes.* Chem. Mater. 31 (2019) 1881–1890.

148. J. L. Wree, J.P. Glauber, D. Ohl, A. Niesen, A. Kostka, D. Rogalla, W. Schuhmann, A. Devi, *Sensing and electrocatalytic activity of tungsten disulphide thin films fabricated via metal–organic chemical vapour deposition,* J. Mater. Chem. C. 9 (2021) 10254.

149. J. Liu, Y. Lu, X. Cui, G. Jin, Z. Zhai, Effect *of depletion layer width on electrical properties of semiconductive thin film gas sensor: a numerical study based on the gradient-distributed oxygen vacancy model.* Appl. Phys. A. 122 (2016) 146.

150. X. He, M. Wu, Z. Ao, B. Lai, Y. Zhou, T. An, S. Wang, *Metal-organic frameworks derived C/*TiO_2 *for visible light photocatalysis: Simple synthesis and contribution of carbon species*, Hazardous Materials, 403 (2021) 124048.

151. T. Anukunprasert a, C. Saiwana , E. Traversa, *The development of gas sensor for carbon monoxide monitoring using nanostructure of Nb–*TiO_2, Science and Technology of Advanced Materials 6 (2005) 359–363.

152. X. Tian, X. Cui, T. Lai, J. Ren, Z. Yang, M. Xiao, B. Wang, X. Xiao, Y. Wang, Gas sensors based on TiO_2 nanostructured materials for the detection of hazardous gases: A review, Nano Materials Science 3 (2021) 390–403.

153. M. Frisch, J. Laun, J. Marquardt, A. Arinchtein, K. Bauerfeind, D. Bernsmeier, M. Bernicke, T. Bredowb and R. Kraehnert, *Bridging experiment and theory: enhancing the electrical conductivities of soft-templated niobium-doped mesoporous titania films*, Phys. Chem. Chem. Phys., 23 (2021) 3219-3224.

154. K. Chena, S. Chenb, M. Pia, D. Zhang, *SnO_2 nanoparticles/TiO_2 nanofibers heterostructures: in situ fabrication and enhanced gas sensing performance*, Solid-State Electronics (2019).

155. S.T. Navale, Z.B. Yanga, Chenshitao Liua, P.J. Caoa, V.B. Patil, N.S. Ramgir, R.S. Manee, F.J. Stadler, *Enhanced acetone sensing properties of titanium dioxide nanoparticles with a sub-ppm detection limit,* Sensors and Actuators B 255 (2018) 1701–1710.

156. M. Vallet-Reg, F. Balas, and D. Arcos, *Mesoporous Materials for Drug Delivery, Angew.* Chem. Int. Ed. 46 (2007) 7548 – 7558.

157. J. Ka¨rger and D. Freude, *Mass transfer in Micro- and Mesoporous material*s, Chem. Eng. Technol. 25 (2002) 769–778.

158. J. Chen, Z. Hua,Y. Yan, A.A Zakhidov, R.H. Baughman, L. Xu, *Template synthesis of ordered arrays of mesoporous titania spheres*, Chem. Commun. 46(11) (2010) 1872.

159. W. Xu, Dr. P. A. Russo, Dr. T. Schultz, Prof. N. Koch, Prof. N. Pinna, *Niobium-Doped Titanium Dioxide with High Dopant Contents for Enhanced Lithium-Ion Storage*, ChemElectroChem, 7 (2020) 4016-4023.

160. R. Abdelghani, H. Shokry Hassan, I. Morsi, A.B. Kashyout, *Nano-architecture of highly sensitive SnO_2–based gas sensors for acetone and ammonia using molecular imprinting technique.* Sens. Actuators B Chem. 297 (2019) 126668.

161. X. Yang, X. Hao, T. Liu, F. Liu, B. Wang, C. Ma, X. Liang, C. Yang, H. Zhu, J. Zheng, et al. *CeO_2-based mixed potential type acetone sensor using La1−xSrxCoO_3 sensing electrode.* Sens. Actuators B Chem. 269 (2018) 118–126.

162. M. Šetka, F.A. Bahos, D. Matatagui, I. Gràcia, E. Figueras, J. Drbohlavová, S. Vallejos, *Love wave sensors with silver modified polypyrrole nanoparticles for VOCs monitoring*. Sensors 20 (2020) 1432.

163. M. Masikini, M. Chowdhury, O. Nemraoui, *Metal oxides: Application in exhaled breath acetone chemiresistive sensors*. J. Electrochem. Soc. 167 (2020) 037537.

164. A. Amann, G. Poupart, S. Telser, M. Ledochowski, A. Schmid, S. Mechtcheriakov, *Applications of breath gas analysis in medicine*. Int. J. Mass Spectrom. 239 (2004) 227–233.

165. T. Goto, T. Itoh, T. Akamatsu, Y. Sasaki, K. Sato, W. Shin, *Heat transfer control of micro-thermoelectric gas sensor for breath gas monitoring*. Sens. Actuators B Chem. 249 (2017) 571–580.

166. S. Zhang, W. Jiang, Y. Li, X. Yang, P. Sun, F. Liu, X. Yan, Y. Gao, X. Liang, J. Ma, et al. *Highly-sensitivity acetone sensors based on spinel-type oxide ($NiFe_2O_4$) through optimization of porous structure*. Sens. Actuators B Chem. 291 (2019) 266–274.

167. M. Righettoni, A. Tricoli, *Toward portable breath acetone analysis for diabetes detection*. J. Breath Res. 5 (2011) 037109.

168. J.-H. Kima, J.-H. Leea, A. Mirzaei, H. W. Kimb, S. S. Kim, *SnO_2 (n)-NiO (p) composite nanowebs: Gas sensing properties and sensing mechanisms*, Sensors and Actuators B 258 (2018) 204–214.

169. M. Barsoum, *Fundamentals of ceramics*, CRC press, (2002).

170. S. Seo, I. J. Park, M. Kim, S. Lee, C. Bae, H.S. Jung, N.-G. Park, J. Y. Kim and H. Shin, *An ultra-thin, un-doped NiO hole transporting layer of highly efficient (16.4%) organic–inorganic hybrid perovskite solar cells*, Nanoscale 8 (2016) 11403.

171. M.H. Raza, K. Movlaee, S. G. Leonardi, N. Barsan, G. Neri, and N. Pinna*, Gas Sensing of NiO-SCCNT Core–Shell Heterostructures: Optimization by Radial Modulation of the Hole-Accumulation Layer*, Adv. Funct. Mater.30 (2020) 1906874.

172. M.H. Raza, R. Di Chio, K. Movlaee, P. Amsalem, N.t Koch, N. Barsan, G. Neri, and N. Pinna, *Role of Heterojunctions of Core−Shell Heterostructures in Gas Sensing*, ACS Appl. Mater. Interfaces 14 (2022) 22041−22052.

173. J. Fanga, Y. Zhua, D. Wua, C. Zhanga, S. Xua, D. Xionga, P. Yanga, L. Wanga, P.K. Chu, *Gas sensing properties of NiO/SnO$_2$ heterojunction thin film,* Sensors and Actuators B 252 (2017) 1163–1168.

174. S. Gun-Joo, K. Hyejoon, C. Seungbok, H.S. Keun, L. Chongmu*, Prominent Gas Sensing Performance of TiO$_2$-Core/NiO-Shell Nanorod Sensors,* Journal of Nanoscience and Nanotechnology, 17 (2017) 4099-4102.

175. G. Ranaa, P. Dhimana, A. Kumar, D.-V. N. Vo, G. Sharmab, S. Sharmab, M. Naushad, *Recent advances on nickel nano-ferrite: A review on processing techniques, properties and diverse applications*, Chemical Engineering Research and Design 175 (2021) 182–208.

176. D. Harikishore K. Reddy, Y.-S. Yun, *Spinel ferrite magnetic adsorbents: Alternative future materials for water purification?*, Coordination Chemistry Reviews, 315 (2016) 90-111.

177. A.M.A. Henaish, O.M. Hemeda, A. Alqarni, D.E. El Refaay, S. Mohamed, M.A. Hamad, *The role of flash auto-combustion method and Mn doping in improving dielectric and magnetic properties of CoFe$_2$O$_4$.* Appl. Phys. A 126 (2020) 834.

178. E.A. Arrasheed, T.M. Meaz, R.M., Shalaby, B.I. Salem, O.M. Hemeda, A.M.A. Henaish, *Rietveld refinement, cation distribution, morphological and magnetic study of NiAl$_x$Fe$_{2-x}$O$_4$ nanoparticles.* Appl. Phys. A 127 (2021) 221.

179. M. Abdullah Dar, J. Shah, W.A. Siddiqui, R.K. Kotnala, *Study of structure and magnetic properties of Ni–Zn ferrite nano-particles synthesized via co-precipitation and reverse micro-emulsion technique.* Appl. Nanosci. 4 (2021) 675–682.

180. S. Liu, F. He, Z. Huang, A. Zheng, Y. Feng, Y. Shen, H. Li, H. Wu, P. Glarborg, *Screening of NiFe$_2$O$_4$ nanoparticles as oxygen carrier in chemical looping hydrogen production.* Energy Fuels 30 (2016) 4251–4262.

181. K. Pubby, S.R. Bhongale, P. Vasambekar, S.B. Narang, *Ni0.1Co0.9Fe2O4 spinel ferrite as a promising magneto-dielectric substrate for X-band microstrip patch antenna.* In: 2019 3rd International Conference on Electronics, Materials Engineering & Nano-Technology (IEMENTech), IEEE, (2019) 1–4.

182. K. Gupta, A. Kaushik, K.B. Tikoo, V. Kumar, S. Singhal, *Enhanced catalytic activity of composites of* $NiFe_2O_4$ *and nano cellulose derived from waste biomass for the mitigation of organic pollutants.* Arab. J. Chem. 13 (2020) 783–798.

183. Y. Cao, Z. Xing, M. Hu, Z. Li, X. Wu, T. Zhao, Z. Xiu, S. Yang, W. Zhou, *Mesoporous black N-*TiO_{2-x} *hollow spheres as efficient visible-light-driven photocatalysts,* J. Catal. 356 (2017) 246–254.

184. V. Mathe, R. Kamble, *Electrical and dielectric properties of nano crystalline Ni–Co spinel ferrites,* Mater. Res. Bull. 48 (2013) 1415–1419.

185. R. Kashyap, R. Kumar, S. Devi, M. Kumar, S. Tyagi and D. Kumar, *Ammonia gas sensing performance of nickel ferrite nanoparticles,* Mater. Res. Express 6 (2019) 125034.

186. Z. Jia, R. Misra, *Magnetic sensors for data storage: perspective and future outlook,* Mater. Technol. 26 (2011) 191–199.

187. K. Pubby, S. Meena, S. Yusuf, S.B. Narang, *Cobalt substituted nickel ferrites via Pechini's sol–gel citrate route: X-band electromagnetic characterization.,* J. Magn. Magn. Mater. 466 (2018) 430–445.

188. S. Ahmed, Z. Ahmad, *Development of hexagonal nanoscale nickel ferrite for the removal of organic pollutant via Photo-Fenton type catalytic oxidation process,* Environ. Nanotechnol. Monit. Manag. 14 (2020) 100321.

189. P. Sivagurunathan, S.R. Gibin, *Preparation and characterization of nickel ferrite nano particles by co-precipitation method with citrate as chelating agent,* J. Mater. Sci. Mater. Electron. 27 (2016) 2601–2607.

190. K. Elayakumar, V. Sathana, R.T. Kumar, *Structural and magnetic characterization of rare earth element cerium-doped nickel ferrite nanoparticles (*$NiCe_xFe_{2-x}O_4$*) by sol-gel method with antibacterial activity.* J. Supercond. Nov. (2020) 1–8.

191. M. Venkatesh, G.S. Kum, S. Viji, S. Karthi, E. Girija, *Microwave assisted combustion synthesis and characterization of nickel ferrite nanoplatelets,* Mod. Electron. Mater. 2 (2016) 74–78.

192. A. Manohar, V. Vijayakanth, R. Hong, *Solvothermal reflux synthesis of* $NiFe_2O_4$ *nanocrystals dielectric and magnetic hyperthermia properties*, J. Mater. Sci. Mater. Electron. 31 (2020) 799–806.

193. A.M.A. Henaish, O.M. Hemeda, A. Alqarni, D.E. Refaay, S. Mohamed, M.A. Hamad, *The role of flash auto-combustion method and Mn doping in improving dielectric and magnetic properties of* $CoFe_2O_4$, Appl. Phys. A 126 (2020) 834.

194. Z. Zhang, G. Yao, X. Zhang, J. Ma, H. Lin, *Synthesis and characterization of nickel ferrite nanoparticles via planetary ball milling assisted solid-state reaction*, Ceram. Int. 41 (2015) 4523–4530.

195. S.I.H. Taqvi, A.R. Solangi, J.A. Buledi, N.H. Khand, B. Junejo, A.F. Memon, S. Ameen, A. Bhatti, P.-L. Show, Y. Vasseghian, H. Karimi-Maleh, *Plant extract-based green fabrication of nickel ferrite (*$NiFe_2O_4$*) nanoparticles: An operative platform for non-enzymatic determination of pentachlorophenol*, Chemosphere 294 (2022) 133760.

196. N. Janudin, N.A.M. Kasim, V.F. Knight, M.N.F. Norrrahim, M.A.I.A. Razak, N. A. Halim, S.A.M. Noor, K. K. Ong, M. H. Yaacob, M. Z. Ahmad and W.M.Z.W. Yunusused, *Fabrication of a Nickel Ferrite/Nanocellulose-Based Nanocomposite as an Active Sensing Material for the Detection of Chlorine Gas*, Polymers 14 (2022) 1906.

197. V.S. Bhati, M. Hojamberdiev, M. Kumar, *Enhanced sensing performance of ZnO nanostructuresbased gas sensors: A review*, Energy Reports, 6 (2020) 46-6.

Chapter 6: Side works

6.1 Overview

This part of the thesis will highlight the collateral work carried out during the PhD period. An overview of biosensors will be made, focusing attention on electrochemical glucose sensors to connect us to the work done. In fact, the development of a glucose sensor will be discussed with an overview of the electrochemical techniques adopted for the work and the data will be shown.

6.2. Biosensors

In this section we will introduce biosensors, how they work and the different types of biosensors that exist. In particular, we will talk about the two enzymatic and non-enzymatic electrochemical detection methods, explaining the difference between the two detection techniques.

A biosensor is a device composed of a biological element, such as an enzyme or an antibody, and an electronic component to generate a measurable signal. The electronic component detects, records and transmits information regarding a physiological change or the presence of various chemical or biological materials in the environment. Biosensors come in different sizes and shapes [1]. To develop a biological sensor, the same parameters discussed previously apply, namely selectivity, sensitivity, linearity, response time, reproducibility and stability [2].

There are various classifications that can be made of a biosensor. In fact, they can be divided based on [3]:

- The *bioreceptor*. The receptor can be an enzyme, which is the most developed class, an immunosensor with high specificity and sensitivity, mainly used in diagnosis, aptamer or nucleic acid-based with high specificity for microbial strains and nucleic acid-containing analyte and microbial biosensors or whole cells.
- The *transducer*. In this class we find electrochemists; further grouped into potentiometric, amperometric, impedance and conductometric; electronic biosensors; thermal, optical, mass-based or gravimetric biosensors.

- the *technology*. The technology can be nano, surface plasmon resonance (SPR), biosensors on chip (lab-on-chip), electrometers.
- The *detection system*. The sensing system can be optical, electrical, electronic, thermal, mechanical and magnetic.

However, it has just been discussed that biosensors can be classified based on the bioreceptor. Bioreceptors are divided into:

- enzymes, whose mechanism is linked to the enzyme-analyte bond and the catalytic reaction generated, but they are sensitive, not very stable and require high costs [4];
- antibodies, whose mechanism is linked to antigen-antibody recognition. They have the structure of immunoglobulins made up of two heavy and two light polypeptide chains [3]. In this type of device, the antibodies are immobilized on the surface of the transducer, which comes into contact with the solution containing the analyte;
- aptamers are chemically synthesized single-stranded nucleic acids of DNA or RNA sequences. They bind selectively to target molecules and can be folded into two-dimensional (2D) and three-dimensional (3D) structures. They can be produced by many target molecules, such as contaminants, pesticides, drug residues, allergens [5];
- whole-cells (fungi, molds and viruses) for the ability to self-replicate and can interact with different analytes [6];
- molecularly imprinted polymers synthesized with specific functional groups and mimic enzymes by creating cross-linked polymer active sites for specific analytes;
- nanomaterials, a new class of biosensors that can be used with a double function as bioreceptor and transducer. They can be inorganic such as metal oxides or organic such as carbon nanotubes and graphene [7].

In this section more attention has been given to electrochemical biosensors. The basic principle of this class of sensors are electrochemical properties of the analyte and the transducer. Electrochemical biosensors exhibit high sensitivity, selectivity, and detection ability. Specifically, an electrochemical reaction takes place on the surface of the transducer between the bioreceptor and the analyte, producing detectable electrochemical signals in terms of voltage, current, impedance and capacitance [8]. Based on the principle of transduction, electrochemical biosensors include *potentiometric* (measure the charge generated by the analyte-bioreceptor interaction on the working electrode relative to the zero current reference electrode. Ion-selective electrodes and ion-sensitive field effect transistors are used to convert the reaction into an electrical signal) [8,9], *amperometric* (measure the current produced by a redox reaction of electroactive species on the working electrode when a constant potential is applied to the working electrode with respect to the reference electrode. The current produced on the surface of the working electrode is proportional to the concentration of the analyte present in the solution) [8], *impedimetric* (they measure the electrical impedance produced at the electrode/electrolyte interface. The in-phase/out-of-phase current response is measured as a function of frequency using an impedance analyzer) [10], *conductometric* (quantify the change in conductance that occurs in a pair of electrodes during an electrochemical reaction. Used to monitor metabolic processes in living biological systems) [11] and *voltammetric* (detect the analyte by measuring the current during the controlled change of the applied potential) [3] sensors. In Figure 6.1 a,b and c a schematic representation of electrochemical biosensors.

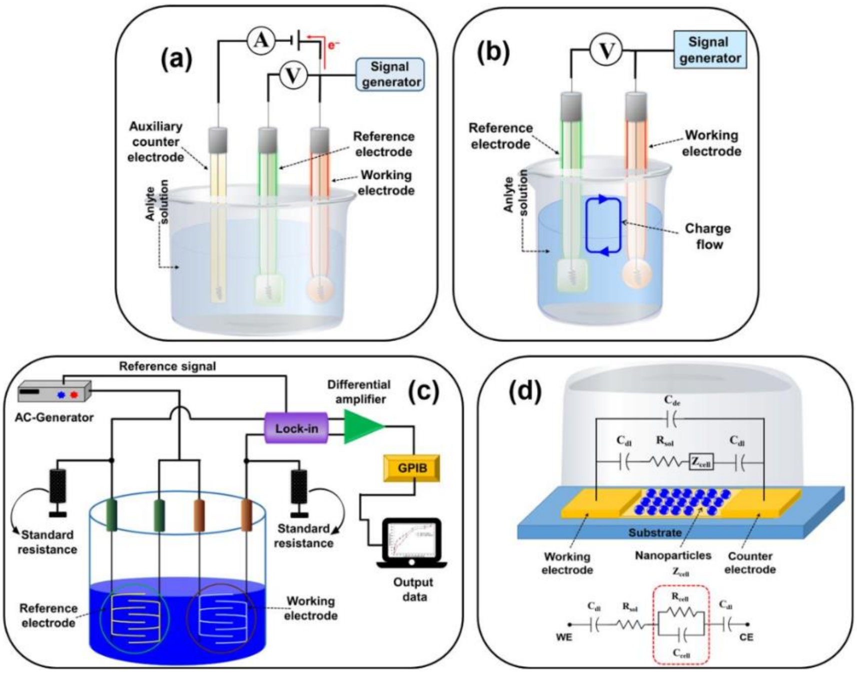

Figure 6.1. Electrochemical biosensors: (a) amperometric/voltammetric biosensors; (b) potenziometric biosensor and (c) impedimetric biosensor [3].

According to what has been discussed, biosensors are very versatile enough to be adopted in various applications, from engineering to biomedicine, to toxicology, they allow monitoring for food safety and above all monitoring to follow the progression of a disease. In recent years there has been an increasing development with new miniaturization, design and production technologies nanostructured devices at the micro level and new nanomaterial synthesis techniques. The possibility of being able to design biosensors with different biorectors was discussed, among them the introduction of nanomaterials as nanowires (NWs), nanoparticles (NPs), nanorods (NRs), carbon nanotubes (CNTs) and quantum dots (QDs) that have improved the sensitivity and stability of biosensors, they have also lowered production costs and have simplified their development with simpler syntheses. They can also be designed to detect specific analytes.

Subsequently, in fact, a biosensor developed with nanomaterials will be discussed.

6.3. Glucose Electrochemical biosensors

The versatility of biosensors has been discussed, therefore there are studies that focus on the development of electrochemical glucose sensors. The importance of these devices is linked to the monitoring of some diseases including diabetes mellitus or checking glucose levels in pregnant women or also food monitoring.

Diabetes is a chronic disease caused by a dysfunction of the pancreas that fails to produce enough insulin to regulate blood sugar or when the body is unable to use insulin produced. If the disease is underestimated, a series of health problems may arise related to the eyes, feet, kidney disease, hypertension, stroke, non-ketonic hyperglycemic syndrome, gastroparesis, heart disease, and mental health disorders, it can also affect pregnancy. A diabetic patient exhibits blood glucose concentrations of 5.6 and 6.9 mM (100-125 mg/dL) before the meal and 7.8 and 11 mM (140-199 mg/dL) 2 hours after a meal. 5 In a healthy patient, however, there are concentrations of 4-6 mM (70-110 mg/dL) before a meal (4-6 mM) and <7.8 mM (<140 mg/dL) 2 hours after a meal [12]. As a result, food and beverage manufacturing industries must reduce and control sugar levels while maintaining the quality and safety of ingredients. This requires monitoring and measuring sugars, phenols and alcohols throughout the manufacturing process and in the final product [13].

A common glucose biosensor is composed of a three-electrode system: working electrodes, reference electrodes and counter electrode. The working electrode is a sensor or transducer that responds to the electrochemical reaction. The reference electrode is stable, and its potential is known, an Ag/AgCl silver-silver chloride electrode is often used. The counter electrode completes the circuit between the electrolyte solution and the working electrode in the electrochemical cell. The counter electrode is usually made of an inert material, such as platinum (Pt), gold (Au), graphite, or carbon [14]. This class of sensors can be further divided into enzymatic and non-enzymatic biosensors.

An *enzymatic* glucose biosensor monitors oxygen consumption according to the following enzyme-catalyzed reaction in Figure 6.2:

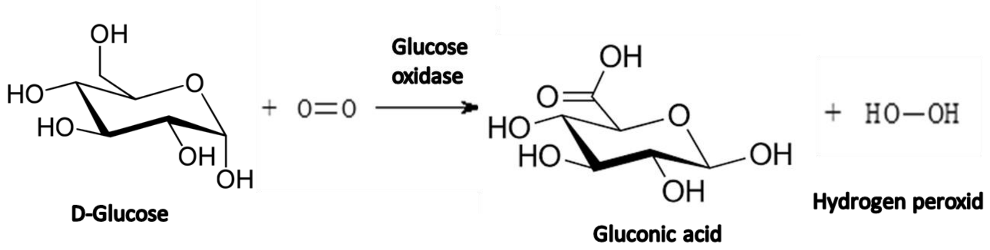

Figure 6.2. enzymatic reaction of glucose.

The first sensors were based on the immobilization of glucose oxidase (GOx) on a platinum (Pt) electrode, but oxygen generated interference, so they designed a two-electrode system that eliminated the interference. Furthermore, the reaction involved the reduction of the flavin group (FAD) to $FADH_2$ [15]. The problem has been overcome by developing sensors with oxidation mediators (Med-ox) or an electron acceptor that allows the reoxidation of GOx-FAD, the reaction is reversible. First generation sensors used O_2 as a Med-ox, second generation sensors used a synthetic acceptor such as a conducting polymer, third generation sensors used an electrode without the presence of a Med-ox, an example is the development of CNTs functionalized with amine groups and tin oxide (NH_2-TiO_2 -CNTs) used for the adsorption of GOx [16]. In Figure 6.3 the schematic representation of glucose reaction.

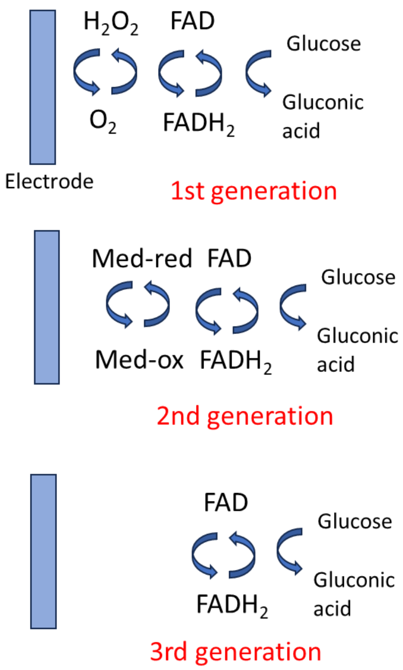

Figure 6.3. Enzymatic glucose oxidation mechanisms for the three different generations of biosensors.

The difficulty of these sensors is linked to the stability of the enzyme over time and the ability to bind it to the substrate. Hence, if enzymatic glucose sensing relies on the catalytic reaction of the enzyme to oxidize glucose, in *non-enzymatic* biosensors, it is the electrode surface that catalyzes the electrooxidation of glucose. Two models explain the operating mechanism. One model is based on activated chemisorption which involves the adsorption-desorption of glucose molecules on the surface of the electrode. In detail, the C-1 and the hydrogen atom of glucose interact with the electrode surface, causing the dehydrogenation of the C-1 and its adsorption on the electrode surface. After electrooxidation of the adsorbent occurs, gluconolactone is oxidized to gluconic acid. This process can be influenced by the electronic state of the redox center, the unoccupied d orbitals of the metals and the presence of possible defects in the metal catalyst (see Figure 6.4a) [12].

The second model, incipient hydrous oxide adatom mediator (IHOAM), focuses on the role of hydroxyl radicals in the electrocatalytic process. This model is based on the presence of active metal atoms, which involve the formation of a first oxidation phase, this phase generates hydrated oxide (OHads) on the electrode and M-OH chemisorption is formed. This facilitates the adsorption and oxidation of glucose molecules. Both consider a noble metal as the electrode, but the same mechanism occurs on metal oxide electrodes on anodic polarization.

The metal oxide is oxidized to a higher oxidation state, allows the absorption of OH ions, hydrated oxide is formed, which then mediates glucose in oxidation process. Oxides generally have a transition metal and the redox center of the transition plays a role in the glucose oxidation reaction. The electrolyte condition suitable for the non-enzymatic glucose biosensor is in alkaline or neutral conditions as the hydrous oxide layer is formed in alkaline conditions. An acidic electrolyte results in destabilizing the transition metal oxide [12]. The mechanism is illustrated in Figure 6.4b.

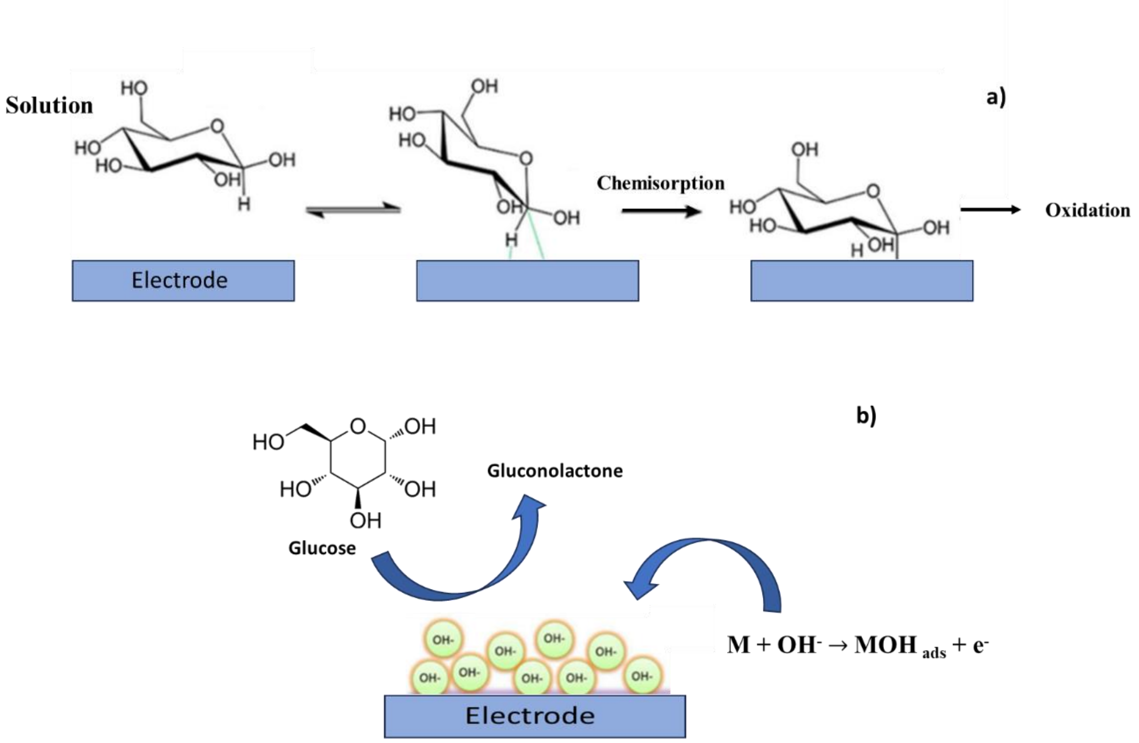

Figure 6.4. non- enzymatic mechanism: (a) activated chemisorption model and (b) incipient hydrous oxide adatom mediator (IHOAM) model.

6.4. Electrochemical Glucose sensors based Nickelferrite ($NiFe_2O_4$)

6.4.1 Introduction

The final part of the fifth chapter the development of a nickel ferrite based conductometric gas sensor was discussed. In this part, the same materials will be used to develop an electrochemical sensor for detecting glucose in the blood. A brief introduction on $NiFe_2O_4$ and their importance has already been covered. Here, the paragraph will focus on the electrochemical part, discussing the techniques and data obtained (see paragraph 5.5.1).

6.4.2 Electrochemical technique

Electrochemical methods are techniques used in the study of chemistry systems, are widely applied to detect and quantify concentrations of analytes in solutions through measurement of potential, charge or current. According to the electrical potential adopted they are classified as potentistatic, potentiometric and impedance. Each method requires the presence of *electrodes* and an *electrolyte solution*. One of the electrodes detects the concentration of the analyte and another reference electrode at constant potential, independent of the properties of the solution. The electrodes are placed inside a *cell* divided into electrolytic (uses an external energy source) and galvanic (produces electrical energy) [17]. Electrodes are connected to a potentiostat that allows to set and control the potential of the working electrode.

The *potentiometric method* is defined as static, whose current is apparently zero. Information on the composition of the analyte is obtained from potential measurements. Generally used to monitor ions in solution [18].

The *potentiostatic* method is a dynamic, potential-controlled technique. The studies are based on the electron transfer that occurs at the interface between the working electrode and the solution. The basic process is regulated by redox processes according to the equilibrium reaction (6.1) [17] :

$$O + ne^- \leftrightarrow R \qquad (6.1)$$

The resulting current determines the velocity of the electrons across the electrode-solution interface. The method is based on the Nernst equation according to (6.2 equation):

$$E = E^0 + \frac{2{,}3\,RT}{nF}\log\frac{C_{ox\,(t,0)}}{C_{red\,(t,0)}} \qquad (6.2)$$

R is constant gas and equal at 8,314 J K mol^{-1}, instead F is Faraday constant and equal 96,487 C. E^0 represent the reaction and if it is negative the oxidant agent is reduced, this favors the reduction reaction, the resulting current is faradic. Graphically, from the technique, a voltammogram is obtained. If the reaction is rate-bound by electroactive species, the current is regulated by mass transport. Mass transport can occur through diffusion, convention and migration. Potentiostat techniques were adopted in the work that will be discussed below together with the impedance technique.

According to the potential applied, potentiostatic techniques can be further classified into step potential, scanning potential and pulse potential methods.

The *chronoamperometry* is technique to step potential method, where a certain potential (defined by the type of analyte) is applied to the working electrode and the resulting current is monitored over time. Redox reactions occur and the mass transport of electroactive species occurs by diffusion. A diffusion process occurs according to a concentration gradient (movement of charges from an area of high charge concentration to a lower one) which occurs at the surface of the working electrode. The process explains the relationship between concentration and time. In fact, at an initial potential value the diffusion layer formed is thin, over time, this layer increases with a consequent exponential decrease in the current. The process is governed by the Cottrell equation (Equation 6.3):

$$i(t) = nFAC\sqrt{\frac{D}{\pi t}} \qquad (6.3)$$

where *i* is the current; *n* is number of transferred electrons; *F* is faraday constant; *A* is electrode surface area; *C* is the concentration of analyte; D is diffusion constant and *t* is the time. The equation allows you to determine the area of the electrode. For a time, t, the faradic current is proportional to concentration of analyte species in the solution [19].

At the scanning potential method includes *the Linear Sweep Voltammetry (LSV) and the Cyclic Voltammetry (CV)* techniques [20-22]. In the LSV the potential varies linearly over time from an initial value, whose species in solution are stable, to a higher value linked to scan rate (υ) and the variation of potential follows the equation 6.4:

$$E(t) = Ei - \upsilon\, t \tag{6.4}$$

Ei is influenced by the scan rate and can be used to obtain information about the electrochemical process. The activation of the redox process occurs when the potential reaches a value close to the discharge potential of the electroactive species, this generates a faradic current flow. The result of the measurement is the sigmoidal curve as in Figure 6.5.

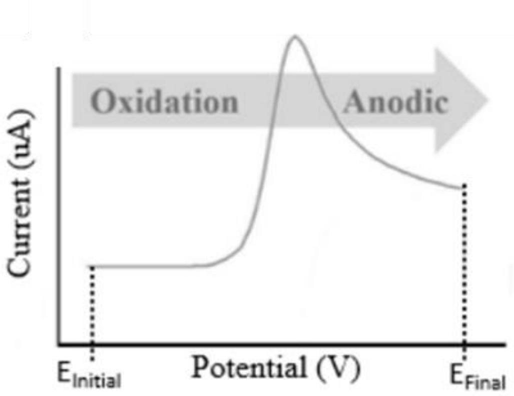

Figure 6.5. Current vs potential to potential variation.

Cyclic voltammetry (CV), on the other hand, allows the acquisition of qualitative information on the electrochemical reaction, ensuring simplicity of execution and simple interpretation of the results. Often used as a preliminary investigation technique because allows you to obtain information on the thermodynamic, kinetic (i.e. electron transfer) or adsorption processes of the redox reactions of interest. the potential periodically oscillates between two values, the speed of these oscillations depends on the scan rate. The generated voltammogram has the potential on the *X* axis and the current on the *Y* axis. By varying the potential, an exchange of electrons will take place with the working electrode, therefore the current will vary, in particular there will be a peak of oxidation current (cathodic potential) at a certain potential which depends on the chemical species analyzed. When the reaction is reversible, by inverting the potential a reduction (anodic potential) will occur and the current circulating in the electrodes will have the opposite direction. These two peaks represent the oxidation-reduction potentials. The concentration of the analyte can be deduced from the width of the peaks, generally the peaks increase as the concentration of the analyte increases. For a reversible redox process, the following equation is written:

$$i = (2{,}69 \, * \, 10^5) n^{3/2} \, ACD^{1/2} \upsilon^{1/2} \tag{6.5}$$

explained by the fact that the current *i* is t $^{1/2}$, therefore independent of the applied potential, in Figure 6.6 the trend of the voltammogram.

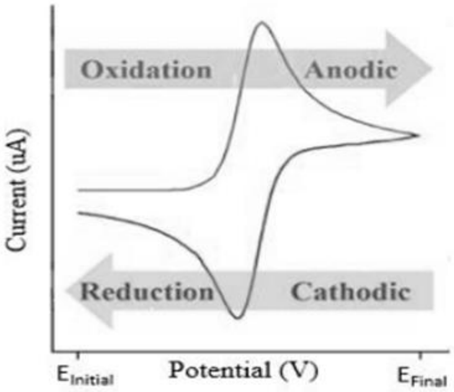

Figure 6.6. Current vs potential to potential variation for CV technique.

Differential Pulse Voltammetry (DPV) and Square Wave Voltammetry (SWV) techniques belong to pulse potential methods. The DPV it is an electrochemical technique that allows to measure current variations as a function of a potential. In this case the applied potential is an increasing impulsive potential (unlike CV which uses a linear potential). The current is measured an instant before the pulse and an instant after the pulse, in this way the decay of the capacitive current is allowed [23,24]. In Figure 6.7. an example of voltammogram.

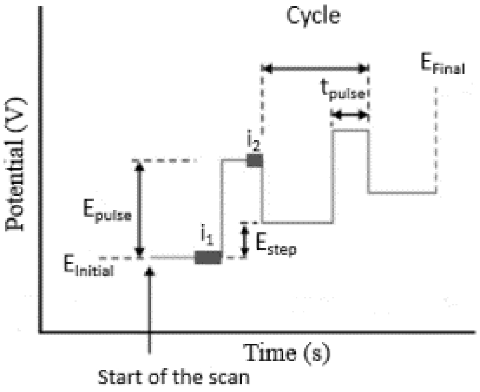

Figure 6.7. DPV voltammogram: potential vs time.

The SWV voltammogram also shows the typical waveform of the potential in the case of square wave voltammetry. The potential pulses are applied in succession without time lapse. The absence of the gap prevents the working electrode from recovering the diffusion layer, this factor distinguishes the technique from DPV. The variables to consider are the pulse width ΔE, the pulse width t_p and the potential step ΔE_x. The pulse width can also be expressed as a function of time, $f=1/2t_p$. However, the direct pulse value causes oxidation of the species, while the reverse impulse introduces their reduction. The current is instead recorded at the end of the second pulse which has the opposite effect direction. So, in the square wave voltammetry method, the current is sampled twice for each potential cycle [25].

Another technique that was used: the *impedance* technique is precisely defined Electrochemical Impedance Spectroscopy (EIS) [26]. Impedance spectroscopy allows to analyze the trend of the material's impedance when the transfer of electrical charges occurs in the redox reaction. In this technique an alternating signal of the type (6.6 equation):

$$E = E^0 \sin(\omega t) \tag{6.6}$$

is used, where E^0 represents the amplitude of the alternating signal, which is set by the person carrying out the measurement, the pulsation ω is equal to $2\pi f$. Impedance is a quantity studied in complex form:

$$Z = A + jB \tag{6.7}$$

There are two types of representation for EIS analysis, the Nyquist diagram and the Bode diagrams. In the *Nyquist diagram* it is represented on the *X* axis the real part of the impedance (i.e. the resistive part) while in the *Y* axis the imaginary part of the impedance taken with the minus sign (because it is generally of the capacitive type i.e $-\frac{1}{j\omega C}$). In the *Bode diagram*, however, the pulsation in the *X* axis is represented and the impedance modulus $|Z|$ in the *Y* axis. Typically, the Nyquist diagram is used for EIS analysis.

6.4.3 Modified electrode fabrication and Electrochemical measurements

The SPCEs platform was adopted to develop the electrochemical glucose sensor. It is a ceramic substrate with a length of 3.5 cm and a diameter of 4 mm. The electrochemical cell is made by three components as a carbon working electrode, a silver pseudo-reference electrode and a carbon counter electrode. The platform was purchased from DropSens (Methrom), in Figure 6.8 the representation of the SPCEs platform. The modified $NiFe_2O_4$/SPCE sensors were developed using a dispersion solution of 1 mg of nanomaterial on 1mL of distilled water sonicated for 15 min. A drop of 5 µL of the dispersion has been deposited on carbon working electrode. After dropping, the electrode is left to dry at room temperature.

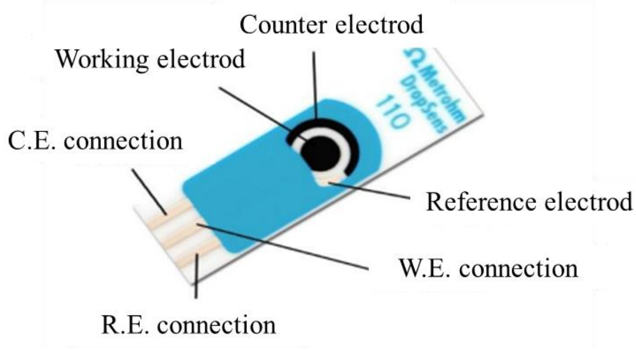

Figure 6.8. SPCEs platform used in electrochemical tests.

Cyclic Voltammetry (CV) is the first technique adopted for the first tests on nickel ferrite ($NiFe_2O_4$) samples. For the measurement, an initial and final voltage range from 0.2 Volt to 0.8 Volt was set. The measurements were carried out in a basic solution of 0.1 M NaOH and the others by adding 1 mM glucose from time to time (corresponding to 40 µL) starting from a concentration of 0.1 mM up to 10 mM. Below are the graphs obtained with the measurements for the various sensors (Figure 6.9 a, b and c). A peak at a potential of approximately 0.60 Volt was observed in the first measurements, in agreement with data in literature [27]. A current variation was observed for the NiF2 and NiF4 sensors, while the NiFe1 sensor showed insignificant current variations.

In addition, the results obtained were compared with other techniques, such as the **Differential Pulse Voltammetry (DPV)** technique, in the potential range from 0.2 to 0.8 Volt and scan rate of 0.01 V/s (Figure 6.10 a,b and c) and the **Square Wave Voltammetry (SWV)** in the same potential range at a frequency of 5Hz (Figure 6.11 a,b and c). For both technique

(DPV and SWV) a greater current variation was observed for the NiF4 sensor. Differently from the CV technique, the current decreases as the analyte concentration increases.

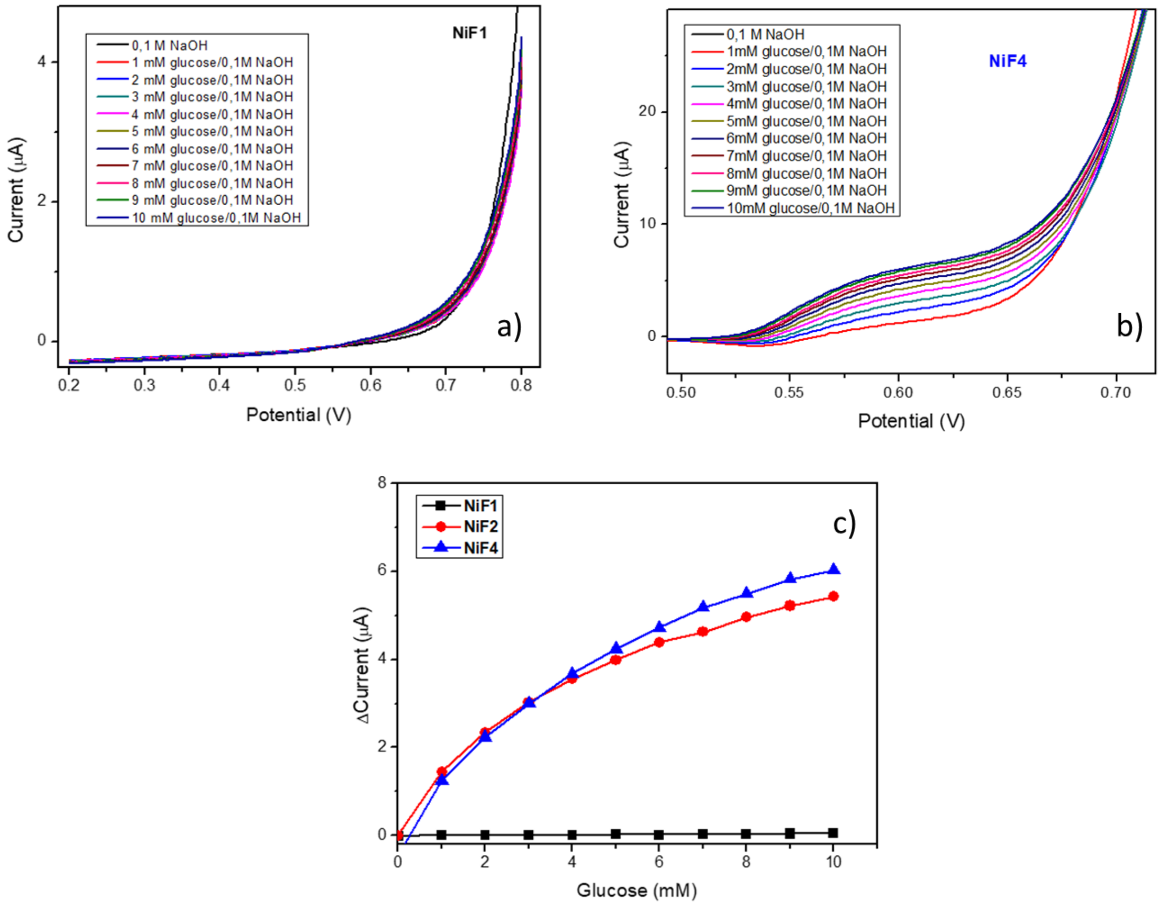

Figure 6.9. (a) CV voltammogram of NiF1 sensor; (b) CV voltammogram of NiF4 sensor and (c) CV calibration curve Δcurrent vs glucose concentration.

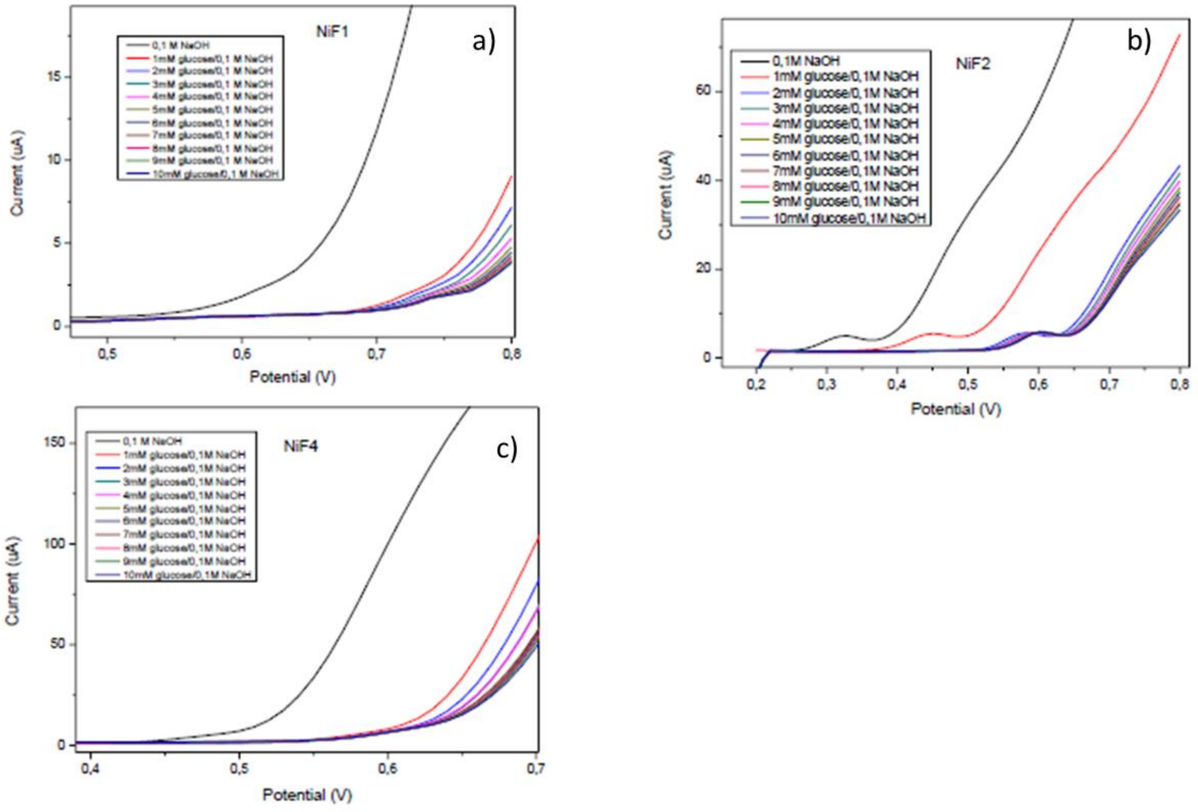

Figure 6.10. DPV voltammograms of all sensors.

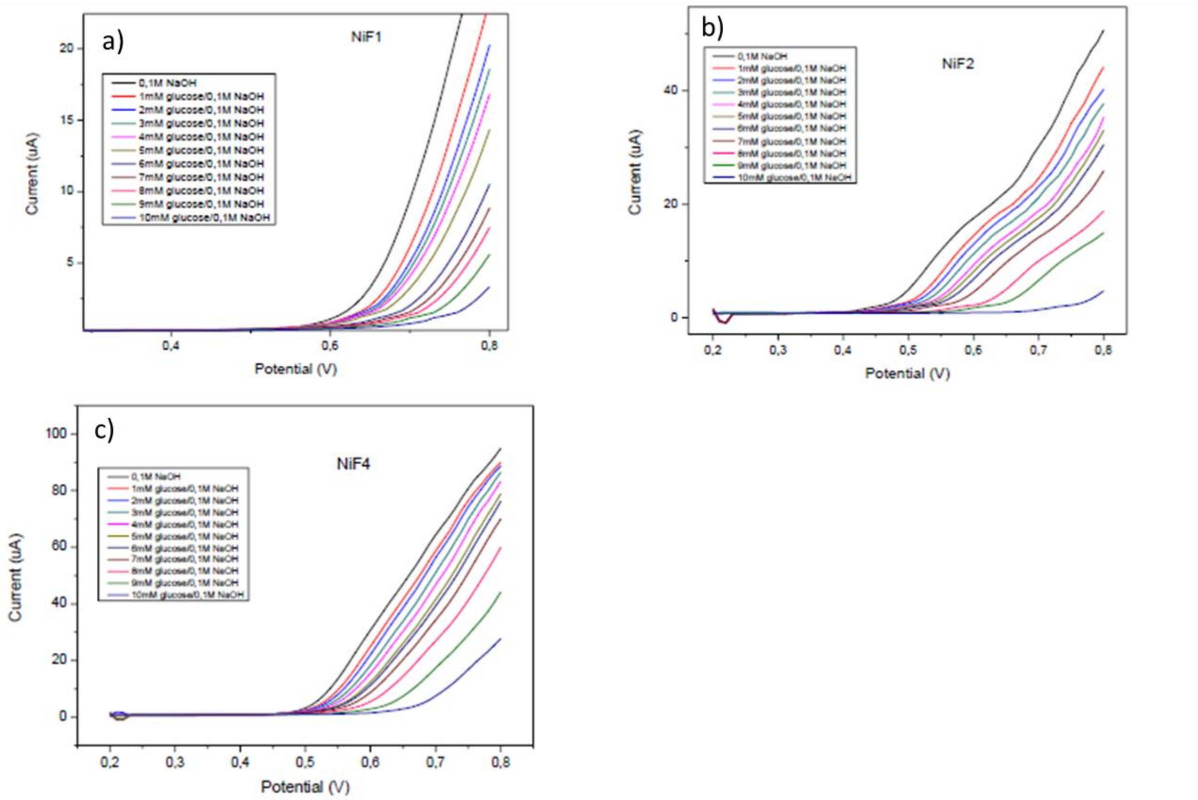

Figure 6.11. SWV voltammograms of all sensors.

The **EIS** technique allows to analyze the variation in impedance of the device as the frequency of the applied signal varies. Each point on the graph represents the impedance measured at different frequency values. Generally, the impedance is maximum at low frequencies and decreases as the frequency increases. The following Figures 6.12 a, b and c show the Nyquist diagrams recorded for the various sensors investigated at different glucose concentrations.

The diagrams shown provide information on how the imaginary part of the impedance grows compared to the real part. It is possible to see from the Nyquist diagrams that the NiF4-based device has a lower impedance in the absence of glucose. In the presence of glucose, the largest impedance changes are once again seen with the NiF4 sensor.

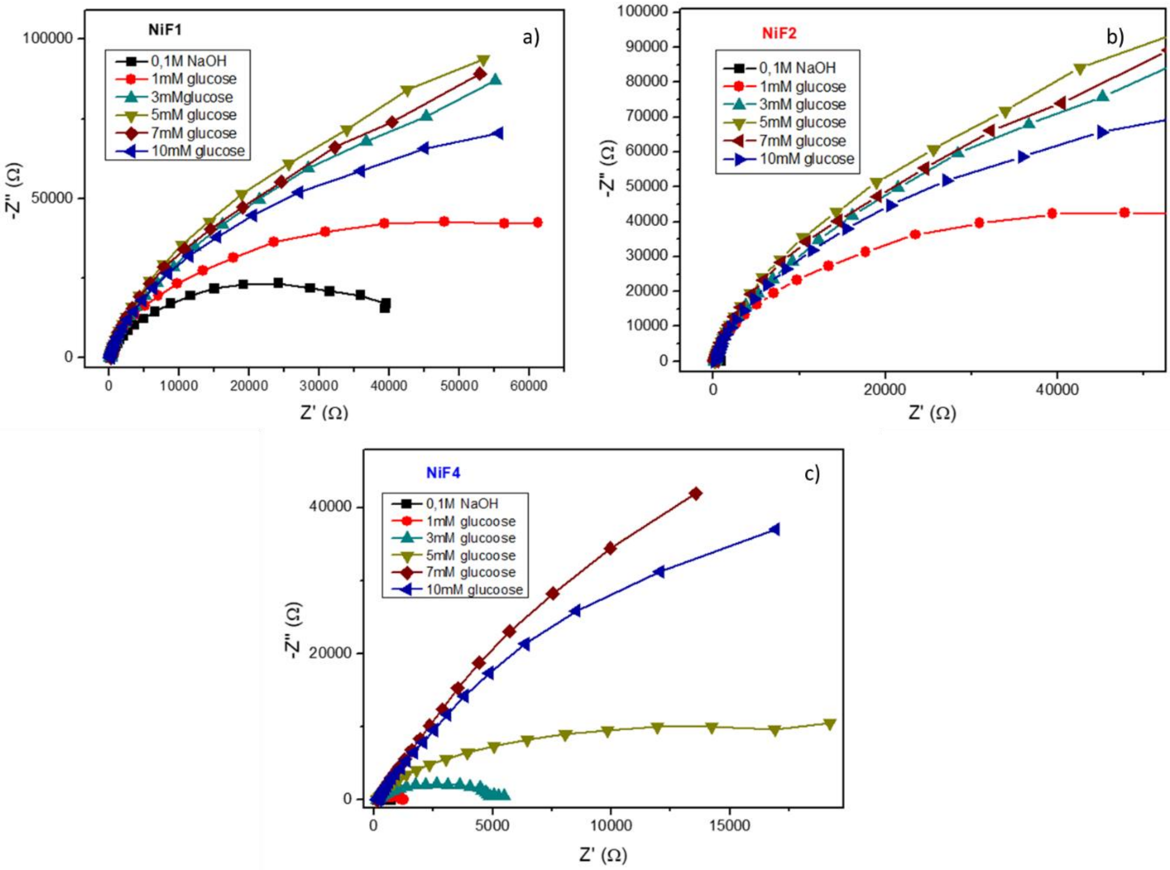

Figure 6.12. Nyquist diagrams: (a) NiF1 sensor; (b) NiF2 sensor and (c) NiF4 sensor.

The **amperometric** method was adopted for subsequent tests. An adequate potential of 0.6 Volt was set, identified *via* cyclic voltammetry and the changes in current measured with each addition of glucose. The measurements were performed with the solution continuously stirred using a small magnet. a calibration curve was also plotted to understand which device presents the greatest current variation. For the NiF1 sensor we noticed that the current increases up to a concentration of 4 mM glucose, at higher concentrations the device no longer provides appreciable increases in current. However, the maximum current that the device provided is approximately 0.08 μA and the variations are very small. For the device with NiF4 it is also noted in this case that the current increases as the glucose concentration increases. This time the maximum current observed is approximately 3 - 4 μA, with larger current variations, in agreement with what was detected via voltammetry and DPV. Figures 6.13 a and b show the chronoamperometric response of the NiF4 sensor to different glucose concentrations and the calibration curve respectively. The calibration curve highlights the NiF4 current variation.

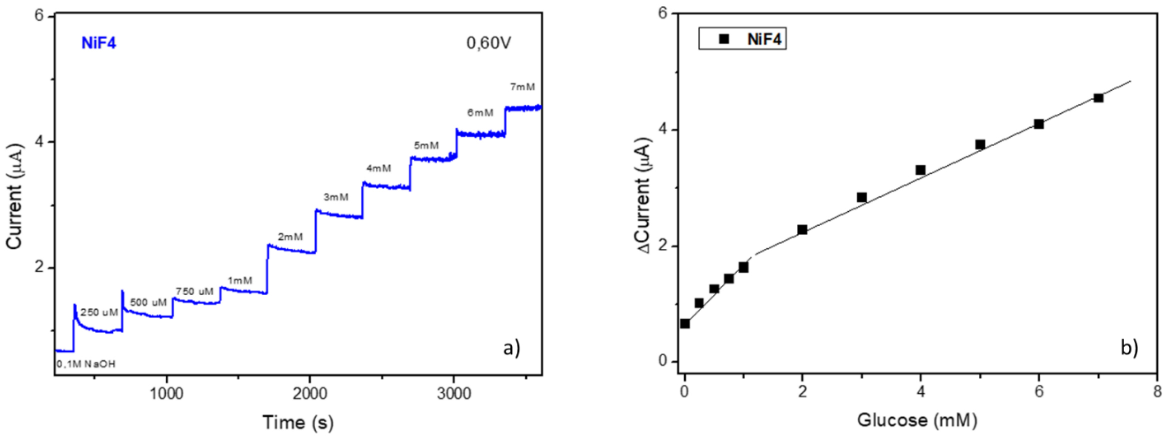

Figure 6.13: (a) Chronoamperometry measurement on NiF4 sensor and (b) calibration curve of NiF4 sensor.

6.4.4 Selectivity tests and Real sample tests

To evaluate the possibility of using this sensor in a real matrix such as blood, selectivity tests were preliminarily carried out towards other interfering analytes present in this physiological fluid. Selectivity tests were then performed for the NiF4 electrode in the presence of glucose interferents, such as Na^+, Ca^{2+}, Mg^{2+}, Fe^{3+}, dopamine, ascorbic acid, uric acid and phenylalanine. Figure 6.14 shows the responses of the NiF4 electrode to glucose compared with those obtained with the other interfering analytes. From the graph you can see how the response to glucose is much higher than that of the other analytes. We can therefore state that there should be no interference when the sensor is used for use with real blood samples.

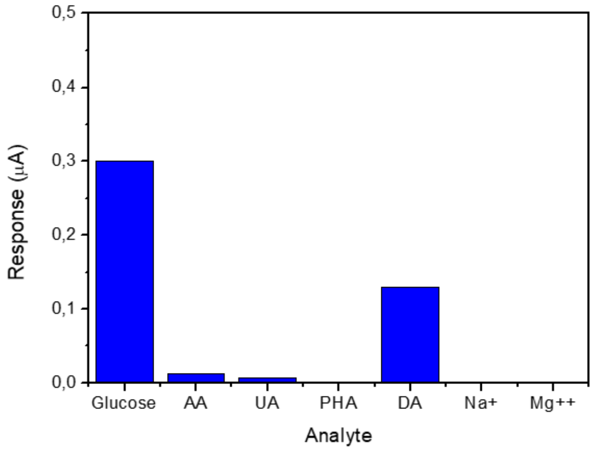

Figure 6.14. Selectivity tests: Chronoamperometric response of the NiF4 sensor in the presence of glucose and other interfering substances.

Tests with a real blood sample were carried out for the NiF4 device. A starting solution of 0.1 M NaOH was used to which a known quantity of blood was added. The amount of glucose in the blood was determined using the *addition method* where known amounts of glucose were added to the known amount of blood (Figure 6.15a). The sensor response is shown in Figure 6.15b. The glucose concentration of the blood sample thus determined is 4.8 mM, in agreement with that determined with the official method (4.4 mM).

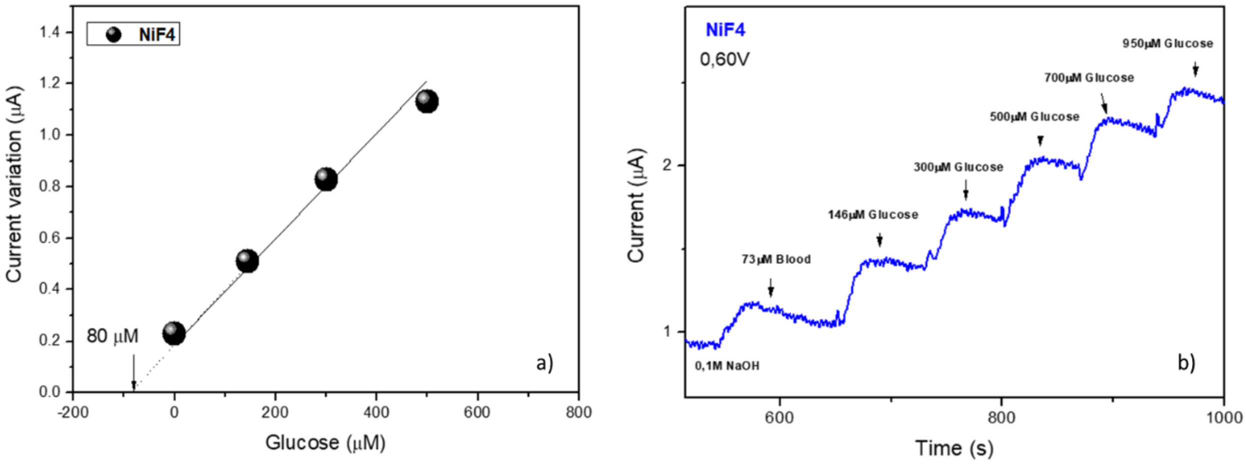

Figure 6.15: (a) Calculation of the concentration with the *successive addition* method and (b) Chronoamperometric response of the NiF4 sensor in the presence of a blood sample.

6.4.5 Electrochemical behavior

In section 5.3 we described two possible mechanisms that occur at the electrode-solution interface. In the case of this work, three different sensors were developed of which different nickel ferrites ($NiFe_2O_4$) were deposited on each electrode.

As already described, nickel ferrites have been distinguished into NiF1, NiF2 and NiF4 according to the different reagents used. In summary, the starting solution contained an aqueous solution containing the precursors Fe, Ni and hibiscus extract. NH_3 was added to the starting solution for NiF1, for NiF2 instead NH_3 and the amine HTMA, for NiF4 only HTMA and NaOH instead of ammonia. The addition of different compounds to the starting solution influenced the chemical composition of each individual nickel ferrite. The same atomic percentage of Fe was found in the three samples, but a different percentage of Ni was observed, which decreases from NiF1 to NiF4. The crystalline structure also changes, for NiF1 the nickel ferrite phase was observed while an additional phase (hematite) was observed for NiF2 and NiF4.

Having briefly summarized the characteristics of the nanomaterials deposited on the electrodes we can discuss the mechanism that occurred in the electrochemical cell. The electrochemical measurements carried out with the different techniques were observed in alkaline conditions in a 0.1M NaOH solution with the addition of different concentrations of glucose. In the first CV data different signal trends were found. NiF1 did not show any current variations, unlike the two samples NiF2 and NiF4 whose variations were observed. The same data were found for the other techniques used (DPV, SWV, EIS and chronoamperimetry). NiF4 has been considered the best performing sensor in glucose detection.

The oxidation of glucose is more favored for the NiF4 sample as the surface is different, as it was obtained from a treatment with NaOH and HTMA which could influence the reaction mechanisms with glucose, probably due to the greater quantity of OH^- on the surface of the electrode.

6.4.6 Conclusions

In this paragraph, the development of a sensor for glucose monitoring with enzyme-free sensors based on nickel-ferrite nanomaterials was presented. The nanomaterials were prepared and deposited on the carbon-based working electrode of commercial screen-printed devices and subsequently their performance in glucose monitoring was analyzed using different electrochemical techniques. The results obtained allowed us to define the sensor based on the NiF4 nanomaterial as the best performing among those investigated for glucose monitoring. Finally, it was demonstrated that the chronoamperometric technique is particularly effective for carrying out the tests, allowing the quantification of glucose in a real matrix (blood) in accordance with the data of the official analysis method.

6.5. References

1. N. Bhalla, P. Jolly, N. Formisano, P. Estrela, *Introduction to biosensors*, Biochemistry Essays 60 (2016) 1–8.
2. C. Dincer, R. Bruch, E. Costa-Rama, M.T. Fernández-Abedul, A. Merkoçi, A. Manz, G.A. Urbano, F. Güder, *Disposable sensors in diagnostics, food and environmental monitoring*, Avv. Mater. 31 (2019) 1806739.
3. V. Naresh and N. Lee, *A Review on Biosensors and Recent Development of Nanostructured Materials-Enabled Biosensors*, Sensors 21 (2021) 1109.
4. H. Liu, J. Ge, E. Mamma, L. Yang, *Advanced biomaterials for biosensors and theranostics*, Biomaterials in Translational Medicine, 1a ed.; L. Yang, S. Bhaduri, T. Webster, Academic press: Cambridge, MA, USA (2019) 213–255.
5. A. Dhiman, P. Kalra, V. Bansale, J.B. Bruno, T.K. Sharma, *Point-of-care diagnostic platforms based on Aptamer*, Sensors and Actuators Chem. B 246 (2017) 535–553.
6. N. Kylilis, P. Riangrungroj, H.-E. Lai, V. Salema, L.F. Fernaández, G.-B.V. Stan, P.S. Freemont, K.M. Polizzi, *Whole-cell biosensor with tunable limit of detection enables low-cost agglutination assays for medical diagnostic applications*, ACS Sensors 4 (2019) 370–378.
7. K.R.B. Singh, V. Nayak, T. Sarkar, R.P. Singh, *Cerium oxide nanoparticles: properties, biosynthesis and biomedical application*, RSC Avv. 10 (2020) 27194–27214.
8. B.D. Malhotra, M.A. Ali, *Nanomaterials in biosensors: Fundamentals and applications*, Nanomaterials for Biosensors, 1st ed.; B.D. Malhotra, , M.A. Ali, Eds. Elsevier: Cambridge, MA, USA (2017) 1–73.
9. A.M. Pisoschi, *Potentiometric biosensors: concept and analytical applications*, An editorial. Biochemistry. Anal. Biochemistry 5 (2016) 19–20.
10. R. Radhakrishnan, I.I. Suni, C.S. Bever, B.D. Hammock, *Impedance biosensors: Applications to sustainability and remaining technical challenges*, ACS Sustain. Chem. Eng. 2 (2014)1649–1655.
11. S. Dzyadevych, N.J. Renault, *Conductometric biosensors*, Biological Identification, 1a ed.; R.P. Schaudies, ed.; Elsevier: Cambridge, MA, USA (2014) 153–193.

12. N. M. Nor, N. S. Ridhuan and K. A. Razak, *Progress of Enzymatic and Non-Enzymatic Electrochemical Glucose Biosensor Based on Nanomaterial-Modified Electrode*, Biosensors 12 (2022) 1136.
13. J. Kitikul, S. Satienperakul, A. Preechaworapun, P. Pookmanee, T. Tangkuaram, *A simple flow amperometric electrochemical biosensor based on chitosan scaffolds and modified gold nanowires on a glassy carbon electrode for the detection of glutamate in food products*, Electroanalysis 29 (2017) 264–271.
14. G. Shruthi, C. Amitha, B.B. Mathew, *Biosensors: A Modern-Day Achievement*. J. Instrum. Tech. 2 (2014) 26–39.
15. C. Chen, Q. Xie, D. Yang, H. Xiao, Y. Fu, Y. Tan, S. Yao, *Recent advances in electrochemical glucose biosensors: a review*, RSC Avv. 3 (2013) 4473–4491.
16. M. Tasviri, H.-A. Rafiee-Pour, H. Ghourchian, M.R. Gholami, *Amine functionalized* TiO_2 *coated on carbon nanotube as a nanomaterial for direct glucose oxidase electrochemistry and glucose biosensing*, J. Mol. Catal. Enzyme B. 68 (2011) 206–210.
17. J. Wang, *Analytical Electrochemistry*, second edition Wiley-VCH (2000). ISBNs: 0-471-22823-0.
18. A.J. Bard and L.R. Faulkner, *Fundamentals and applications*, Electrochemical methods, 2(482) (2001) 580-632.
19. G. Inzelt, *Chronoamperometry, Chronocoulometry, and Chronopotentiometry*, in Encyclopedia of Applied Electrochemistry, G. Kreysa, K.-i. Ota, and R.F. Savinell, Editors. (2014) Springer New York: New York, NY. 207-214.
20. *Linear Sweep and Cyclic Voltametry: The Principles*, Available from: https://www.ceb.cam.ac.uk/research/groups/rg-eme/Edu/linear-sweep-andcyclic-voltametry-the-principles.
21. *Chemical dictionary*. Available from: https://www.chemicool.com/definition/linear_sweep_voltammetry.html.
22. B. Rezaei, and N. Irannejad, Chapter 2 - *Electrochemical detection techniques in biosensor applications*, in Electrochemical Biosensors, A.A. Ensafi, Editor. (2019) Elsevier. 11-43.
23. F.R. Simões, and M.G. Xavier. 6 – *Electrochemical Sensors* (2017).

24. , N. Aqmar et al. *Embedded 32-bit differential pulse voltammetry (DPV) technique for 3-electrode cell sensing*, in IOP Conference Series: Materials Science and Engineering, (2018) IOP Publishing.
25. V. Mirceski et al., *Square-wave voltammetry: a review on the recent progress,* Electroanalysis 25(11) (2013) 2411-2422.
26. B.-Y. Chang and S.-M. Park, *Electrochemical Impedance Spectroscopy*, Annu. Rev. Anal. Chem. 3 (2010) 207–29.
27. M. H. Raza, K. Movlaee, Y. Wu, S. M. El-Refaei, M. Karg, S. G. Leonardi, G. Neri, and N. Pinna, *Tuning the NiO Thin Film Morphology on Carbon Nanotubes by Atomic Layer Deposition for Enzyme-Free Glucose Sensing*, ChemElectroChem 6 (2019) 383–392.

Chapter 7: General Conclusions

7.1 Conclusions

This thesis and the entire PhD project focused on the development of chemical sensors, such as conductometric gas sensors and in the final part, glucose biosensors. The objective was to develop sensors for environmental monitoring given the importance of the topic and given the need to develop new sensors as the classic techniques involve a waste of time and high costs to carry out simple routine monitoring.

The introductory part of the thesis in fact discussed the environmental impacts caused by the emissions of pollutants and the current monitoring systems for each individual pollutant. We discussed how traditional monitoring systems are not as versatile as sensors. This is where the entire topic of the thesis connects.

A brief overview was given by classifying the sensors and chemical sensors and then focusing on chemoresistive sensors. Chemoresistive sensors were discussed in detail, dealing with the mechanisms, interference phenomena, and then followed by discussing the sensitive materials that can be adopted and the synthesis methods to develop them. Subsequently, everything related to the design and manufacturing of a chemoresistive sensor was discussed, describing the possible techniques for deposition of the sensitive material on the device and the type of device adopted.

The fourth and fifth chapters represent the heart of the thesis and concern all the research activity carried out during the entire PhD period. The experimental part has been divided into two chapters to highlight everything concerning the design of a conductometric gas sensor and the applications of the developed nanomaterials. In fact, the fifth chapter focused on the synthesis, characterization and deposition of the sensitive material on the device and instrumental apparatus used; the sixth was further divided by classifying the nanomaterials according to the synthesis methods and treated in detail.

Briefly summarizing the nanomaterials from which the sensors were obtained we can say that:

- from the adoption of the **sol-gel method** two new sensitive materials have been obtained, Al,Ca doped-ZnO and an heterojunction of Co_3O_4/Fe_2O_3.

  The performances of a conductometric HCHO gas sensor based on the Al,Ca-doped zinc oxide composite have been presented. The results demonstrated that by optimizing the doping loading, a promising sensitive material showing good sensitivity, selectivity, and reproducibility for monitoring the low concentration of HCHO in air, was obtained. The ethanol gas sensing performance of the synthesized powders was investigated at various ethanol concentrations and temperatures. A Co_3O_4/Fe_2O_3 (composition $1Co_3O_4/0.8Fe_2O_3$) nanocomposite was developed showing good sensitivity to ethanol at a temperature of 250 °C. The improved gas sensing properties of the composite sensor were mainly due to the increased modulation of the conduction channel width and the modulation of the potential barrier formed. Furthermore, the observed difference in the morphology, microstructure, and optical energy band gap of the composite samples is also suggested to play a determining role in the observed difference in gas sensing performance compared to the target gas.

- Carbon dots was developed from **pyrolysis method** using olive waste of different geographic origins which resulted in sensitivity to different gases, NO and NO_2. We observed opposite sensitivity and selectivity towards these gases, which has been explained by the presence of different functional groups on the surface of these CDs. We believe that developing controllable synthetic and production methods, will greatly extend the application of CDs-sensors for other target gases.

- **ALD** has given the possibility to synthesize and obtain films with controlled thickness, in fact new heterojunctions as sensitive material have been developed. CNT/WS_2 core-shell heterostructures were prepared of tungsten disulfide (WS_2) on carbon nanotubes (CNTs). The WS_2 shell layers showed different thicknesses and morphology depending on the number of ALD cycles. Their gas-sensing behavior was tested for the monitoring of NO_2. The tests made it possible to demonstrate that the electrical properties of CNT/WS_2 core-shell heterostructures are strongly dependent on the thickness of the WS_2 shell layer. Among CNT/WS_2 core-shell heterostructures, those having a WS_2-shell thickness in the range from 10 to 15 nm showed superior electrical capabilities.

A mesoporous titania compound was modified by doping with 35 percent in mol Nb and deposition of NiO layers via ALD. The composite was deposited directly onto the resistive device by the same ALD technique. Different sensors were obtained starting from m-TiOx and NbTiOx as reference to deposit different thicknesses of NiO. The NbTiOx sensor having a thickness of 2.60 nm (5 cycles of ALD reaction) showed performance such that it could have very good selectivity to acetone over ethanol. The surface reaction mechanism verified computational studies and confirmed the influence of NiO on the composite in comparison with other heterojunctions. The sensing mechanism is closely related to the presence of the dopant in the crystal structure and the presence of a thin NiO layer. A thin NiO thickness results in a shorter Debye length and thus a greater contribution of holes as charge carriers in the conduction process and interaction with acetone, a strongly reducing gas.

- A new synthesis method from **plant-assisted** was reported. A hibiscus flower extract was used as a precursor to develop nickel ferrites ($NiFe_2O_3$). The NiF4 sensor has been proven to perform better in detecting NO_2.

- A Mnx-Zn-ZIF based nanomaterial has been developed through the co-precipitation method, a new simple and green method to obtain Metal Organic Framework (MOF). A highly selective resistive sensor for the gaseous chemical species NO_2 and ethanol operating at different temperatures. This invention is the subject of a patent filing. The main advantages of this new material compared to the common ZIF-8 concern the increase in thermal stability, high sensitivity at low temperatures and good selectivity. All these advantages make this material interesting for future applications in the sensor sector for environmental and industrial monitoring.

The development of a glucose biosensor was discussed in Chapter 7 to distinguish it from gas sensors. In this part we found a good sensitivity of the same nickel ferrite NiF4 seen previously for glucose, obtained from a new synthesis method that uses hibiscus extract as a precursor. Good results were found on a real blood sample.

In this paragraph, the development of a sensor for glucose monitoring with enzyme-free sensors based on nickel-ferrite nanomaterials was presented. The nanomaterials were prepared and deposited on the carbon-based working electrode of commercial screen-printed devices and subsequently their performance in glucose monitoring was analyzed using different electrochemical techniques. The results obtained allowed us to define the sensor based on the NiF4 nanomaterial as the best performing among those investigated for glucose monitoring. Finally, it was demonstrated that the chronoamperometric technique is particularly effective for carrying out the tests, allowing the quantification of glucose in a real matrix (blood) in accordance with the data of the official analysis method.

Chapter 8: Appendix

8.1 List of publications

1. **Patent:** Conoci S., Neri G., Donato N., Moulaee K., Petralia S., Condorelli G.G., Monforte F., Crispi S., *Innovative nanostructured materials based on ZIF including Manganese for gas monitoring,* Apr. (2022).

2. S. Crispi and G. Neri, *Development of a Conductometric Sensor Based on Al,Ca-Doped ZnO for the Detection of Formaldehyde*, Sensors 22 (2022) 7465. https://doi.org/10.3390/s22197465.

3. S. Crispi, G. Nocito, F. Nastasi, G. Condorelli, A.G. Ricciardulli, P. Samorì, S. Conoci, G. Neri, *Development of a novel C-dots conductometric sensor for NO sensing*, Sensors and Actuators: B. Chemical 390 (2023) 133957. https://doi.org/10.1016/j.snb.2023.133957.

4. M. Khan, S. Crispi, M. Hussain, Z. Sarfraz, and G. Neri, *Gas sensing performance of Fe2O3-Co3O4 nano heterojunctions for ethanol detection,* J Mater Sci: Mater Electron (2023) 34:1982. https://doi.org/10.1007/s10854-023-11340-7.

5. M. Khan, A. Ferlazzo, S. Crispi, M. Hussain, and G. Neri, *Easy preparation of cobalt oxide/copper oxide composites for gas sensing application, Phys. Scr.* **98**(2023) 125927. https://doi.org/10.1088/1402-4896/ad0821

8.2 List of conference

1. 10-13 September 2023, **XXXV Eurosensors Conference**, Poster presentation: "*Development of biomass-derived NO and* NO_2 *conductometric sensors*".

2. 3-4 March 2023, **International Conference on Global Warming, Climate Change and Pollution Control (GWCCPC-23)**, Project "*Effect of* Ag_2O *promoter in* Co_3O_4 *for* H_2 *Sensing*".

3. 22-23 June 2022, **IX Workshop Interdivisional Group Green Chemistry**, Oral presentation: "Development of sensors for monitoring indoor environments", Pavia, Italy.

4. 16-18 June 2022, **National IX Workshop AICIng,** Oral presentation: "*Gas sensing modulation of CNTs and m-TiO2 nanomaterials by atomic layer deposition (ALD)*", Ancona, Italy.

5. 5 May 2022, **Seminary organized by Department of Engineering**, "Development of sensors for environmental monitoring", Messina, Italy.

6. 10-11 Febr. 2022, **XXI National Conference Sensors and Microsistems, AISEM**, Oral presentation "*Carbon dots as a novel sensing material for Nitrogen Monoxide*", Rome, Italy.

7. 5-8 Sept. 2021, **XII National Conference AICIng**, Oral presentation: "*Sensors for monitoring the quality of the living environment",* Reggio Calabria, Italy.

8. 25 February, 23 March, 11 May and 9 June 2021, **Cycle of seminary Horizon Europe**, Messina, Italy.

8.3 List of Schools

1. 24-26 Nov. 2021, **VI National School of Environmental monitoring "Conteminated sites"**, Rome, Italy.

2. 4-10 July 2021, **Green Chemistry Summer School,** Poster presentation *"Sensors for monitoring the quality of the living environment",* Venice, Italy.

8.4 Additional activities

1. 2021-2023: Participation at the **formative lessons** offered by the Department of Engineering at the University of Messina, Messina, Italy.

2. May-December 2023**: Chemistry Course Tutor** for Engineering Department students, Messina, Italy.

3. 1 september- 18 December 2022: **Research activities in Europe** at Humboldt University of Berlin, Germany.

4. September 2022: Online Participation in the **course** "*Contesti applicativi di materiali macroporosi silossanici: dalla progettazione alla verifica sperimentale*" organized by Elpida Piperopoulos, Luigi Calabrese, and Claudia Espro, Messina, Italy.

5. July 2022: Participation in the **course** "*Materiali nanostrutturati per applicazioni in sistemi di conversione energetica*" organized by Prof.ssa R. Passalacqua, Messina, Italy.